

AD-A148 084

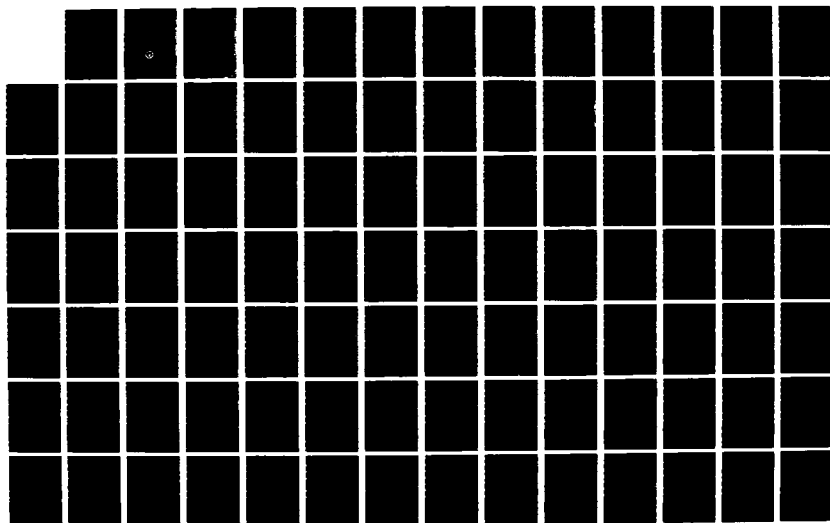
THE SHOCK AND VIBRATION BULLETIN PART 3 STRUCTURAL  
ANALYSIS FATIGUE(U) NAVAL RESEARCH LAB WASHINGTON DC  
SHOCK AND VIBRATION INFORMATION CENTER SEP 78  
BULL-48-PT-3

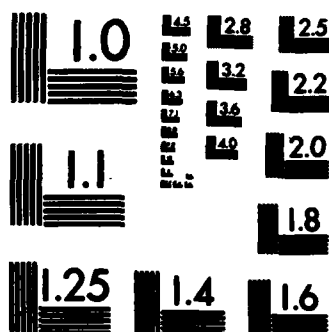
1/2

UNCLASSIFIED

F/G 20/11

NL





MICROCOPY RESOLUTION TEST CHART  
NATIONAL BUREAU OF STANDARDS-1963-A

# **THE SHOCK AND VIBRATION BULLETIN**

**Part 3**  
**Structural Analysis, Fatigue**

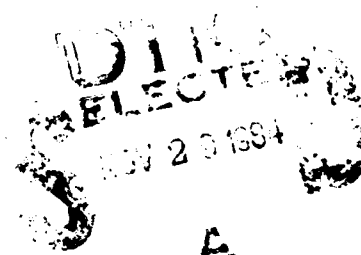
**SEPTEMBER 1978**

**A Publication of  
THE SHOCK AND VIBRATION  
INFORMATION CENTER  
Naval Research Laboratory, Washington, D.C.**



**Office of  
The Director of Defense  
Research and Engineering**

**Approved for public release; distribution unlimited.**



**A**

**84 11 26 198**

**DTIC FILE COPY**

**AD-A148 084**

**SYMPOSIUM MANAGEMENT**

**THE SHOCK AND VIBRATION INFORMATION CENTER**

**Henry C. Pusey, Director  
Rudolph H. Volin  
J. Gordan Showalter  
Barbara Szymanski  
Carol Healey**

**Bulletin Production**

**Graphic Arts Branch, Technical Information Division,  
Naval Research Laboratory**




**Bulletin 48**  
**(Part 3 of 4 Parts)**

# **THE SHOCK AND VIBRATION BULLETIN**

**September 1978**

**A Publication of  
THE SHOCK AND VIBRATION  
INFORMATION CENTER  
Naval Research Laboratory, Washington, D.C.**

**The 48th Symposium on Shock and Vibration was held at the Von Braun Civic Center, Huntsville, Alabama on October 18-20, 1977. The U.S. Army Missile Research and Development Command, Redstone Arsenal, Huntsville, Alabama was the host.**

  
**Office of  
The Director of Defense  
Research and Engineering**

Accession For

NTIS GPR&I

DTIC TAB

Unannounced

Justification

A-1

# CONTENTS

## PAPERS APPEARING IN PART 3

Partial contents:

### Structural Analysis - -

A SOURCE OF LARGE ERRORS IN CALCULATING SYSTEM FREQUENCIES, R.M. Mains, Washington University, St. Louis, MO	1
RESEARCH METHOD OF THE EIGENMODES AND GENERALIZED ELEMENTS OF A LINEAR MECHANICAL STRUCTURE, R. Fillod and J. Piranda, Laboratoire de Mécanique Appliquée, Besancon, France	5
CALCULATION OF NATURAL FREQUENCIES AND MODE SHAPES OF MASS LOADED AIRCRAFT STRUCTURES, P.W. Whaley, Air Force Flight Dynamics Laboratory, Wright-Patterson AFB, OH	13
ROCKET MOTOR RESPONSE TO TRANSVERSE BLAST LOADING, N.J. Huffington, Jr. and H.L. Wisniewski, U.S. Army Ballistic Research Laboratory, Aberdeen Proving Ground, MD	21
EXPERIMENTAL AND THEORETICAL DYNAMIC ANALYSIS OF CARBON-GRAPHITE COMPOSITE SHELLS, A. Harari and B.E. Sandman, Naval Underwater Systems Center, Newport, RI	33
USE OF SHOCK SPECTRA TO EVALUATE JITTER OF A FLEXIBLE MANEUVERING SPACECRAFT, W.J. Kacena, Martin Marietta Corporation, Denver, CO	39
BUCKLING OF EULER'S ROD IN THE PRESENCE OF ERGODIC RANDOM DAMPING, H.H.E. Leipholz, University of Waterloo, Waterloo, Ontario, Canada	49
WAVE PROPAGATION IN A CYLINDRICAL SHELL WITH JOINT DISCONTINUITY, A. Harari, Naval Underwater Systems Center, Newport, RI	53
RESPONSE TO MOVING LOADS OVER A CRYSTALLINE HALF-SPACE, S. De, Old Engineering Office, West Bengal, India	63

(cont)

- **ADJUSTMENT OF A CONSERVATIVE NON GYROSCOPIC MATHEMATICAL  
MODEL FROM MEASUREMENT**, ..... 71  
L. Bugeat, R. Fillod, G. Lallement, and J. Piranda, Laboratoire de  
Mecanique Appliquee, Besancon, France

- **FIRST-PASSAGE FAILURE PROBABILITY IN RANDOM VIBRATION  
OF STRUCTURES WITH RANDOM PROPERTIES**, ..... 83  
N. Nakagawa, and R. Kawai, Kobe University, Kobe, Japan  
K. Funahashi, Kawasaki Heavy Industries, Ltd. Kobe, Japan

Fatigue - -

- **FRACTURE MECHANICS APPLIED TO STEP-STRESS FATIGUE UNDER  
SINE/RANDOM VIBRATION**, ..... 93  
R.G. Lambert, General Electric Company, Utica, NY

- **RANDOM FATIGUE DAMAGE APPROACH TO MACHINERY MAINTENANCE** .... 103  
T.S. Sankar and G.D. Xistris, Concordia University, Montreal, Quebec, Canada  
G.L. Ostiguy, Ecole Polytechnique, Montreal, Quebec, Canada

**PAPERS APPEARING IN PART 1**

Keynote Address

**KEYNOTE ADDRESS**

Dr. John L. McDaniel, Deputy/Technical Director, U.S. Army Missile  
Research and Development Command, Redstone Arsenal, AL

Invited Papers

**SHOCK RESPONSE RESEARCH AT THE WATERWAYS EXPERIMENT  
STATION**

Colonel John L. Cannon, U.S. Army Engineer Waterways  
Experiment Station, Vicksburg, MS

**TECHNICAL INFORMATION RESOURCES FOR THE SHOCK AND  
VIBRATION COMMUNITY**

E.J. Kolb, U.S. Army Material Development and Readiness Command  
Alexandria, VA

**EARTHQUAKES: THEIR CAUSES AND EFFECTS**

R.M. Hamilton, U.S. Geological Survey, Reston, VA

Panel Sessions

**SOFTWARE EVALUATION**

**DATA MANAGEMENT**

## Modal Test and Analysis

### **FORCE APPORTIONING FOR MODAL VIBRATION TESTING USING INCOMPLETE EXCITATION**

G. Morosow, Martin Marietta Corporation, Denver, CO  
R.S. Ayre, University of Colorado, Boulder, CO

### **ON THE DISTRIBUTION OF SHAKER FORCES IN MULTIPLE-SHAKER MODAL TESTING**

W.L. Hallauer, Jr. and J.F. Stafford, Virginia Polytechnic Institute and State University, Blacksburg, VA

### **MODAL CONFIDENCE FACTOR IN VIBRATION TESTING**

S.R. Ibrahim, Old Dominion University, Norfolk, VA

### **A BUILDING BLOCK APPROACH TO THE DYNAMIC BEHAVIOR OF COMPLEX STRUCTURES USING EXPERIMENTAL AND ANALYTICAL MODAL MODELING TECHNIQUES**

J.C. Cromer and M. Lalanne, Institut National des Sciences Appliquées, Villeurbanne, France  
D. Bonnetcase and L. Gaudriot, Metravib, Ecully, France

### **TRANSFER FUNCTION APPLICATIONS TO SPACECRAFT STRUCTURAL DYNAMICS**

J.R. Fowler, Hughes Aircraft Co., El Segundo, CA  
E. Dancy, Hewlett-Packard Co., Los Angeles, CA

### **LOAD TRANSFORMATION DEVELOPMENT CONSISTENT WITH MODAL SYNTHESIS TECHNIQUES**

R.F. Hrudá and P.J. Jones, Martin Marietta Corporation, Denver, CO

### **REDUCED SYSTEM MODELS USING MODAL OSCILLATORS FOR SUBSYSTEMS (RATIONALLY NORMALIZED MODES)**

F.H. Wolff and A.J. Molnar, Westinghouse R&D Center, Pittsburgh, PA

### **CHARACTERIZATION OF TORPEDO STRUCTURAL MODES AND RESONANT FREQUENCIES**

C.M. Curtis, R.H. Messier, and B.E. Sandman, Naval Underwater Systems Center, Newport, R.I. and  
R. Brown, Bolt, Beranek and Newman, Cambridge, MA

### **LAGUERRE FUNCTION REPRESENTATION OF TRANSIENTS**

G.R. Spalding, Wright State University, Dayton, OH

## **PAPERS APPEARING IN PART 2**

### Isolation and Damping

### **SPECIFICATION OF DAMPING MATERIAL PERFORMANCE**

D.I.G. Jones and J.P. Henderson, Air Force Materials Laboratory, Wright-Patterson AFB, OH

**A REDUCED-TEMPERATURE NOMOGRAM FOR CHARACTERIZATION OF  
DAMPING MATERIAL BEHAVIOR**

D.I.G. Jones, Air Force Materials Laboratory, Wright-Patterson AFB, OH

**COMPUTERIZED PROCESSING AND EMPIRICAL REPRESENTATION OF  
VISCOELASTIC MATERIAL PROPERTY DATA AND PRELIMINARY  
CONSTRAINED LAYER DAMPING TREATMENT DESIGN**

L. Rogers and A. Nashif, Air Force Flight Dynamics Laboratory,  
Wright-Patterson AFB, OH

**NEW STRUCTURAL DAMPING TECHNIQUE FOR VIBRATION CONTROL**

B.M. Patel and G.E. Warnaka, Lord Kinematics, Erie, PA  
D.J. Mead, The University Southampton, United Kingdom

**VIBRATIONS OF A COMPRESSOR BLADE WITH SLIP AT THE ROOT**

D.I. G. Jones, Air Force Materials Laboratory, Wright-Patterson AFB, OH  
A. Muszyńska, Institute of Fundamental Technological Research,  
Polish Academy of Sciences, Warsaw, Poland

**RESPONSE OF A HELICAL SPRING CONSIDERING HYSTERETIC AND  
VISCOUS DAMPING**

P.F. Mlakar and R.E. Walker, U.S. Army Engineer Waterways Experiment  
Station, Vicksburg, MS

**DAMPING OF AN ENGINE EXHAUST STACK**

J.J. DeFelice, Sikorsky Aircraft, Stratford, CT  
A.D. Nashif, Anatrol Corporation, Cincinnati, OH

**MULTI-VARIABLE OPTIMIZATION FOR VIBRATION ISOLATION OF  
ROAD VEHICLES**

E. Esmailzadeh, Arya Mehr University of Technology, Tehran, Iran

**ISOLATION MOUNTS FOR THE HEAO-B X-RAY TELESCOPE**

H.L. Hain, Lord Kinematics, Erie, PA  
R. Miller, American Science and Engineering, Inc. Cambridge, MA

**Impact**

**BIRD IMPACT LOADING**

J.S. Wilbeck, Air Force Materials Laboratory, Wright-Patterson AFB, OH

**FREQUENCY RESPONSE AND DIFFERENTIATION REQUIREMENTS  
FOR IMPACT MEASUREMENTS**

A.S. Hu and H.T. Chen, New Mexico State University, Las Cruces, NM

**STRUCTURAL RESPONSE OF EARTH PENETRATORS IN  
ANGLE-OF-ATTACK IMPACTS**

J.D. Colton, SRI International, Menlo Park, CA

**SCALING AND PREDICTION OF IMPACT PUNCTURE OF SHIPPING  
CASKS FOR RADIOACTIVE MATERIALS**

W.E. Baker, Southwest Research Institute, San Antonio, TX

**FINITE ELEMENT ANALYSIS OF MULTICOMPONENT STRUCTURES  
IN RIGID BARRIER IMPACTS**

J.K. Gran, L.E. Schwer, J.D. Colton and H.E. Lindberg,  
SRI International, Menlo Park, CA

**Blast**

**TESTING PIPING CONSTRAINT ENERGY ABSORBERS FOR REACTOR  
CONTAINMENT APPLICATIONS**

R.C. Yaeger and R.C. Chou, Franklin Institute Research Laboratories,  
Philadelphia, PA

**PREDICTION OF CONSTRAINED SECONDARY FRAGMENT VELOCITIES**

P.S. Westine, Southwest Research Institute, San Antonio, TX  
J.H. Kineke, Jr., Ballistic Research Laboratories, Aberdeen, MD

**IMPEDANCE TECHNIQUES FOR SCALING AND FOR PREDICTING  
STRUCTURE RESPONSE TO AIR BLAST**

F.B. Safford, Agabian Associates, El Segundo, CA  
R.E. Walker, U.S. Army Waterways Experiment Station, Vicksburg, MS  
T.E. Kennedy, Defense Nuclear Agency, Washington, DC

**PROBABILISTIC FAILURE ANALYSIS OF LINED TUNNELS IN ROCK**

D.A. Evensen and J.D. Collins, J.H. Wiggins Company, Redondo Beach, CA

**PAPERS APPEARING IN PART 4**

**Vibration Testing**

**A MATHEMATICAL METHOD FOR DETERMINING A LABORATORY  
SIMULATION OF THE CAPTIVE-FLIGHT VIBRATIONAL  
ENVIRONMENT**

S. Ogden, Pacific Missile Test Center, Point Mugu, CA

**ACOUSTICS OR SHAKERS FOR SIMULATION OF CAPTIVE  
FLIGHT VIBRATION**

A.M. Spandrio and M.E. Burke, Pacific Missile Test Center, Point Mugu, CA

**AUTOMATIC ENVIRONMENTAL CONTROL SYSTEM FOR MISSION  
PROFILE TESTING**

R. Schilken, Pacific Missile Test Center, Point Mugu, CA

**BROAD-BAND MECHANICAL VIBRATION AMPLIFIER**

R.T. Fandrich, Harris Corporation, Melbourne, FL

**STABILITY AND FREQUENCY RESPONSE OF HYDRO-MECHANICAL  
SHAKERS IN VIBRATION RIGS**

**S. Sankar, Concordia University, Montreal, Canada**

**MIL-STD-781C RANDOM RELIABILITY TESTING PERFORMED BY  
USING ACOUSTIC COUPLING**

**S.M. Landre, Harris Corporation, Melbourne, FL**

**CONSERVATISM IN RANDOM VIBRATION ANALYSIS AND TESTING**

**T.L. Paez, Sandia Laboratories, Albuquerque, NM**

**INCANDESCENT LAMP LIFE UNDER RANDOM VIBRATION**

**C.J. Beck, Jr., Boeing Aerospace Company, Seattle, WA**

**Instrumentation**

**ANGULAR VIBRATION MEASUREMENT TECHNIQUES**

**P.W. Whaley and M.W. Obal, Air Force Flight Dynamics Laboratory,  
Wright-Patterson AFB, OH**

**HIGH FREQUENCY GROUND VIBRATION MEASUREMENT**

**H. Nolle, Monash University, Clayton, Victoria, Australia**

**THE RECIPROCITY CALIBRATION OF VIBRATION STANDARDS  
OVER AN EXTENDED FREQUENCY RANGE**

**R.R. Bouche, Bouche Laboratories, Sun Valley, CA**

**A NON-CONTACTING BETA BACKSCATTER GAGE FOR EXPLOSIVE  
QUANTITY MEASUREMENT**

**P.B. Higgins, F.H. Mathews and R.A. Benham, Sandia Laboratories,  
Albuquerque, NM**

**DATA ACQUISITION SYSTEMS FOR THE IMMEDIATE FUTURE**

**J.F. Schneider, Air Force Weapons Laboratory, Kirtland AFB, NM**

**Loads and Environments**

**THE VIBRATION RESPONSE OF THE PHOENIX MISSILE IN THE F-14  
AIRCRAFT CAPTIVE-FLIGHT ENVIRONMENT**

**M.E. Burke, Pacific Missile Test Center, Point Mugu, CA**

**SOME DYNAMIC RESPONSE ENVIRONMENTAL MEASUREMENTS  
OF VARIOUS TACTICAL WEAPONS**

**W.W. Parmenter, Naval Weapons Center, China Lake, CA**

**TURBULENT-BOUNDARY-LAYER EXCITATION AND RESPONSE THERETO  
FOR A HIGH-PERFORMANCE CONICAL VEHICLE**

**C.M. Ailman, McDonnell-Douglas Astro. Corp. Employee for this work.  
Currently an independent researcher in Los Angeles, CA**

**CALCULATION OF ATTACH POINT LOADS DUE TO POSSIBLE COMBUSTION  
INSTABILITY IN THE SPACE SHUTTLE SOLID ROCKET BOOSTERS**  
F.R. Jensen and D.T. Wang, Hercules Inc., Magna, UT

**Tracked Vehicles**

**HULL VIBRATORY POWER FLOW AND RESULTING INTERIOR NOISE  
ON THE M113A ARMORED PERSONNEL CARRIER**  
P.E. Rentz, Bolt Beranek and Newman, Canoga Park, CA

**REDUCING TRACKED VEHICLE VIBRATION AND NOISE HARDWARE  
CONSIDERATIONS**  
R.B. Hare and T.R. Norris, FMC Corporation, San Jose, CA

**THE USE OF AN EARTH BERM TO REDUCE THE ENVIRONMENTAL  
NOISE IMPACT OF THE TEST TRACK AT DETROIT ARSENAL**  
N.D. Lewis, U.S. Army Environmental Hygiene Agency,  
Aberdeen Proving Ground, MD

**PAPERS APPEARING IN THE SUPPLEMENT**

**ANALYSIS OF ACOUSTIC COATINGS BY THE FINITE  
ELEMENT METHOD**  
Anthony J. Kalinowski, Naval Underwater Systems Center,  
New London, CT

**DEVELOPMENT AND VALIDATION OF PRELAUNCH SHOCK CAPABILITY  
FOR THE NAVY TOMAHAWK CRUISE MISSILE**  
W.M. Dreyer, R.E. Martin, R.G. Huntington, General Dynamics  
Convair Division, San Diego, CA



# STRUCTURAL ANALYSIS

## A SOURCE OF LARGE ERRORS IN CALCULATING

### SYSTEM FREQUENCIES

Robert M. Mains  
Department of Civil Engineering  
Washington University  
St. Louis, Missouri

Attention is called to errors in system frequency calculations resulting from the use of non-diagonal mass matrices with eigenvalue routines that replace the mass matrix with its eigenvalues before proceeding to the calculation of system frequencies. The errors are illustrated in several different solutions of an 18 degree-of-freedom system. What can be done to avoid these errors is presented.

In some specific instances recently, the author has observed errors in the determination of system frequencies by factors of 3 to 10. These errors were costly in replacement or retrofit, so an investigation was undertaken to determine the cause of the errors. In each case, the Archer formulation of consistent mass was computer generated, and so was the stiffness matrix. These matrices were then run through one of several widely used eigenvalue routines to get system frequencies and mode shapes. If the stiffness and mass matrices had been repetitive, all would have been well, but in these cases both the stiffness and mass matrices had considerable texture (more than 1000 to 1 variation in magnitudes). Further examination of the eigenvalue routines revealed that they used the device of formulating  $M^{-1} * K * M^{-1}$  to achieve symmetry. For a diagonal mass matrix,  $M^{-1}$  is no problem, but with the non-diagonal mass matrices generated in the programs, the eigenvalue routines first found the eigenvalues of the mass matrix and used the inverse square root of these eigenvalues to get a diagonal  $M^{-1}$ . Unfortunately, the routines ordered the eigenvalues of the mass matrix and scrambled the coordinate order in the process. Since the eigenvalues of the mass matrix constitute a transformed set of coordinates, they cannot be used to multiply the untransformed stiffness coordinates.

To study this problem further, the system shown in Fig. 1 was used. This system was chosen for two reasons: first, the author had used this system for several years as a check problem on different computers with consistent results; second, the stiffness had a range of 2250 to 1, and the mass had a range of 5400 to 1. If the foregoing hypothesis were correct, this system should show it strongly. The main diagonals of stiffness, diagonal mass, and

consistent (Archer) mass are shown in Table 1, together with the eigenvalues of the consistent mass matrix.

Eight different solutions for eigenvalues were made with the results shown in Table 2, in which

- Column 1. Frequencies from  $M_D^{-1} * K * M_D^{-1}$ , with EIGN5/RMM,  $M_D$  = diagonal mass matrix by eyeball.
2. Frequencies from  $K * M_D^{-1}$ , with EIGRF/IMSL, wholly real.
  3. Frequencies from  $K * M_C^{-1}$ , with EIGRF/IMSL,  $M_C$  = consistent mass per Archer, wholly real.
  4. Frequencies from  $M_E^{-1} * K * M_E^{-1}$ , with EIGN5/RMM,  $M_E$  = eigenvalues of  $M_C$  arranged in near natural order by eyeball.
  5. Frequencies from  $M_{DA}^{-1} * K * M_{DA}^{-1}$ , with EIGN5/RMM,  $M_{DA}$  = diagonal mass arranged in ascending order.
  6. Frequencies from  $M_{EA}^{-1} * K * M_{EA}^{-1}$ , with EIGN5/RMM,  $M_{EA}$  = eigenvalues of  $M_E$  arranged in ascending order.
  7. Frequencies from  $M_{DD}^{-1} * K * M_{DD}^{-1}$ , with EIGN5/RMM,  $M_{DD}$  = diagonal mass arranged in descending order.
  8. Frequencies from  $M_{ED}^{-1} * K * M_{ED}^{-1}$ , with EIGN5/RMM,  $M_{ED}$  = eigenvalues of  $M_E$  arranged in descending order.

EIGRF/IMSL "calculates eigenvalues and eigenvectors of a real, general matrix," not

required to be symmetric. Eigenvalues and eigenvectors may be complex.

EIGN5/RMM calculates eigenvalues and eigenvectors from  $M^{-1} * K * M^{-1}$ . When M is not diagonal, the eigenvalues of M are used instead and are ordered ascending or descending.

NROOT, from the IBM system 360 Scientific Subroutine Package (SSRP), "finds the eigenvalues and eigenvectors of a real, square non-symmetric matrix of the special form  $B^{-1} * A$ , where both B and A are real, symmetric matrices and B is positive definite." This routine calls EIGEN from the SSRP to determine the eigenvalues of B, orders them in descending order, and then finds the eigenvalues of  $B^{-1} * A * B^{-1}$ .

In Table 2, the first two columns were identical all the way. Columns 3 and 4 were close to 1 and 2 for the lower third of the frequencies and differed appreciably thereafter. Columns 5 and 6 are close to each other in the lower third, but a factor of 10 different from 1 and 2. The same comments apply to columns 7 and 8 as to 5 and 6.

The eigenvector sets for the various solutions were too voluminous to be reproduced here

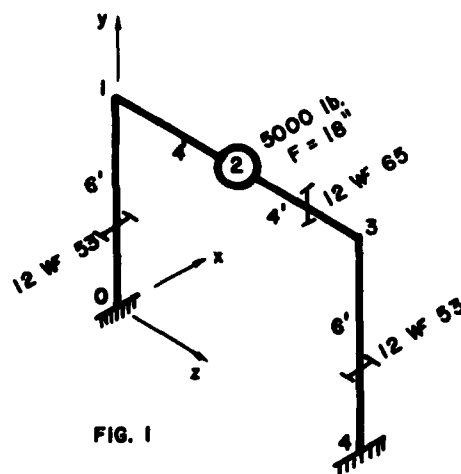


FIG. 1

except for eigenvectors number one and two from solutions 1 and 2, which are shown in Table 3. While the frequencies from 1 and 2 were identical, the vector shapes were radically different, so that further calculations involving the vector shapes (as for stress) would also be different.

From the numbers in Table 2, it seems clear that the use of a non-diagonal mass matrix in dynamic system analysis can lead to large errors if the eigenvalue routine uses the eigenvalues of the mass matrix in place of the matrix. If the  $K * M^{-1}$  formulation is used with a routine like EIGRF/IMSL, the eigenvalues are correct, but the eigenvectors are not orthogonal and subsequent calculations need to be modified. Both of these problems can be gotten around if the non-diagonal mass matrix is replaced by its triangular decomposition such that  $M = L * L^T$ . This replacement permits the eigenvalue solution of  $L^{-1} * K * L^{-1}$ , which is symmetric and has orthogonal eigenvectors, so that subsequent calculations can be carried through the same as for a diagonal mass matrix. The use of the triangular decomposition of the mass matrix was called to the author's attention by Mr. Eugene Sevin of the Defense Nuclear Agency, and the author gratefully acknowledges this.

TABLE 1  
Diagonals of Matrices Used

Diagonal of Stiffness lb/in	Diagonal of Mass lb sec <sup>2</sup> /in	Diagonal of Consistent Mass lb sec <sup>2</sup> /in	Eigenvalues of Consistent Mass lb sec <sup>2</sup> /in
0.13491+07	0.77700+00	0.57720+00	0.12211+00
0.98719+09	0.77700+01	0.77700+01	0.77447+01
0.76931+07	0.77700+00	0.57720+00	0.12211+00
0.50572+09	0.77700+01	0.77700+01	0.77447+01
0.16010+08	0.77700+00	0.57720+00	0.12211+00
0.52064+09	0.77700+01	0.77700+01	0.77447+01
0.21801+07	0.12950+02	0.12950+02	0.13430+02
0.30418+10	0.42000+04	0.42000+04	0.42000+04
0.23592+07	0.12950+02	0.12950+02	0.13430+02
0.22293+10	0.42000+04	0.42000+04	0.42000+04
0.31847+08	0.12950+02	0.12950+02	0.13430+02
0.12500+08	0.42000+04	0.42000+04	0.42000+04
0.13491+07	0.77700+00	0.57720+00	0.12277+00
0.98719+09	0.77700+01	0.77700+01	0.82076+01
0.76931+07	0.77700+00	0.57720+00	0.12277+00
0.50572+09	0.77700+01	0.77700+01	0.82076+01
0.16010+08	0.77700+00	0.57720+00	0.12277+00
0.52064+09	0.77700+01	0.77700+01	0.82076+01

TABLE 2  
Frequencies for Different Solutions, Hz

1	2	3	4	5	6	7	8
8.50	8.50	8.50	8.51	0.95	0.95	0.75	0.80
16.12	16.12	15.95	16.31	11.59	11.44	6.25	6.25
16.22	16.22	16.00	16.70	21.60	22.36	13.34	13.40
35.46	35.46	37.27	42.61	51.97	55.98	25.24	26.30
50.46	50.46	50.11	49.57	59.39	62.37	54.41	53.67
117.9	117.9	124.2	127.1	64.37	64.45	94.25	93.01
126.7	126.7	126.5	274.1	115.6	115.2	97.08	199.3
142.4	142.4	140.0	283.9	117.2	195.1	200.7	228.5
484.1	484.1	584.3	1186.	201.4	220.8	279.0	285.5
485.6	485.6	587.5	1192.	217.1	248.8	473.8	855.8
722.2	722.2	723.9	1264.	473.6	1188.	760.7	991.1
763.9	763.9	784.5	1301.	760.5	1356.	864.6	1186.
1293.	1293.	3039.	1334.	1378.	1830.	1009.	1836.
1294.	1294.	3049.	1369.	2317.	2371.	2367.	2486.
1306.7	1306.7	3221.	1786.	3215.	3149.	3119.	3054.
1306.8	1306.8	3226.	1814.	4121.	10285.	4120.	10317.
1798.9	1798.9	3668.	1837.	4292.	10366.	4293.	10394.
1799.2	1799.2	3705.	1861.	5692.	14319.	5692.	14280.

TABLE 3  
Comparison of Eigenvectors

Eigenvector no.1		Eigenvector no.2	
EIGR1	EIGN5	EIGR1	EIGN5
+0.47581-02	-0.24729-01	+0.55669-01	+0.21024+00
-0.13071-15	-0.60205-10	-0.38610-13	-0.23599-08
+0.34562-15	-0.74144-09	-0.94688-14	-0.60161-08
+0.11659-03	-0.27964-02	+0.58575-02	+0.25372-01
-0.20680-14	-0.32534-07	-0.11484-11	-0.70346-06
-0.12083-02	-0.66189-03	-0.99394-02	+0.71654-02
+0.82262-01	-0.26185-01	+0.11770+01	+0.26594+00
+0.88150-14	-0.16893-10	+0.17071-11	+0.17459-09
-0.45832-15	-0.23894-08	-0.20972-14	-0.91465-09
-0.24881-07	-0.83066-05	-0.36160-06	+0.70316-04
-0.36048-13	-0.32728-07	-0.19227-10	-0.70646-06
-0.15969+02	+0.15354-01	+0.21944+01	+0.15332-02
+0.47581-02	-0.24729-01	+0.55669-01	+0.21024+00
+0.12481-15	-0.15504-09	-0.38603-13	-0.23962-08
+0.27998-15	+0.42277-10	+0.91848-14	+0.57532-08
-0.11659-03	+0.60594-04	-0.58575-02	-0.22122-02
-0.22953-14	-0.32657-07	-0.11491-11	-0.70350-06
-0.12083-02	+0.62796-03	-0.99394-02	-0.37538-02

## DISCUSSION

Mr. Gupta, (IIT Research Institute): I was curious as to which programs the two consultants used. I am really skeptical in the sense that there are many commercial programs which are available and usually they do try to solve problems and show that they are able to solve certain problems; but having a error of the order of magnitude which you showed certainly is not the answer.

Dr. Mains: In the case of the floor system the programs that were used and the people doing the analysis are a part of one of the largest dynamic analysis operations in the country. They purport to do this kind of thing all day every day and I know that they have an automatic consistent mass calculator built into their programs. Their programs also substitute the eigenvalues of the mass matrix in that particular case. The other used a commercially available program that is widely used around the country. I know of three companies that use this program routinely for dynamic analysis. One of these was the contractor involved in the blast test that I spoke of, another is a large company in the St. Louis area, and the third is a very large company not very many miles south of here. I have observed this and I am pretty sure of my ground.

Mr. Paz, (University of Louisville): I don't know if the problem I am going to present is directly related to yours but we also had trouble with a consistent mass matrix some years ago. I suggested that a student who was working on a master's thesis compare results using the consistent mass, a lumped mass, and also what might be called the exact solution of the Bernoulli-Euler equations. He found tremendous differences. To test the programs he used simple numbers like units for everything, such as the modulus of elasticity and he found tremendous differences in computing the consistent mass. So I investigated this further and made a series expansion of the exact solution; I found out that the consistent mass is the first two terms of the series expansion, where one term is the stiffness and the other term would be the mass that we used in the consistent. By using these simple numbers to test the programs he was out of the range of convergence of the series so this explained why the consistent mass gave wrong answers. This might not be your case because you checked this with another program, it is probably a question of programming. But I thought it might be of interest to know that because with consistent mass we have to be careful in the convergence of the series that actually represents these terms.

Mr. Mains: One of the things I try very hard to do with my classes is to make sure that the students understand what they are doing. So I make them go through dynamic analysis the hard way with the hands-on operation of the programs, so that they know what is going on at each step and so that they come out of it with a set of solved problems that they can use to check out any black box they are subjected to later on. When they go out from the University to the job, quite routinely they are handed a problem and told to put this on the computer and get some answers. They have no opportunity to find out what the computer has on it. I think this is a fairly widespread practice I get feed back from it. Every student that goes out and then comes back to visit a year or two later tells me the same story.

RESEARCH METHOD OF THE EIGENMODES  
AND GENERALIZED ELEMENTS OF A LINEAR MECHANICAL STRUCTURE

R. FILLOD Dr. Ing. and J. PIRANDA Dr. Ing.  
Laboratoire de Mécanique Appliquée, associé au CNRS, Besançon, France

The determination of the eigenfrequencies, eigenmodes and generalized elements of a structure is fundamental in the study of its dynamic behavior (e.g. fluttering of planes). Of all the methods tested, those based on the appropriation of modes seem to give the most accurate results. The experimental methods used today are often unreliable and do not always guarantee that all the eigenmodes corresponding to a given frequency range have been isolated. The method which we suggest does not present these drawbacks. This method is based on the appropriation method and permits to determine the eigenvectors and generalized elements directly by calculus from the forced responses to a given frequency.

#### I - DEFINITION OF APPROPRIATION

Appropriation consists of finding which system of forces must be applied to a structure in order to obtain :

- a response proportional to an eigenmode of the associated conservative system ;
- the eigenfrequency corresponding to this mode.

Most experimental methods are based on the fact that all points of the structure have the same phase angle when the excitation is appropriate.

In the simplest methods, the experimenter proceeds tentatively by modifying the level of exciting forces and the frequency as best he can in order to minimise the force and velocity phase difference for all points. A method based on this principle was tested by LEWIS and WRISLAY [1] at the M.I.T. in 1950.

A. DECK [2] from the ONERA has developed an automatic method for appropriation which proceeds by successive approximations assuming that fre-

quencies have been isolated. Basically the minimum of the in phase response relative to the excitation is detected by varying each applied force and the excitation frequency successively. This method offers the advantage of being well-suited to automation but it is unsuccessful whenever the eigenfrequencies are too close to one another.

With the method developed by D. CLERC [3] appropriate forces can be calculated directly from a set of  $p$  responses at a given frequency related to  $p$  linearly independent excitation configurations. Such a method is systematic, it takes the information from all pickups into account and two close modes or more can easily be detected, but a great amount of measurements and calculus is required to determine one eigenmode.

TRIAL-NASH [4] had already used a less sophisticated form of this idea as early as 1958.

J.J. ANGELINI [5] introduced the matrix  ${}^T V.F$  calculated from the real part  $V$  of  $p$  responses to  $p$

linearly independent excitation configurations stored in the matrix F. He takes advantage of the vanishing property of the  $^{TVF}$  determinant when the excitation frequency is similar to the eigenfrequency. Such a method requires a great deal number of measurements and only takes account of displacements at the excitation points. Such methods have obvious drawbacks resulting either from exploitation (number of measurements required) or lack of efficiency (eigenmodes undetected in the case of close frequencies).

The aim of this paper is to develop a process allowing all the eigenmodes near the excitation frequency to be located, then secured from a limited set of measurements.

### 11 - Preliminary considerations

In forced harmonic conditions, the movement of a discrete linear system is defined by the equation :

$$M\ddot{y} + B\dot{y} + Ky = f \cdot e^{j\omega t}, \quad (1)$$

M, B, K being the mass, damping and stiffness matrices respectively.

$$\bar{y} = y e^{j\omega t}, \quad \text{leads to}$$

$$(K - \omega^2 M + j\omega B) y = f \quad (2)$$

To the damped initial system, we can associate the conservative system defined by the eigenproblem

$$(K - \lambda M) y = 0, \quad \lambda = \omega^2, \quad (3)$$

from which we deduce :

- the modal matrix Y of eigenvectors  $y_v$
- the spectral matrix  $\Lambda$  of eigenvalues  $\lambda_v$

According as the eigenvectors are arbitrarily normed ( $z_v$ ) or relatively to the mass matrix ( $y_v$ ), we obtain the classical relations :

$$Y^T M Y = E, \quad Y^T K Y = \Lambda, \quad Y^T Z M Z = \mu, \quad Y^T Z K Z = \mu \cdot \Lambda = \gamma \quad (4)$$

where  $\mu$  is the diagonal matrix of the generalized masses,  $\gamma$  that of the generalized stiffness.

The forced displacements of the damped system can be decomposed on the basis of the eigenvectors  $y_v$  or  $z_v$  of the associated conservative system. Then, we obtain :

$$y(\lambda) = Y \Omega^T Y^T f \quad \text{or} \quad y(\lambda) = Z \Omega^T Z^T f \quad (5)$$

$$\text{with } \Omega = (\Lambda - \lambda E + j\sqrt{\Lambda}B)^{-1} \quad \text{or} \quad \tilde{\Omega} = (\gamma - \lambda \mu + j\sqrt{\Lambda}b)^{-1} \quad (6)$$

$$\beta = Y^T B Y \quad b = Z^T B Z = \mu^{1/2} \beta \mu^{1/2} \quad (7)$$

where  $\beta$  and  $b$  are the normed and non-normed generalized damping matrices.

### 12 - Determination of appropriate forces

It is known [6] that a linear self-adjoint system can be appropriate to an eigen circular frequency  $\omega_v$  with a system of forces all in phase (or anti phase). For example, at the circular frequency  $\omega_v$ , the movement is described by :

$$(K - \lambda_v M + j\sqrt{\Lambda}B)z = f$$

$$\text{if } z = Z \cdot e_v = z_v \quad (K - \lambda_v M)z_v = 0 \text{ then}$$

$$j\sqrt{\Lambda}BZ \cdot e_v = f_v \quad \text{or still}$$

$$j\sqrt{\Lambda}^T Z^T B Z e_v = j\sqrt{\Lambda}b e_v = Y^T Z \cdot f_v$$

$$f_v = j\sqrt{\Lambda}^T Z^{-1} \cdot b \cdot e_v = j\sqrt{\Lambda}^T Y^{-1} \beta e_v \quad (8)$$

If  $b$  is diagonal (Basile's hypothesis verified [7]), this force  $f_v$  will excite an eigenmode which is out of phase in relation to the excitation whatever the frequency.

$$\text{Let } z = Z \cdot c$$

At the circular frequency  $\omega = \sqrt{\lambda}$ , the response  $z$  to the appropriate excitation will be defined by :

$$(K - \lambda M + j\sqrt{\Lambda}B)z = f_v$$

hence :

$$Y^T Z (K - \lambda M + j\sqrt{\Lambda}B) Z \cdot c = j\sqrt{\Lambda}b e_v$$

$$(\gamma - \lambda \mu + j\sqrt{\Lambda}b) \cdot c = j\sqrt{\Lambda}b e_v$$

$$c = j\sqrt{\Lambda} \frac{b_{vv}}{\gamma_{vv} - \lambda \mu_{vv} + j\sqrt{\Lambda} b_{vv}} e_v$$

All the points of the structure vibrate in phase. The phase difference  $\phi$  between the movement and excitation force is defined by :

$$\tan \phi = \frac{\sqrt{\lambda} \cdot b_{vv}}{\lambda_{vv} - \gamma_{vv}} = \frac{\sqrt{\lambda} \cdot \beta_{vv}}{\lambda - \lambda_v} \quad (9)$$

Reciprocally, assuming that a real force vector  $f$  is found, whose response to any circular frequency is

$$y = M Y \cdot f = V f + j f$$

with  $V \cdot f = k W \cdot f$ , and  $k$  = real constant,

then  $f$  is an appropriate force to an eigenvector. Indeed we have :

$$\begin{aligned} V &= Y R(\Omega) \quad T_Y & R(\Omega) \text{ real part of } \Omega \\ W &= Y J(\Omega) \quad T_Y & J(\Omega) \text{ imaginary part of } \Omega. \end{aligned}$$

$\Omega$  diagonal matrix of general term

$$\frac{\lambda_v - j\sqrt{\lambda}\beta_{vv}}{(\lambda_v - \lambda)^2 + \lambda\beta_{vv}^2}$$

The above equality  $V \cdot f = k \cdot W \cdot f$  leads to

$$Y \left[ \frac{\lambda_v - \lambda}{D} \right] T_Y \cdot f = k Y \left[ -\frac{\sqrt{\lambda}\beta_{vv}}{D} \right] T_Y \cdot f$$

$$D = (\lambda_v - \lambda)^2 + \lambda\beta_{vv}^2.$$

Multiplying this equation by  $\left[ -\frac{D}{\sqrt{\lambda} \cdot \beta_{vv}} \right] \cdot Y^{-1}$  we obtain :

$$\left[ \left[ \frac{\lambda - \lambda_v}{\sqrt{\lambda}\beta_{vv}} \right] - k E \right] T_Y \cdot f = 0 \quad (10)$$

Therefore there is an eigenvalue  $\lambda_v$  such that

$$k = \frac{\lambda - \lambda_v}{\sqrt{\lambda} \cdot \beta_{vv}}.$$

The corresponding eigenvector is of the form

$$T_Y \cdot f = \begin{pmatrix} 0 \\ 0 \\ \cdot \\ \alpha \\ \cdot \\ 0 \end{pmatrix}$$

Therefore,  $f$  is proportional to the appropriate force to the  $v^{\text{th}}$  eigenmode. For instance  $f_v$  is defined by :

$$f_v = M Y \sqrt{\lambda} \begin{pmatrix} 0 \\ 0 \\ \cdot \\ \beta_{vv} \\ \cdot \\ 0 \end{pmatrix} \text{ which leads to } T_Y \cdot f_v = \sqrt{\lambda} \begin{pmatrix} 0 \\ 0 \\ \cdot \\ \beta_{vv} \\ \cdot \\ 0 \end{pmatrix}$$

Such result multiplied by an arbitrary constant is the same as equation (8) because  $T_Y^{-1} = M Y$ .

Consequently, if a force  $f$  can be found so that  $V \cdot f = k W \cdot f$ , this force is appropriate to an eigenmode of the structure, and the displacement  $y$  is proportional to this eigenmode. This properly constitute the basis of the appropriation criterion suggested.

$k$  can be a double eigenvalue :

$$k = \frac{\lambda - \lambda_v}{\sqrt{\lambda} \beta_{vv}} = \frac{\lambda - \lambda_\sigma}{\sqrt{\lambda} \beta_{\sigma\sigma}}.$$

In that case two linearly independent eigenvectors will correspond to this double value of  $k$ .

$$T_Y \cdot f_v = \begin{pmatrix} 0 \\ 0 \\ \cdot \\ \alpha_v \\ \cdot \\ 0 \end{pmatrix} \quad \text{and} \quad T_Y \cdot f_\sigma = \begin{pmatrix} 0 \\ 0 \\ \cdot \\ \cdot \\ \alpha_\sigma \\ 0 \end{pmatrix}$$

The force  $f$  found will then be  $f_v$  or  $f_\sigma$  or more generally a linear combination of both. Such indetermination can always be erased by selecting another excitation frequency.

### 13 - Appropriation criterion when Basile's hypothesis is verified

$p$  excitation configurations linearly independent can be applied to the structure in  $p$  points at a given  $\omega$  circular frequency and the responses in phase and quadrature with the excitation in  $n$  points be noted. The responses in phase and in quadrature as well as the forces can be rearranged under matrix form resulting in matrices  $V(n,p)$ ,  $W(n,p)$  and  $F(p,p)$  respectively. We can assume for instance  $F=E$ ,  $E$  being the uni-

ty matrix.

With such linear system, a response to any vector force "a" will be  $Va + jWa$ . An appropriate force to an eigenmode will be the vector " $a_v$ " such that :

$$V.a_v = k W a_v \quad (11)$$

In the case when the matrix of applied forces  $\tilde{F}$  is not a unity matrix, we can measure responses in phase and quadrature  $\tilde{V}$  and  $\tilde{W}$  where each column is a linear combination of the V and W columns. We can therefore write them under the form :

$$\tilde{V} = V . \tilde{F} \quad \text{and} \quad \tilde{W} = W . \tilde{F} .$$

We try to find the values of k such that :

$$\tilde{V} a_v = k \tilde{W} a_v \quad \text{for instance}$$

$$V \tilde{F} a_v = k W \tilde{F} a_v$$

An appropriate force in this case is equivalent to  $\tilde{F} a_v$ . For simplicity, we now assume that

$$\tilde{F} = F = E$$

In practice, we strictly cannot guarantee equality (11). We try to find the vector "a" and the scalar k such that  $V.a - kW.a = \epsilon$  is minimum.

$$\text{Let } T_{\epsilon\epsilon} = T_a (T_V - k T_W) (V - kW) a$$

To minimize  $T_{\epsilon\epsilon}$  it is necessary to compare  $T_{\epsilon\epsilon}$  to a norm taking into account the amplitude of the movement. We are led to minimize the parameter  $\delta$ .

$$\delta = \frac{T_{\epsilon\epsilon}}{\|Va\| + \|Wa\|} = \frac{T_a (T_V - k T_W) (V - kW) a}{T_a (T_{VV} + T_{WW}) a}$$

The extremes of  $\delta$  are given by the zero of the partial derivatives  $\frac{\partial \delta}{\partial a_i} = 0, i=1, \dots, p$  and

$$\frac{\partial \delta}{\partial k} = 0 \quad \text{which leads to}$$

$$[T_{VV} - k(T_{VW} + T_{WV}) + k^2 T_{WW} - \delta(T_{VV} + T_{WW})] a = 0 \quad (12)$$

$$k = \frac{T_a T_{WVa}}{T_a T_{WVa}} \quad (13)$$

(12) is an eigenvalue problem in  $\delta$  non-linear in relation to the parameter k. It suffices to find which are the values  $k_v$  of k making the smallest eigenvalue  $\delta$  minimum. To each  $k_v$  there is a corresponding eigenvector " $a_v$ " which is the appropriate force to the  $v^{\text{th}}$  eigenmode. We check that the equation (13) is satisfied for each solution found.

#### 14 - Form of the appropriate forces such that $V.a = kW.a$ when Basile's hypothesis is not verified

In this case in order to obtain  $V.a = kW.a$  at  $\lambda \neq \lambda_v$ , complex forces  $F_R + jF_i$  must be applied. We can show that the generalized forces appropriated to the  $v^{\text{th}}$  eigenmode defined by

$$T_Z(F_R + jF_i) = f_R + j f_i$$

are of the form :

$$f_R = \begin{vmatrix} -\sqrt{\lambda} b_{1v} \\ -\sqrt{\lambda} b_{2v} \\ . \\ . \\ -\sqrt{\lambda} b_{vv} + k(\lambda_{vv} - \lambda \mu_{vv}) \\ . \\ . \\ -\sqrt{\lambda} b_{nv} \end{vmatrix} f_i = \begin{vmatrix} k\sqrt{\lambda} b_{1v} \\ k\sqrt{\lambda} b_{2v} \\ . \\ . \\ k\sqrt{\lambda} b_{vv} + (\gamma_{vv} - \lambda \mu_{vv}) \\ . \\ . \\ k\sqrt{\lambda} b_{nv} \end{vmatrix} \quad (14)$$

k can be chosen such that  $f_i$  is null when b is diagonal. If for instance

$$k = \frac{\lambda \mu_{vv} - \gamma_{vv}}{\sqrt{\lambda} b_{vv}} = \frac{\lambda - \lambda_v}{\sqrt{\lambda} \beta_{vv}} \quad (15)$$

The generalized forces are then written :

$$f_R = -\sqrt{\lambda} \begin{vmatrix} b_{1v} \\ b_{2v} \\ . \\ . \\ b_{vv}(1+k^2) \\ . \\ . \\ b_{nv} \end{vmatrix} \quad f_i = k\sqrt{\lambda} \begin{vmatrix} b_{1v} \\ b_{2v} \\ . \\ . \\ 0 \\ . \\ . \\ b_{nv} \end{vmatrix} \quad (16)$$



In practice  $b_{iv} (i \neq v) \ll b_{vv}$ , furthermore in the proximity of  $\lambda \neq \lambda_v$ ,  $k \neq 0$ . Consequently, the imaginary force is negligible compared to the real force, and the appropriation criterion suggested may be applied at the proximity of  $\lambda = \lambda_v$  even when Basile's hypothesis is not verified.

## II - PRACTICAL CALCULATION OF APPROPRIATE FORCES

### 21 - $\delta = f(k)$ curve plotting.

The calculation is carried out as follows [8]: Given a  $k_0$  value of  $k$  (for example  $k_0 = 0$ ), the values of  $\delta$  solutions of the eigenproblem (12) and the corresponding eigenvectors are deduced. Then by increasing  $k$  and plotting  $\delta = f(k)$ . We get the diagram: (Fig.1)

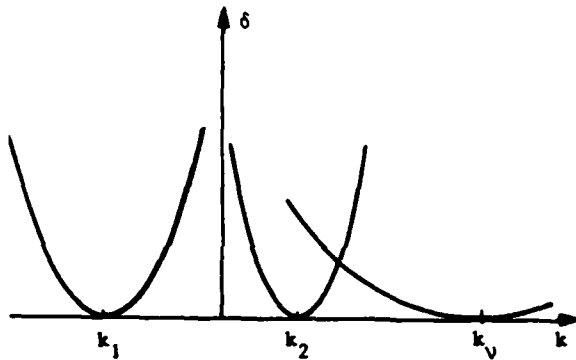


FIG.1 Curves  $\delta = f(k)$

For each value  $k_v$  of  $k$  with  $\delta$  is minimum, there is a corresponding force vector " $a_v$ " appropriate to an eigenmode of the structure.  $W a_v$  is proportional to the eigenmode.

The appropriation to a mode is all the more accurate as the corresponding value of  $\delta$  is smaller.

Such calculation is comparatively long and entails a lot of iterations to obtain a  $k_v$  with  $\delta$  minimum.

A quicker alternative can be summarized as follows: given an arbitrary initial values of

$k$ , the eigenproblem (12) can be solved and a new value  $k'_0$  of  $k$  calculated from the eigenvector obtained using the relation (13). The value  $k'_0$  obtained is very close to a  $k_v$  value with  $\delta$  minimum. The value  $k$  can be obtained rapidly through iteration.

In practice, two or three iterations are sufficient to obtain fairly accurate values of  $k_v$ .

The method still gives good results when two eigenfrequencies or more are close or equal. Two  $k$  values or more are found to which two appropriate forces, or more, are associated.

The relation  $k = \frac{\lambda - \lambda_v}{\sqrt{\lambda} \beta_{vv}}$  shows that even when two eigenvalues  $\lambda_\sigma$  and  $\lambda_v$  are equal, we still have two separate values for  $k$  if  $\beta_{vv} \neq \beta_{\sigma\sigma}$ . Any combination of the two obtained vectors is an eigenvector. The two determined eigenvectors correspond to the two modes for which the damping coefficient  $\beta_{\sigma v}$  is minimum. The above relation also infers that it is possible to obtain a double value for  $k$  even if  $\lambda_\sigma \neq \lambda_v$ . In this case, two separate values for  $k$  are obtained by changing the excitation frequency.

## III - CALCULATION OF MASSES AND GENERALIZED DAMPINGS

The circular frequency  $\omega_v = \sqrt{\lambda_v}$ , generalized mass  $\mu_{vv}$  and the damping  $\beta$  have to be determined for each eigenmode.

For that, after locating a frequency and calculating the appropriate corresponding force  $a_v$ , we apply this force to the structure. A step to step predetermined frequency micro-sweeping device records the system complex responses:

$$y(\omega) = y_R(\omega) + j y_i(\omega).$$

### 31 - Eigen circular frequency $\omega_v$ and generalized damping $\beta_{vv}$ determination.

Using the following method to determine  $\omega_v$

and  $\beta_{VV}$  we obtained fairly satisfactory results.

For a set of value of  $\lambda \neq \lambda_V$ , the appropriate force  $a_V$  is applied and

$$k(\lambda) = \frac{T_{Y_R} \cdot y_i}{T_{Y_i} \cdot y_i} = \frac{\lambda - \lambda_V}{\sqrt{\lambda} \cdot \beta_{VV}} \text{ is plotted}$$

Then  $k(\lambda) = 0$  gives  $\lambda = \lambda_V$  and the slope of the curve  $k(\lambda)$  gives the generalized damping  $\beta_{VV}$ :

$$\left(\frac{dk}{d\lambda}\right)_{\lambda=\lambda_V} = \frac{1}{\sqrt{\lambda_V} \cdot \beta_{VV}} \text{ hence } \beta_{VV} = \frac{1}{\sqrt{\lambda_V} \left(\frac{dk}{d\lambda}\right)_{\lambda=\lambda_V}} \quad (17)$$

### 32 - Generalized mass determination

Generalized mass and damping can be obtained by the diagram of complex power [9]  $P_R$  and  $P_i$  as a function of  $\lambda$ .

$$P_R = T_{a_V} \cdot y_R \quad P_i = T_{a_V} \cdot y_i$$

For  $\lambda \neq \lambda_V$ , it is known [4] that:

$$P_R = (\lambda_V - \lambda) \mu_{VV} \quad (18)$$

$$P_i = (2\sqrt{\lambda_V} - \sqrt{\lambda}) b_{VV}. \quad (19)$$

Hence for  $\lambda = \lambda_V$ ,

$$P_R = 0, \quad \frac{dP_R}{d\lambda} = -\mu_{VV}, \quad (20)$$

$$P_i = -b_{VV} \sqrt{\lambda} = -\mu_{VV} \beta_{VV} \sqrt{\lambda_V} \text{ from which}$$

$$\mu_{VV} = -\frac{P_i}{\sqrt{\lambda_V} \beta_{VV}} \quad (21)$$

A simple geometric diagram allows to check the coherence of the results obtained (fig.2).

The experiment shows that:

- The curve  $k(\lambda)$  (17) provides accurate values for  $\lambda_V$  and  $\beta_{VV}$  since all the points where pickups have been placed are taken into account.

- The values of  $\mu_{VV}$  and  $\lambda_V$  given by (20) are weighted with errors which are due to the fact that  $\frac{dP_R}{d\lambda}$  varies very quickly in the proximity of  $\lambda = \lambda_V$ ;

- The extreme of  $P_i$  is slightly modified

due to error effects in measurements and (21) enables one to obtain  $\mu_{VV}$  accurately.

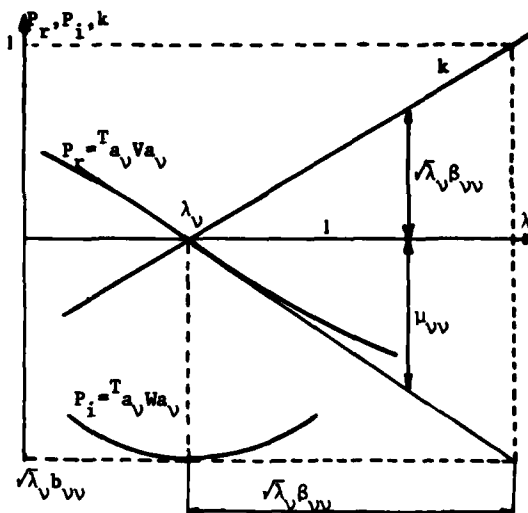


FIG.2 Curves  $k(\lambda)$  and complex power

### 33 - Applications of the suggested method

Experimental checking of the method has been carried out at the ONERA [10]. Fairly good results have been obtained using a plane sub-structure. Obtained results from numerical simulation by the finite elements method of a system having close natural frequencies, are given here. This system is a clamped, free beam folded up as shown Fig.3. It can be shown that such a structure evinces a succession of eigen-frequencies by pairs.

The eigenfrequencies in each pair are all the closer as  $l_1 - l_2$  gets smaller

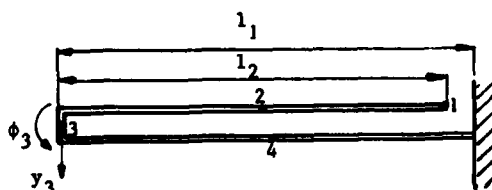


FIG.3. Folded beam for example

The first four eigen-frequencies of the

system are :

$$F_1=13.1 \text{ Hz} \quad F_2=13.3 \text{ Hz} \quad F_3=119 \text{ Hz} \quad F_4=120.8 \text{ Hz}$$

In the finite element method, three degrees of freedom are associated to each mode (transverse, longitudinal and angular displacements) which leads to a 12 degrees freedom system when four elements are concerned.

In the generalized damping matrix introduced the value of the quality factor  $Q=\omega_v/\beta_{vv}$  of all modes is 20 or about and coupled terms are added between the first three modes.

The submatrix  $\beta$  is represented below

$$\beta = \begin{bmatrix} 4.05 & -0.54 & -0.27 \\ -0.54 & 3.24 & -0.81 \\ -0.27 & -0.81 & 27 \end{bmatrix}$$

The simulated testing was carried out as follow : at a given frequency, responses to forces equal to 1 applied successively to each transverse degree of freedom are computed. The responses are stored into the V and W matrices from which  $k = f(\lambda)$  is plotted.

The following graph is obtained by selecting an excitation frequency between the first two eigenfrequencies ( $f = 13.2 \text{ Hz}$ )

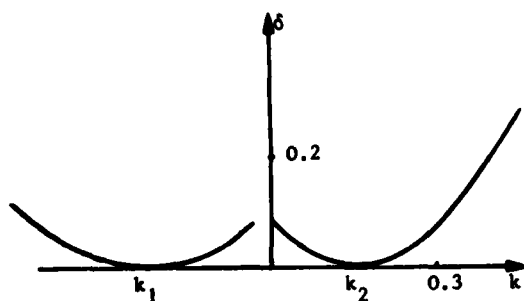


FIG. 4 Curves  $\delta = F(k)$

The two parabolic curves  $\delta = f(k)$  clearly show that the system has two eigenfrequencies located on both sides of the excitation frequency. Then the appropriate forces to the two

modes can be computed.

Force  $a_1$  appropriate to the first eigenmode is computed at an excitation frequency equal to 12.13 Hz. A microsweping from  $f=11.9 \text{ Hz}$  to  $f=12.3 \text{ Hz}$  gives the following curves (fig.5) for  $k, T_{aVa}, T_{aWa}$ .

Similary, force  $a_2$  appropriate to the second eigenmode is computed at an excitation frequency equal to 13.27 Hz. A microsweping from  $f=13.1$  to  $f=13.5 \text{ Hz}$  gives the results in fig.5.

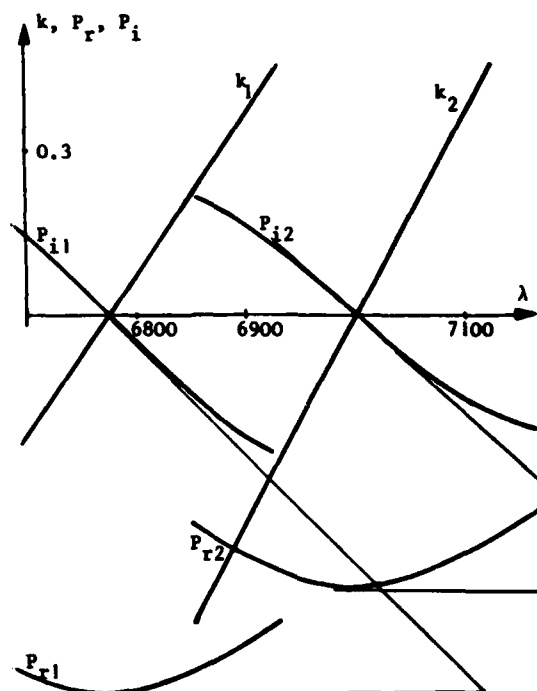


FIG. 5  $k(\lambda)$  and complex power. Modes 1 and 2

The generalized parameters of eigenmodes are obtained from relations (17) and (21). The following table allows the computed results to be compared with the exact values.  $\omega, \beta, \mu, y_i, \phi_i$ , are the circular frequency, the generalized damping and mass the displacement and the rotation of the  $i$ th cross-section. It can be seen that results are obtained with good accuracy though the two modes are very close and strongly coupled. It has also been verified that correct results can be secured when error effects in mea-

measurements are simulated.

	First Mode		Second Mode	
	Exact Values	Computed Values	Exact Values	Computed values
$\omega^2$	6775	6775	7000	7000
$\beta$	4.05	4.17	3.24	3.26
$\mu$	$2.05 \cdot 10^{-3}$	$2 \cdot 10^{-3}$	0.181	0.183
$y_1$	-11.4	-11.1	332	332
$\phi_1$	0.130	0.128	-1.39	-1.37
$y_2$	7.8	7.91	131	134
$\phi_2$	0.127	0.126	-1.27	-1.25
$y_3$	26.2	26.2	-16.1	-12.4
$\phi_3$	0.123	0.122	-0.59	-0.57
$y_4$	8.63	8.65	14.6	16.6
$\phi_4$	0.1	0.1	0.07	0.09

#### IV - CONCLUSION

The suggested method has been tested twice on a numerical computer, adding simulated errors of measurements and on plane substructure [10]. Even when two or more neighbouring eigenfrequencies are very closed together, the appropriate force can be easily calculated and the eigenmodes restored with a negligible amount of errors compatible with measurement accuracy.

As a conclusion, the originality of the method can be summarised as follows : a single set of measurements with given frequencies enables one to determine the appropriate force with several eigenmodes, and the determination of the values of  $k$  such that  $\delta$  is minimum enables one to locate these eigenfrequencies ;

- multiple or neighbouring are automatically detected even though eigenmodes are strongly coupled by damping ;

- if we agree to make a few measurements in the proximity of an eigenfrequency, the diagram in function of  $\lambda$  of  $k$ ,  $P_R$  and  $P_i$  enables one to determine :

- the eigen-circular frequency  $\omega_v$  ;
- the generalized damping  $\beta_{vv}$  ;
- the generalized mass  $\mu_{vv}$ .

#### BIBLIOGRAPHY

- [1] ROBERT C., LEWIS and Donald L. WHISLAY (MIT)  
A system for the excitation of pure natural modes of complex structure. Journal of Aeronautical sciences - novembre 1950
- [2] DECK - Contribution à l'étude d'une méthode semi-automatique d'appropriation - Note technique ONERA - N°129 (1968) ONERA - 92320 Chatillon (France)
- [3] CLERC D. - Une méthode d'appropriation des forces d'excitation aux modes propres non amortis d'une structure - Recherche Aérospatiale n°85 (1961)
- [4] R.W. TRIAL-NASH - On the excitation of pure natural modes in aircraft resonance testing. Journal of the Aero-space Sciences - décembre 1958 (pp.775-778)
- [5] J.J. ANGELINI - Une nouvelle méthode de mesure des formes modales des structures aéronautiques - Xème Congrès International des Sciences Aeronautiques - Ottawa 1976 (ICAS paper n°76-27)
- [6] O. DANEK - Referenci buzni. Proceedings of the VIII<sup>th</sup> Conference Dynamics of Machines, PRAHA - Liblice, september 1973
- [7] R. BASILE - P.S.T. du Ministère de l'air. Colloque international de Mécanique, POITIERS (1950)
- [8] R. FILLOD, J. PIRANDA - Etude d'une méthode d'appropriation des systèmes linéaires. Proceedings of the VIII<sup>th</sup> Conference - Dynamics of Machines, PRAHA, Liblice, september 1973
- [9] E. BONNEAU - Détermination des caractéristiques vibratoires d'une structure à l'aide de l'expression de la puissance complexe fournie Recherche Aérospatiale, n°130, juin 1969
- [10] NGUYEN Xuan Thanh - Restitution par calcul des modes propres à partir d'excitations non appropriées. Note tech. ONERA n°1975-9.

## CALCULATION OF NATURAL FREQUENCIES AND MODE SHAPES OF MASS LOADED AIRCRAFT STRUCTURES

P. Wayne Whaley  
Air Force Flight Dynamics Laboratory  
Wright-Patterson AFB, OH 45433

Aircraft optical packages are forced by the local random vibration response characteristics of the airframe. Hence, the vibration characteristics must be known by the designer of optical packages. However, since the environment changes with the addition of the electro-optical system, it is necessary to predict the modified vibration environment, either by flight testing with mass simulations or conducting structural analysis. This paper poses the problem of loaded random vibration response estimation using Galerkin's method, a direct method, and a generalized coordinates approach. Results indicate that both the direct method and the generalized coordinates solution give very good estimates of the first four modes of a mass loaded simply supported beam, with the generalized coordinates solution giving better accuracy than the direct method. Galerkin's method gives unacceptable results. In addition, a matrix iteration scheme for computing loaded modes, given unloaded modes, is presented. Results show that over 50% reduction in execution time is possible in computing the first four modes, with good accuracy maintained.

### INTRODUCTION

In the design of airborne optical packages, the angular and rectilinear vibration response characteristics of the airframe represent the input forcing functions to the optical systems [1]. Hence, it is necessary to collect vibration data for the aircraft structure on which the optical system is to be mounted. The problem with such data is that installing the optical system in the aircraft may change the airframe vibration response characteristics. Therefore, it is desirable to collect aircraft data with a mass simulation installed. However, when the flight test is conducted, the optical system design may not be finalized, so the most appropriate simulation mass may not be known. In addition, unloaded data may already be available for the aircraft in which case it is more desirable to use existing data than increase cost by collecting additional data. A better approach would be to calculate or estimate the mass loaded random response, using some relatively simple procedure, rather than to rely on installing mass simulations and then conducting flight tests. This paper is an analysis of four procedures for calculating the mass loaded vibration response of aircraft structures.

Finite element analysis is frequently used to compute the loaded random vibration response of aircraft structures. However, unless a finite element model already exists, such a process would be time consuming. Even if a finite element model did exist, the manner of mass loading would have to be included and possible matrix size reduction techniques implemented. In addition, there are persistent problems concerning the choice of appropriate forcing functions used as inputs. Thus, finite element modeling might be more expensive and time consuming in some instances than conducting flight tests.

Three analytical techniques for computing the mass loaded response of aircraft structures are compared to the finite element answer. Those analytical techniques are: Galerkin's method, a generalized coordinates approach, and a direct method based on Hamilton's law of varying action. In addition, an alternative method of computing the loaded response using finite element analysis and knowing the unloaded response is presented.

### ANALYSIS

Approximations to the solutions of

difficult problems may be obtained by a variety of methods. Three are chosen here because of their ease of application to vibration problems. Galerkin's method involves assuming a solution, substituting the assumed solution into the original differential equations to define a residue, then setting the integral of this residue to zero. The generalized coordinates approach is based on the fact that a partial differential equation may be transformed into a set of ordinary differential equations. The ordinary differential equations are then solved in any available manner. The direct method gets its name from the fact that no differential equations are solved; eigenvalues and eigenvectors are obtained directly from energy equations. Details of the derivations are given below.

#### Galerkin's Method

The differential equation for the system of Fig. 1 may be derived by utilizing Hamilton's principle. The kinetic and potential energy expressions are used to define a modified Lagrangian density function.

$$L_m = \frac{1}{2} \rho \left( \frac{\partial y}{\partial t} \right)^2 - \frac{1}{2} EI \left( \frac{\partial^2 y}{\partial x^2} \right)^2 + \frac{1}{2} \frac{M_0}{L} \left( \frac{\partial^2 y}{\partial t^2} \right)^2 \delta(x - x_0) + \frac{1}{2} \frac{M_0 R^2}{L} \left( \frac{\partial^3 y}{\partial x \partial t^2} \right)^2 \delta(x - x_0) \quad (1)$$

Applying Hamilton's principle to Eq. (1), the resulting equation of motion is

$$-EI \frac{\partial^4 y}{\partial x^4} - \rho \frac{\partial^2 y}{\partial t^2} - \frac{M_0}{L} \frac{\partial^2 y}{\partial t^2} \delta(x - x_0) + \frac{M_0}{L} R^2 \frac{\partial^3 y}{\partial x \partial t^2} \delta(x - x_0) = 0 \quad (2)$$

An approximate solution to Eq. (2) may be assumed. (See Ref. [2].)

$$y_n(x, t) = A_n \sin \frac{n\pi x}{L} \sin \omega t$$

Since this is an approximate solution, substituting into Eq. (2) will not give zero, but is set equal to a residue. By integrating the residue over one cycle and taking the first variation of the integral, it is possible to solve for the natural frequencies. The loaded natural frequency divided by the unloaded natural frequency is

$$\frac{\omega}{\omega_0} = \sqrt{\frac{1}{1 + \frac{M_0}{\rho L} \left( \frac{4}{(n\pi)^2} \sin \frac{n\pi x_0}{L} \left[ 1 + \left( \frac{R}{L} \right)^2 (n\pi)^2 \right] \right)}} \quad (3)$$

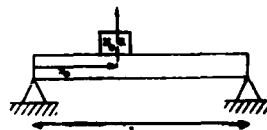


Fig. 1 - Mass loaded simply supported beam.

#### Generalized Coordinates

By defining generalized coordinates as in Eq. (4), a structure's response may be characterized in a more analytically convenient notation.

$$y(x, t) = \sum_{i=1}^{\infty} q_i \phi_i(x) \quad (4)$$

In Eq. (4),

$\phi_i(x)$  are the mode shapes

$q_i$  are the generalized coordinates.

Using Eq. (4), the equation of motion for Fig. 1 may be written as

$$M_1 \ddot{q}_1 + K_1 q_1 = F(x_0, t) \phi_1(x_0) + M(x_0, t) \phi_1'(x_0). \quad (5)$$

(See Ref. [3].)

$$M_1 = \int_0^L \rho \phi_1^2(x) dx = \rho \frac{L}{2}$$

$$K_1 = \int_0^L EI \left( \frac{d\phi_1}{dx} \right)^2 dx = EI \left( \frac{d\phi_1}{dx} \right)^2 \frac{L}{2}$$

$$F(x_0, t) = -M_0 \int \ddot{q}_j \phi_j(x_0)$$

$$M(x_0, t) = -M_0 R^2 \int \ddot{q}_j \phi_j'(x_0)$$

Making these substitutions in Eq. (5) and collecting like terms, the coefficients of  $q_i$  take the form

$$-\omega_1^2 [M_1 + M_0 \phi_1^2(x_0) + M_0 R^2 \phi_1'^2(x_0)] + K_1$$

$$-\omega_1^2 [M_0 \phi_1(x_0) \phi_j(x_0) + M_0 R^2 \phi_1'(x_0) \phi_j'(x_0)] = 0$$

Since  $K_1/M_1 = \omega_1^2$  for the unloaded beam,

dividing Eqs. (6) by  $K_1$  yields a normalized set of equations in terms of the natural frequency ratio  $\omega_1/\omega_0$ . Since this ratio is close to one for moderately loaded structure, the frequency

ratio can be set equal to one for the off-diagonal terms as a first approximation. This yields the eigenvalue problem given in Eq. (6).

$$\begin{bmatrix} A_{11} & A_{12} & A_{13} & \dots & A_{1n} \\ A_{21} & A_{22} & \dots & \dots & \dots \\ \vdots & \vdots & \vdots & \ddots & \vdots \\ A_{n1} & \dots & \dots & \dots & A_{nn} \end{bmatrix} \begin{bmatrix} q_1 \\ q_2 \\ \vdots \\ q_n \end{bmatrix} = \begin{bmatrix} 0 \\ 0 \\ \vdots \\ 0 \end{bmatrix} \quad (6)$$

$$A_{ij} = \begin{cases} -\frac{\omega_1^2}{\omega_0^2} \left[ 1 + \frac{M_0}{M_1} \phi_1^2(x_0) + \frac{M_0 R^2}{M_1} \phi_1'^2(x_0) \right] & \text{for } i = j \\ \frac{M_0}{M_1} \phi_1(x_0) \phi_j(x_0) + \frac{M_0 R^2}{M_1} \phi_1(x_0) \phi_j'(x_0) & \text{for } i \neq j \end{cases}$$

Eqs. (6) result in an eigenvalue problem of order  $n \times n$  where  $n$  modes are desired.

#### Direct Method

The direct method is based on a concept known as Hamilton's law of varying action. (See Ref. [4] for details). That law is stated in Eq. (7).

$$\delta \int_{t_0}^{t_1} (T - V) dt - \frac{\partial T}{\partial \left( \frac{\partial y}{\partial t} \right)} \delta y \Big|_{t_0}^{t_1} = 0 \quad (7)$$

$T$  and  $V$  are:

$$T = \frac{1}{2} \int_0^L \left[ \rho \left( \frac{\partial y}{\partial t} \right)^2 dx + \frac{M_0}{L} \left( \frac{\partial y}{\partial t} \right)^2 \delta(x - x_0) + \frac{M_0 R^2}{L} \left( \frac{\partial^2 y}{\partial t^2} \right)^2 \delta(x - x_0) \right] dx$$

$$V = \frac{1}{2} \int_0^L EI \left( \frac{\partial^2 y}{\partial x^2} \right)^2 dx.$$

Assuming  $y(x, t) = A_n \sin \frac{n\pi x}{L} \sin \omega t$ , Eq. (7) becomes,

$$\int_{t_0}^{t_1} \int_0^L -\omega^2 \rho A_n^2 \sin^2 \left( \frac{n\pi x}{L} \right) \sin^2 \omega t \delta A_n dx dt - \int_{t_0}^{t_1} \frac{M_0 \omega^2}{L} A_n \sin^2 \left( \frac{n\pi x_0}{L} \right) \sin^2 \omega t \delta A_n dt - \int_{t_0}^{t_1} \frac{M_0 R^2}{L} \omega^2 \left( \frac{n\pi}{L} \right) A_n \cos^2 \left( \frac{n\pi x_0}{L} \right) \sin^2 \omega t \delta A_n dt + \int_{t_0}^{t_1} \int_0^L EI \left( \frac{n\pi}{L} \right) A_n \sin^2 \left( \frac{n\pi x}{L} \right) \sin^2 \omega t \delta A_n dx dt = 0. \quad (8)$$

By insisting that  $\delta A_n$  not be zero and integrating over one cycle, Eq. (8) becomes, after carrying out the integration and dividing by the unloaded natural frequency,

$$\frac{\omega}{\omega_0} = \sqrt{\frac{1}{1 + \frac{2M_0}{\rho L} \sin^2 \frac{n\pi x_0}{L} + \frac{2M_0}{\rho L} \left( \frac{R}{L} \right)^2 (n\pi)^2 \cos^2 \frac{n\pi x_0}{L}}}. \quad (9)$$

#### Discussion

A finite element analysis of the simply supported beam was conducted in order to determine the accuracy of the various analytical techniques presented here. A beam with 25 grid points including transverse and rotational deflections at each grid point was modeled using finite elements [6]. The finite element analysis used for comparison to these analytical results yielded accuracies for the unloaded simply supported beam as listed in Table I. The added mass was chosen as half the beam mass, and the radius of gyration was five percent of the beam length.

TABLE I.

## Accuracy of Finite Element Method

Mode	Exact Solution, Hz	Finite Element Solution, Hz
1	664.05	664.05
2	2656.2	2656.2
3	5976.5	5976.6
4	10624.	10625.
5	16601.	16603.
6	23906.	23912.

Fig. 2 is a plot of the loaded first natural frequency divided by the unloaded first natural frequency versus the normalized position of the added mass. Ten modes are considered in computing the first loaded natural frequency by generalized coordinates. Four techniques are used in Fig. 2 to compute natural frequencies: Galerkin's method, generalized coordinates, direct method, and a finite element solution. As seen from Fig. 2, generalized coordinates and the direct method both agree very well with the finite element solution. Galerkin's method is in considerable error and is felt to be inappropriate for this analysis, and is therefore omitted from the rest of this discussion.

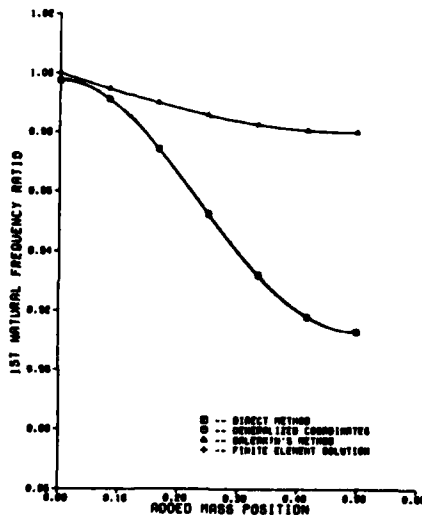


Fig. 2 - First natural frequency ratio plotted versus added mass position by three methods;  $M_0 = 0.50\rho L$ ,  $R = 0.05L$ .

Fig. 3 is a plot of the loaded second natural frequency divided by the unloaded second natural frequency versus normalized position of the added mass. Fig. 3 shows that the generalized coordinates method gives results which are almost identical to the finite element solution. Figs. 4 and 5 show plots of normalized natural frequency versus normalized position for third and fourth modes. For third mode, the generalized coordinates answer is almost identical to the finite element answer while the direct method is in error. For the fourth mode, the generalized coordinates answer is in slight error, but still much better than the direct method. From Figs. 2-5 it appears that the generalized coordinates solution gives better results than the direct method for lower modes, with both methods in greater error for higher order modes. Table II shows maximum error tabulated for the direct method and generalized coordinates. The direct method is as good as generalized coordinates for lower modes, but is in significantly greater error for higher modes.

TABLE II.

Maximum Error of the Direct Method and of the Generalized Coordinates Analysis

Mode	Maximum Error, Percent	
	Direct Method	Generalized Coordinate
1	.02	.04
2	.046	.037
3	.5	.026
4	.71	.003

In summary, of the three analytical methods examined here generalized coordinates method gives the best accuracy in computing natural frequency. Generalized coordinates analysis has potential for three important reasons: (1) A complicated structure may be analyzed in terms of  $n$  ordinary differential equations, where  $n$  is the number of modes required, (2) The matrix sizes can be much smaller since only those modes which lie within the frequency band of interest need to be included, (3) Using generalized coordinates, one need only know the modes, therefore negating any need to model any but the local part of this structure of interest. If one can measure modes using one of the many available modal analysis mini-computer systems then there is no need to be concerned with boundary conditions, and it is possible to analyze only those subsections of interest in the airframe [5].



For the analysis given here, the loaded mode shape is assumed to be the same as the unloaded mode shape. While for moderate loading conditions this assumption is acceptable, for larger added mass that assumption fails to be valid. Hence, this is a shortcoming of the analytical methods presented here. A technique which utilizes corrected mode shape information is included in the next section.

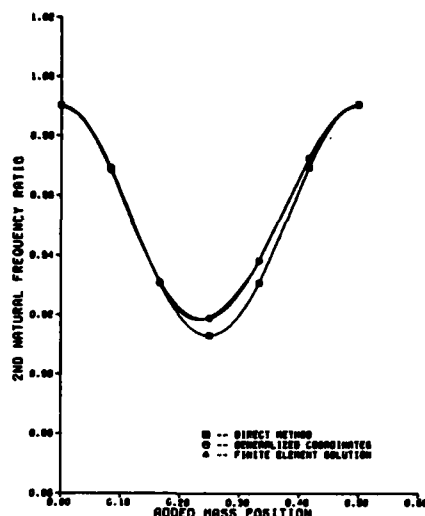


Fig. 3 - Second natural frequency ratio plotted versus added mass position by two methods;  $M_0 = 0.50\rho L$ ,  $R = 0.05L$ .

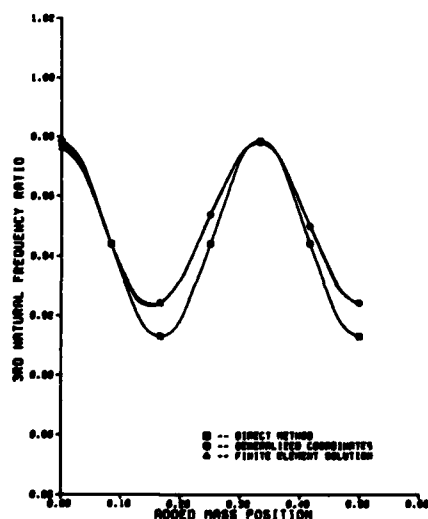


Fig. 4 - Third natural frequency ratio plotted versus added mass position by two methods;  $M_0 = 0.50\rho L$ ,  $R = 0.05L$ .

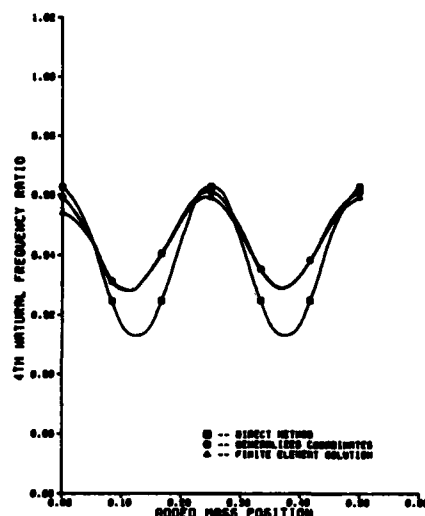


Fig. 5 - Fourth natural frequency ratio plotted versus added mass position by two methods;  $M_0 = 0.50\rho L$ ,  $R = 0.05L$ .

#### MATRIX ITERATION

The matrix iteration scheme used here is the power method using matrix deflation [6]. The method is based on the idea that the vector  $\{u\}$  in Eq.(10) may be obtained by choosing an initial estimate and substituting into the left-hand side of Eq.(10) repeatedly until both sides of Eq.(10) agree.

$$[K^{-1}] [M] \{u\} = \frac{1}{\omega^2} \{u\} \quad (10)$$

Higher order modes can be solved once the lower modes are known by using Eq.(11).

$$([K^{-1}] [M] - \lambda_1 \{u_1\} \{u_1\}^T [M]) \{u_2\} = \frac{1}{\omega^2} \{u_2\} \quad (11)$$

where  $\{u_1\}^T [M] \{u_1\} = 1$ ,

$$e = \max \{u_2\} - \max \{u_1\}.$$

Matrix iteration may thus be used to compute as many mode shapes and natural frequencies as are desired.

Matrix iteration was used to solve the

finite element model of the previous section. Results of that analysis are summarized in Tables III and IV. From Table III it is shown that for computing only the first few modes, matrix iteration can yield significant cost savings. Increasing the convergence criteria affects the lower modes by only a few percent, while a more rigid convergence criterion improves the accuracy of the higher modes. It may be that one should formulate convergence criteria which vary with the modes, demanding more accuracy for lower modes and less accuracy for higher modes.

In Table III, it takes more time to compute more modes because the algorithm requires iteration for each mode. For the eigenvalue analysis, however, the cost is the same for computing a given number of modes, and the number of modes is equal to the number of elements for this finite element model.

From Table IV, accuracy with  $\epsilon = .1$  for the first four modes is on the order of 17. With  $\epsilon = .01$ , accuracy is somewhat better, especially for the higher order modes, although the sixth mode is still in considerable error.

TABLE III.

Comparisons of the Computational Speeds of Matrix Iteration and Eigenvalue Analysis

Number of Modes	Matrix Iteration Execution Time, Sec		Eigenvalue Execution Time, Sec	Percent Reduction	
	$\epsilon = .1$	$\epsilon = .01$		$\epsilon = .1$	$\epsilon = .01$
1	1.7	1.66	4.6	63	60
2	2.2	2.21	4.6	51	47
3	2.8	2.79	4.6	38	33
4	3.4	3.39	4.6	25	19
5	4.2	4.38	4.6	9	-4
6	4.8	5.06	4.6	-.06	-20.

TABLE IV.

Comparisons of the Accuracies of Matrix Iteration with Eigenvalue Analysis

Mode	Matrix Iteration Natural Frequencies, Hz		Eigenvalue Analysis Natural Frequencies, Hz	Percent Error	
	$\epsilon = .1$	$\epsilon = .01$		$\epsilon = .1$	$\epsilon = .01$
1	605.5	605.5	605.97	.07	.07
2	2575	2630.8	2633	2.22	.08
3	5546	5517.5	5509	.67	.15
4	10400	10193	10301	-.96	1.05
5	12128	14292	15365	-21.0	-7.0
6	86547	10096	22403	-61.0	-55.0

Accuracy for higher modes is lower, because errors made in computing lower modes are additive.

In summary, it appears that using matrix iteration in solving the loaded modes when one knows the unloaded modes can provide significant cost savings. Although the cost savings do not appear to be enough to enable one to use finite element analysis to predict the vibration environment of loaded structure, it is significant enough to merit further consideration as a potential application to other analysis techniques.

The reason for the success of matrix iteration is that maximum advantage is taken of all that is known about the structure. In general, matrix iteration is not a common technique since it requires an initial estimate for the mode shape. Usually, such an estimate is not readily available and convergence depends on the accuracy of the initial "guess." However, in the case of loaded structures on which unloaded modes and mode shapes are known, that initial "guess" is very close to the final mode shape, so convergence is very rapid.

## CONCLUSIONS

A desirable feature for an analytical technique to be used in computing an estimate of the loaded structural mode shapes from the unloaded, is that optimum advantage be taken of the known unloaded mode shapes. The suggested vibration estimation process might be as follows: (1) Use existing unloaded aircraft vibration data when available, collecting all data without concern for mass simulations. (2) Measure the necessary modes and natural frequencies of the portion of the aircraft to be analyzed using modal testing techniques. (3) Apply a relatively simple algorithm to the unloaded vibration response to get an estimate of the loaded vibration response. Such a vibration estimation process has the advantage that design studies are possible for estimating the best location for the airborne optical package. This iterative design process would be prohibitively expensive when mass simulations must be flight tested.

Only one of the analytical techniques presented here appears to have potential in fulfilling these requirements. Galerkin's method depends on an existing differential equation, unlikely for complicated built-up structure. The direct method depends on the existence of energy functions, again difficult for complicated structure. The generalized coordinates approach, however, depends only on knowledge of unloaded mode shapes and natural frequencies. Once modes are known, generalized elements may be computed for  $n$  natural frequencies,  $n$  second order ordinary differential equations result. The problem with all three of these techniques is that they do not allow

for correction of the unloaded mode shapes to upgrade the accuracy of the solution.

Matrix iteration holds promise since the nature of the unloaded structure is used to advantage. For moderate loading conditions, convergence is very rapid in solving for the lower few modes. Significant savings in computational speed are demonstrated with acceptable corresponding accuracy. However, it is felt that using matrix iteration in conjunction with finite element analysis will yield only limited success. The preparation of data and validation of the model requires an enormous amount of time for most complicated aircraft structures. It is suggested that use of generalized coordinates in conjunction with matrix iteration should be studied further.

## LIST OF SYMBOLS

$A_{ij}$  = elements of generalized coordinates coefficient matrix

$A_n$  = arbitrary constant in approximate solution

$E$  = Young's modulus

$F(x_0, t)$  = applied inertia force

$I$  = beam cross-section moment of inertia

$K$  = finite element stiffness matrix

$K_I$  = generalized stiffness

$L$  = beam length

$L_m$  = Lagrangian density function

$M$  = finite element mass matrix

$M_I$  = generalized mass

$M_0$  = mass of added mass load

$n$  = number of modes

$q_i$  = generalized coordinate

$R$  = radius of gyration of added mass load

$T$  = kinetic energy

$t_0$  = initial time

$t_1$  = final time

$V$  = potential energy

$x_0$  = location of added mass load

#### Greek Symbols

- $\delta$  = variational operator
- $\delta(x-x_0)$  = dirac delta function
- $\epsilon$  = matrix iteration convergence criterion
- $\rho$  = beam mass density
- $\phi_i$  = mode shape
- $\mu$  = mode shape estimate for matrix iteration
- $\lambda_i$  = matrix iteration eigenvalue,  $1/\omega_r^2$
- $\omega$  = loaded beam natural frequency
- $\omega_0$  = unloaded beam natural frequency
- $\omega_r$  = frequency estimate for matrix iteration

#### DISCUSSION

##### Mr. Smallwood, (Sandia Laboratories):

I gathered from the flavor of the talk that the whole purpose is to determine the change in the response of the structure when a substructure is added to it. I was wondering if you have considered the application of mechanical impedance techniques for doing this particular job? For example if you know the unloaded motion of the structure at the attachment point, if you know the mechanical impedance of a substructure that you will attach to the structure, then you can determine the motion of the interface with the substructure attached to the principal structure.

Mr. Whaley: I haven't looked at impedance techniques particularly for this problem but that has been done by our group. Captain Bob Davis did some of that on an aircraft to predict its response once the laser was installed. That sounds like something I would like to pursue.

#### REFERENCES

1. Lloyd, W. B., D. R. Logan, and J. Pearson, "Vibration Control of Optical Packages in Aircraft," 1977 National Aerospace Electronic Conference, Dayton, OH, May 17-19, 1977.
2. Forray, N. J., Variational Calculus in Science and Engineering, New York, 1968, pp 189-191.
3. Thomson, W. T., Vibration Theory and Applications, Englewood Cliffs, New Jersey, 1965, pp 299-304.
4. Bailey, C. D., "A New Look at Hamilton's Principle," Foundations of Physics, vol 5, no. 3, 1975.
5. Richardson, M., and R. Potter, "Identification of the Modal Properties of an Elastic Structure From Measured Transfer Function Data," 20th International Instrumentation Symposium, Albuquerque, N. M., 1974.
6. Meirovitch, L., Elements of Vibration Analysis, New York, 1975, pp 159-164.

## ROCKET MOTOR RESPONSE TO TRANSVERSE BLAST LOADING

Norris J. Huffington, Jr., and Henry L. Wisniewski  
U.S. Army Ballistic Research Laboratory  
Aberdeen Proving Ground, Maryland

The effects of propellant inertia and of internal pressurization on the structural response of solid propellant rocket motors subjected to transverse air blast loading have been investigated, both analytically and numerically. The numerical predictions were accomplished using the BRL version of the PETROS 3.5 computer program, which employs the finite difference method to solve the equations governing finite amplitude elastoplastic response of thin shells. The response of a typical rocket motor configuration was calculated for the limiting situations of the bare motor case and of the motor case containing the complete propellant grain, each with no internal pressurization and with the pressurization resulting from propellant combustion. These calculations showed that the unpressurized motors experience a much larger deformation than the pressurized motors for the same blast loading. The most significant result is the quantification of the greater vulnerability of rocket motors prior to their ignition, whether on the launcher or as upper stages of in-flight missiles.

### INTRODUCTION

This paper is concerned with analysis of the vulnerability of solid propellant rocket motors to air blast loading in combination with other operational loads. In treating this subject it is appropriate to consider the methodology currently being employed in the design of motors for interceptor missiles and artillery rockets [1]. This methodology may be characterized as a quasi-static two-dimensional finite element modeling of longitudinal and transverse slices through rocket motors supplemented by a one-dimensional treatment of radiation-induced stress wave propagation. The Ballistic Research Laboratory is monitoring the augmentation of these finite element codes to permit a plane strain analysis of the response of a transverse slice of a motor (including the viscoelastic propellant grain) to side-on blast loading.

Additionally, the authors have conducted a parallel investigation of this problem using the BRL version of the PETROS 3.5 computer program [2], which employs the finite difference method to solve the equations governing finite amplitude elastoplastic response of thin shells. Although this computer code cannot model the behavior of the propellant (except in a lumped mass manner to be described) it does have the capability to treat the response

of an entire motor case including head and nozzle. However, the results to be presented in the sequel were obtained for a plane strain cylinder in order to provide a comparison with results to be derived by the finite element analysis cited above.

The representation employed for the blast loading includes both the diffraction and the drag phases of loading since both phases contribute to the response to nuclear blast. Nevertheless, the methodology is equally applicable for predicting response to blast from conventional weapons.

The first author has also obtained an analytical solution for the effect of internal pressurization on the vibration frequencies of elastic plane strain cylinders. Although the details of this analysis will be presented elsewhere, the insights derived from this solution assist in the interpretation of the numerical results acquired by use of the PETROS 3.5 code.

### PROBLEM DEFINITION

When resorting to numerical analysis one must naturally assign values to all parameters appearing in the formulation. The values selected below are not identified with any

existing system but do fall within ranges of practical interest.

#### A. Rocket Motor Parameters

A representative solid propellant rocket motor cross section (see Fig. 1) was selected for exercise of the PETROS 3.5 computer program in its plane strain option. In addition to the geometric data shown on this Figure, the material property parameters listed in Table 1 were selected. The steel motor case was assumed to have the linear strain hardening uniaxial stress-strain characteristics shown in Fig. 2 and to exhibit no strain-rate effects. Bi-axial plastic flow was analyzed using the von Mises yield criterion and the associated flow rule in accordance with the mechanical sublayer model [3]. Although the propellant

is being modeled as a viscoelastic material in the cited finite element analysis, the lumped mass treatment of the propellant in the PETROS 3.5 calculations required use of only the propellant density.

#### B. Blast Loading Model

The blast loading is introduced as a plane shock wave having an exponentially decaying tail, moving down from above as shown in Fig. 1. Although surface overpressures  $p(\theta, t)$  obtained experimentally or by refined hydrodynamic calculations can be readily introduced into the PETROS 3.5 code, it is convenient to employ the following functional representation for the blast loading which includes the essential aspects of wave reflection, diffraction, and post-envelopment drag loading:

$$p(\theta, t) = \begin{cases} 0 & \text{for } t < t_a \\ \left[ \begin{array}{l} [p_r \cos \theta + p_s(1 - \cos \theta)]e^{-\beta(t-t_a)} \\ p_s e^{-\beta(t-t_a)} \end{array} \right. & \left. \begin{array}{l} \text{for } -90^\circ < \theta < 90^\circ \\ \text{for } 90^\circ < |\theta| < 180^\circ \end{array} \right\} \text{for } t > t_a \quad (1)$$

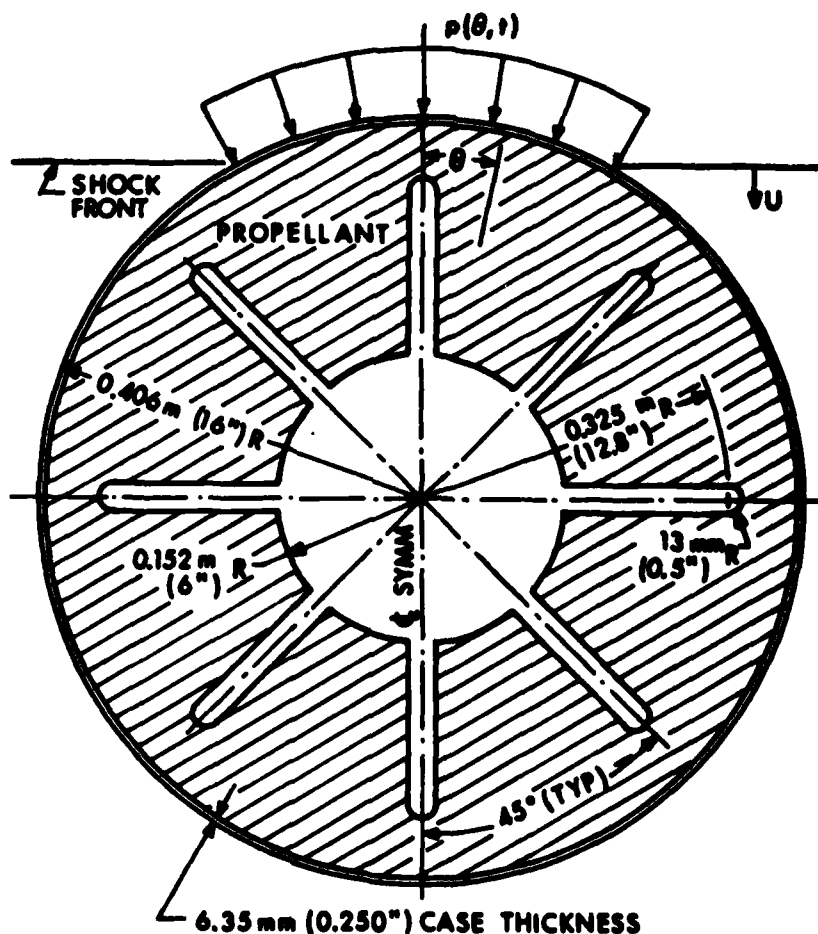


Fig. 1. Rocket Motor Cross Section

TABLE 1  
Material Properties

Motor Case (Steel)	
Young's modulus	$E_c = 200 \text{ GPa} = 29 \times 10^6 \text{ psi}$
Poisson's ratio	$\nu_c = 0.3$
Yield stress	$\sigma_o = 483 \text{ MPa} = 70,000 \text{ psi}$
Mass density	$\rho_c = 7850 \text{ kg/m}^3 = 0.000735 \text{ lb sec}^2/\text{in}^4$
Propellant (Viscoelastic Solid)	
Young's modulus	$E_p = 689 \text{ MPa} = 100,000 \text{ psi}$
Poisson's ratio	$\nu_p = 0.472$
Mass density	$\rho_p = 1660 \text{ kg/m}^3 = 0.000155 \text{ lb sec}^2/\text{in}^4$

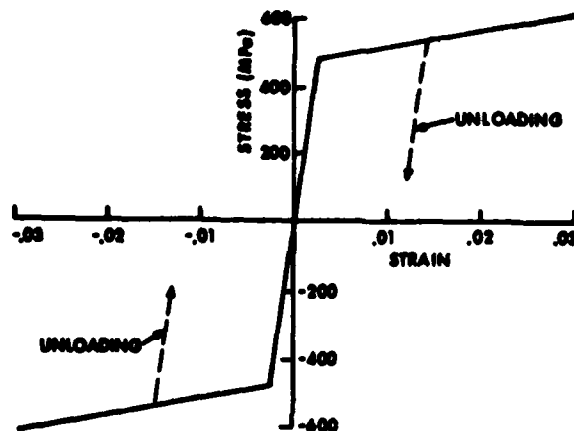


Fig. 2. Postulated Uniaxial Stress-Strain Curve for Motor Case Material

where

- $p_o$  = ambient pressure
- $p_s$  = side-on overpressure of incident shock
- $p_r$  = reflected peak overpressure
- $a_o$  = sonic velocity at ambient conditions
- $U$  = shock front velocity
- $t_a$  = arrival time of shock front
- $R$  = outside radius of cylinder
- $\beta$  = decay coefficient

and

$$p_r = 2p_s \left( \frac{7p_o + 4p_s}{7p_o + p_s} \right) \quad (2)$$

$$U = a_o \sqrt{1 + \frac{6p_s}{7p_o}} \quad (3)$$

$$t_a = \frac{R(1 - \cos\theta)}{U} \quad (4)$$

While response predictions have been made for several values of incident overpressure, the results which follow have been obtained for one level of blast loading, the parameters for which are listed in Table 2.

TABLE 2  
Blast Wave Parameters

Parameter	SI Units	English Units
$a_o$	340 m/s	13400 in/sec
$p_o$	101 kPa	14.7 psi
$p_s$	79.3 kPa	11.5 psi
$U$	440 m/s	17300 in/sec
$\beta$	$4.35 \text{ s}^{-1}$	$4.35 \text{ sec}^{-1}$
$p_r$	207 kPa	30.0 psi

The value of the decay coefficient  $\beta$  was estimated from blast data curves [4] for a one kiloton nuclear weapon.

### C. Internal Loading

In addition to response predictions using the foregoing external loading, which would correspond to the pre-ignition response for the rocket motor stage under consideration, calculations have also been performed for cases where the motor had an additional internal pressurization  $p_i$  (produced by propellant combustion) prior to this blast loading. For the most part the value  $p_i = 6.89 \text{ MPa}$  (1000 psi) has been used for this internal pressure.

although a limited study of the effect of varying this parameter will also be reported.

## FINITE DIFFERENCE MODELING

### A. Computational Grid

The finite difference grid employed for all the PETROS 3.5 calculations is shown in Fig. 3. Since both the responding structure and the applied loads are symmetric with respect to the vertical plane, it is only necessary to model the response of one-half of the cylinder. Further, because there is no longitudinal variation of any quantities involved in a plane strain analysis there are only two independent variables, the angles  $\theta$  and time, resulting in quite economical computer runs.

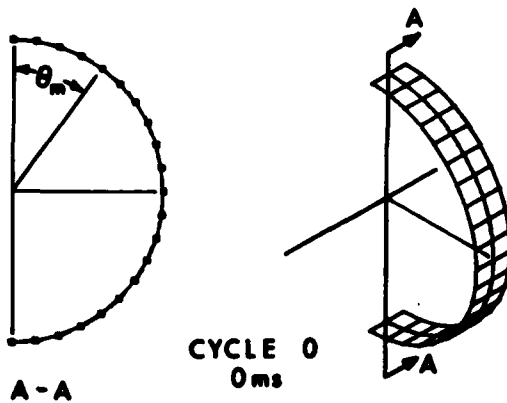


Fig. 3. Finite Difference Grid

### B. Propellant Mass Effect

In the finite difference equations of motion for the mesh point at  $\theta_m$  ( $m = \text{integer}$ ) the mass is that of the shell (motor case) lying between the radial planes at angles  $(\theta_{m-1} + \theta_m)/2$  and  $(\theta_m + \theta_{m+1})/2$ . When it was desired to take account of the mass of the propellant in the response prediction the mass of propellant lying between the same two radial planes was added to the motor case mass at  $\theta_m$ . Therefore, the effective mass will vary as a function of the discrete angles  $\theta_m$  owing to the slots in the star pattern of the propellant grain (see Fig. 1). It is recognized that this procedure provides a rather crude approximation to the propellant mass effect since many two-dimensional response modes are thereby inhibited. Nevertheless it appears to be the most rational procedure which does not entail extensive modification of the shell response code. The resistance of the propellant grain to deformation is also neglected in this modeling, an approximation which may not be too serious owing to the relatively low strength of the propellant in comparison to that of the steel motor case (see Table 1) and the weakening effect of the slots in the propellant grain.

### C. Rigid Body Motion

There is another modeling consideration which arises as a consequence of the assumption that the motor case is in a state of plane strain. In this stress state there can be no resultant force acting tangential to a cross section of the motor. Consequently, when a non-self-equilibrating external loading (such as results from side-on blast) is applied to the cylinder a lateral acceleration results. In order to appreciate the extent of deformation the cylinder experiences it is necessary to subtract out this "rigid body" component of the motion. This was accomplished in the PETROS 3.5 calculations by recomputing the location of the mass center at each time step and subtracting this quantity from the position vector of each mesh point before displaying graphical results.

## NUMERICAL ANALYSIS RESULTS

### A. Unpressurized Cylinders

In Fig. 4 the undeformed cylinder cross section of the bare motor case is compared with that at 30 ms, which is approximately the time of maximum deflection. It should be emphasized that in this figure the deflections are plotted to the same scale as the initial deflection; i.e., the deflections are large, entailing both nonlinear geometric effects and elastoplastic material behavior. The deflected cross section corresponds principally to the lowest frequency flexural mode for a ring or cylinder (the  $n = 2$ ,  $s = 1$  mode, see Appendix). The deflection responses of a point on the crown line ( $\theta = 0^\circ$ ) of cylinders having no internal pressurization are shown in Fig. 5, for both the bare motor case and the motor configuration of Fig. 1 (where the effect of propellant mass has been included as described above). As expected, the effect of the propellant is to reduce both the amplitude and frequency of the response.

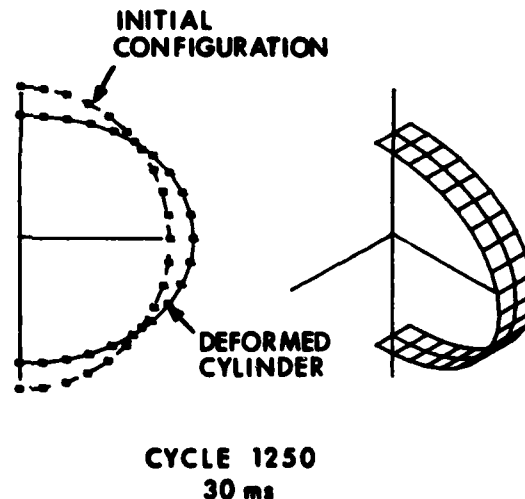


Fig. 4. Deflection Pattern for Unpressurized Bare Cylinder



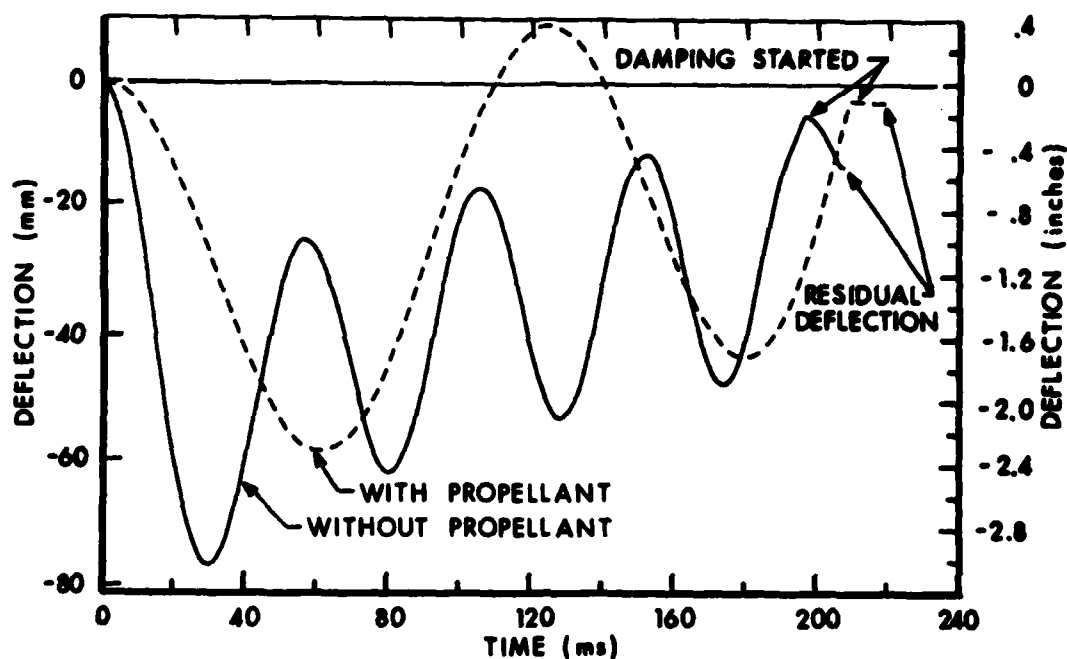


Fig. 5. Deflections at  $\theta = 0^\circ$  for No Internal Pressurization

The predicted circumferential strains at the crown line are displayed in Fig. 6. Since the curves for the inner and outer surfaces (of

the motor case) are nearly symmetric with respect to the zero strain line it may be inferred that the response is mostly flexural,

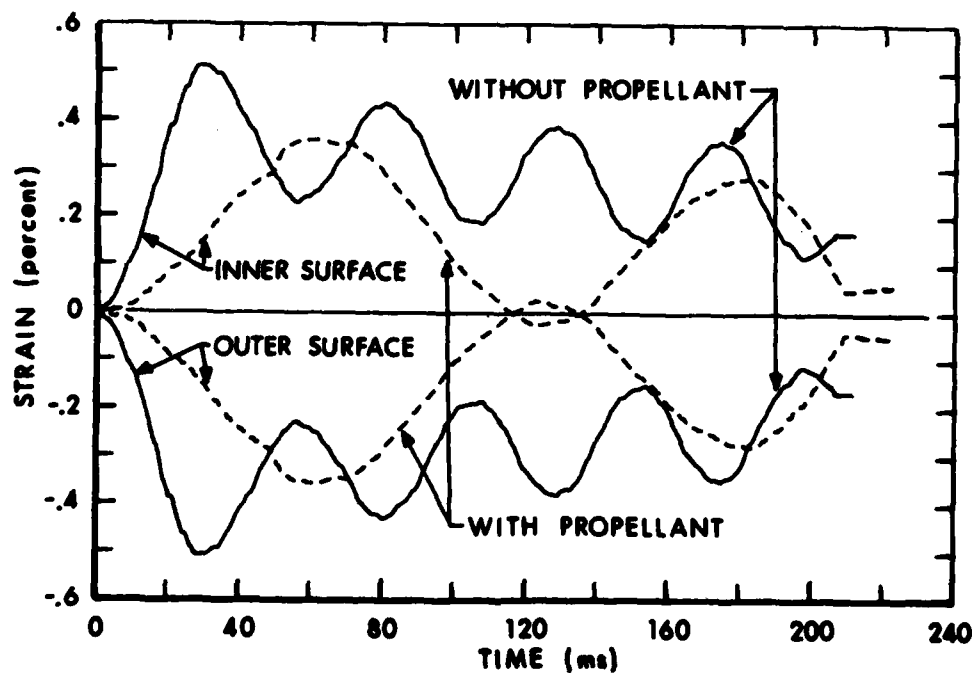


Fig. 6. Circumferential Strains at  $\theta = 0^\circ$  for No Internal Pressurization

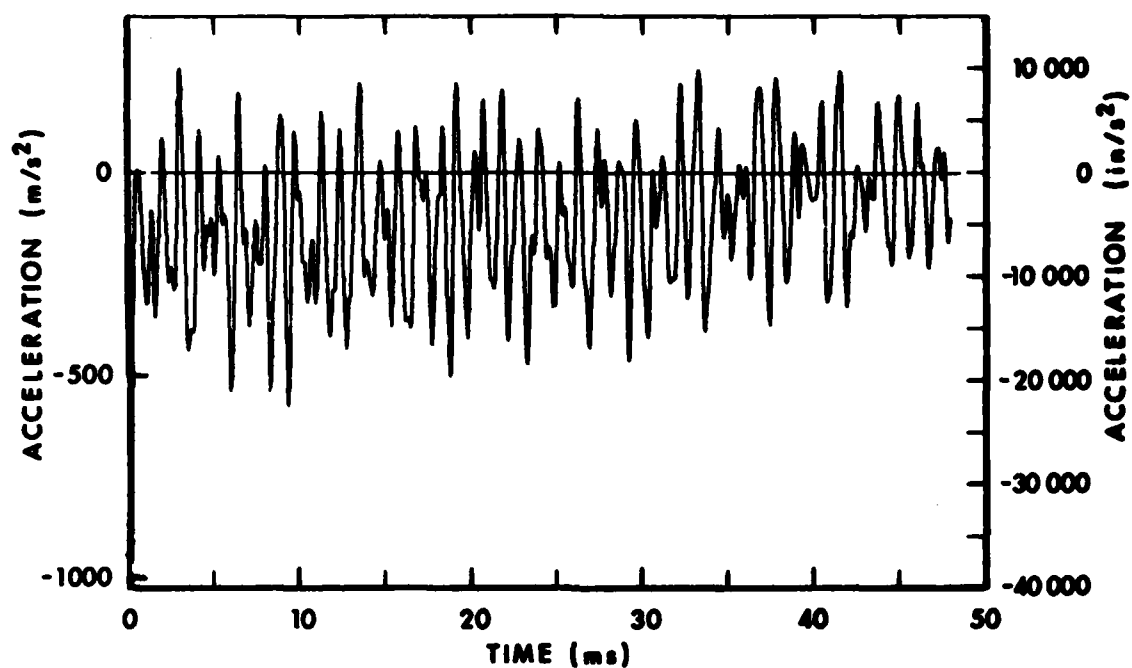


Fig. 7. Acceleration at  $\theta = 0^\circ$  for Unpressurized Motor Case Containing Propellant

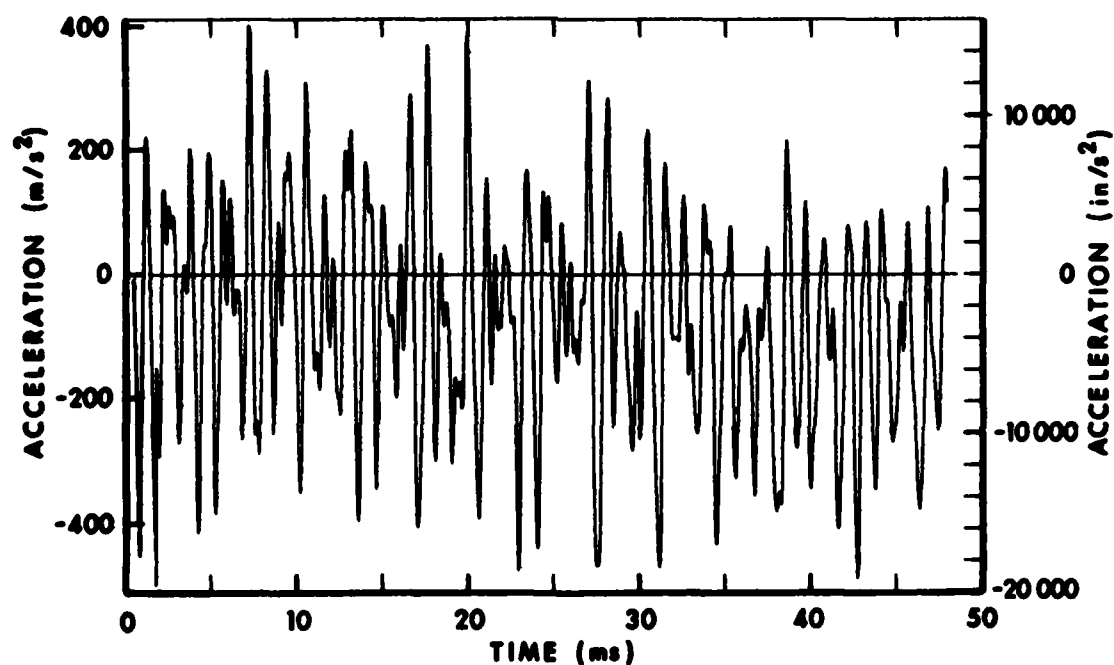


Fig. 8. Acceleration at  $\theta = 180^\circ$  for Unpressurized Motor Case Containing Propellant

which is consistent with Fig. 4. Similar strain variations were obtained at  $\theta = 90^\circ$  and  $180^\circ$ . At 192 ms, by which time all plastic deformation had ceased, the external load was removed and an artificial damping was introduced to rapidly dissipate the remaining kinetic energy. In this manner it was possible to identify the values of residual deflection and residual strains indicated on Figs 5 and 6, respectively.

For the motor case containing propellant it is also of interest to estimate the normal stresses acting at the interface between motor case and propellant. This can be done in a manner consistent with the lumped mass model by multiplying the element of propellant mass assigned to a nodal point by the absolute acceleration of the nodal point and dividing by the appropriate interface surface area. The acceleration histories\* of the nodal points at  $\theta = 0^\circ$  and  $\theta = 180^\circ$  are shown in Figs. 7 and 8,

respectively. Tensile interface stresses are associated with positive accelerations at  $\theta = 0^\circ$  and negative accelerations at  $\theta = 180^\circ$ . The maximum of these accelerations is  $-496 \text{ m/s}^2$  ( $-19500 \text{ in/sec}^2$ ) corresponding to a tensile stress of 80.2 kPa (11.6 psi) at  $\theta = 180^\circ$ . While interface stresses of this magnitude should not cause debonding of the propellant, conclusions regarding bond failure should be deferred until the results of the two-dimensional finite element analysis become available.

#### B. Effect of Internal Pressure

When treating cases of cylinders with internal pressurization (due to propellant combustion) a quasi-static PETROS 3.5 run was made at each pressurization level to establish the initial conditions of deflection and stress extant prior to arrival of the blast wave. These quasi-static solutions, which are plotted in negative time in Fig. 9, are fully damped

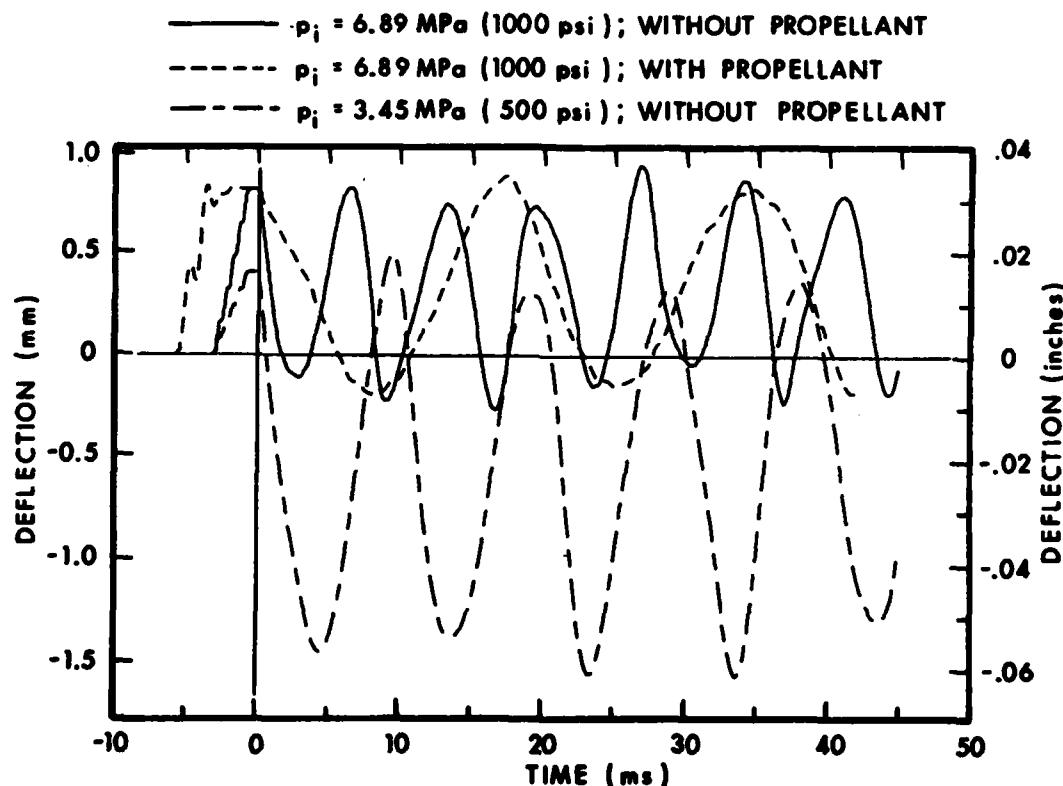


Fig. 9. Deflection at  $\theta = 0^\circ$  with Internal Pressurization

\*The presence of high frequency oscillations in these plots may appear suspicious in view of the rather low frequency deflection response in Fig. 5. However, relatively low amplitude extensional modes (the  $s = 2$  family discussed in the Appendix) when amplified by the square of their large circular frequencies (as is effectively done when calculating accelerations) can become dominant in the manner shown in Figs. 7 and 8. Love [5] remarks that such modes would probably be difficult to excite. It appears that diffracting a shock wave around a cylinder is quite effective in exciting these high frequency modes.

before the blast loading is initiated at time = 0. The transient responses to the standard blast pulse are plotted in positive time for three cases: the motor bottle with and without propellant having an internal pressure of 6.89 MPa (1000 psi), which is understood to be a representative operating pressure for a rocket motor, and the motor without propellant with half the above internal pressure which was run to study the effect of varying the internal pressure. One sees that increasing the internal pressure raises the frequency of oscillation and decreases the amplitude of response (provided the shell remains elastic). At the operating pressure adding propellant lowers the frequency of response and has little effect on the amplitude.

Figure 10 presents cross section views of cylinder response at two times for the case represented by the solid curve in Fig. 9. In these views the departure from the initial unpressurized configuration has been magnified by a factor of one hundred. For Cycle 0 we see the axisymmetric extensional deformation pattern which exists immediately before the arrival of the blast loading. With the 6.89 MPa (1000 psi) internal pressure the circumferential membrane stress is 91 percent of the uniaxial yield stress while the maximum bending stresses are less than one percent of this quantity. The cross section for Cycle 377, which may be associated with the second inward peak displacement shown in Fig. 9, exhibits an essentially inextensional flexural deformation superposed upon the extensional pattern for

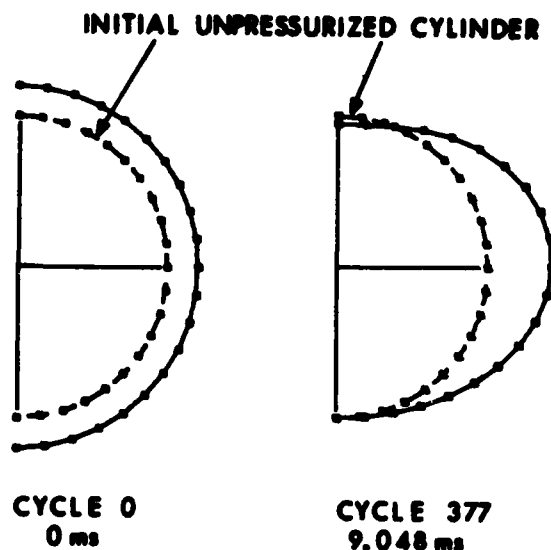


Fig. 10. Cross Sections of Pressurized Cylinder

Cycle 0. The corresponding quasi-static and transient strains at the crown line are depicted in Fig. 11. Clearly, the blast-induced strain fluctuations are small in comparison to the pressurization-induced strain. In fact, in spite of the large pre-stressing, none of the problems treated in Fig. 9 were predicted to experience permanent deformation of the motor case as a result of the blast loading.

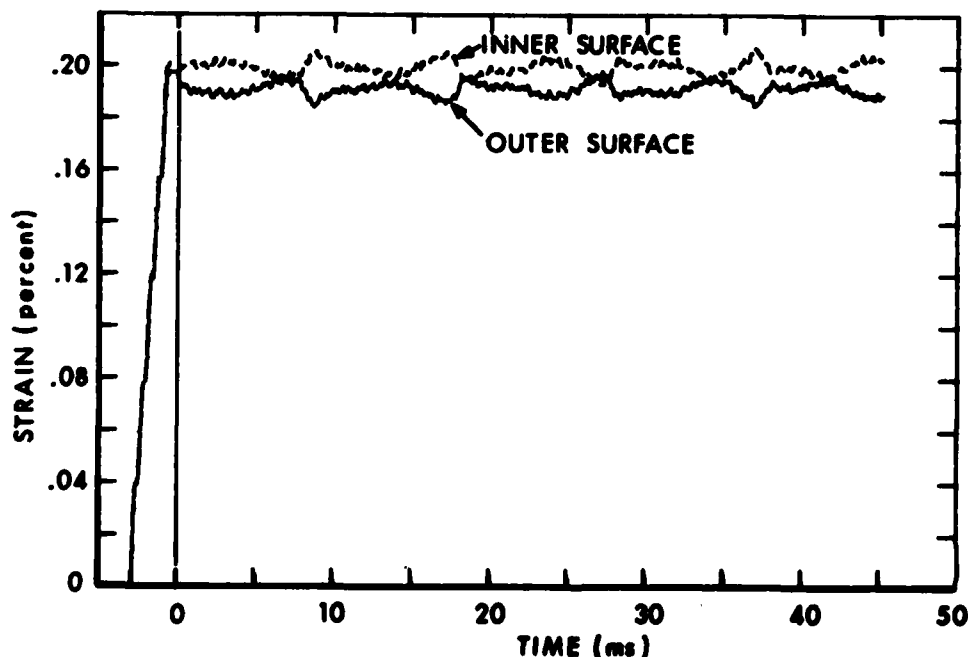


Fig. 11. Circumferential Strain at  $\theta = 0^\circ$  for  $p_i = 6.89$  MPa (1000 psi) Without Propellant

The stiffening effect of internal pressurization is demonstrated in Fig. 12, which shows the variation of maximum deflection of the bare cylinder as a function of internal pressure for a constant external blast loading. The black dots on this figure are values obtained by PETROS 3.5 calculations and the curve is a line faired through these values. The curve is dashed beyond  $p_i = 8.48$  MPa (1230 psi) to

indicate that a different trend may be expected after the internal pressure alone is sufficient to produce yielding. The great magnification of response in the neighborhood of  $p_i = 0$  is of considerable practical significance. This can be readily explained in terms of Fig. 13, which shows the dependence of natural frequencies  $f_{n,1} (= \omega_{n,1}/2\pi)$  of the lower inextensional modes discussed in the Appendix on the internal pressure. One sees that this family of modes is strongly affected by the quasistatic pressurization  $p_i$  and that the lowest flexural mode frequency  $f_{2,1}$  vanishes for  $p_i = -0.214$  MPa (-31.1 psi). This intercept on the  $p_i$  axis represents the value of external pressure for which static buckling of the cylinder would occur without any additional blast loading. The actual blast loading can be decomposed into a transient uniformly distributed external

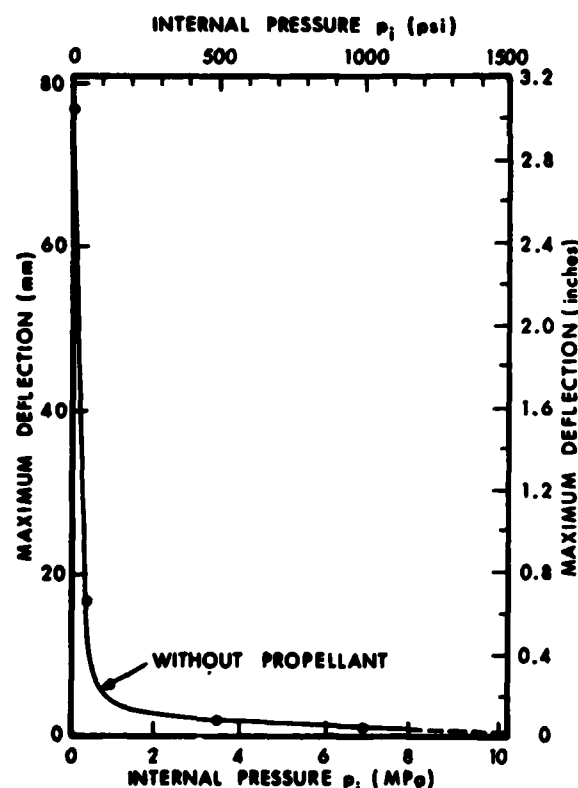


Fig. 12. Effect of Internal Pressure on Peak Response

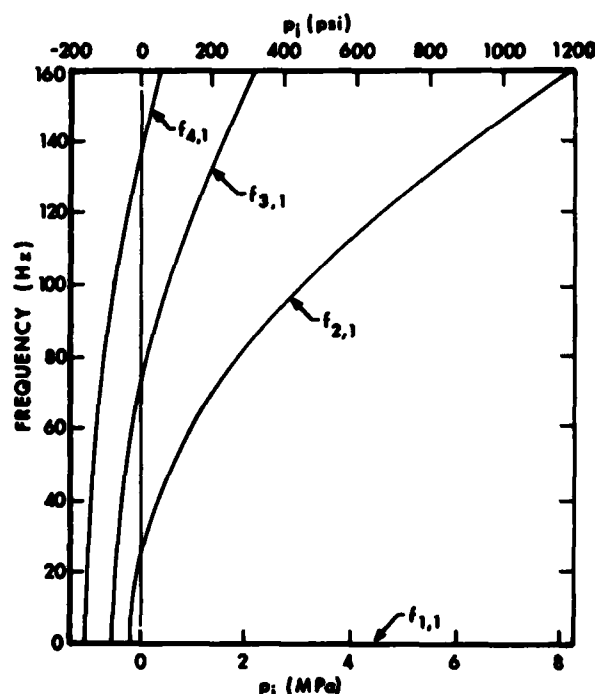


Fig. 13. Effect of Internal Pressure on Certain Inextensional Mode Frequencies

pressure and a non-uniform transient loading. The latter serves to deform the cylinder from the initial circular cross section (analogous to a large initial imperfection) while the uniform component provides a nonlinear amplification of response if its magnitude is a significant fraction of the pressure required for static buckling. For the blast loading employed in the PETROS 3.5 calculations the temporal variation of the uniform component is shown in Fig. 14. This pressure component reaches a maximum of 0.119 MPa (17.3 psi), which is 55.6% of the static buckling pressure, and decays slowly with respect to the period of the fundamental bending mode (39.3 ms) so there is ample time for a large deflection to occur. For large internal pressurization the circumferential membrane stresses remain tensile in spite of the blast loading so there is no near-buckling effect. In fact, consonant with the raising of the frequency spectrum of the inextensional modes with increasing  $p_i$ , there is a decrease in response amplitude (at least until  $p_i$  alone causes plastic yielding). For completeness it should be noted that the extensional family of vibration modes ( $s = 2$ ) whose frequencies are defined by Eq. (A-3) of the Appendix are quite insensitive to variation of  $p_i$ , as indicated by Fig. 15.

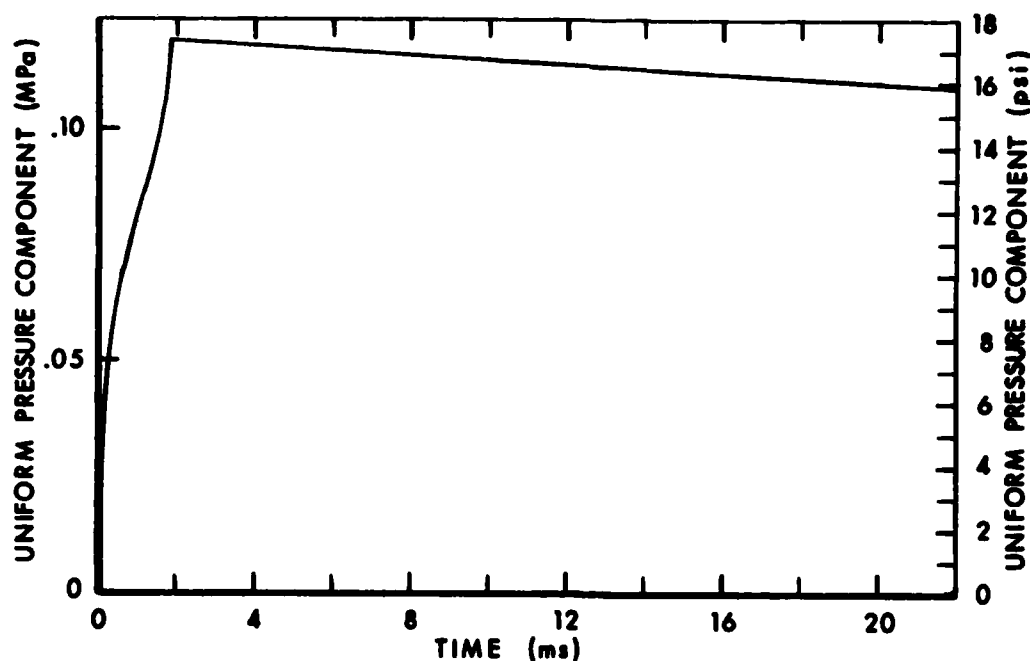


Fig. 14. Variation of Mean External Pressure

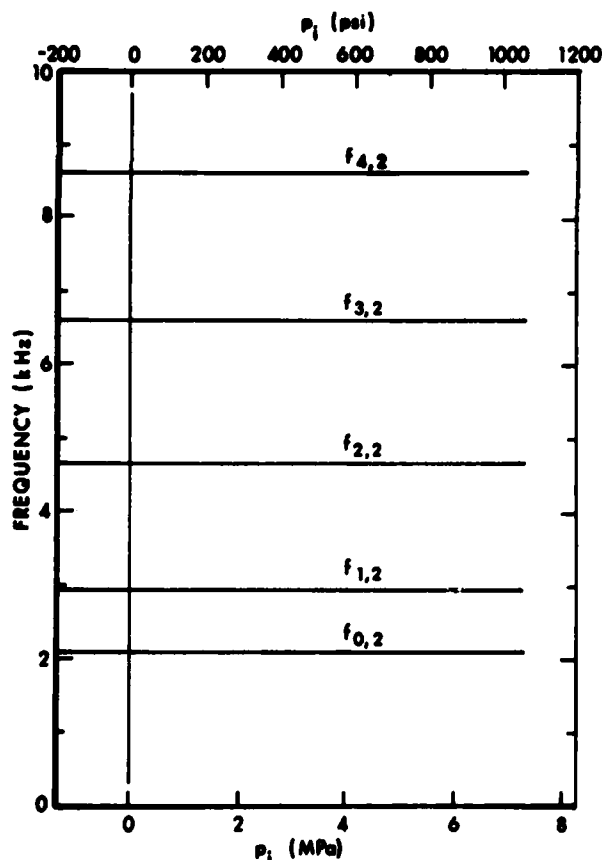


Fig. 15. Effect of Internal Pressure on Frequencies of Extensional Modes

#### CONCLUDING REMARKS

The finite amplitude elastoplastic shell response code PETROS 3.5, while not capable of fully representing the response of a rocket motor containing propellant, has provided useful baseline data for evaluating predictions derived with other models. The linearized analytical model referred to in the Appendix provides insight into the meaning of the results of the nonlinear numerical analysis.

The response of a typical rocket motor configuration was calculated for the limiting situations of the bare motor case and of the motor case containing the complete propellant grain, each with no internal pressurization and with the pressurization resulting from propellant combustion. It was found that the unpressurized motors had a much larger deformation than the pressurized motors. Also, for the motors containing propellant it was possible to obtain an estimate of the tensile stress to which the propellant/case bond would be subjected.

The most significant result is the quantification of the greater vulnerability of rocket motors prior to their ignition, whether on the launcher or as upper stages of in-flight missiles.

# ACKNOWLEDGMENT

This work was supported by the U.S. Army

Harry Diamond Laboratories under Department of Army Project 1L162118AH75.

# REFERENCES

1. T. L. Cost and G. E. Weeks, "Automated Evaluation of Interceptor Rocket Motor Designs Under Combined Operational and Nuclear Effects Loads," University of Alabama BER Report No. 176-97, July 1974.
2. S. D. Pirotin, B. A. Berg, and E. A. Witmer, "PETROS 3.5: New Developments and Program Manual for the Finite-Difference Calculation of Large Elastic-Plastic Transient Deformations of Multilayer Variable-Thickness Shells," U.S. Army Ballistic Research Laboratories Contract Report No. 211, February 1975.
3. L. Marino, J. W. Leech, and E. A. Witmer, "PETROS 2: A New Finite-Difference Method and Program for the Calculation of Large Elastic-Plastic Dynamically-Induced Deformations of General Thin Shells," U.S. Army Ballistic Research Laboratories Contract Report No. 12, December 1969.
4. S. Glasstone (Editor), "The Effects of Nuclear Weapons," United States Atomic Energy Commission, April 1962.
5. A. E. H. Love, "A Treatise on the Mathematical Theory of Elasticity," Fourth Edition, Dover Publications, 1944, p. 454.

# Appendix

## VIBRATION CHARACTERISTICS OF PRESSURIZED ELASTIC CYLINDERS

The small amplitude elastic oscillations of internally pressurized plane strain cylinders have been investigated and, while the formulation will not be presented herein, certain results which are useful for interpreting the numerical solutions obtained with the PETROS 3.5 code will be stated.

Let  $v(\theta, t)$  and  $w(\theta, t)$  be the tangential and radial components of deflection, respectively. Then a free vibration mode consists of a deflection component pair of the form

$$w_{n,s} = A_{n,s} \cos n\theta \sin(\omega_{n,s}t + \psi_{n,s}) \quad (A-1)$$

$$v_{n,s} = B_{n,s} \sin n\theta \sin(\omega_{n,s}t + \psi_{n,s}) \quad (A-2)$$

where  $n = 0, 1, 2, 3, 4, \dots$  and  $s = 1, 2$ . The circular frequencies  $\omega_{n,s}$  are determined from the equation

$$\omega_{n,s} = \left[ \frac{\alpha}{2} \left\{ 1 + (1+2q)n^2 + k(1-n^2)^2 \right. \right. \\ \left. \left. \pm \left[ (1+n^2)^2 + 4(2+q)qn^2 + 2k(1-n^2)^3 + k^2(1-n^2)^4 \right]^{1/2} \right\} \right]^{1/2} \quad (A-3)$$

where

$$k = \frac{1}{12} \left( \frac{h}{a} \right)^2, \quad q = \frac{(1-\nu_c^2)p_i a}{E_c h}, \quad \alpha = \frac{E_c}{(1-\nu_c^2)\rho_c a^2} \quad (A-4)$$

$h$  = thickness of cylinder

$a$  = radius of mid-surface of cylinder

Eq. (A-3) provides two values of circular frequency for each value of  $n$ ; the smaller of these is designated  $\omega_{n,1}$  and the larger  $\omega_{n,2}$ .

The modal amplitude coefficients  $A_{n,s}$ ,  $B_{n,s}$  are not independent. If  $A_{n,s}$  is chosen arbitrarily, then  $B_{n,s}$  is proportional to  $A_{n,s}$  and to a rather complex function of  $\omega_{n,s}$  and  $q$ . Since  $\omega_{0,1} = \omega_{1,1} = 0$  the corresponding displacements are not vibratory modes. The case  $n = 0, s = 1$  represents a static axisymmetric expansion or contraction of the cylinder while the case  $n = 1, s = 1$  corresponds to a rigid body translation of the cylinder in the direction of the  $\theta = 0^\circ$  plane. For  $n > 2, s = 1$  the ratio  $B_{n,1}/A_{n,1}$  takes on values such that the middle surface extension is negligible; i.e., this lower frequency family of modes can be characterized as an essentially inextensional, flexural set. The  $s = 2$  family of modes, whose lowest frequency is two orders of magnitude greater than the fundamental flexural frequency in the unpressurized case, may be characterized as the extensional vibratory set which, in general, also entail flexural stresses. The  $n = 0, s = 2$  mode of this set is the axisymmetric breathing mode of the cylinder.

## DISCUSSION

Voice: Apparently you are going into a finite element analysis would you tell us why the existing code does not solve your problem?

Mr. Huffington: The existing code does not exactly solve the problem with the propellant in the motor case and we are not satisfied with lumping the mass. We ignored the stiffness of the propellant entirely. The properties of the propellant that I showed revealed that it is quite weak with respect to the strength of the motor case, so I don't think that ignoring the stiffness is too serious. However we wanted to carry out the analysis where the propellant is modeled as a viscoelastic solid and we have not done that in the model that I have shown.

Voice: You also mentioned fairly good agreement with experimental data; could you quantify that?

Mr. Huffington: I didn't mean to imply that I compared it with experimental data, I simply said that it is consistent with the fact that internal pressurization is known to produce a stiffening effect; just as blowing up an intertube makes the torus stiffer. We don't have any data to make a comparison at the present time.



# EXPERIMENTAL AND THEORETICAL DYNAMIC ANALYSIS OF CARBON-GRAPHITE COMPOSITE SHELLS

A. Harari and B. E. Sandman  
Naval Underwater Systems Center  
Newport, Rhode Island 02840

A comparison between experimental and theoretical models of a carbon-graphite/honeycomb composite shell vibrating in air and submerged in water is presented. Mode shapes and resonant frequencies are identified according to theory and experiment both for in-air and in-water vibration. Excellent agreement is exemplified.

## INTRODUCTION

In addition to the well-known advantages of utilizing composite materials in the fabrication of light-weight, high-strength structures, composite materials also exhibit properties which are desirable in terms of reducing structural vibration and noise transmission. In particular, a carbon-graphite, fiber/epoxy matrix composite exhibits both high rigidity and high internal damping [1] which are desirable characteristics in the design of a structure which displays high impedance to dynamic disturbing forces and low transmission of dynamic energy. Sandwich cylindrical shells have been designed and fabricated with carbon-graphite fiber composite facings and honeycomb cores for light-weight, high-strength applications. It is apparent that the determination of the dynamic characteristics of these shells in terms of noise transmission and radiation is essential for the overall assessment of their application. The inherent characteristics of the carbon graphite composite shells offer possible solutions and benefiting factors in reducing the levels of farfield radiated noise and structural-borne noise transmission.

The high levels of structural stiffness and internal damping provide the possibility of reduced levels of radiated noise, and the properties of the layered composite construction with differing velocities of longitudinal wave propagation in each layer impedes the path of transmission [2] for high frequency components of noise. Although the

above discussion is purely qualitative in nature, the indications are that the carbon graphite composite may offer considerable advantages in the area of noise reduction. Experimental and analytical studies were conducted to determine the dynamic characteristics of a carbon-graphite shell in air and in water. The analytical study is based on the formulation described in Ref. [3]. Comparison between the experimental and analytical results is contained in the following description of the current investigation.

## THEORETICAL COMPOSITE SHELL ANALYSIS

The shell structure consists of three layers of orthotropic materials, as shown in Fig. 1. The analysis of the shell utilizes Hamilton's principle to derive the equations of motion. Continuity of the displacements is enforced at the interface between the core and the layers. Transverse shear deformation is considered and higher order terms are retained in order to make the analytical model valid for thick shells. The partial differential equations can be written in the following manner:

$$LD = -(P + F)$$

where L is a (5 x 5) matrix differential operator, and D is the (5 x 1) displacement vector

$$D = \begin{pmatrix} u \\ v \\ w \\ Ru_1 \\ Rv_1 \end{pmatrix}$$

containing the displacement components  $u, v, w$  and shear angles  $u_1, v_1$  with  $R$  denoting the mean radius of the shell.  $P$  symbolizes the induced fluid pressure loading  $(5 \times 1)$  vector,  $P_{143} = 0$ , and  $F$  is the externally applied force  $(5 \times 1)$  vector.

The solution for a simply supported shell is found by expanding the displacement vector in the following manner:

$$D = \sum_m \sum_n X_{mn} D_{mn} e^{i\omega t}$$

where

$$X_{mn} = \begin{bmatrix} \cos \alpha_m \xi \cos n\theta & 0 \\ \sin \alpha_m \xi \cos n\theta & 0 \\ \sin \alpha_m \xi \cos n\theta & 0 \\ \cos \alpha_m \xi \cos n\theta & 0 \\ 0 & \sin \alpha_m \xi \sin n\theta \end{bmatrix}; \quad \alpha_m = \frac{m\pi R}{L}$$

and the  $D_{mn}$  are the model components of displacement. The external forces and pressure loading are expanded into Fourier's components. For a given external force and frequency of excitation, the solution to a truncated set of linear algebraic equations yields the amplitude response. The elements of analysis employed are directly applicable to the study of the vibration and response of sandwich shells. Both in-air and in-water vibrations can be considered without difficulty. In order to assess the validity of the theoretical model outlined above, experimental tests were performed for in-air and in-water vibration of a carbon-graphite/honeycomb sandwich shell. Subsequently, the comparison of theory and experiment provides the validation phase of this study.

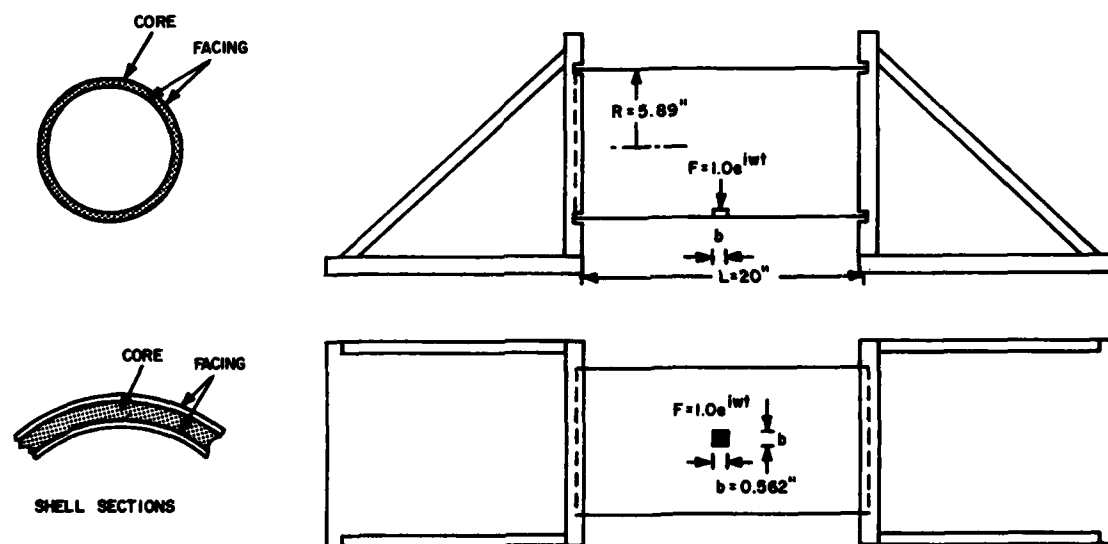


Fig. 1 - Sandwich shell and experimental fixture configuration

## EXPERIMENT

Figure 1 gives an illustrated outline of the test fixture which was used for the dynamic excitation of the carbon-graphite shell. The shell is mounted between two massive supporting end-plates. The edges of the shell are constrained in the radial direction, allowed free rotation, and allowed to move in the axial direction. In the circumferential direction the shell is allowed to move, but, due to friction enhanced by the radial force, this

movement is partially inhibited. The boundary condition is therefore an approximation to the analytical boundary condition which assumes zero tangential displacement at the edges of the shell. The material properties of the shell were taken from tables prepared by the manufacturers. The aluminum honeycomb properties were taken from tables prepared by "Honeycomb Company of America, Inc.". The carbon-graphite properties were taken from tables prepared by "Fiberite Corporation". The material and geometrical properties of the shell are as shown in Table 1.

TABLE 1  
Carbon-Graphite/Honeycomb Sandwich Shell Properties

Parameters	Top Layer	Bottom Layer	Core
h, Thickness (cm)	0.33	0.35	1.78
$E_x$ , Tensile modulus in axial direction (dyn/cm <sup>2</sup> )	$0.55 \times 10^{12}$	$0.55 \times 10^{12}$	0
$E_\theta$ , Tensile modulus in circumferential direction (dyn/cm <sup>2</sup> )	$1.03 \times 10^{12}$	$1.03 \times 10^{12}$	0
$E_{x\theta}$ , (Poisson ratio) $\times$ (Tensile modulus) (dyn/cm <sup>2</sup> )	$0.21 \times 10^{12}$	$0.21 \times 10^{12}$	0
$G_{x\theta}$ , Shear modulus (dyn/cm <sup>2</sup> )	$0.31 \times 10^{12}$	$0.31 \times 10^{12}$	0
$G_{zx}$ , Shear modulus (dyn/cm <sup>2</sup> )	--	--	$0.93 \times 10^{10}$
$G_{z\theta}$ , Shear modulus (dyn/cm <sup>2</sup> )	--	--	$0.55 \times 10^{10}$
P, density (kg/m <sup>3</sup> )	$0.23 \times 10^4$	$0.23 \times 10^4$	$0.25 \times 10^3$

Resonant frequencies of the shell in air and in water were identified by locating the low points in the plot of shell impedance during a frequency sweep of sinusoidal excitation. Although the shell excitation and response was monitored at the approximate center-span of the shell, it was found that low-level anti-symmetric modes appeared in the response spectrum. This is probably due to errors in both the location of the shaker and a lack of complete shell configuration symmetry. The mode type corresponding to a given resonant frequency was determined by mapping the vibrating surface of the shell with a hand-held accelerometer. It was found that the mode shape was relatively insensitive to a hand-held accelerometer both in air and in water. Also it was determined that the resonant frequency of an in-water mode was not strongly influenced by the depth of submergence in the neighborhood of the surface of the acoustic tank. This factor allowed relative ease in the identification of in-water shell modes with a hand-held accelerometer while the shell was near the surface of the water. It is noted that not all modes of the shell were necessarily identified in a given frequency range. In

particular, due to low levels of response, no circumferential breathing ( $n=0$ ) type modes were found.

#### DISCUSSION OF ANALYTICAL AND EXPERIMENTAL RESULTS

Table 2 lists and illustrates the resonant frequencies and corresponding mode types as obtained by theory and experiment for vibration of the carbon-graphite/honeycomb sandwich shell in air. The theoretical frequencies were obtained by performing a discrete numerical frequency sweep with a digital computer program of the equations which provide the theoretical solution. Although there exists some disparity at the lower frequencies, which may be attributed to the boundary conditions, the overall agreement is seen to be excellent. The agreement is indeed remarkable in view of the fact that an exact knowledge of the shell properties is not established and the properties used in the theory are "good" estimates. Table 3 presents the results of theory and experiment as they were obtained for in-water vibration. Again, the agreement between theory and experiment is remarkably good with the exception of only one or two frequencies.

TABLE 2

Comparison of Theoretical and Experimental  
Resonant Frequencies for In-air Vibration of  
Carbon-Graphite/Honeycomb Composite Shell

MODE TYPE (m, n)	FREQUENCY (Hz)	
	EXPERIMENT	THEORY
(1, 2)	1053	1210
(1, 1)	1195	1650
(1, 3)	1938	2016
(2, 3)	2363	2650
(1, 4)	3072	3050
(2, 4)	3382	3400
(3, 3)	3650	3700
(1, 5)	4026	4028

TABLE 3

Comparison of Theoretical and Experimental Resonant  
Frequencies for In-water Vibration of Carbon-Graphite/  
Honeycomb Composite Shell

MODE TYPE (m, n)	FREQUENCY (Hz)	
	EXPERIMENT	THEORY
(1, 2)	537	616
(1, 1)	757	820
(1, 3)	1033	1120
(2, 3)	1324	1560
(1, 4)	1717	1786
(3, 3)	1993	2252
(1, 5)	2344	2520

## CONCLUSIONS

Experimental and theoretical analyses of a filament-wound, carbon-graphite, honeycomb sandwich shell were performed to determine both in-air and in-water resonant frequencies. Within the limitations and scope of this study, the results in regard to the agreement of theory and experiment are shown to be excellent. Thus, preliminary validation of the theoretical model has been achieved in the completion of this investigation. The extension of this work to include higher-order modes, which were not readily identifiable with a hand-held accelerometer, would enhance the results presented here. Also, for future study, it is planned to investigate the ability of the theoretical model to adequately predict levels of shell response and acoustical radiation in air and in water. This phase of validation will require a reasonably good estimate of structural damping.

## ACKNOWLEDGEMENT

The authors would like to express their appreciation to Mr. Louis Pettit of NUSC for providing the essential experimental data for this work.

## REFERENCES

1. D. Miller, "Structural and Damping Effects of Graphite Fiber-Epoxy Resin Composite Structures," presented at the Sixth St. Louis Symposium on Composite Materials in Engineering Design, St. Louis, Missouri, 1972.
2. R. M. Christensen, "Attenuation of Harmonic Waves in Layered Media," *Journal of Applied Mechanics*, Vol. 40, pp. 155-160, 1973.
3. A. Harari and B. E. Sandman, "Vibratory Response of Laminated Cylindrical Shells Embedded in an Acoustic Fluid," *The Journal of the Acoustical Society of America*, Vol. 60, No. 1, July 1976.

# USE OF SHOCK SPECTRA TO EVALUATE JITTER OF A FLEXIBLE MANEUVERING SPACECRAFT

William J. Kacena  
Martin Marietta Corporation  
Denver, Colorado

Structural dynamic analysts are responsible for evaluating the effects of vibration on the operation of displacement sensitive spacecraft instruments. One example is an optical pointing instrument that is vibrating because an orbital maneuver has just been performed. This paper shows that a residual displacement shock spectrum of the rotational acceleration time history defines the vibration modes and the maneuvers which are critical to pointing accuracy. In addition, several realistic maneuvers are discussed and their effects on vibration are compared.

## INTRODUCTION

The performance of displacement sensitive instruments on a spacecraft may be degraded by maneuver induced vibration, or jitter. Just as a wiggled camera gives a blurry picture, a vibrating star sensor may produce a distorted record of star location. Any precision alignment instrument that operates on optical principals to record or transmit from an inertial platform in space (be it a star sensor, camera, telescope, antenna, laser, or a variety of other sensors) is subject to vibratory pointing error. When large control torques are used, spacecraft optimization studies must consider which torque time histories can best achieve the desired maneuver without introducing excessive jitter. This paper shows that a residual displacement shock spectrum of the resulting acceleration time history provides necessary data for such a study.

The pointing error in each vibration mode results from solving a differential equation. With appropriate assumptions about the forcing function, each modal equation is driven by a modal constant times the spacecraft rotational acceleration time history. Given a maneuver history, the envelope of its residual displacement shock response spectrum accounts for changes in the time scale that can interchange spectral peaks and valleys, and the effects of various modes are compared by multiplying the envelope value at each modal frequency by the modal constant. In addition to defining which modes are important to pointing accuracy, the shock spectrum approach identifies the time scale for a family of similar maneuvers that produces nearly worst case results. The presence of spectral peaks at the critical modal frequencies provides

this identification.

When structural dynamic analysts conduct these worst mode and worst maneuver identification studies, closed loop control studies can evaluate pointing performance directly without the need for retaining uninteresting modes or searching for a bad maneuver. Hence, these identification studies can represent a considerable cost savings in route to a correct interpretation of spacecraft pointing performance.

An additional advantage of the shock spectrum approach is the comparison of dissimilar families of maneuvers. Trade study results of this nature are of value in deciding what control software is best suited to the pointing operation of a particular spacecraft system. For this reason, a spectral comparison study for dissimilar maneuvers typical of actual control systems is presented on an envelope line basis. Finally, the appendix summarizes an efficient algorithm for determining the residual spectrum on a digital computer.

## NOMENCLATURE

### Matrices

$[m]$	mass
$[k]$	stiffness
$[m_g]$	generalized mass
$\{\phi\}$	normal modes
$[A]$	a transformation
$[T]$	a geometric transformation
$[I]$	mass moments-of-inertia
$[P]$	pointing transformation

## Vectors

$\{X\}$	discrete coordinates
$\{F\}$	discrete forcing functions
$\{q\}$	generalized, modal coordinates
$\{\omega\}$	natural frequencies
$\{M\}$	rigid-body moments
$\{V\}$	direction cosines

## Symbols

$a, b, B, C$	constants
$E$	envelope line
$f$	frequency (Hz)
$J$	maximum jerk
$p$	pointing error = $[P]\{X\}$
$q$	generalized coordinate
$S, \mathcal{L}(\ )$	Laplace transform notations
$t$	independent time variable
$T$	half the maneuver time
$\ddot{\theta}, \ddot{\phi}, \ddot{\psi}$	jerk, acceleration, rate and angle of maneuver
$\Delta t$	a time step
$\omega$	frequency (rad/sec)

## APPROXIMATE EQUATIONS OF MOTION

The linear equations of motion for the maneuver excited vibration of a spacecraft are

$$[m] \{\ddot{x}\} + [k] \{x\} = \{F(t)\} \quad (1)$$

When the free system normal modes and natural frequencies are used to uncouple the equations, (1) becomes

$$\{\ddot{q}\} + \{\omega^2 q\} = [m_g^{-1}] [\phi]^T \{F(t)\} \quad (2)$$

Several assumptions about the behavior of the control system allow us to simplify the forcing function to the more useable form

$$\{F(t)\} = \{\text{Constant}\} \ddot{\theta}(t), \quad (3)$$

where  $\ddot{\theta}(t)$  is the angular acceleration time history about the maneuver axis of the spacecraft.

Euler's moment equations [1] for rigid-body dynamics involve angular acceleration terms and terms which include products of angular rates. For relatively small angle maneuvers of a spacecraft with an active control system, the rates are generally small, and the nonlinear rate product terms can be neglected compared to the acceleration terms. This same assumption is implied whenever linear rigid-body modes of a free system are used for structural dynamic analyses. With this approximation the rigid-body rotational dynamics are written as

$$\{M\} = [I] \{\ddot{\theta}\}, \quad (4)$$

where the  $M$ 's are external moments, the  $I$ 's are mass moments-of-inertia about the CG, and  $\ddot{\theta}$ 's are angular accelerations, all associated with body axes that are not necessarily principal axes.

A second assumption is that the control logic executes the maneuver with correlated accelerations about the body axes. In other words, the angular acceleration axis in a body coordinate system is a constant, and the acceleration vector is written as

$$\{\ddot{\theta}(t)\} = \{V\} \ddot{\theta}(t), \quad (5)$$

where  $\{V\}$  is a vector of direction cosines for the body-fixed rotation axis. A combination of (4) and (5) gives

$$\{M(t)\} = [I] \{V\} \ddot{\theta}(t) \quad (6)$$

The rigid-body moments are related to the discrete forces and moments applied to structural node points through a geometric transformation  $[T]$ .

$$\{M(t)\} = [T] \{F(t)\} \quad (7)$$

Then (6) and (7) combine to yield

$$[I] \{V\} \ddot{\theta}(t) = [T] \{F(t)\} \quad (8)$$

Finally, (8) is solved for  $\{F(t)\}$  to achieve the form of (3)

$$\{F(t)\} = [A] [I] \{V\} \ddot{\theta}(t) = [A] \{M(t)\} \quad (9)$$

But what is  $[A]$ ? The columns of  $[A]$  are arrangements of body forces which, when pre-multiplied by  $[T]$ , will give a unit moment on the  $x$ ,  $y$  and  $z$  axes, respectively. In general,  $[T]^T [T]$  is singular, and constraint equations associated with the detailed control torque logic must be applied before (8) can be solved for  $[A]$ .

For early system design studies, where this kind of analysis is most likely to be used, the control torque logic is unknown, and  $[A]$  cannot be determined directly. However, a straight forward approach is to arbitrarily choose one of the many  $[A]$  matrices that satisfies both (7) and (9). Although this may seem like a gross simplification, this author's experience shows that for real systems there is little difference in the modal forcing functions, regardless which  $[A]$  is selected. One reason for this is that control torques are generally lower frequency than the structure, and the free elastic structure responds as though it is driven by a base-motion at the CG which results from the applied torques. Some discretion in the choice of  $[A]$  is recommended in the form of the guidelines below:

- 1) forces should be applied to stiff structure near the actual control force locations;
- 2) forces should not be applied to the ends of deployed appendages, unless the actual control forces are applied there; and
- 3) forces should not be applied adjacent to the pointing instruments under

evaluation, unless the actual control forces are in that area.

Finally, (9) and (2) are combined to form the approximate modal equations of motion

$$\begin{aligned} \{\ddot{q}\} + \{\omega^2 q\} &= [m_g^{-1}] [\phi]^T [A] [I] \{v\} \ddot{\theta}(t) \\ &= \{B\} \ddot{\theta}(t), \end{aligned} \quad (10)$$

where  $\{B\}$  is a constant associated with a particular body axis of rotation. For a known maneuver acceleration about a known axis, the modal responses  $\{q\}$  are determined from (10).

#### POINTING RESPONSE SPECTRUM

The discrete response displacements in the  $i$ th mode of vibration are

$$\{x_i(t)\} = \{\phi_i\} q_i(t) \quad (11)$$

Generally, the modal pointing error of the scientific instrument of interest can be written as

$$p_i = [P] \{\phi_i\} q_i(t) = (P\phi)_i q_i(t) \quad (12)$$

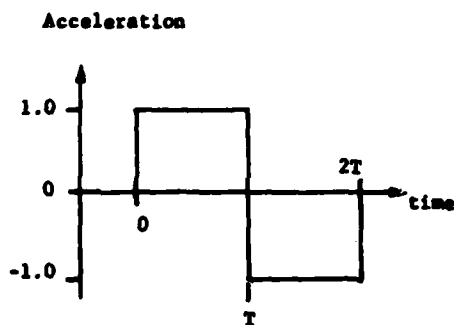
where the row matrix  $[P]$  constructs the pointing error as a linear combination of the system deflections. This transformation to performance coordinates says that a single number for each mode,  $(P\phi)_i$ , can be used in a closed loop control analysis to evaluate pointing performance directly. However, intermediate analyses are necessary to identify which vibration modes and which maneuvers create pointing problems.

To this end, we combine (10) and (12) for the  $i$ th mode of vibration

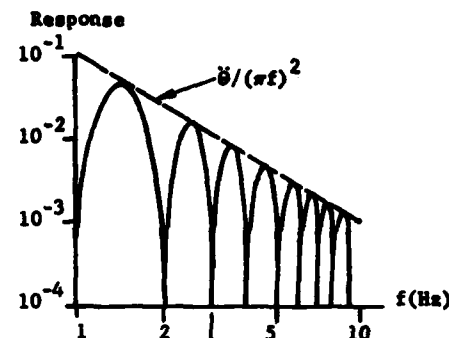
$$\ddot{p}_i + \omega_i^2 p_i = (P\phi)_i B_i \ddot{\theta}(t) = C_i \ddot{\theta}(t) \quad (13)$$

The parameter of interest is the maximum magnitude of the pointing error,  $p$ , after the maneuver is over. Since the equations like (13) for all modes of vibration differ only in the magnitudes of the constants  $C_i$  and  $\omega_i$ , a residual displacement shock spectrum of  $\ddot{\theta}(t)$  is a convenient way to compare the modal effects as functions of natural frequencies. This displacement spectrum may look something like that for the rectangular wave shown in Fig. 1.

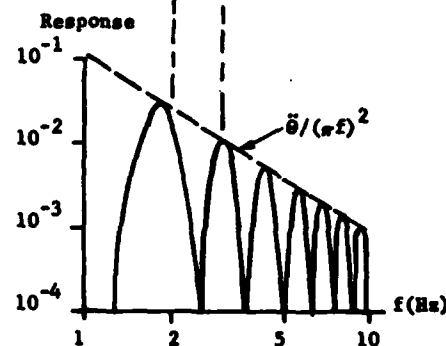
The figure illustrates that the spectrum has peaks at some frequencies and valleys at others. In addition, an envelope curve, which decreases with increasing frequency, bounds all the peaks. Fig. 1(c) shows that, when the time scale on the forcing function is changed to represent a smaller maneuver, the same envelope line results, but peaks may occur where valleys used to exist. These results show that the envelope line, and not the spectrum, is the proper rationale for identifying critical modes. The frequency scale from 1 to 10 Hz is used in the figure for illustration purposes only. For some spacecraft, a different range (say from 5 to 50 Hz) will better represent the



a) Rectangular Wave



b) Spectrum for  $T = 1.0$  sec



c) Spectrum for  $T = 0.8$  sec

Fig. 1 - Residual Displacement Spectra

dominant spacecraft modes. Zero damping is assumed in equation (13) and in the spectral results of Fig. 1. This assumption is made to avert the ever-present problem of defending the selection of a small yet specific value for structural damping. In addition, showing that pointing performance is good for zero damping eliminates the need for a vibration settling time requirement prior to pointing instrument operation.



For very simple maneuvers, like the rectangular wave of Fig. 1, the residual displacement spectrum of equation (13) is easily determined by hand using Laplace transforms [2]. However, slight increases in waveform complexity dictate the use of a numerical solution on a high-speed digital computer. A simple computationally efficient algorithm for determination of this spectrum is described in the Appendix. Before describing the spectra of other maneuver time histories, a discussion of real maneuver waveforms is in order.

#### TYPICAL MANEUVERS CHARACTERIZED

Actual maneuvers typically have acceleration time histories that look like the simple waveforms of Fig. 2. In general, structural and power considerations within the control system itself limit accelerations as indicated by the rectangular wave. In many cases, the same considerations result in jerk ( $\ddot{\theta}$ ) limits as indicated by the finite slope of the trapezoidal wave. Time gaps are depicted with these waveforms to illustrate that control systems may also have velocity or momentum limits that can cause the starting and stopping pulses to be separated by a period of constant velocity rotation. However, the velocity limit can be

reached before the acceleration limit to give a triangular wave with a time gap. The triangular wave shown with no gap implies that there are small angle maneuvers for which neither velocity nor acceleration limits are reached.

These waveforms are all shown symmetric to characterize the maneuvers of most interest as those for which the spacecraft has approximately the same angular velocity before and after the maneuver. This implies that the maneuver angle is small and that the residual body rate vector (which corrects for orbit effects) retains almost the same amplitude and inertial direction that existed before the maneuver. That is not to say that this analysis approach is limited to symmetric waveforms (it is not); but rather, that most maneuvers are approximately symmetric.

Notice, also, that the waveforms presented in Fig. 2 have a high frequency dither riding on the basic pulses. It illustrates that a control system produces high frequency oscillations in addition to the basic maneuver. These oscillations may be related to noise, sampling or command frequencies or feedback of structural vibrations. Although these effects exist and may be somewhat maneuver dependent, they are best evaluated in a closed-loop control analysis.

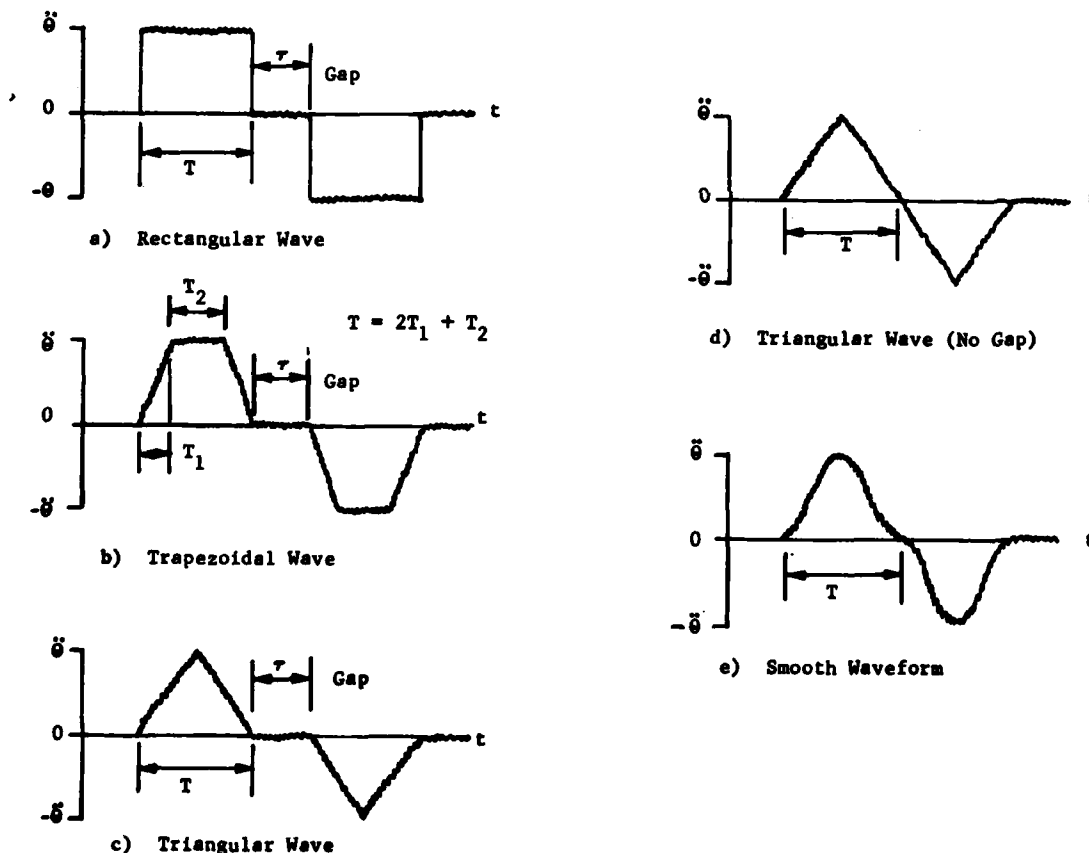


Fig. 2 - Typical Maneuver Acceleration Time Histories

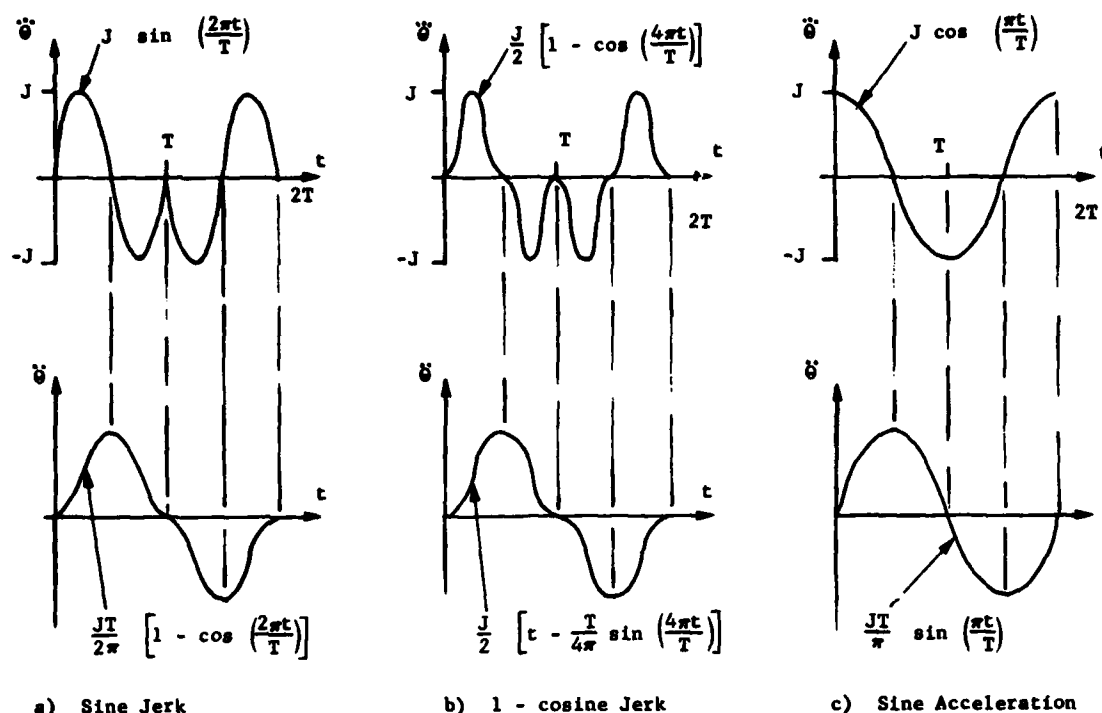


Fig. 3 - Smooth Acceleration Waveforms

Our objective with the shock spectrum technique is screening the basic maneuvers to determine which maneuvers and which vibration modes are bad for pointing. This way the expensive end-to-end control analysis can be limited to critical maneuvers and key modes when evaluating instrument pointing performance.

Finally, Fig. 2(e) indicates that sophisticated control logic may command jerk time histories that are tailored to produce a smooth acceleration. Fig. 3 illustrates that sequential jerk pulses having equations  $\ddot{\theta} = J \sin \omega t$  and  $\ddot{\theta} = J/2 (1 - \cos 2\omega t)$  are reasonable examples of this, while the acceleration equation  $\ddot{\theta} = \ddot{\theta}_{\max} \sin \omega t/2$  is not because the jerk is discontinuous at the beginning and the end of the maneuver. The following section compares the effects these two smooth waveforms along with the simple pulses from Fig. 2 on a residual displacement spectrum basis.

#### MANEUVER SPECTRA COMPARED

We saw in Fig. 1 that the envelopes for rectangular pulses without time gaps are acceleration dominated,  $0.10 \ddot{\theta}/f^2$ . When triangular and trapezoidal pulses without time gaps are similarly investigated the envelopes for both

are jerk controlled at  $0.021 J/f^3$ . However, there is a transition frequency between the acceleration and jerk controlled envelopes as illustrated in Fig. 4. The acceleration envelope controls below  $f = 0.21 J/\ddot{\theta}_{\max}$ , and jerk envelope prevails above this frequency. Fig. 5 depicts typical triangular and trapezoidal spectra: the peaks of the triangular spectrum are more regular relative to the envelope line. Changes in the time scales for these pulses may interchange peaks and valleys, just as observed for rectangular pulses.

When time gaps are added to the rectangular waves, the spectrum becomes irregular relative to the envelope, but the same envelope equation is retained. However, the addition of time gaps to triangular and trapezoidal waveforms not only creates an irregular spectrum, but generally increases the envelope line to  $0.032 J/f^3$ . This result is relatively independent of the magnitude of the time gap; but when  $\tau$  (from Fig. 2) is an even multiple of  $T$ , the envelope equations return to  $0.021 J/f^3$ . Trapezoidal waveforms with time gaps and for which the top time ( $T_2$  in Fig. 2) is a multiple of the rise time do not produce

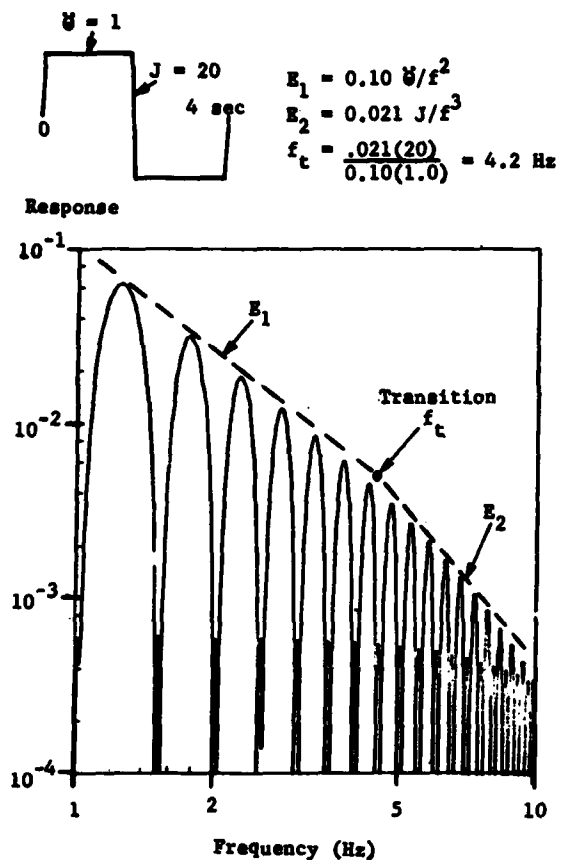


Fig. 4 - Envelope Transition

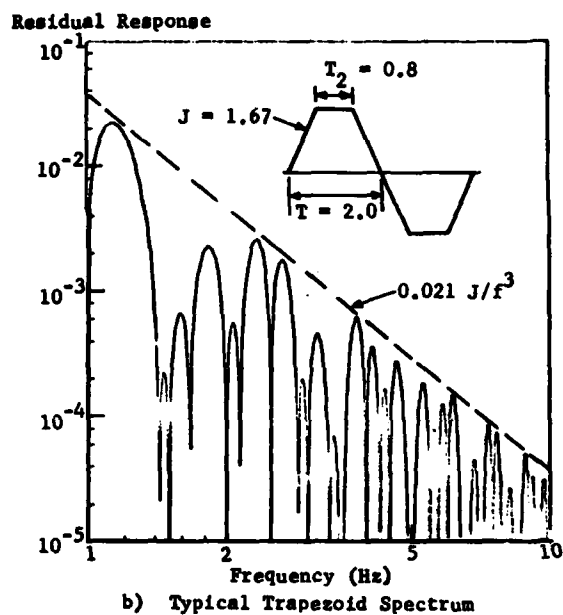
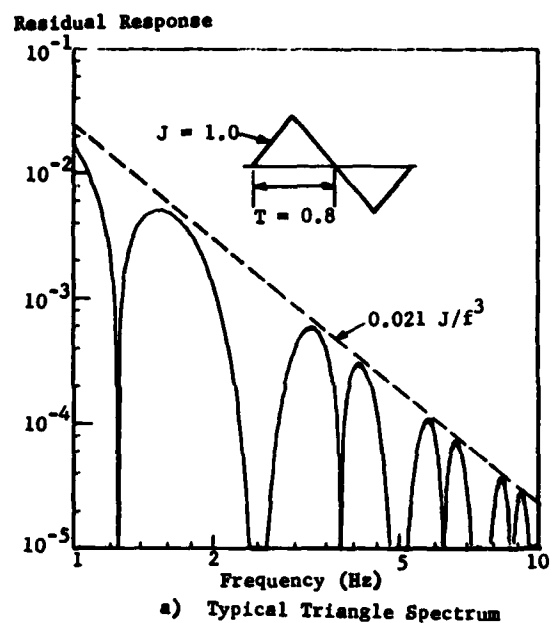


Fig. 5 - Typical Residual Displacement Spectra

the higher envelope lines either. Since control systems do not produce perfectly clean waveforms, it is expected that imperfections in the acceleration waveforms will yield the  $0.032 J/f^3$  envelope equation even when a perfect triangle or trapezoid without a time gap is commanded.

A typical spectrum for a smooth acceleration waveform is presented in Fig. 6. Despite envelope lines that are approximately  $0.02 J/f^3$ , these spectra are dominated by a valley near  $f = 4\pi/T$  that is several Hz wide and two orders of magnitude less than the overall envelope. This result suggests that shaped acceleration pulses are desirable because they excite the structure less. However, Fig. 7 shows that when the forcing function is a series of ramps rather than a smooth curve, the wide valley becomes two smaller ones. This result indicates that a noisy maneuver history may give considerably less benefit than Fig. 6 suggests, as digital command updates may produce this kind of waveform distortion. A time gap in the smooth waveform causes the envelope to increase slightly, but the deep wide valley is retained.

Based on all these results, the general envelope lines are summarized in Table 1. Although the smooth pulses produce lower responses for the same jerk, they are not capable of producing the same angles and angular rates in the same time without going to higher jerks and accelerations.

Table 1 - Envelope Lines Summarized

Wave Description	Envelope Equation
Rectangle	$0.10 \delta/f^2$
Triangle	$0.021 J/f^3$
Trapezoid	$0.021 J/f^3$
Triangle with gap	$0.032 J/f^3$
Trapezoid with gap	$0.032 J/f^3$
Sine Jerk	$0.022 J/f^3$
(1 - cos) Jerk	$0.020 J/f^3$
Sine Jerk with gap	$0.028 J/f^3$
(1 - cos) Jerk with gap	$0.023 J/f^3$

Table 2 presents a different perspective by comparing the maneuvers on a basis of achieving the same angle and rate capability in the same time. This shows that from an overall envelope standpoint, triangular waves are easiest on the structure - either with or without the time gaps. For high frequencies and long times ( $fT > 2$ ), all waveforms except the rectangle have an overall envelope within 40% of one another. Hence, there is little penalty in the adverse frequency ranges if a smooth waveform is used to detune critical modes.

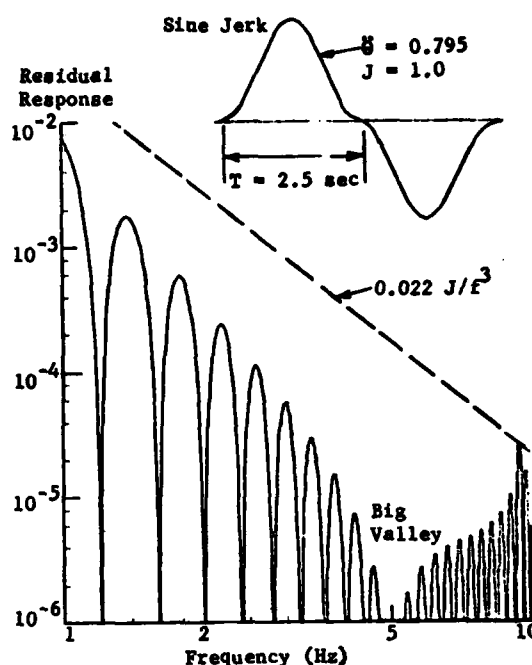


Fig. 6 Big Valley from Smoothness

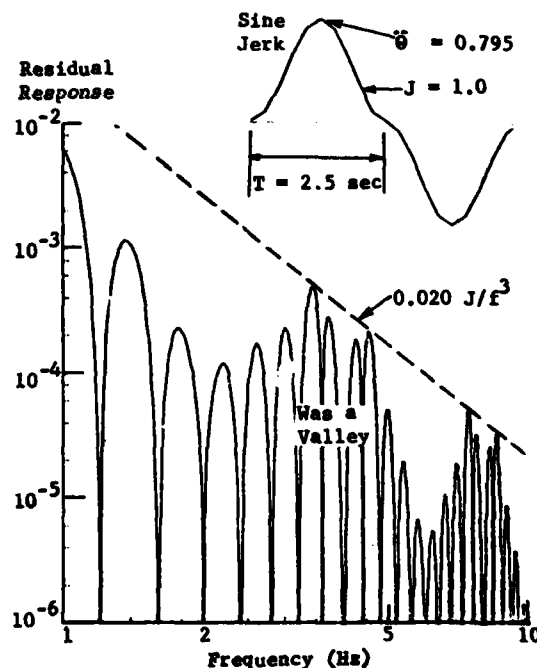


Fig. 7 - Effect of Roughness

Table 2 - Maneuvers Compared for Equal Angle and Rate Capability

Parameter	Maneuver Acceleration Waveforms				
	Rectangle	Triangle	Trapezoid*	Sin Jerk	(1-cos) Jerk
Angle	$\theta$	$\theta$	$\theta$	$\theta$	$\theta$
Rate	$\theta/T$	$\theta/T$	$\theta/T$	$\theta/T$	$\theta/T$
Acceleration	$\theta/T^2$	$2\theta/T^2$	$4\theta/(3T^2)$	$2\theta/T^2$	$2\theta/T^2$
Jerk	$\infty$	$4\theta/T^3$	$16\theta/(3T^3)$	$2\pi\theta/T^3$	$8\theta/T^3$
Envelope Equation	$0.10 z f T$	$(z = \theta/(fT)^3)$		$0.14 z$	$0.16 z$
With Gap	$0.10 z f T$	$0.13 z$	$0.17 z$	$0.18 z$	$0.18 z$
* $T = 2T_1 + T_2$ & $2T_1 \approx T_2$ (a typical trapezoid)					

## CONCLUSIONS

A residual displacement shock spectrum of the rotational acceleration time history ( $\ddot{\theta}$ ) is shown to be a convenient technique for evaluating the effect of maneuvering on the performance of displacement sensitive instruments. The response spectrum for virtually any maneuver is enveloped by all the curves

$$\begin{aligned} E_{\text{jerk}} &= 0.032 J_{\text{max}}/f^3 \\ E_{\text{acceleration}} &= 0.10 \ddot{\theta}_{\text{max}}/f^2 \\ E_{\text{velocity}} &= 0.18 \dot{\theta}_{\text{max}}/(f^3 T^2) \end{aligned} \quad (14)$$

where  $T$  is the time required to reach the limiting velocity. The potential effect of each vibration mode on pointing performance is estimated by evaluating the minimum  $E$  at the modal frequency and multiplying by a modal pointing constant defined herein. A "worst case" estimate of the pointing error is the sum of all the modal effects.

A closed-loop control analysis of pointing may be desirable to evaluate the effects of noise and phasing of the dominant modes. When this is done, maneuvers that excite all the significant modes should be analyzed. Such maneuvers are selected by choosing a time scale which results in a spectral peak very near the frequency of each dominant mode. In this way, a simple shock spectrum analysis tool eliminates using the expensive control analysis on a trial-and-error basis to identify the pointing critical maneuvers.

The residual spectrum results presented for typical waveforms show that significant performance advantages may result from smooth maneuvers. Vibration responses are reduced when the maneuver is adjusted to give a large spectral valley in the region of critical modal frequencies. However, noise and command

frequency characteristics of the particular control system must be evaluated on an individual basis (perhaps using the residual spectrum tool) to determine if the elaborate jerk commands are worth the additional spacecraft cost.

## APPENDIX - COMPUTER ALGORITHM FOR RESIDUAL DISPLACEMENT SPECTRUM

A ramp forcing function is assumed between sequential time history samples to give the single degree-of-freedom equation of motion

$$\ddot{q} + \omega^2 q = a + bt \quad (15)$$

For initial conditions  $q_0$  and  $\dot{q}_0$ , the Laplace Transform of (15) is

$$\mathcal{L}(q) = \frac{a/s + b/s^2 + q_0 s + \dot{q}_0}{s^2 + \omega^2} \quad (16)$$

The inverse Transform of (16) at the end of each time step,  $\Delta t$ , yields

$$\begin{aligned} q(\Delta t) &= (a + b \Delta t)/\omega^2 + (q_0 - a/\omega^2) \cos(\omega \Delta t) \\ &\quad + (\dot{q}_0 - b/\omega^2) \sin(\omega \Delta t)/\omega \end{aligned} \quad (17)$$

$$\begin{aligned} \text{and } \dot{q}(\Delta t) &= b/\omega^2 + (a - q_0 \omega^2) \sin(\omega \Delta t)/\omega \\ &\quad + (\dot{q}_0 - b/\omega^2) \cos(\omega \Delta t), \end{aligned}$$

which are the initial conditions for the next time step. When the forcing function is over, the inverse of (16) is

$$q(t) = q_0 \cos(\omega t) + \frac{\dot{q}_0}{\omega} \sin(\omega t) \quad (18)$$

Finally, the spectrum value is the modulus of (18), which is

$$\text{Spectrum}(\omega) = [q_0^2 + \dot{q}_0^2/\omega^2]^{1/2} \quad (19)$$

4

A residual spectrum subroutine includes the following steps:

- 1) The frequencies,  $\omega$ , to be examined and the force and time values for each sample of the forcing function are input data. Since we are not concerned about the response during the time the force is non-zero, the time steps need not be equal. This allows great flexibility in examining ramps and simple pulses.
- 2) Based on these force and time values  $a$ ,  $b$  and  $\Delta t$  for each time step are calculated - just once.
- 3) The original set of initial conditions  $q_0$  and  $\dot{q}_0$  are set to zero.
- 4) Equation (17) is solved for the new set of initial conditions,  $q_0$  and  $\dot{q}_0$ .
- 5) Step 4 is repeated for each time step.
- 6) Equation (19) is solved for the spectrum magnitude, which is saved.
- 7) Steps 3 through 6 are repeated until the spectrum at all frequencies is determined.

This algorithm is simple and minimizes the required number of computations.

#### REFERENCES

1. W. T. Thompson, Introduction to Space Dynamics, John Wiley & Sons, New York, 1961.
2. C. R. Wylie, Jr., Advanced Engineering Mathematics, McGraw Hill Book Company, Incroproated, 1960.

# BUCKLING OF EULER'S ROD IN THE PRESENCE OF ERGODIC RANDOM DAMPING

H. H. E. Leipholz

Department of Civil Engineering, Solid Mechanics Division  
University of Waterloo  
Waterloo, Ontario, Canada

This paper is concerned with the buckling of Euler's rod in the presence of ergodic random damping. For a small mean value of viscous damping, superposed by an ergodic random damping fluctuation, it is shown that for a sufficiently small expected value of the fluctuation's magnitude, almost certain asymptotic stability can be guaranteed. Moreover, if the expected value does not exceed a certain fraction of the damping's mean value, the critical value of the load for deterministic damping remains the stability limit despite of the randomly superposed damping fluctuation.

## Introduction

A modern approach to problems in mechanics requires the inclusion of the stochastic aspect of these problems. This is specifically true for stability problems for which randomly distributed imperfections are of great influence with respect to the stability limit. As far as the buckling of rods is concerned, the randomness of the load [1], and the randomness of the geometry (initial curvature) [2] has previously been taken into account. But it may also be of interest to consider the buckling of the rod in the presence of ergodic, random damping. This is desirable as in real systems there is always damping, and the mathematical model should simulate reality as closely as possible. Also, the effect of damping has led to unexpected results in many stability problems, for example for rods subjected to follower forces [3]. Therefore, it seems to be advisable to investigate random damping as well.

Consider Euler's rod shown in Figure 1. Using the notations given in this figure, and observing the boundary conditions, the following boundary-eigenvalue problem is obtained:

$$\alpha v^{IV} + Pv'' + m\ddot{v} + \beta \dot{v} = 0, \quad (1)$$

$$v(0,t) = v(l,t) = v''(0,t) = v''(l,t) = 0. \quad (2)$$

Separation of the variables  $x$  and  $t$  can be accomplished using

$$v(x,t) = f(t) \sin \frac{\pi x}{l}. \quad (3)$$

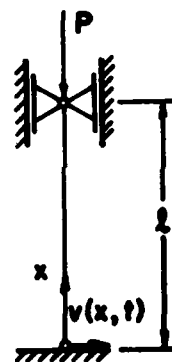


Figure 1 - Euler's Rod

$\alpha$  = const, flexural rigidity  
 $m$  = mass per unit length  
 $\beta$  = coefficient of viscous damping  
 $P$  = load  
 $v$  = transversal deflection

Obviously, the boundary conditions (2) are being satisfied by (3). The differential equation (1) is satisfied if  $f(t)$  is taken as the solution of

$$\ddot{f} + \frac{\beta}{m} \dot{f} + \frac{\pi^2}{ml^2} (P_E - P)f = 0. \quad (4)$$

The behaviour of  $f(t)$  decides upon the stability or instability of the rod. In (4),  $P_E$  is Euler's buckling load.

For

$$\rho = \beta / 2m\omega_0, \quad (5)$$

$$\omega_0^2 = \pi^2(P_E - P) / m\ell^2, \quad (6)$$

equation (4) changes into

$$\ddot{f} + 2\rho\omega_0\dot{f} + \omega_0^2 f = 0 \quad (7)$$

If damping is small,

$$0 < \rho < 1 \quad (8)$$

holds true, and the solution of (7) reads

$$f(t) = Ce^{-\rho\omega_0 t} \sin(1-\rho^2)^{1/2} \omega_0 t. \quad (9)$$

This result for  $f(t)$  obviously indicates stability. The load  $P$ , corresponding to this state of stability, follows from (5), (6) and (8). First, consider

$$\rho = \frac{\beta}{2m\omega_0} < 1, \quad \text{i.e., } \beta < 2m\omega_0. \quad (10)$$

Hence,

$$\frac{\beta^2}{4m^2} < \omega_0^2 = \frac{\pi^2(P_E - P)}{m\ell^2}.$$

But then,

$$P < P_E - \frac{\beta^2 \ell^2}{4m\pi^2} = P^*.$$

The conclusion is that for  $P < P^*$  there is stability. Thus,

$$P^* = P_E - \frac{\beta^2 \ell^2}{4m\pi^2} \quad (11)$$

is the stability limit in the case of small, deterministic damping.

#### Stochastic Viscous Damping

Assume the mean value  $\beta$  of the damping coefficient in (4) being superposed by an ergodic random fluctuation  $b(t)$  of the damping coefficient. Then, (4) becomes

$$\ddot{f} + \left[ \frac{\beta}{m} + \frac{b(t)}{m} \right] \dot{f} + \frac{\pi^2}{m\ell^2} (P_E - P) f = 0. \quad (12)$$

Introducing

$$b(t)/m = \alpha(t), \quad (13)$$

and using (5) and (6), the previous equation can be changed into

$$\ddot{f} + 2\rho\omega_0\dot{f} + \omega_0^2 f = -\alpha(t)\dot{f}. \quad (14)$$

The solution of (14) is known to be

$$f(t) = f_0 h(t) - \int_0^t h(t-\tau) \alpha(\tau) \dot{f}(\tau) d\tau, \quad (15)$$

where, in the case of (8),

$$h(t) = Ce^{-\rho\omega_0 t} \sin D \omega_0 t, \quad (16)$$

$$C = [\omega_0(1-\rho^2)^{1/2}]^{-1}, \quad D = (1-\rho^2)^{1/2}. \quad (17)$$

Obviously,  $h(t)$  coincides with (9).

From (15) follows

$$\begin{aligned} \dot{f}(t) &= \dot{f}_0 h(t) - \int_0^t h(t-\tau) \alpha(\tau) \dot{f}(\tau) d\tau \\ &\quad - h(0) \alpha(t) \dot{f}(t). \end{aligned}$$

But  $h(0) = 0$ . Therefore,

$$\dot{f}(t) = \dot{f}_0 h(t) - \int_0^t h(t-\tau) \alpha(\tau) \dot{f}(\tau) d\tau, \quad (18)$$

and

$$\begin{aligned} |\dot{f}(t)| &\leq |\dot{f}_0| |h(t)| + \\ &\quad \int_0^t |h(t-\tau)| |\alpha(\tau)| |\dot{f}(\tau)| d\tau. \end{aligned} \quad (19)$$

Using (16),

$$\dot{h}(t) = [-C\rho\omega_0 \sin D\omega_0 t + CD\omega_0 \cos D\omega_0 t] e^{-\rho\omega_0 t} \quad (20)$$

is obtained. Hence,

$$|\dot{h}| < C(\rho\omega_0 + D\omega_0) e^{-\rho\omega_0 t}$$

or

$$|\dot{h}| < Ke^{-\rho\omega_0 t}, \quad (21)$$

where

$$K = C\omega_0(\rho + D). \quad (22)$$

By virtue of (17), (22) becomes

$$K = \frac{\rho + (1-\rho^2)^{1/2}}{(1-\rho^2)^{1/2}}. \quad (23)$$

Combining (19) and (21) yields

$$\begin{aligned} |\dot{f}(t)| &\leq |\dot{f}_0| Ke^{-\rho\omega_0 t} + \\ &\quad + \int_0^t Ke^{-\rho\omega_0 t} e^{\rho\omega_0 \tau} |\alpha(\tau)| |\dot{f}(\tau)| d\tau \end{aligned} \quad (24)$$



and

$$\begin{aligned} |\dot{f}(t)| e^{\rho\omega_0 t} &\leq |f_0| K + \\ &+ \int_0^t K |\alpha(\tau)| e^{\rho\omega_0 \tau} |\dot{f}(\tau)| d\tau. \end{aligned} \quad (25)$$

Setting

$$\begin{aligned} |\dot{f}(t)| e^{\rho\omega_0 t} &= v(t), \\ |f_0| K &= g, \end{aligned} \quad (26)$$

and

$$K |\alpha(\tau)| = H(\tau),$$

(25) can be transformed into

$$v(t) \leq g + \int_0^t H(\tau) v(\tau) d\tau. \quad (27)$$

With (27), a relationship has been obtained to which Gronwall's lemma [4] can be applied. In doing so,

$$v(t) \leq g \exp \left\{ \int_0^t H(\tau) d\tau \right\} \quad (28)$$

results. Using (26), (28) can be rewritten to yield

$$|\dot{f}(t)| e^{\rho\omega_0 t} \leq |f_0| K \exp \left\{ K \int_0^t |\alpha(\tau)| d\tau \right\}$$

or

$$\begin{aligned} |\dot{f}(t)| &\leq |f_0| K \exp \left\{ K \frac{1}{t} \int_0^t |\alpha(\tau)| d\tau \right. \\ &\left. - \rho\omega_0 \right\} t. \end{aligned} \quad (29)$$

However, since the random process is assumed to be ergodic, with probability one,

$$\frac{1}{t} \int_0^t |\alpha(\tau)| d\tau = E\{|\alpha|\}, \quad (30)$$

where  $E\{|\alpha|\}$  is the expected value of  $|\alpha|$ . Therefore, (29) can be brought into the form

$$|\dot{f}(t)| \leq |f_0| K \exp \{ K E\{|\alpha|\} - \rho\omega_0 \} t. \quad (31)$$

Now, consider

$$f(t) = f(0) + \int_0^t \dot{f} dt = f_0 + \int_0^t \dot{f} dt$$

which yields

$$|f(t)| \leq |f_0| + \int_0^t |\dot{f}| dt. \quad (32)$$

With

$$K_1 = \rho\omega_0 - KE, \quad (33)$$

$$|\dot{f}| \leq |f_0| K e^{-K_1 t}$$

follows from (31). Hence,

$$\begin{aligned} \int_0^t |\dot{f}| dt &\leq -|f_0| \frac{K}{K_1} e^{-K_1 t} \Big|_0^t = \\ &= |f_0| \frac{K}{K_1} - |f_0| \frac{K}{K_1} e^{-K_1 t}. \end{aligned} \quad (35)$$

Using (35) in (32) leads to

$$\begin{aligned} \lim_{t \rightarrow \infty} |f(t)| &\leq |f_0| + |f_0| \frac{K}{K_1} - \\ &- \lim_{t \rightarrow \infty} |f_0| \frac{K}{K_1} e^{-K_1 t}. \end{aligned} \quad (36)$$

For  $K_1 > 0$ ,

$$\lim_{t \rightarrow \infty} |f_0| \frac{K}{K_1} e^{-K_1 t} = 0,$$

and

$$\lim_{t \rightarrow \infty} |f(t)| \leq |f_0| \left( 1 + \frac{K}{K_1} \right) = K_2 = \text{const.} \quad (37)$$

Since (37) indicates almost certain asymptotic stability, the conclusion is that for

$$K_1 > 0, \quad \text{i.e., } E < \frac{\rho\omega_0}{K} \quad (38)$$

there is almost certain asymptotic stability of the rod. According to (23), the stability condition (38) reads

$$E\{|\alpha|\} < \frac{\rho\omega_0(1-\rho^2)^{1/2}}{\rho+(1-\rho^2)^{1/2}} \quad (39)$$

#### Discussion of the Stability Condition

Condition (39) imposes a requirement on the load  $P$  of the road. This requirement shall now be specified under the assumption that  $\beta$  is so small that  $\beta^2$  is negligible, i.e.,

$$\beta^2 \approx 0 \quad (40)$$

shall hold true. In that case, using (5), (39) yields

$$E < \frac{\frac{\beta\omega_0}{2m}}{\frac{\beta}{2m} + \omega_0}, \quad (41)$$

an inequality which can be brought into the form

$$\omega_0 > \frac{E\beta}{\beta - 2Em}. \quad (42)$$

For (42) to be meaningful,  $E < \beta/2m$  must hold. But this is certainly the case by virtue of (41). Hence, (42) can be used to yield

$$\omega_0^2 > \frac{E\beta^2}{(\beta-2Em)^2}, \quad (43)$$

By means of (6), (43) can be transformed into

$$\frac{\pi^2(P_E - P)}{mL^2} > \frac{E\beta^2}{(\beta-2Em)^2}$$

and furthermore into

$$P < P_E - \frac{[E\{|\alpha|\}]^2 \beta^2 mL^2}{\pi^2 (\beta-2Em)^2} = P^{**}. \quad (44)$$

With (44), the wanted condition for  $P$  has been found.

If  $P^{**} \geq P^*$ , the randomness of damping has no effect on the stability of the rod. According to (11) and (44), this is the case if

$$\frac{E\beta^2 mL^2}{\pi^2 (\beta-2Em)^2} \leq \frac{\beta^2 L^2}{4m\pi^2}. \quad (45)$$

But (45) is equivalent to

$$E\{|\alpha|\} \leq \frac{\beta}{4m}. \quad (46)$$

#### Conclusion

Let the damping of Euler's rod be an ergodic random process consisting of a random fluctuation  $\alpha(t)$  about a mean value  $\beta$ . If  $\beta$  is

small enough so that (8) holds true, then, for a sufficiently small expected value of  $|\alpha|$  which satisfies condition (39), almost certain asymptotic stability of the rod prevails. Moreover, if  $\beta$  is so small that (40) holds true, and if the expected value of  $|\alpha|$  satisfies (46), i.e., if this expected value is only a fraction of the small mean value  $\beta$ , then the stability limit  $P^{**}$  given by (44) is above the stability limit  $P^*$  given by (11) and valid for deterministic damping. That means in the case of (40) and (46), the randomness of the damping coefficient does not impair stability.

#### Acknowledgement

This research was carried out with the support of the National Research Council under Grant No. A7297.

#### References

- [1] Ariaratnam, S.T., Dynamic Stability of a Column Under Random Loading, in "Dynamic Stability of Structures," Proceedings of an Int. Conference held at Northwestern University, Evanston, Illinois, October 18-20, 1965, Pergamon Press, Oxford, New York, 1966.
- [2] Bolotin, V.V., "Statistical Methods in Structural Mechanics," Holden-Day, Inc., San Francisco, Cambridge, London, Amsterdam, 1969, pp. 87-89.
- [3] Ziegler, H., "Principles of Structural Stability," Blaisdell Publ. Co., Waltham, Massachusetts, Toronto, London, 1968, pp. 93-96.
- [4] Walter, W., "Differential-und Integral-Ungleichungen," Springer-Verlag, Berlin, Göttingen, Heidelberg, New York, 1964, p. 13.

# WAVE PROPAGATION IN A CYLINDRICAL SHELL WITH JOINT DISCONTINUITY

A. Harari  
Naval Underwater Systems Center  
Newport, Rhode Island 02840

The effects of joint discontinuity on wave propagation in a cylindrical shell are investigated in this paper. The joint discontinuity consists of an elastic interlayer at the joint and structural discontinuity of the joint. The transmitted and reflected efficiencies are found for several cases of interest.

## INTRODUCTION

Long hull structures of cylindrical shape are often made from several cylindrical segments. The joints connecting the various segments are often lined with softer material and are designed to prevent leakage and rattling. Noise generated by a motor or any other vibratory source on the shell is transmitted via the shell structure and interferes with the function of instruments attached to the shell. The joint structure introduces a discontinuity. In addition to the joint discontinuity, the edges of the joint are thicker than the shell thickness thus forming stiffening belts and introducing additional discontinuity. The analysis considers a free traveling wave that encounters joint discontinuity. The joint discontinuity will reflect and transmit waves of various types. In addition to the traveling waves along the shell, there occur exponentially decaying near-field waves that do not transport energy. The particular aim of the study is to find the frequency ranges where energy is transmitted or attenuated and to discover how the joint affects wave propagation. The analysis investigates the transmitted and reflected power due to incident waves impinging upon the discontinuity caused by the presence of the joint. The power lost due to the damping properties of the joint is also found. The transmitted and reflected efficiencies are determined for various cases of interest. The transmission efficiency and the reflection effi-

ciency are defined as the ratio of power transmitted and power reflected to incident power. The elastic interlayer in the joint is considered to have complex spring-type properties. The stiffening belts are analyzed as shell segments. Transmission loss in beams and plates due to structural and material discontinuities was studied by several authors [1-3]. Wave propagation in a cylindrical shell with finite numbers of stiffeners was studied in Ref. [4]. The analysis in Ref. [4] used classical beam theory for the finite number of stiffeners in an infinitely long cylindrical shell. The analysis of a cylindrical shell with joint discontinuity was not studied previously.

## CYLINDRICAL SHELL ANALYSIS

Consider a thin elastic cylindrical shell of thickness  $h$  and mean radius  $a$ . The mid-surface of the shell is described in terms of a  $x, \theta$  coordinate system. The  $x$  coordinate is taken in the axial direction of the shell and the  $\theta$  coordinate is taken in the circumferential direction. The components of the displacements of the mid-surface of the shell are designated by  $u, v$ , and  $w$  (Fig. 1a). The

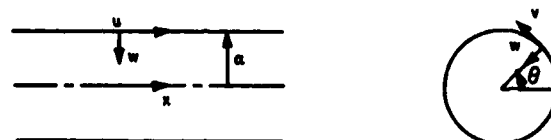


Fig. 1a - Cylindrical shell coordinates and displacements

equations of shell motion governing  $u$ ,  $v$ , and  $w$  are the Sanders-Koiter shell equations in Ref. [5]. The equations are written as follows:

where

$$\begin{aligned} & u_{\xi\xi} + \frac{(1-\nu)}{2} (1 + \frac{b}{4}) u_{\theta\theta} + \left[ \frac{1+\nu}{2} - \frac{3}{8} (1-\nu)b \right] v_{\xi\theta} \\ & - \frac{(1-\nu)}{2} b v_{\xi\theta\theta} - \nu w_{\xi} - \rho \frac{a^2}{E} (1-\nu^2) \psi = 0 \\ & \left[ \frac{1+\nu}{2} - \frac{3}{8} (1-\nu)b \right] u_{\xi\theta} + \frac{(1-\nu)}{2} (1 + \frac{9}{4}b) v_{\xi\xi} \\ & + (1+b) v_{\theta\theta} + b \frac{(3-\nu)}{2} w_{\xi\xi\theta} + b w_{\theta\theta\theta} - w_{\theta} \\ & - \rho \frac{a^2}{E} (1-\nu^2) \psi = 0 \\ & - \nu u_{\xi} - b \frac{(1-\nu)}{2} u_{\theta\theta\xi} + b \frac{(3-\nu)}{2} v_{\xi\xi\theta} + b v_{\theta\theta\theta} \\ & - v_{\theta} + b (w_{\xi\xi\xi\xi} + w_{\theta\theta\theta\theta} + 2 w_{\xi\xi\theta\theta}) + w \\ & + \rho \frac{a^2}{E} (1-\nu^2) \psi = 0 \end{aligned} \quad (1)$$

$$\xi = \frac{x}{a}, \quad ( )_{\xi} \equiv \frac{\partial}{\partial \xi} ( ), \quad ( )_{\theta} \equiv \frac{\partial}{\partial \theta} ( ),$$

$$( )_{\xi\xi} \equiv \frac{\partial^2}{\partial \xi^2} ( ), \quad b = \frac{h^2}{12a^2}$$

$E$  is Young's modulus, Poisson's ratio is denoted by  $\nu$ , and  $\rho$  is the mass density.

The displacements  $w$ ,  $u$ , and  $v$  may be expanded by the Fourier series in

$$\begin{aligned} w(\xi, \theta, t) &= \sum_{n=0}^{\infty} w_n \cos(n\theta) \\ u(\xi, \theta, t) &= \sum_{n=0}^{\infty} u_n \cos(n\theta) \\ v(\xi, \theta, t) &= \sum_{n=0}^{\infty} v_n \sin(n\theta) \end{aligned} \quad (2)$$

the circumferential,  $\theta$ , coordinate direction. The solution is then sought in the following form:

$$w_n(\xi, t) = C_n \exp(i\omega t + p_n \xi)$$

$$u_n(\xi, t) = C'_n \exp(i\omega t + p_n \xi)$$

$$v_n(\xi, t) = C''_n \exp(i\omega t + p_n \xi) \quad (3)$$

where  $\omega$  is the circular frequency and  $C_n$ ,  $C'_n$ , and  $C''_n$  are constants. Substituting Eqs. (2) and (3) in Eq. (1), one obtains three homogeneous algebraic equations on the constants  $C_n$ ,  $C'_n$ , and  $C''_n$ , the determinant of which when set to zero yields a fourth order equation on  $p_n^2$ . Eight roots, are obtained, thus

$$(P_k)_n = (\delta_k)_n + i(\gamma_k)_n, \quad k = 1, \dots, (8) \quad (4)$$

yielding eight independent solutions. Depending on the nature of the roots, the solution describes propagating or near-field wave solutions. Using Eq.

(1), the constants  $C_n$  and  $C'_n$  can be written in terms of the constant  $C''_n$ . Since the analysis is done for every  $n$  component separately, it is convenient to drop the subscript  $n$  from subsequent expression and discussion, with the understanding that the analysis is for a particular  $n$  mode. The eight independent solutions can be separated into two groups of four, where each group is associated with a semi-infinite shell excited at the edge. The first group contains solutions where

$\delta_k = 0$ ,  $\gamma_k > 0$  and solutions where  $\delta_k > 0$ . The solutions describe backward propagating waves and near-field waves associated with a semi-infinite shell,  $-\infty < \xi < 0$  (left side), excited at the edge  $\xi = 0$ . The second group contains solutions where  $\delta_k = 0$ ,  $\gamma_k < 0$  and solutions where  $\delta_k < 0$ . The solutions describe forward propagating waves and near-field waves associated with a semi-infinite shell,  $0 < \xi < \infty$ , (right side), excited at the edge  $\xi = 0$ .

#### Solution to the Problem of Wave Propagation in a Cylindrical Shell with Joint Discontinuity

The solution to the problem of a traveling wave encountering joint discontinuity consists of solving the cylindrical shell differential equation

and matching the boundary condition at the joint. The analysis considers two semi-infinite cylindrical shells connected by an elastic inter-layer and an incident wave traveling from the left in the positive axial direction. The first case that is considered here is a joint without the stiffening belts, i.e., the effect of introducing the elastic interlayer. The schematic diagram is shown in Fig. 1b. Since the

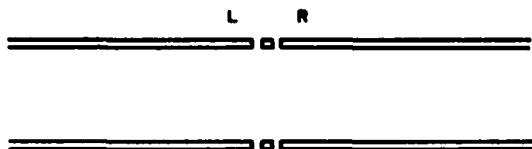


Fig. 1b - Cylindrical shell with material discontinuity

dimensions of the elastic interlayer are small, its response can be simplified and considered to be the response of a mass-less continuous spring at frequencies that are not too high. The stiffness of the spring per unit circumferential length depends on the elastic properties of the layer and its axial and normal dimensions. The stiffness of the spring in a specific direction can be simplified and evaluated as follows:

$$s_k = E^*(1+i\eta) \frac{T_k}{L_k}$$

where  $E^*$  is Young's modulus or the shear modulus of the elastic inter-layer,  $\eta$  is the loss factor,  $T$  and  $L$  are the appropriate dimensions of the layer and considered to be thickness and length. The index  $k = 1, 3$  refers to the axial, tangential and normal direction. The expression for the moment stiffness can be written as follows:

$$s_4 = E^*(1+i\eta) \frac{T_4^3}{12L_4}$$

Consider a wave traveling in the positive direction and encountering the elastic layer discontinuity. The boundary condition requires continuity between the elastic layer and the two semi-infinite shells and equilibrium of the forces. The boundary condition can be written as:

$$u^L + u^i - u^R = -\frac{N^R}{s_1}$$

$$v^L + v^i - v^R = -\frac{N^R}{s_2}$$

$$w^L + w^i - w^R = -\frac{Q^R}{s_3}$$

$$\frac{w^L}{a} + \frac{w^i}{a} - \frac{w^R}{a} = -\frac{M^R}{s_4}$$

$$N_x^L + N_x^i - N_x^R = 0$$

$$N^L + N^i - N^R = 0$$

$$Q^L + Q^i - Q^R = 0$$

$$M^L + M^i - M^R = 0 \quad (5)$$

evaluated at the joint, where

$$Q = -\frac{Eh^3}{12(1-\nu^2)a^3} \left[ w_{\xi\xi\xi} + (2-\nu) w_{\xi\theta\theta} + \frac{(3-\nu)}{2} v_{\xi\theta} - \frac{(1-\nu)}{2} u_{\theta\theta} \right]$$

$$N_x = \frac{Eh}{(1-\nu^2)a} \left[ u_{\xi} + \nu (v_{\theta} - w) \right]$$

$$N = \frac{Eh}{2(1+\nu)a} \left[ \left(1 + \frac{9}{4}b\right) v_{\xi} + \left(1 - \frac{3}{4}b\right) v_{\theta} + 3b w_{\xi\theta} \right]$$

$$M = \frac{Eh^3}{12(1-\nu^2)a^2} \left[ w_{\xi\xi} + \nu (w_{\theta\theta} + v_{\theta}) \right]$$

The superscripts L and R indicate that the displacements or the stress-resultants are associated with the semi-infinite shell on the left, or on the right, side of the joint, respectively. The superscript i indicates that the displacements or the stress-resultants

are associated with the incident wave. Eq. (5) represents the boundary condition without cross-coupling between the kinematical and dynamical variables in the axial, tangential, normal direction and the rotation. The boundary condition for joint design with coupling between the edge variables may be described by the equations evaluated at

$$\begin{aligned} D^L + D^I - D^R &= -\lambda F^R \\ F^L + F^I - F^R &= 0 \end{aligned} \quad (6)$$

the joint, and where D is 4x1 matrix representing the displacements, and F is a 4x1 matrix representing the stress-resultants and where  $\lambda$  is a

$$\begin{aligned} D &= \begin{bmatrix} w & u & v & w_\xi \end{bmatrix}^T \\ F &= \begin{bmatrix} Q & N_x & N & M_x \\ E & E & E & E\alpha \end{bmatrix}^T, \end{aligned} \quad (7)$$

4x4 matrix representing the joint properties. The nondiagonal terms represent the cross-coupling between the edge variables. Eq. (6) reduces to Eq. (5) if the diagonal terms are equal to  $\lambda_{kk} = \frac{E}{S_k}$  and all non-diagonal terms are equal to zero. Rigid connection can be specified by setting all elements of the matrix  $\lambda$  equal to zero. Soft connection can be specified by high value  $\lambda_{ij}$ . Properly chosen values of  $\lambda_{ij}$  can describe joint design where the two shells are rigidly connected with respect to some kinematic variables at the joint and free with respect to others. Hinge joint is an example of such a case. The edges of the shells are free to rotate while the normal axial and tangential displacements are rigidly connected. The expression for the vectors D and F associated with the semi-infinite shell  $-\infty < \xi < 0$  on the left side of the joint can be written in the form

$$D^L = AC_1, F^L = GC_1 \quad (8)$$

where A and G are 4x4 matrices and where  $C_1$  is a 4x1 matrix representing the unknown constants. The expressions for the vectors D and F associated with the semi-infinite shell,  $0 \leq \xi < \infty$ , on the right side of the joint, can be written as follows:

$$D^R = BC_2, F^R = HC_2 \quad (9)$$

where B and H are 4x4 matrices and where  $C_2$  is a 4x1 matrix representing the unknown constants. Substituting Eqs. (8) and (9) into Eq. (6) one obtains

$$\begin{bmatrix} A & (\lambda H - B) \\ G & -H \end{bmatrix} \begin{bmatrix} C_1 \\ C_2 \end{bmatrix} = - \begin{bmatrix} D^I \\ F^I \end{bmatrix}. \quad (10)$$

Solving Eq. (10) one obtains the constants  $C_1$  and  $C_2$ . Once the constant vectors  $C_1$  and  $C_2$  are known, the reflected and the transmitted waves can be found. The power transmitted and the power reflected can also be found from the velocities and the stress-resultants. Figure 1c is a

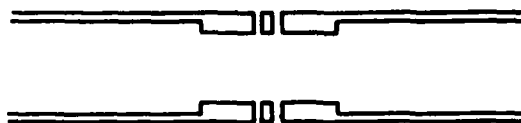


Fig. 1c - Cylindrical shell with stiffness and material discontinuity

schematic diagram of an infinite cylindrical shell interrupted by a joint with stiffening belts. The boundary conditions are imposed at the three points of discontinuities. Two of the discontinuities are change of thickness discontinuities and one is elastic layer discontinuity. The stiffening belts are analyzed here as cylindrical shell segments rather than stiffeners because of the relatively large width. The boundary conditions are:

$$\begin{aligned} D^L + D^I - D^R &= 0 \\ F^L + F^I - F^R &= 0 \end{aligned} \quad (11)$$

at the left thickness discontinuity;

$$\begin{aligned} D^L - D^R + \lambda F^R &= 0 \\ F^L - F^R &= 0 \end{aligned} \quad (12)$$

at the elastic interlayer discontinuity; and

$$\begin{aligned} D^L - D^R &= 0 \\ F^L - F^R &= 0 \end{aligned} \quad (13)$$

at the right thickness discontinuity,

where the superscripts L and R indicate that the vector is associated with the shell to the left or to the right of the discontinuity. The superscript i indicates association with the incident wave. Eqs. (11), (12), and (13) lead to non-homogeneous equations on 24 unknown constants. Four unknown constants are associated with each of the semi-infinite shells and eight are associated with each of the stiffening belts. Once the unknown constants are known, the transmitted and reflected waves can be found. The transmitted and reflected power can also be found once the velocities and stress-resultants are known.

### Numerical Results

The numerical analysis presented here investigates the transmitted and reflected efficiencies due to an incident wave impinging upon the discontinuity caused by the joint. The transmission efficiency  $T_{ij}$  and the reflection efficiency  $R_{ij}$  are defined as the ratio of power transmitted and power reflected to the incident power. Double subscripts are used for  $T_{ij}$  and  $R_{ij}$  to indicate the incident and the resulting type waves. The first subscript indicates the incident wave and

the second subscript indicates the resulting wave. The traveling waves are indicated by the order of their appearance along the frequency scale, i.e., i=1 indicates the first traveling wave etc. The frequency parameter is  $\tau = \alpha \omega \sqrt{\frac{\rho}{E}} (1-\nu^2)$ . Thickness of shell to radius ratio is 0.02 and Poisson's ratio is 0.3. The incident wave considered in the examples presented in Figs. 2-8 is the first traveling wave. The incident wave considered in the example presented in Fig. 9 is the second traveling wave. The first traveling wave ( $\delta = 0, \gamma \neq 0$ ) starts at  $\tau = 0.0155$  and can be classified as a bending wave; however, at low frequency, the wave is essentially a membrane wave. The second traveling wave starts at  $\tau = 1.185$  and can be classified as a torsional wave at intermediate and high frequencies. At low frequencies the wave is a longitudinal wave. Figures 2, 3, and 4 present results that show how the magnitude of  $\lambda$  affects the transmitted and reflected efficiencies. In each case the same value was taken for the diagonal elements  $\lambda_{11} = \lambda_{22} = \lambda_{33} = \lambda_{44} = \alpha$ . The non-diagonal elements of the matrix  $\lambda$  were taken to be zero. Figures 2 and 3 present two extreme cases. The value of  $\alpha = 10$  was used for the diagonal element in the example presented in Fig. 2. The low value of  $\alpha$  represents an almost rigid connection. The consequence of the low value of  $\alpha$  is that the transmission efficiency  $T_{11}$

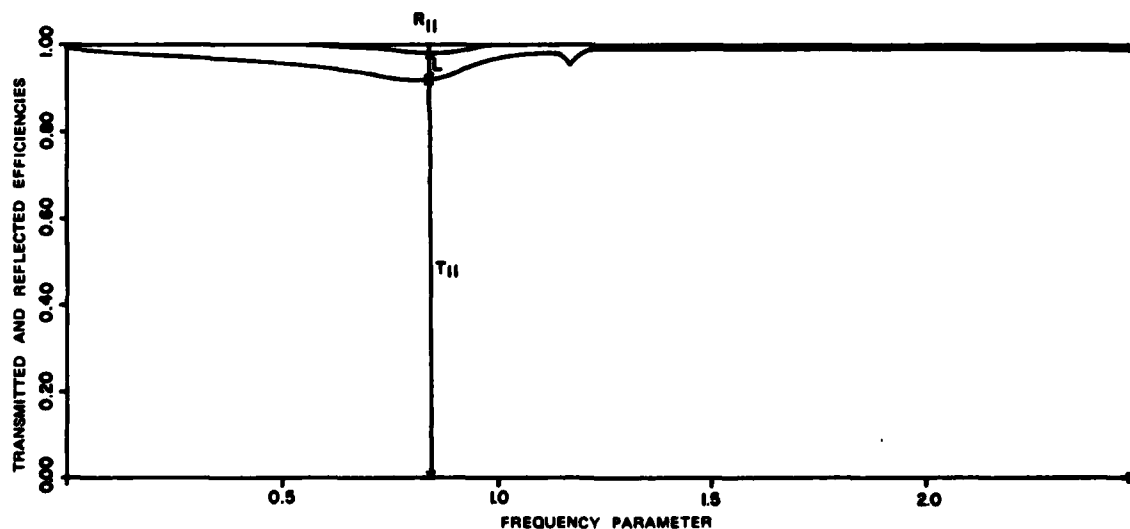


Fig. 2 - Transmitted and reflected efficiencies versus frequency parameter for a bending wave impinging on a point with  $\lambda_{11} = \lambda_{22} = \lambda_{33} = \lambda_{44} = 10$  and no stiffening belts. The circumferential mode is  $n = 2$

dominates the results presented in Fig. 2. The value  $\alpha = 10^6$  was used in the example presented in Fig. 3. The high value of  $\alpha$  represents very soft connection ( $\alpha = \infty$  represents free edge). The consequence of the high value of  $\alpha$  is that the reflection efficiency  $R_{11}$  dominates the results presented in Fig. 3. The transmitted and reflected efficiencies for an intermediate value of  $\alpha = 10^2$  are presented in Fig. 4. In general, the elements of the matrix

$\lambda$  do not have the same value. In particular  $\lambda_{44}$  is very large due to the fact that the layer is thin and the bending stiffness is very small. Figures 5, 6, and 7 present the transmitted and reflected efficiencies for the following circumferential modes,  $n = 0, 1$  and  $n = 2$ , respectively. The value of the non-zero elements of the matrix  $\lambda$  was taken to be  $\lambda_{11} = \lambda_{22} = \lambda_{33} = 10^2$ , and  $\lambda_{44} = 10^6$ . The high value of  $\lambda_{44}$  indicates an almost hinge

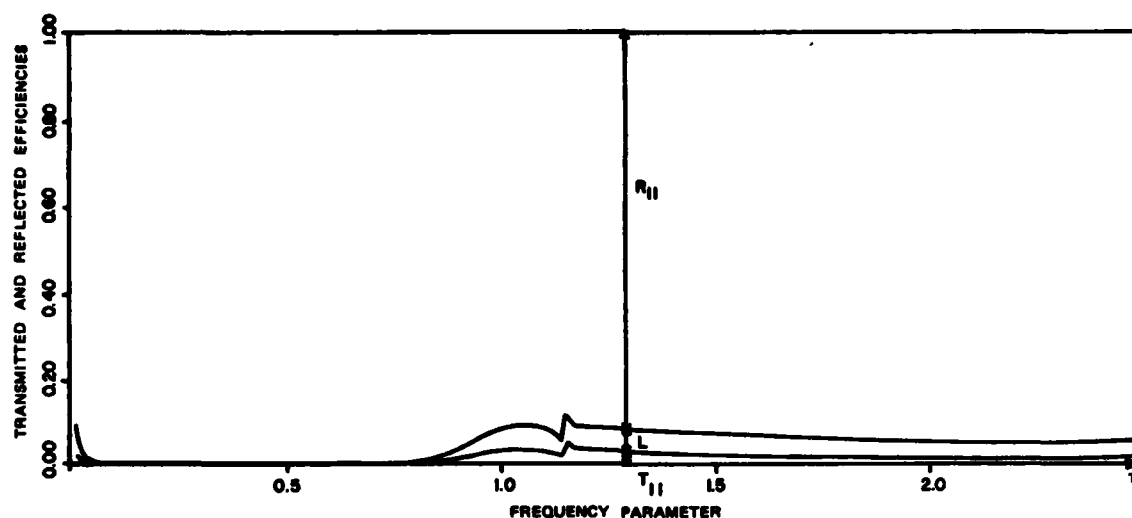


Fig. 3 - Transmitted and reflected efficiencies versus frequency parameter for a bending wave impinging on a joint with  $\lambda_{11} = \lambda_{22} = \lambda_{33} = \lambda_{44} = 10^6$  and no stiffening belts. The circumferential mode is  $n = 2$

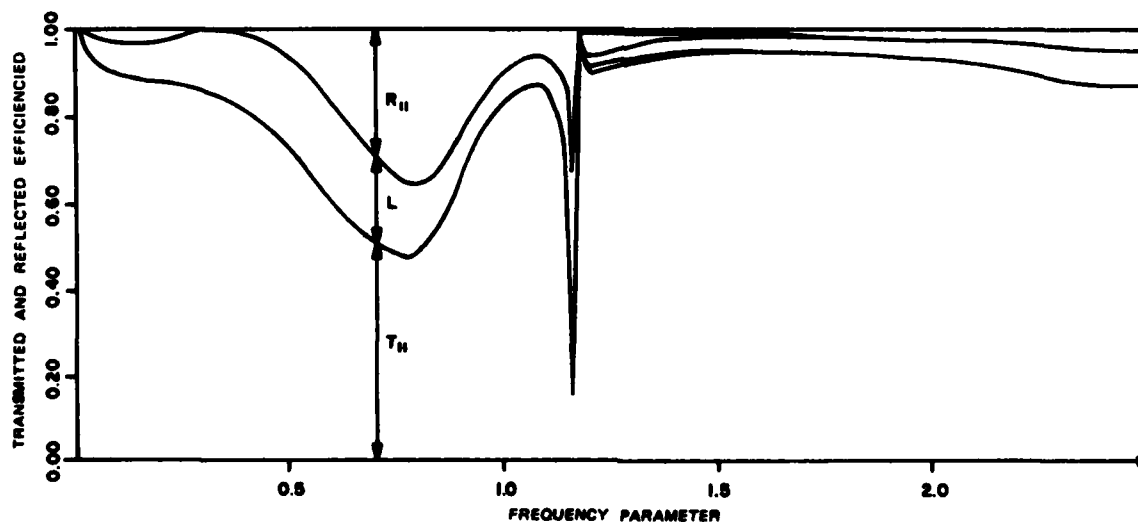


Fig. 4 - Transmitted and reflected efficiencies versus frequency parameter for a bending wave impinging on a joint with  $\lambda_{11} = \lambda_{22} = \lambda_{33} = \lambda_{44} = 10^2$  and no stiffening belts. The circumferential mode is  $n = 2$



connection where the edges can rotate relative to each other. Figure 8 presents the transmitted and reflected efficiencies due to a joint with stiffening belts. The ratio between the thickness of the stiffening belts and the thickness of the shell is 2. The ratio between the length of the stiffening belts and the radius of the shell is 0.5. The non-zero elements of the matrix  $\lambda$  are as follows,

$\lambda_{11} = \lambda_{22} = \lambda_{33} = 10^2$ ,  $\lambda_{44} = 10^6$ . The

circumferential mode is  $n = 2$ . The second traveling wave is the incident wave in the example presented in Fig. 9. The cutoff frequency of the second traveling wave is at  $\tau = 1.185$ . The wave can be classified a torsional wave at intermediate and high frequencies. At low frequencies the second wave is a longitudinal wave. The neighborhood of the cutoff frequency of the second traveling wave is marked with sharp response. The transition from the solution with one traveling wave to a

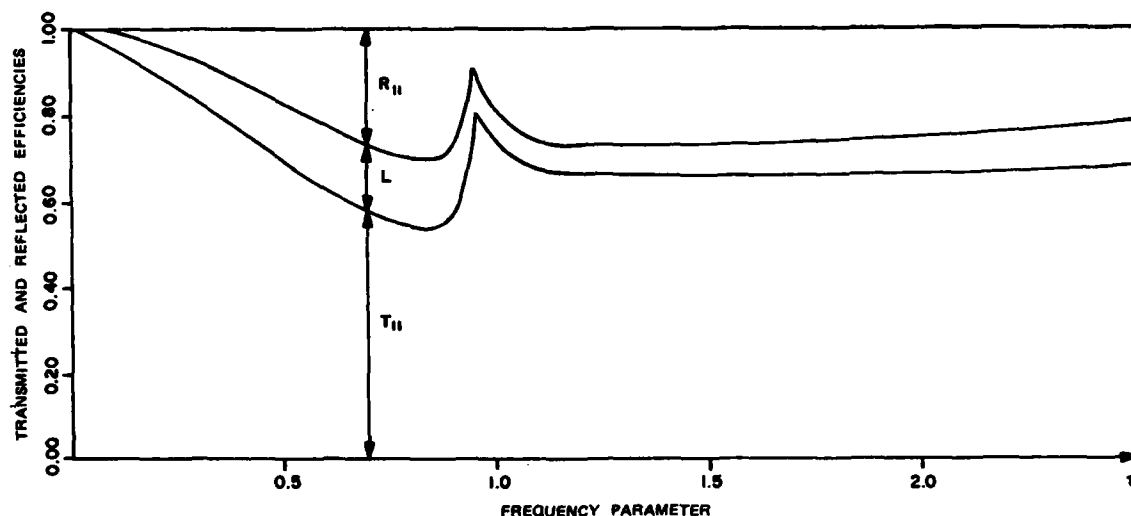


Fig. 5 - Transmitted and reflected efficiencies versus frequency parameter for a bending wave impinging on a joint with  $\lambda_{11} = \lambda_{22} = \lambda_{33} = 10^2$ ,  $\lambda_{44} = 10^6$  and no stiffening belts. The circumferential mode is  $n = 0$

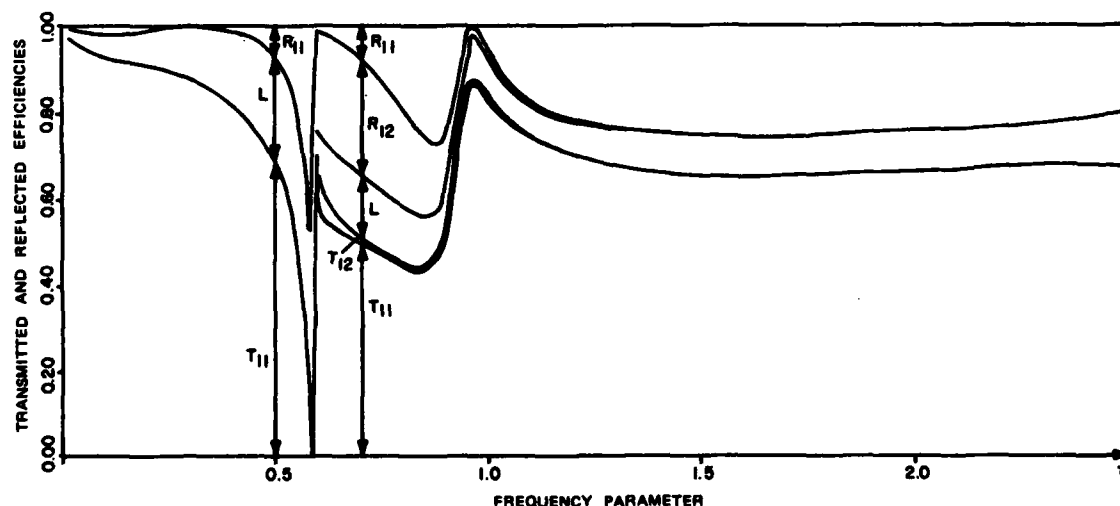


Fig. 6 - Transmitted and reflected efficiencies versus frequency parameter for a bending wave impinging on a joint with  $\lambda_{11} = \lambda_{22} = \lambda_{33} = 10^2$ ,  $\lambda_{44} = 10^6$  and no stiffening belts. The circumferential mode is  $n = 1$

solution with two traveling waves involves a process in which a near-field, exponentially decaying type solution is transformed into a traveling type wave. As the frequency approaches the cutoff frequency, the near-field solution gets larger approaching no decay at infinity. Beyond the cutoff frequency, and starting with an infinity wave length, the wave is sinusoidal along the axis of the shell. For  $n = 2$ , the motion of

frequency is primarily axial. The elements of the impedance matrix associated with the axial direction become very small at the cutoff frequency. The impedance mismatch varies rapidly due to the rapid changes in the response of the shell relative to the response of the layer. In addition to the sharp response around the cutoff frequency, the impinging wave causes reflection and transmission of the second traveling wave. The presence of the near-field solutions brought about

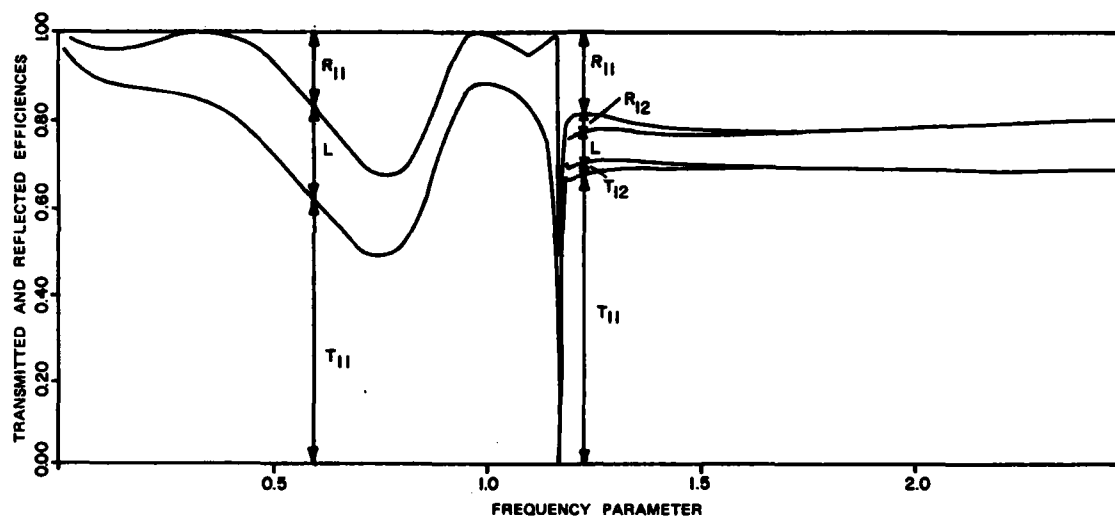


Fig. 7 - Transmitted and reflected efficiencies versus frequency parameter for a bending wave impinging on a joint with  $\lambda_{11} = \lambda_{22} = \lambda_{33} = 10^2$ ,  $\lambda_{44} = 10^6$  and no stiffening belts. The circumferential mode is  $n = 2$

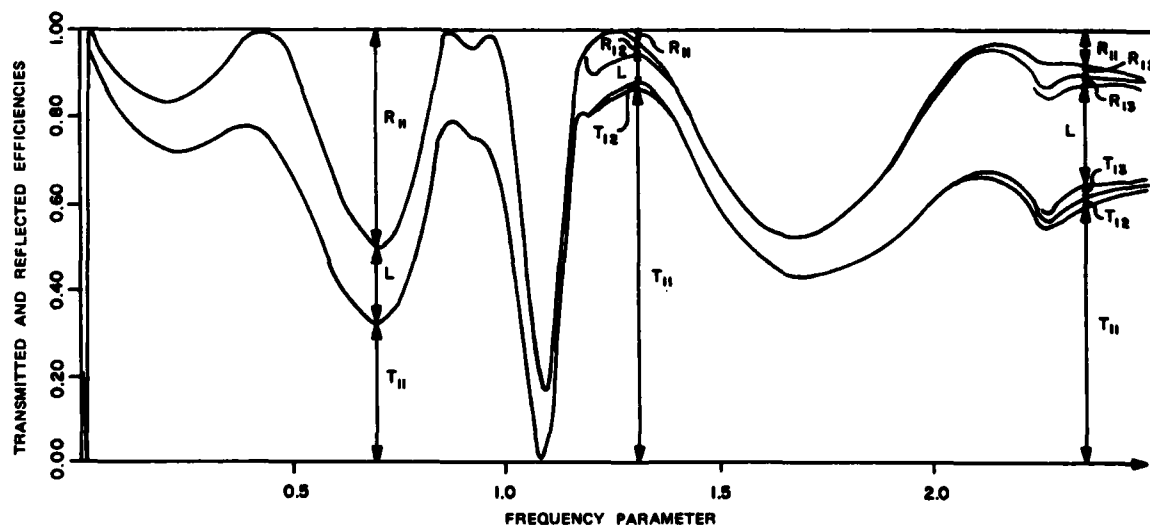


Fig. 8 - Transmitted and reflected efficiencies versus frequency parameter for a bending wave impinging on a joint with  $\lambda_{11} = \lambda_{22} = \lambda_{33} = 10^2$ ,  $\lambda_{44} = 10^6$  with stiffening belts. The circumferential mode is  $n = 2$

by the discontinuity affects the transmission or attenuation of the wave. The near-field solutions can create a region around the discontinuity that in effect blocks or bridges the transfer of energy. In order to find the points of maximum transmission, or attenuation, one has to perform a frequency sweep for the shell considered, Figs. 2-9. Explicit expressions for these points can be written for simpler cases like a beam, etc. The resonances and the overall response of the stiffening rings introduce an additional effect on the transmitted and reflected efficiencies as can be seen in Fig. 8. The effects of stiffeners on sound transmission in a cylindrical shell is discussed in Ref. [4].

#### CONCLUSIONS

The analysis of wave propagation in a cylindrical shell with joint discontinuity was derived. Numerical examples were presented for several cases of interest. A parametric study of the elastic layer effect on the transmitted and reflected efficiencies

was presented. The effects of the stiffening belts on the transmitted and reflected efficiencies were also shown.

#### REFERENCES

1. L. L. Beranek, Noise and Vibration Control, McGraw-Hill, New York, 1971.
2. E. Skudrzyk, Simple and Complex Vibratory Systems, The Pennsylvania State University Press, 1968.
3. L. Creamer, M. Heckl, E. E. Unger, Structure-Borne Sound, Springer-Verlag New York Heidelberg Berlin, 1973.
4. A. Harari, "Wave Propagation in Cylindrical Shells with Finite Region of Structural Discontinuity." To be published, JASA 1977.
5. J. L. Sanders, Jr., "An Improved First-Approximation Theory for Thin Shells," NASA Technical Report R-24, June 1959.

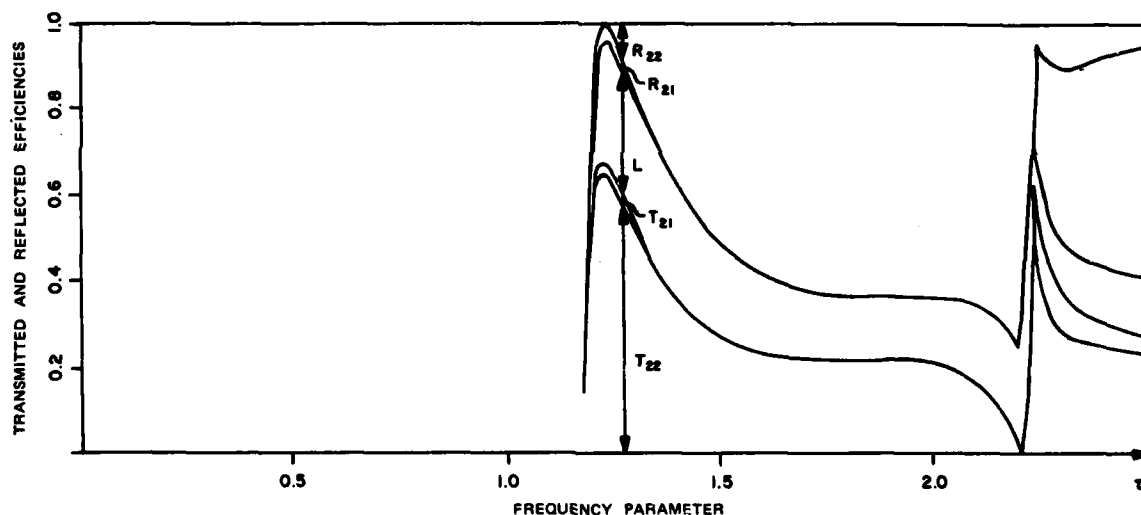


Fig. 9 - Transmitted and reflected efficiencies versus frequency parameter for a longitudinal/torsional wave (second travelling wave) impinging on a joint with  $\lambda_{11} = \lambda_{22} = \lambda_{33} = 10^2$ ,  $\lambda_{44} = 10^6$  and no stiffening belts.

The circumferential mode is  $n = 2$

## RESPONSE TO MOVING LOADS OVER A CRYSTALLINE HALF-SPACE

Saschar De  
Old Engineering Office (Qrs.)  
Santiniketan, Birbhum  
West Bengal, India

The mathematical analysis to study the steady-state response to a line load moving with a constant speed over a crystalline half-space is considered here. The half-space is supposed to be composed of monoclinic, orthorhombic and cubic crystals. The solutions for the cases of supersonic, subsonic and transonic are investigated.

The problem has importance in crystal physics and also finds an application to study the motion of the ground composed of crystalline rocks under pressure waves generated by nuclear explosions.

### INTRODUCTION

The wave propagation in crystalline media plays an interesting role in seismology as well as in crystal physics. The surface waves in crystalline media have been studied among others by Stonely (1955), Deresiewicz and Mindlin (1957) and more recently by De (1975, 1976).

Plane waves on a plane surface of a cubic crystal are considered for the case in which the wave front and the surface of the crystal are parallel to a principal axis of elastic symmetry [cf. Stonely (1955)]. When the sagittal plane (the plane perpendicular to both the wave front and the surface of the crystal) is not a plane of elastic symmetry, waves of plane strain are not possible. Important examples are those of the rotated-L-cut quartz plates, in which the stress-strain relation exhibits monoclinic symmetry when referred to the rotated axes.

The problem of generation of waves in a semi-infinite elastic medium has been studied among others by Lamb (1904),

Pekeris and Lifson (1957), Chao (1960), Eringen and Suhubi (1958). The stresses produced by moving loads in a semi-infinite medium have been further considered by Cole & Ruth (1958) and more recently by De (1975). Sneddon (1951) solved the two-dimensional dynamic problem of a semi-infinite elastic solid when a load moves uniformly over the boundary. Fung (1965) considered a problem to determine the steady state response to moving loads over an isotropic elastic solid. In the present paper, we want to investigate the mathematical solution of such a problem where a line load moves with a constant speed  $V$  over a crystalline half-space. The half-space is supposed to be composed of monoclinic, orthorhombic or cubic crystals. We assume that a plane strain state prevails and that the load has been applied and moving for an infinitely long time so that a steady state prevails in the neighbourhood of the loading as seen by an observer moving with the load. Our aim is here to find out a mathematical solution of this steady-state response without considering the propagation of the initial disturbance. The equations for the steady-state velocities

and stresses in any anisotropic elastic half-space caused by a moving line load can now be derived.

#### FUNDAMENTAL EQUATIONS AND THE BOUNDARY CONDITIONS

We use a rectangular cartesian coordinate system in which the components of the displacements are denoted by  $u_i$ . For the strain components, we have

$$S_{ij} = \frac{1}{2} (u_{i,j} + u_{j,i}), \quad (1)$$

where the comma stands for the partial differentiation with respect to the coordinates.

From Hooke's law, the stress-strain relations are written as

$$T_{ij} = c_{ijkl} S_{kl}, \quad (2)$$

where  $i, j, k, l = 1, 2, 3$ ;  $c_{ijkl} = c_{klij}$ ,

$c_{ijkl}$  are termed the elastic stiffnesses.

The stress-strain relations in contracted notation are given by

$$T_q = c_{qr} S_r, \quad (q, r = 1, 2, 3, 4, 5 \text{ or } 6). \quad (3)$$

The equations of motion in the absence of body forces are given by

$$\frac{\partial T_{ij}}{\partial x_j} = \rho \frac{\partial^2 u_i}{\partial t^2}, \quad (4)$$

where  $\rho$  is the density of the material.

The full tensor suffixes of the stresses and strains are contracted and written as

$$\begin{aligned} T_{11} &= T_1, T_{22} = T_2, T_{33} = T_3, T_{23} = T_4, \\ T_{13} &= T_5, T_{12} = T_6, S_{11} = S_1, S_{22} = S_2, \\ S_{33} &= S_3, S_{23} = S_4, S_{13} = S_5, \\ S_{12} &= S_6. \end{aligned} \quad (5)$$

For a monoclinic crystal (all classes with  $2(x_1)$  or  $m(x_1) \angle x_1 = 2 \text{ fold}$ ), the stiffnesses are  $c_{11}, c_{12}, c_{13}, c_{14}, c_{22}, c_{23}, c_{24}, c_{33}, c_{34}, c_{44}, c_{55}, c_{56}, c_{66}$ .

For the other two orientations of the 2-fold axis of the monoclinic system, we have

$$2(x_2) \text{ or } m(x_2): c_{11}, c_{12}, c_{13}, c_{15}, c_{22}, c_{23}, c_{25}, c_{33}, c_{35}, c_{44}, c_{45}, c_{55}, c_{66}$$

$$\text{and } 2(x_3) \text{ or } m(x_3): c_{11}, c_{12}, c_{13}, c_{16}, c_{22}, c_{23}, c_{26}, c_{33}, c_{36}, c_{44}, c_{46}, c_{55}, c_{66}.$$

For an orthorhombic crystal (all classes  $mm, 222, mmm$ ), the stiffnesses are  $c_{11}, c_{12}, c_{13}, c_{22}, c_{23}, c_{33}, c_{44}, c_{55}, c_{66}$ .

For a cubic crystal (classes  $23, m\bar{3}, 43m, 432, m\bar{3}m$ ), we have three stiffnesses,  $c_{11}, c_{12}, c_{44}$  and for an isotropic material, these reduce to two.

We consider a crystalline medium which occupies the half-space  $x_2 \geq 0$  (fig.1). We assume that the load moves in the negative  $x_1$ -axis direction at a constant speed  $V$ . An observer moving with the load at this speed would see the load as stationary. Thus, if a Galilean transformation

$$x'_1 = x_1 + Vt, \quad x'_2 = x_2, \quad t' = t, \quad (6)$$

is introduced, the boundary conditions would be independent of  $t'$ .

The boundary conditions in the moving coordinates for a concentrated load are

$$T_2 = -P\delta(x'_1) T_4 = T_6 = 0 \text{ on } x'_2 = 0, \quad (7)$$

where  $\delta(x'_1)$  is the Dirac-delta function, which is zero everywhere except at  $x'_1 = 0$  where it tends to infinity in such a way that

$$\int_{-\infty}^{\infty} \delta(x'_1) dx'_1 = 1. \quad (8)$$

For a plane wave travelling along the diagonal axis in the neighbourhood of the surface  $x_2 = 0$  of a monoclinic crystal, we choose (ref. f)

$$u_j = \frac{1}{2\pi} \int_{-\infty}^{\infty} U_j e^{i\gamma x'_1} e^{-\beta\gamma x'_2} d\gamma, \quad (j=1,2,3) \quad (9)$$

$U_j$  and  $\gamma$  are constants.

#### FORMULATION OF THE PROBLEM

Using equation (4) with equations 1-3, 5, 9 and considering the monoclinic symmetry for the two-fold axis, we obtain the following three equations

$$\begin{aligned} (\beta^2 - g_{11} + \nu) U_1 - i\kappa\beta U_2 - i\kappa\beta U_3 &= 0 \\ i\kappa\beta U_1 + (1 - g_{22}\beta^2 - \nu) U_2 + (g_{56} - g_{24}\beta^2) U_3 &= 0 \\ i\kappa\beta U_1 + (g_{56} - g_{24}\beta^2) U_2 + (g_{55} - g_{44}\beta^2 - \nu) U_3 &= 0, \end{aligned} \quad (10)$$

where

$$g = fV^2/c_{66}, \quad g_{rs} = c_{rs}/c_{66}, \quad h = g_{44} + g_{56}, \quad \kappa = 1 + g_{12}.$$

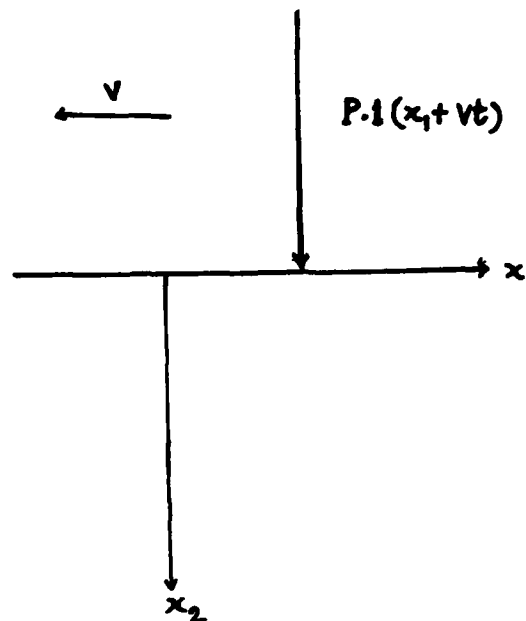


Fig. 1. Moving load over a crystalline half-space

Eliminating  $U_1$ ,  $U_2$  and  $U_3$ , we get the condition for a steady-state, non-zero solution.

$$\begin{vmatrix} \beta^2 g_{11} + \nu & -ik\beta & -ik\beta \\ ik\beta & 1 - g_{22}\beta^2 - \nu & g_{56} - g_{24}\beta^2 \\ ik\beta & g_{56} - g_{24}\beta^2 & g_{55} - g_{44}\beta^2 \end{vmatrix} = 0 \quad (11)$$

This can be written as

$$a_1 \beta^6 - b_1 \beta^4 + c_1 \beta^2 + d_1 = 0, \quad (11a)$$

$$a_1 \equiv g_{22} g_{44} - g_{24}^2,$$

$$b_1 \equiv 2ikg_{24} - k^2 g_{22} - 2g_{56} g_{24} -$$

$$\begin{aligned} & - g_{24}^2 g_{11} + g_{24}^2 \nu + g_{22} g_{55} + g_{44} \\ & - g_{44} \nu + g_{11} g_{22} g_{44} - g_{22} g_{44} \nu \\ & - g_{22} \nu - k^2 g_{44}, \end{aligned}$$

$$\begin{aligned} c_1 & \equiv 2ikg_{56} - k^2 + k^2 \nu - g_{56}^2 \\ & - 2g_{56} g_{24} g_{11} + 2g_{56} g_{24} \nu + g_{55} \\ & - \nu g_{55} + g_{11} g_{22} g_{55} - g_{22} g_{55} \nu \\ & + g_{11} g_{44} - g_{11} g_{44} \nu - \nu + \nu^2 \\ & - g_{11} g_{22} \nu + g_{22} \nu^2 - k^2 g_{55} + 2k^2 \\ & - \nu g_{44} + \nu^2 g_{44}, \\ d_1 & \equiv g_{56}^2 g_{11} - g_{56}^2 \nu - g_{11} g_{55} + g_{11} g_{55} \nu \end{aligned}$$

$$+ 2g_{55} - g_{55}^2 + g_{11} - g_{11}^2 - g^2 + g^3.$$

This is a bicubic equation and we write

$$\beta_j^2 = \beta_j^2(g), \quad j = 1, 2, 3, \quad (12)$$

and  $\beta$  is related to  $V$  and  $\rho$ .

On examining the roots of (11), we find that three cases arise according as

(i)  $V < \sqrt{c_{11}/\rho}, \sqrt{c_{44}/\rho}, \sqrt{c_{55}/\rho}$  which we call subsonic case,

(ii)  $V > \sqrt{c_{11}/\rho}, \sqrt{c_{44}/\rho}, \sqrt{c_{55}/\rho}$  which is supersonic case, and

(iii)  $V < \sqrt{c_{11}/\rho}$  but  $> \sqrt{c_{44}/\rho}, \sqrt{c_{55}/\rho}$  which we shall call transonic case.

For a subsonic case, the displacements are now written as

$$\begin{aligned} u_1 &= \frac{1}{2\pi} \int_{-\infty}^{\infty} \sum U_{1j} e^{i\gamma x_1} e^{-\beta_j \gamma x_2} d\gamma, \\ u_2 &= \frac{1}{2\pi} \int_{-\infty}^{\infty} \sum U_{2j} \tau_j e^{i\gamma x_1} e^{-\beta_j \gamma x_2} d\gamma, \\ u_3 &= \frac{1}{2\pi} \int_{-\infty}^{\infty} \sum U_{3j} s_j e^{i\gamma x_1} e^{-\beta_j \gamma x_2} d\gamma, \end{aligned} \quad (13)$$

where

$$\begin{aligned} \tau_j &= U_{2j}/U_{1j} \\ &= [(\beta_j^2 - g_{11} + 2)(g_{55} - g_{44}\beta_j^2 - 2) - k^2\beta_j^2]/4j, \end{aligned}$$

$$\begin{aligned} s_j &= U_{3j}/U_{1j} \\ &= [(\beta_j^2 - g_{11} + 2)(g_{24}\beta_j^2 - g_{56}) + k\beta_j^2]/4j, \end{aligned}$$

$$\begin{aligned} 4j &= i\beta_j [k(g_{55} - g_{44}\beta_j^2 - 2) \\ &\quad + k(g_{24}\beta_j^2 - g_{56})], \quad j = 1, 2, 3. \end{aligned} \quad (13a)$$

(The values of  $U_{ij}$  are associated with the roots  $\beta_j$  of equation (11).)

For the supersonic case, the displacements are written in the form (13), where  $\beta_j$  are only replaced by  $i\beta_j$  and for the transonic case  $\beta_j$  are simply replaced throughout by  $\beta_{2,3}$ .

Now, for the conditions at infinity, (i) all displacements and stresses must remain finite at infinity, and (ii) at large distances from the point of application of the load the disturbance must consist of outgoing waves. These are called the finiteness and radiation conditions, respectively.

We have considered here those solutions which satisfy the radiation condition at infinity. The solutions of the form  $e^{i\gamma(x_1 + \beta_j x_2)}$  are not considered on the basis of the radiation condition because they represent disturbances which originate at infinity and converge toward the load [Fung (1965)].

Our problem is now to find out the mathematical solutions of the above three cases for monoclinic, orthorhombic and cubic crystals subject to the boundary conditions given by (7).

#### SOLUTION OF THE PROBLEM

##### Case 1. Subsonic

Using equations (13) and (7), we get

$$\begin{aligned} a_{11} U_1 + a_{12} U_2 + a_{13} U_3 &= -\frac{P'}{\gamma} \delta(x_1) \\ a_{21} U_1 + a_{22} U_2 + a_{23} U_3 &= 0 \\ \beta_1 a_{31} U_1 + \beta_2 a_{32} U_2 + \beta_3 a_{33} U_3 &= 0, \end{aligned} \quad (14)$$

where

$$\begin{aligned} P' &= P/c_{66} \\ a_{1j} &= i g_{12} - \beta_j \tau_j g_{22} - \beta_j s_j g_{24}, \\ a_{2j} &= i g_{14} - \beta_j \tau_j g_{24} - \beta_j s_j g_{44}, \\ a_{3j} &= 1 - i\beta_j^{-1} \tau_j - i\beta_j^{-1} s_j g_{56}, \end{aligned} \quad (15)$$

and the integral form of the delta function has been replaced by  $\delta(x_1)$  which has a meaning like a Heaviside step function.

From equations (14), we get

$$U_1 = -x_1 \frac{P \delta(x_1)}{\gamma}$$

$$\begin{aligned} u_2 &= -x_2 \frac{P_1(x'_1)}{\gamma} \\ u_3 &= -x_3 \frac{P_1(x'_1)}{\gamma} \end{aligned} \quad (16)$$

where

$$\begin{aligned} x_1 &\equiv \frac{d_{22}\beta_3 d_{33} - d_{23}\beta_2 d_{32}}{c_{66} \Delta}, \\ x_2 &\equiv \frac{d_{23}\beta_1 d_{31} - d_{21}\beta_3 d_{33}}{c_{66} \Delta}, \\ x_3 &\equiv \frac{d_{21}\beta_2 d_{32} - \beta_1 d_{31} d_{22}}{c_{66} \Delta}, \end{aligned} \quad (17)$$

$$\Delta = \begin{vmatrix} d_{11} & d_{12} & d_{13} \\ d_{21} & d_{22} & d_{23} \\ \beta_1 d_{31} & \beta_2 d_{32} & \beta_3 d_{33} \end{vmatrix}$$

and  $\beta_j^2$  are the roots of the equation given by (11).

Therefore, we have

$$u_1(x'_1, x'_2) = \frac{1}{2\pi} \int_{-\infty}^{\infty} i(x_1 e^{-\beta_1 x'_2 \gamma} + x_2 e^{-\beta_2 x'_2 \gamma} + x_3 e^{-\beta_3 x'_2 \gamma}) \left( -\frac{P_1(x'_1)}{i\gamma} \right) e^{i\gamma x'_1} d\gamma \quad (18)$$

Now, the first part of the integral is

$$-\frac{1}{2\pi} P \lim_{\epsilon \rightarrow 0} \int_{-\infty}^{\infty} \frac{1}{\epsilon + i\gamma} e^{i\gamma x'_1} e^{-\beta_1 x'_2 \gamma} d\gamma$$

$$= -P \left( \frac{1}{2} - \frac{1}{\pi} \tan^{-1} \frac{\beta_1 x'_2}{x'_1} \right)$$

$$[cf. Shedd (1951)]. \quad (19)$$

Hence, we have

$$\begin{aligned} u_1(x'_1, x'_2) &= -P \left[ i x_1 \left( \frac{1}{2} - \frac{\theta_1}{\pi} \right) \right. \\ &\quad \left. + i x_2 \left( \frac{1}{2} - \frac{\theta_2}{\pi} \right) + i x_3 \left( \frac{1}{2} - \frac{\theta_3}{\pi} \right) \right], \end{aligned} \quad (20)$$

where

$$\begin{aligned} \theta_j &\equiv \tan^{-1} \frac{\beta_j x'_2}{x'_1}, \quad j=1, 2, 3, \\ u_2(x'_1, x'_2) &= -P \left[ i x_1 \left( \frac{1}{2} - \frac{\theta_1}{\pi} \right) + i x_2 \left( \frac{1}{2} - \frac{\theta_2}{\pi} \right) + i x_3 \left( \frac{1}{2} - \frac{\theta_3}{\pi} \right) \right], \\ u_3(x'_1, x'_2) &= -P \left[ i x_1 \left( \frac{1}{2} - \frac{\theta_1}{\pi} \right) + i x_2 \left( \frac{1}{2} - \frac{\theta_2}{\pi} \right) + i x_3 \left( \frac{1}{2} - \frac{\theta_3}{\pi} \right) \right]. \end{aligned} \quad (21)$$

The non-zero stresses are given by

$$\begin{aligned} T_2 &= -\frac{P}{\pi} \left[ i x_1 (c_{12} \sin \theta_1 - c_{22} \tau_1 \beta_1 \cos \theta_1 \right. \\ &\quad \left. - c_{24} s_1 \beta_1 \cos \theta_1) + i x_2 (c_{12} \sin \theta_2 - c_{22} \tau_2 \beta_2 \cos \theta_2 - c_{24} s_2 \beta_2 \cos \theta_2) + i x_3 \right. \\ &\quad \left. (c_{12} \sin \theta_3 - c_{22} \tau_3 \beta_3 \cos \theta_3 - c_{24} s_3 \beta_3 \cos \theta_3) \right], \\ T_4 &= -\frac{P}{\pi} \left[ i x_1 (c_{14} \sin \theta_1 - c_{24} \tau_1 \beta_1 \cos \theta_1 - c_{44} s_1 \beta_1 \cos \theta_1) + i x_2 (c_{14} \sin \theta_2 - c_{24} \tau_2 \beta_2 \cos \theta_2 - c_{44} s_2 \beta_2 \cos \theta_2) + i x_3 (c_{14} \sin \theta_3 - c_{24} \tau_3 \beta_3 \cos \theta_3 - c_{44} s_3 \beta_3 \cos \theta_3) \right], \end{aligned} \quad (22)$$

$$\begin{aligned} T_6 &= -\frac{P}{\pi} \left[ i x_1 (c_{66} \tau_1 \sin \theta_1 - c_{66} \beta_1 \cos \theta_1 + c_{56} s_1 \sin \theta_1) + i x_2 (c_{66} \tau_2 \sin \theta_2 - c_{66} \beta_2 \cos \theta_2 + c_{56} s_2 \sin \theta_2) + i x_3 (c_{66} \tau_3 \sin \theta_3 - c_{66} \beta_3 \cos \theta_3 + c_{56} s_3 \sin \theta_3) \right]. \end{aligned}$$

It is noted that if  $\Delta = 0$ , the velocity of Rayleigh surface waves in the monoclinic crystal can be obtained. To determine this surface wave velocity, three different positive values of  $q$  which satisfy the equation and the root which makes all of the  $\beta_1^2, \beta_2^2, \beta_3^2$  real and positive are determined. This root only will give the velocity of Rayleigh waves (ref. f). If the load moves at exactly the speed of Rayleigh surface waves, the responses will be infinitely large.

## Case 2. Supersonic

We proceed exactly in a similar way as given by case 1 and replace  $\beta_j = i\bar{\beta}_j$  throughout. Therefore, we get

$$\begin{aligned} u_1(x'_1, x'_2) &= \frac{1}{2\pi} \int_{-\infty}^{\infty} i(x_{01} e^{-i\bar{\beta}_1 x'_2 \gamma} + x_{02} e^{-i\bar{\beta}_2 x'_2 \gamma} + x_{03} e^{-i\bar{\beta}_3 x'_2 \gamma}) \left( -\frac{P_1(x'_1)}{i\gamma} \right) e^{i\gamma x'_1} d\gamma, \end{aligned} \quad (23)$$

where  $x_{0j}$  are the same as  $x_j$ , only  $\beta_j$  should be replaced by  $i\bar{\beta}_j$ .

$$\begin{aligned} \text{Now, } \frac{1}{2\pi} \int_{-\infty}^{\infty} -\frac{P_1(x'_1)}{i\gamma} e^{i\gamma(x'_1 - \bar{\beta}_j x'_2)} d\gamma \\ = \int_{-\infty}^{\infty} \rho(\gamma) e^{i\gamma(x'_1 - \bar{\beta}_j x'_2)} d\gamma \end{aligned} \quad (24)$$

where  $\rho(\gamma)$  is the Fourier transform of

$$-\int_0^{x'_1} p(x'_1) dx'_1 \quad (25)$$



and  $p(x'_1) = p(x_1 + Vt)$  is the pressure distribution over the surface  $x'_2 = 0$ .

Or, the integral part is

$$- \int_0^{x'_1 - \bar{\beta}_1 x'_2} p(x'_1) dx'_1. \quad (25)$$

Considering the load  $p(x'_1)$  is a concentrated force  $P$ , we have

$$\begin{aligned} u_1(x'_1, x'_2) &= -P [x_{01} i \frac{1}{2} (x'_1 - \bar{\beta}_1 x'_2) + x_{02} i \frac{1}{2} (x'_1 - \bar{\beta}_2 x'_2) + x_{03} i \frac{1}{2} (x'_1 - \bar{\beta}_3 x'_2)] \\ u_2(x'_1, x'_2) &= -P [x_{01} r_1 i \frac{1}{2} (x'_1 - \bar{\beta}_1 x'_2) + x_{02} r_2 i \frac{1}{2} (x'_1 - \bar{\beta}_2 x'_2) + x_{03} r_3 i \frac{1}{2} (x'_1 - \bar{\beta}_3 x'_2)] \\ u_3(x'_1, x'_2) &= -P [x_{01} s_1 i \frac{1}{2} (x'_1 - \bar{\beta}_1 x'_2) + x_{02} s_2 i \frac{1}{2} (x'_1 - \bar{\beta}_2 x'_2) + x_{03} s_3 i \frac{1}{2} (x'_1 - \bar{\beta}_3 x'_2)] \end{aligned} \quad (26)$$

The stresses are

$$\begin{aligned} T_2 &= -P [x_{01} i \delta(x'_1 - \bar{\beta}_1 x'_2) (c_{12} - c_{22} r_1 \bar{\beta}_1 - c_{24} s_1 \bar{\beta}_1) + x_{02} i \delta(x'_1 - \bar{\beta}_2 x'_2) (c_{12} - c_{22} r_2 \bar{\beta}_2 - c_{24} s_2 \bar{\beta}_2) + x_{03} i \delta(x'_1 - \bar{\beta}_3 x'_2) (c_{12} - c_{22} r_3 \bar{\beta}_3 - c_{24} s_3 \bar{\beta}_3)] \\ T_4 &= -P [x_{01} i \delta(x'_1 - \bar{\beta}_1 x'_2) (c_{14} - c_{24} r_1 \bar{\beta}_1 - c_{44} s_1 \bar{\beta}_1) + x_{02} i \delta(x'_1 - \bar{\beta}_2 x'_2) (c_{14} - c_{24} r_2 \bar{\beta}_2 - c_{44} s_2 \bar{\beta}_2) + x_{03} i \delta(x'_1 - \bar{\beta}_3 x'_2) (c_{14} - c_{24} r_3 \bar{\beta}_3 - c_{44} s_3 \bar{\beta}_3)] \\ T_6 &= -P [x_{01} i \delta(x'_1 - \bar{\beta}_1 x'_2) (-c_{66} \bar{\beta}_1 + c_{66} r_1 + c_{56} s_1) + x_{02} i \delta(x'_1 - \bar{\beta}_2 x'_2) (-c_{66} \bar{\beta}_2 + c_{66} r_2 + c_{56} s_2) + x_{03} i \delta(x'_1 - \bar{\beta}_3 x'_2) (-c_{66} \bar{\beta}_3 + c_{66} r_3 + c_{56} s_3)] \end{aligned} \quad (28a)$$

Unlike the isotropic case, here it is observed that the disturbances are marked by three waves  $x'_1 - \bar{\beta}_1 x'_2 = 0$ ,  $x'_1 - \bar{\beta}_2 x'_2 = 0$  and  $x'_1 - \bar{\beta}_3 x'_2 = 0$ . (27)

The medium is undisturbed in front of these waves.

### Case 3. Transonic case

Replacing  $\bar{\beta}_{1,2}$  by  $i\bar{\beta}_{1,2}$ , the displacements and the stresses in a monoclinic crystal can be found out from the above analyses.

Thus,

$$\begin{aligned} u_1(x'_1, x'_2) &= -P [i x_{01} (\frac{1}{2} - \frac{\theta_1}{\pi}) + \{x_{02} i \frac{1}{2} (x'_1 - i\bar{\beta}_2 x'_2) + x_{03} i \frac{1}{2} (x'_1 - i\bar{\beta}_3 x'_2)\}] \\ u_2(x'_1, x'_2) &= -P [r_1 i x_{01} (\frac{1}{2} - \frac{\theta_1}{\pi}) + \{x_{02} r_2 i \frac{1}{2} (x'_1 - i\bar{\beta}_2 x'_2) + x_{03} r_3 i \frac{1}{2} (x'_1 - i\bar{\beta}_3 x'_2)\}] \\ u_3(x'_1, x'_2) &= -P [i s_1 x_{01} (\frac{1}{2} - \frac{\theta_1}{\pi}) + \{x_{02} i s_2 \frac{1}{2} (x'_1 - i\bar{\beta}_2 x'_2) + x_{03} i s_3 \frac{1}{2} (x'_1 - i\bar{\beta}_3 x'_2)\}] \end{aligned} \quad (27)$$

### ORTHORHOMBIC SYMMETRY

The complexity of solution in the former case arises due to the presence of the coupling constants  $c_{14}$ ,  $c_{24}$  and  $c_{35}$ , as a result of which the displacements  $u_1$  and  $u_2$ , in the sagittal plane, are coupled with the displacement  $u_3$  normal to it. For an orthorhombic crystal, these coupling constants (and also  $c_{34}$ ) are absent. Equations (10) then have the two solutions

$$U_1 \neq 0, U_2 \neq 0, U_3 = 0$$

$$\text{and } U_1 = 0, U_2 = 0, U_3 \neq 0. \quad (28)$$

Considering the first case only, which is a wave of plane strain, we have

$$(\beta^2 - \beta_{11} + \nu)(1 - \beta_{11} \beta^2 - \nu) - \kappa^2 \beta^2 = 0, \quad (29)$$

which is a quadratic equation in  $\beta^2$ . If  $\beta_j^2$  ( $j = 1, 2$ ) be the two roots, we get

$$\begin{aligned} \beta_1^2 + \beta_2^2 &= -[2 - 1 + \kappa^2 + \beta_{11}(\nu - \beta_{11})]/\beta_{11} \\ \beta_1^2 \beta_2^2 &= (\nu - 1)(\nu - \beta_{11})/\beta_{11} \\ r_j &= \frac{U_{2j}}{U_{1j}} = -i(\beta_j^2 - \beta_{11} + \nu)/\kappa \beta_j \end{aligned} \quad (30)$$

### Subsonic case.

We take the displacements in the form

$$u_1(x'_1, x'_2) = \frac{1}{2\pi} \int_{-\infty}^{\infty} \sum_j U_{1j} e^{i\gamma x'_1} e^{-\beta_j \gamma x'_2} d\gamma \quad (31)$$

and

$$u_2(x'_1, x'_2) = \frac{1}{2\pi} \int_{-\infty}^{\infty} \sum_j U_{2j} r_j e^{i\gamma x'_1} e^{-\beta_j \gamma x'_2} d\gamma \quad (j=1, 2).$$

Considering the boundary conditions (where the equation for  $T_4$  is identically zero), we have

$$U_1 = - \frac{P \delta(x'_1)}{\eta i \Delta_1} (\tau_2 + i \beta_2) \quad (32)$$

and

$$U_2 = \frac{P \delta(x'_1)}{\eta i \Delta_1} (\tau_1 + i \beta_1),$$

$$\Delta_1 = c_{66} [(\tau_2 + i \beta_2)(\vartheta_{12} + i \vartheta_{22} \tau_1 \beta_1) - (\tau_1 + i \beta_1)(\vartheta_{12} + i \vartheta_{22} \tau_2 \beta_2)].$$

Proceeding like before, we get

$$u_1(x'_1, x'_2) = \frac{P}{\Delta_1} \left[ -(\tau_2 + i \beta_2) \left( \frac{1}{2} - \frac{\vartheta_1}{\pi} \right) + (\tau_1 + i \beta_1) \left( \frac{1}{2} - \frac{\vartheta_2}{\pi} \right) \right],$$

$$\vartheta_1 \equiv \tan^{-1} \frac{\beta_1 x'_2}{x'_1}, \quad \vartheta_2 \equiv \tan^{-1} \frac{\beta_2 x'_2}{x'_1}, \quad (33)$$

$$u_2(x'_1, x'_2) = \frac{P}{\Delta_1} \left[ -\tau_1 (\tau_2 + i \beta_2) \left( \frac{1}{2} - \frac{\vartheta_1}{\pi} \right) + \tau_2 (\tau_1 + i \beta_1) \left( \frac{1}{2} - \frac{\vartheta_2}{\pi} \right) \right].$$

If  $\Delta_1 = 0$ , we get the speed of Rayleigh surface waves. In that case, we have

$$(\tau_2 + i \beta_2)(c_{12} - c_{22} \tau_1 \beta_1) = (\tau_1 + i \beta_1)(c_{12} - c_{22} \tau_2 \beta_2), \quad (34)$$

where  $\beta_{1,2}^2$  are obtained from (30). After simplification, a fourth degree equation for  $V$  is obtained, one root of which ( $V = c_{11}$ ) will give zero displacement. Removing this root, we get

$$(1-a)q^3 - (1-b+2f)q^2 + f(f+2)q - f^2 = 0, \quad (34a)$$

where

$$q = fV^2/c_{66}, \quad a = c_{66}/c_{12}, \quad b = c_{11}/c_{22},$$

$$f = \frac{c_{11}}{c_{66}} - \frac{c_{12}^2}{c_{22}c_{66}}.$$

In this case, three different positive roots ( $VP \equiv fV^2/c_{66}$ ) which satisfy the above equation is first determined and the root which makes all of the  $\beta_1^2, \beta_2^2$  real and positive will give the velocity of surface wave. If the load moves steadily at this speed, the responses will be infinitely large.

#### Supersonic case

Replacing  $\beta_1 = i \bar{\beta}_1$  and  $\beta_2 = i \bar{\beta}_2$ , we get

$$U_1 = - \frac{P \delta(x'_1)}{i \eta \Delta_2} (\tau_2 - \bar{\beta}_2)$$

$$U_2 = \frac{P \delta(x'_1)}{i \eta \Delta_2} (\tau_1 - \bar{\beta}_1) \quad (35)$$

$$\Delta_2 = c_{66} [(\tau_2 - \bar{\beta}_2)(\vartheta_{12} - \vartheta_{22} \tau_1 \bar{\beta}_1) - (\tau_1 - \bar{\beta}_1)(\vartheta_{12} - \vartheta_{22} \tau_2 \bar{\beta}_2)].$$

Therefore, we have

$$u_1(x'_1, x'_2) = \frac{1}{2\pi \Delta_2} \left[ -(\tau_2 - \bar{\beta}_2) \int_{-\infty}^{\infty} \frac{P \delta(x'_1)}{i \eta} e^{i \eta (x'_1 - \bar{\beta}_1 x'_2)} d\eta + \right.$$

$$\left. + (\tau_1 - \bar{\beta}_1) \int_{-\infty}^{\infty} \frac{P \delta(x'_1)}{i \eta} e^{i \eta (x'_1 - \bar{\beta}_2 x'_2)} d\eta \right] \quad (36)$$

Or,

$$u_1(x'_1, x'_2) = \frac{1}{\Delta_2} \left[ -(\tau_2 - \bar{\beta}_2) \int_0^{x'_1 - \bar{\beta}_1 x'_2} p(x'_1) dx'_1 + (\tau_1 - \bar{\beta}_1) \int_0^{x'_1 - \bar{\beta}_2 x'_2} p(x'_1) dx'_1 \right].$$

If  $p(x'_1)$  is a concentrated force  $P$ , we get

$$u_1(x'_1, x'_2) = \frac{1}{\Delta_2} \left[ (\tau_1 - \bar{\beta}_1) \delta(x'_1 - \bar{\beta}_2 x'_2) - (\tau_2 - \bar{\beta}_2) \delta(x'_1 - \bar{\beta}_1 x'_2) \right]. \quad (37)$$

Similarly, we have

$$u_2(x'_1, x'_2) = \frac{1}{\Delta_2} \left[ \tau_2 (\tau_1 - \bar{\beta}_1) \delta(x'_1 - \bar{\beta}_2 x'_2) - \tau_1 (\tau_2 - \bar{\beta}_2) \delta(x'_1 - \bar{\beta}_1 x'_2) \right]. \quad (38)$$

In this case, the displacements are marked by two waves

$$x'_1 - \bar{\beta}_1 x'_2 = 0, \quad x'_1 - \bar{\beta}_2 x'_2 = 0, \quad (39)$$

which shows that the medium is undisturbed here also in front of these waves.

#### Transonic case

We consider the case where  $V < \sqrt{c_{66}/\rho}$  but  $> \sqrt{c_{44}/\rho}$ .

Replacing  $\beta_2 = i \bar{\beta}_2$  in (32), we get

$$U_1 = - \frac{P \delta(x'_1)}{\eta i \Delta_3} (\tau_2 - \bar{\beta}_2),$$

$$\begin{aligned}
u_2 &= \frac{P_1(x'_1)(\tau_1 + i\beta_1)}{2i\beta_3}, \\
\Delta_3 &= c_{66}[(\tau_2 - \bar{\beta}_2)(\beta_{12} + i\beta_{22}\tau_1\beta_1) - (\tau_1 + i\beta_1)(\beta_{12} - \beta_{22}\tau_2\bar{\beta}_2)], \\
\tau_1 &= -i(\beta_1^2 - \beta_{11} + 2)/\kappa\beta_1, \\
\tau_2 &= (\bar{\beta}_2^2 + \beta_{11} - 2)/\kappa\bar{\beta}_2.
\end{aligned} \quad (40)$$

Therefore, we have

$$\begin{aligned}
u_1(x'_1, x'_2) &= \frac{P}{\Delta_3} [-(\tau_2 - \bar{\beta}_2)(\frac{1}{2} - \frac{1}{n} \\
&\tan^{-1} \frac{\beta_1 x'_2}{x'_1}) + (\tau_1 + i\beta_1)\frac{1}{2}(x'_1 - \bar{\beta}_2 x'_2)], \\
\end{aligned} \quad (41)$$

and

$$\begin{aligned}
u_2(x'_1, x'_2) &= \frac{P}{\Delta_3} [-(\tau_2 - \bar{\beta}_2)\tau_1 \\
&(\frac{1}{2} - \frac{1}{n} \tan^{-1} \frac{\beta_1 x'_2}{x'_1}) + (\tau_1 + i\beta_1)\tau_2 \\
&\frac{1}{2}(x'_1 - \bar{\beta}_2 x'_2)].
\end{aligned}$$

If we now introduce the conditions  $c_{22} = c_{11}$ ,  $c_{66} = c_{44}$  appropriate to a cubic system in the above equations, the corresponding results in the direction of the cubic axes can be obtained.

The present analysis indicates that the problem of steady-state response to a line load moving with a constant speed over any crystalline rock including trigonal, tetragonal, hexagonal, etc. can be studied (De, 1976) (for certain orientation of the axes of the crystal). The paper also serves to find out a solution of the problem when such rocks exist under initial stress (De, 1977).

#### ACKNOWLEDGMENT

The author is grateful to C.S.I.R. (New Delhi) for financial support. The author is also indebted to Prof. P.K.Ghosh, Head of the Department of Applied Mathematics, Calcutta University for his keen interest and constant encouragement.

#### REFERENCES

- a. C.C. Chao, "Dynamical Response of an Elastic Half-space to Tangential Surface Loadings," J. Appl. Mech., Vol. 27, pp. 569-57, 1960
- b. J. Cole, and J. Euth, "Stresses Produced in a Half-plane by Moving Loads," J. Appl. Mech., Vol. 25, pp. 453-36, 1958
- c. S. De, "Stresses Produced by a Normal Pressure over the Boundary of a Granular Layer Resting on Rigid Foundation," Acta Geophysica Pol., Vol. 25, No. 2, pp. 139-45, 1975
- d. S. De, "On the Propagation of Love Waves in a Crystalline Medium," J. Phys. Earth, Vol. 23, pp. 219-285, 1975
- e. S. De, "Study of the Elastic Constants of Crystals and the Problem of Surface waves over Liquid and Crystalline Layers," J. Phys. Earth (Submitted for publication), 1976
- f. S. De, "Problem of Surface Waves over Liquid and Crystalline Layers-II," J. Phys. Earth (Submitted for publication), 1976
- g. S. De, "Problem of Surface Waves in Crystalline Media-II," Acta Geophysica Polonica, In press, 1976
- h. S. De, "Influence of Initial Stress on the Wave Propagation in Crystalline Media," Geophysical Research Bull., In press, 1977
- i. A.C. Eringen, and J.C. Samuels, "Impact and Moving Loads on a Slightly Curved Elastic Half-space," J. Appl. Mech., Vol. 26, pp. 491-98, 1959
- j. Y.C. Fung, "Foundations of Solid Mechanics," Prentice-Hall, Inc., Englewood Cliffs, New Jersey, 1965
- k. H. Lamb, "On the Propagation of Tremors over the Surface of an Elastic Solid," Phil. Trans. Roy. Soc. (London), Ser. A, Vol. 203, pp. 1-42, 1904
- l. G.C. Pakeria, and H. Lifson, "Motion of the Surface of a Uniform Elastic Half-space Produced by a Buried Pulse," J. Acoust. Soc. Am., Vol. 29, pp. 1235-39, 1957
- m. I.N. Sneddon, "Fourier Transforms," New York, McGraw-Hill, pp. 445-49, 1951

ADJUSTMENT OF A CONSERVATIVE NON GYROSCOPIC  
MATHEMATICAL MODEL FROM MEASUREMENT<sup>(\*)</sup>

L. BUGEAT, R. FILLOD, G. LALLEMENT, J. PIRANDA  
Laboratoire de Mécanique Appliquée, associé au C.N.R.S.  
Faculté des Sciences de Besançon, FRANCE<sup>(\*\*)</sup>

We are presenting a method of calculating the modifications of a discrete, conservative model, which enables one to reduce the distance between its dynamic behaviour and the one identified on the physical structure. An initial approximate model is known and results from a discretization "a priori" for example by finite element method. The comparisons of the partial eigensolutions of this model, together with the corresponding eigensolutions identified on the physical structure, enable one to locate the spatial area (or groups of degrees of freedom) where the initial model reveals dominant errors. The exploitation of the perturbation method enables one further to calculate the variations of the physical construction parameters, such that the modified model becomes, on a certain frequential field, dynamically similar to the physical structure. The results of a numerical simulation are, then, presented.

#### INTRODUCTION

The recent development of the modal identification methods of the mechanical systems enables one to envisage a more effective exploitation of their results. Particularly, the degree of accuracy obtained on the eigensolutions identified enables one to exploit them in view of improving the mechanical model representing the structure. We are limiting this study to the case of system whose mechanical characteristics are representable after discretization, by real, constant, symmetrical matrices. We also assume that the dissipating forces in the structure are small in comparison with the conservative forces, and that the eigensolution of the conservative structure associated to the real structure are, therefore identifiable with good precision. The adjustment method presented here only concerns the conservative model. The propounded objective consists of determining the modifications of inertia and stiffness that are

to be introduced in an initial, conservative model, such that the new conservative model of similar order, thus obtained, admits for eigensolutions, those which have been identified on the structure.

The advantage of the solution of this type of problem is confirmed by a recently-proposed method [1], whose aims is to adjust the eigenfrequencies through parametric modifications in the areas where potential and kinetic energies are dominant. These areas do not necessarily correspond to those areas where the initial model reveals the greatest errors. The physical interpretation of such a modified model is, therefore, particularly delicate.

#### 2 - DATA OF THE PROBLEM

The data of the problem are as follows: the matrices of inertia  $M^{(e)}$  and stiffness  $K^{(e)}$  are of order  $(N \times N)$ , real, symmetric, constant

definite positives. They correspond to the initial model and are assumed to be obtained by finite element method.

Then we calculate the corresponding modal and spectral sub-matrices,  $Y_1^{(e)}$  and  $\Lambda_1^{(e)}$  respectively, of order  $(N,n)$  and  $(n,n)$  characterizing the first  $n$  eigensolutions. These different matrices satisfy the orthonormality relations :

$$\begin{aligned} T_{Y_1}^{(e)} M^{(e)} Y_1^{(e)} &= E_1 \quad \text{where } E_1 \text{ is the } n \text{ order} \\ &\quad \text{unity matrix} \\ T_{Y_1}^{(e)} K^{(e)} Y_1^{(e)} &= \Lambda_1^{(e)} \end{aligned} \quad (1)$$

It is also assumed that the experiments on the structure have permitted the identification of the modal and spectral sub-matrices  $Y_1^{(m)}$  and  $\Lambda_1^{(m)}$  respectively, of order  $(N,n)$  and  $(n,n)$  characterizing the first  $n$  eigensolutions of the conservative structure associated to the real mechanical structure. We admit that the precision of initial modelization is reasonable, such that the distance between the calculated and identified eigensolutions is sufficiently small and enables one to carry out a mode-to-mode correspondence. The method of mode-to-mode pairing adapted to our formulation of the problem is based on the quasi orthonormality of the modes identified compared with the modes calculated. This property is used to construct a matrix of linear combination  $(E_1 + A_{11})$  (cf. : relation 6) with dominant diagonal and minimum norm. We shall not go into a detailed expose of this method. It should, however, be pointed out that the method propounded by R.E. HULL, B.I. BEJMUJ and J. NICHOLS [2] also enables one to solve the pairing problem. Let us also point out that we consider the case where the modal sub-matrix  $Y_1^{(m)}$  is only partly identified. (For example, lack of information corresponding to the rotation degrees of freedom, abbreviated by D.O.F., or the interior D.O.F. inaccessible to measures.

Based on these data, we attempt to determine the additional matrices  $\Delta M$  and  $\Delta K$  such that the modified model :  $M^{(e)} + \Delta M$  ;  $K^{(e)} + \Delta K$

admits as first  $n$  eigensolutions  $Y_1^{(m)}$  and  $\Lambda_1^{(m)}$ . The method propounded consists of two distinct stages : the first stage is one of localization which consists of finding the area or groups of degrees of freedom of the structure for which the initial modelization reveals dominant errors. The second stage consists of calculating, in the previously-located areas, the modifications of physical parameters to be introduced in the initial model in order to have its first  $n$  eigensolutions coincide with the identified eigensolutions. This calculation is based on a sensitivity method.

### 3 - LOCALIZATION OF MODELIZATION ERRORS

The exploitation of the perturbation method and of equilibrium equations enables one to determine the dominant areas of the additional matrices of inertia  $\Delta M$  and of stiffness  $\Delta K$ . Their locations define more accurately the positions of the group of points of connexion and D.O.F.'s and, consequently, the spatial areas of the structure in which the principal modifications should be carried out. This process enables one to reduce, in a large proportion, the number of unknown quantities and transform an initially highly - under - determined problem to an over-determined one. Among the infinite number of possible solutions, the calculated solution taking into account only the dominant areas, seems to present an acceptable physical meaning.

#### 3.1 - Exploitation of the perturbation method

The distance between the initial model and the identified (or measured) models is assumed small. In other words, the additional matrices  $\Delta M$  and  $\Delta K$  are assumed to perturb slightly the initial model. The perturbations are regular and small in the sense that :

- a - the same number  $N$  of D.O.F. is retained ;
- b - they produce small modifications of the eigenvalues  $\lambda_v^{(e)}$  and eigenvectors  $y_v^{(e)}$ ,  $v=1,2,\dots,n$ .

In this case, the new model represented by :  $M^{(m)} = M^{(e)} + \Delta M$  ;  $K^{(m)} = K^{(e)} + \Delta K$ , admits as modal and spectral sub-matrices :

$$Y_1^{(m)} = Y_1^{(e)} + \Delta Y_1 ; \Lambda_1^{(m)} = \Lambda_1^{(e)} + \Delta \Lambda_1 \quad (3)$$

where :  $\|\Delta Y_1\| \ll \|Y_1^{(e)}\|$  ;  $\|\Delta \Lambda_1\| \ll \|\Lambda_1^{(e)}\|$ .

Moreover, these matrices satisfy the orthonormality relations :

$$T_{Y_1}^{(m)} M^{(m)} Y_1^{(m)} = E_1, \quad T_{Y_1}^{(m)} K^{(m)} Y_1^{(m)} = \Lambda_1^{(m)} \quad (4)$$

Let us now consider the set of  $N$  eigenvectors of the initial model represented by  $Y^{(e)}$  ( $N \times N$ ) and the  $N$  corresponding eigenvectors of the structure represented by  $Y^{(m)}$  ( $N \times N$ ). Expressing  $Y^{(m)}$  on the basis  $Y^{(e)}$  we obtain :

$$Y^{(m)} = Y^{(e)} [E + A] \quad (5)$$

The separation into two sub-bases, making the  $n$  calculated and identified eigensolutions appear, leads to the following partitioning :

$$Y^{(e)} = \begin{bmatrix} Y_1^{(e)} \\ Y_2^{(e)} \end{bmatrix} ; Y^{(m)} = \begin{bmatrix} Y_1^{(m)} \\ Y_2^{(m)} \end{bmatrix} ; A = \begin{bmatrix} A_{11} & A_{12} \\ A_{21} & A_{22} \end{bmatrix}$$

The method is based on the following approximations :

a)  $\|A_{11}\| \ll \|E_1\|$  where  $A_{11}$  and  $E_1$  are square matrices of order  $n$ .

b)  $A_{12} = A_{21} = 0$  ; relations which express that each modal sub-matrix  $Y_1^{(m)}$  and  $Y_2^{(m)}$  can be represented with sufficient approximation in terms of only the corresponding eigenvectors of the initial model :

$$Y_1^{(m)} = Y_1^{(e)} [E_1 + A_{11}] ; \quad (6)$$

$$Y_2^{(m)} = Y_2^{(e)} [E_2 + A_{22}] \quad (7)$$

where  $E_1$  and  $E_2$  are unity matrices of order  $n$  and  $N-n$  respectively. From the physical view point, these approximations are equivalent to :

- a similarity of the number of half waves in the correspondence between the  $n$  calculated and measured eigenvectors ;

- a rather clear separation between both sub-spectrum characterized by the spectral sub-matrices  $\Lambda_1^{(e)}$  ( $n \times n$ ) and  $\Lambda_2^{(e)}$  ( $N-n \times N-n$ ). Among the two previous relations, only (6) is exploitable ; it leads to two methods of calculating the matrix  $A_{11}$  :

- In the case where the modal sub-matrix  $Y_1^{(m)}$  of order ( $N, n$ ) is totally identified, we obtain the following by exploiting the orthonormality relations (1) :

$$A_{11} = T_{Y_1}^{(e)} M^{(e)} Y_1^{(m)} - E_1 \quad (8)$$

The matrix  $A_{11}$  thus calculated is one that minimizes the potential and kinetic energies calculated by means of the components of the error vectors :

$\epsilon_v = \Delta y_v - Y_1^{(e)} a_{11v}$  where  $\Delta y_v = y_v^{(m)} - y_v^{(e)}$  and  $a_{11v} = A_{11} e_v$  ( $e_v$  being the  $v^{th}$  column of the unity matrix).

- In the case where the modal sub-matrix  $Y_1^{(m)}$  is partly identified, the previous method is not applicable.  $A_{11}$  is, therefore, expressed by the following pseudo-inverse :

$$A_{11} = [T_{Y_1}^{(e)} Y_1^{(e)}]^{-1} T_{Y_1}^{(e)} (Y_1^{(m)} - Y_1^{(e)}) \quad (9)$$

which is an approximate solution of (6) obtained by calculating the matrix  $A_{11}$  column by column and minimizing the square of each  $\|\epsilon_v\|$  norm of the error vectors :  $\epsilon_v = \Delta y_v - Y_1^{(e)} a_{11v}$ ,  $v=1, 2, \dots, n$ . In the relation (9) zeroes should be introduced on the lines of  $Y_1^{(e)}$  and  $Y_1^{(m)}$  corresponding to unidentified D.O.F.'s.

Taking into account the approximations a) and b), the development of the orthonormality relations (4) leads to the following relations :

$$A_{11} + T_{A_{11}} + T_{Y_1}^{(e)} \Delta M Y_1^{(e)} = 0 \quad (10a)$$

$$T_{Y_2}^{(e)} \Delta M Y_1^{(e)} = 0 \quad (10b)$$

$$\Lambda_1^{(e)} A_{11} + T_{A_{11}} \Lambda_1^{(e)} + T_{Y_1}^{(e)} \Delta K Y_1^{(e)} = \Delta \Lambda_1 \quad (11a)$$

$$T_{Y_2}^{(e)} \Delta K Y_1^{(e)} = 0 \quad (11b)$$

from which we obtain :

$$\Delta M Y_1^{(e)} = C \quad \text{where } C = -M^{(e)} Y_1^{(e)} |A_{11}| + T A_{11} \quad (12)$$

$$\Delta K Y_1^{(e)} = G \quad \text{where } G = M^{(e)} Y_1^{(e)} |\Delta A_1 - (\Lambda_1^{(e)} A_{11} + T A_{11} \Lambda_1^{(e)})| \quad (13)$$

The rectangular matrices C and G of order Nxn are immediately calculable and, as will be seen later, play the role of localization matrices.

### 3.2 - Exploitation of the modal equilibrium equations

We can do away with the previous hypotheses by direct comparison of the modal equilibrium equations of the initial model and of the model corresponding to measurements :

$$K^{(e)} Y_1^{(e)} - M^{(e)} Y_1^{(e)} \Lambda_1^{(e)} = 0 \quad (14)$$

$$(K^{(e)} + \Delta K) Y_1^{(m)} - (M^{(e)} + \Delta M) Y_1^{(m)} \Lambda_1^{(m)} = 0 \quad (15)$$

By combining both equations we obtain :

$$\Delta K Y_1^{(m)} - \Delta M Y_1^{(m)} \Lambda_1^{(m)} = H \quad \text{where}$$

$$H = M^{(e)} |\Delta Y_1 \Lambda_1^{(m)} + Y_1^{(e)} \Delta \Lambda_1| - K^{(e)} \Delta Y_1 \quad (16)$$

The rectangular matrix H, of order N.n, is directly calculable and will also play the role of location matrix.

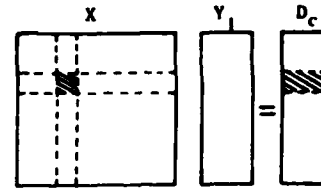
The relation (16), not based upon any approximation, has all the advantages of an exact relation. On the other hand, it does not allow separating the predominant areas of  $\Delta M$  from those of  $\Delta K$ . Additionally, (16) is very sensitive to measurement and identification errors.

### 3.3 - Localization of the errors of discretization

The relations (12), (13) and (16) enable us to locate the dominant blocks of the matrices  $\Delta M$  and  $\Delta K$ . The three matrices C, G and H have basically the same structure with respect to errors and they will be exploited either separately or jointly by comparing and cross-checking

their common dominant blocks. The relations (12), (13) and (16) take the general form :  $X \cdot Y_1 = D_c$

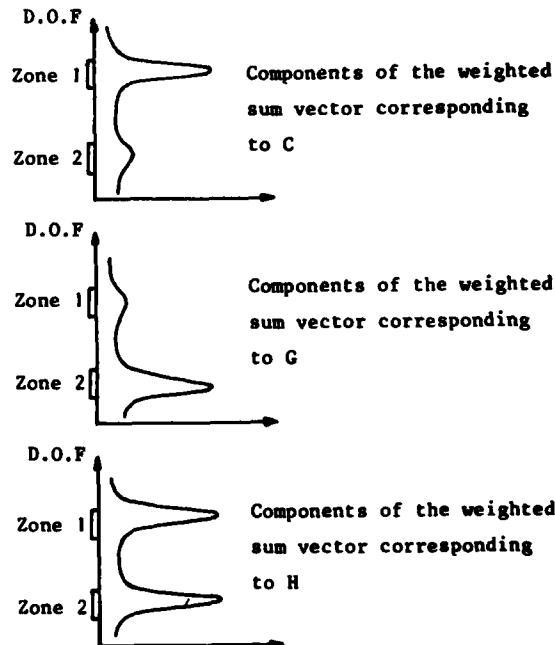
Where X designates the matrix whose dominant blocks are to be identified,  $Y_1$  denotes a modal sub-matrix, and  $D_c$  a known matrix.



The localization is based on the fact that, to each predominant block in X, there is a corresponding group of lines of greater weight in  $D_c$ .

The method consists of constructing, by means of the n column vectors of each of the matrices such as  $D_c$ , a weighted sum vector whose components are representative of the relative importances of the lines of  $D_c$ .

Example : A perturbation of mass in zone 1 and of stiffness in zone 2 will be revealed by the configurations of the following weighted sums vectors :



The determination of the zones and their limits (selection of the D.O.F.'s) is then carried out by arbitrarily setting two thresholds on the components of each vector :

- threshold 1 is an arbitrary fraction of the maximum component of the sum vector considered,
- the aim of threshold 2 is to eliminate doubts resulting from approximations, numerical, experimental and identification errors. A D.O.F. will be retained if the corresponding component of the weighted sum vector is greater than the thresholds 1 and 2.

### 3.4 - Practical conditions of application

- The  $n$  column vectors  $a_{11v}$ ,  $v = 1, 2, \dots, n$  of the matrix  $A_{11}$  condense information relative to eigenvectors differences. The matrix  $A_{11}$  is thereby not very sensitive to measurement and identification errors.

- The practical limits deduced from the test cases treated are as follows :

$$\left| \frac{\lambda_v^{(m)} - \lambda_v^{(e)}}{\lambda_v^{(e)}} \right| < 0.3; |a_{11v\sigma}| < 1, \text{ where}$$

$$a_{11v\sigma} = {}^T e_v A_{11} e_\sigma \text{ and } v, \sigma = 1, 2, \dots, n.$$

- The numerical simulation showed that the localization obtained by direct exploitation of the equilibrium equation (matrix  $H$ ) is very sensitive to small variations of the elements of the modal sub-matrix  $Y_1^{(m)}$ . In practice, it is logical to think that noise produced by measurement, identification and numerical errors would lead to an erroneous localization. Therefore, in order to determine the matrix  $H$ , it is better to use the approximation of  $Y_1^{(m)}$  given by :

$Y_1^{(m)} \approx Y_1^{(e)} [E_1 + A_{11}]$ . The simulated test cases shows that this procedure leads to an accurate localization.

## 4 - DYNAMICAL ADJUSTMENT

We now endeavour by means of a sensitivity

method [3],[4],[5], to reduce the distance between, calculated and identified eigensolutions. The physical construction parameters on which we are working in order to obtain this adjustment is limited only to those parameters intervening in the previously located, dominant areas of  $\Delta M$  and  $\Delta K$ . This method enables us to construct a conservative model of order  $N$ , whose first  $n$  eigensolutions are similar to the  $n$  identified eigensolutions of the conservative structure associated to the real structure. By restricting ourselves only to the terms of the first order we calculate the sensitivity matrix  $S(n^2 + nx)$  by means of the mechanical characteristics  $M^{(e)}$ ;  $K^{(e)}$  and partial dynamics characteristics  $\Lambda_1^{(e)}$ ;  $Y_1^{(e)}$ . This matrix links the differences of eigensolutions represented by the matrices  $\Delta \Lambda_1$  and  $\Delta Y_1$  regrouped in the vector  $b(n^2 + nx)$ , to the vector  $\Delta p/p(q \times 1)$  of the relative variations of the construction parameters.

The initial selection of these parameters is carried out so as to satisfy the condition :  $q < n^2 + n$ . We now endeavour to obtain the approximate solution of the linear system  $b = S \Delta p/p$  based on a criterion minimizing the squares of the weighted norm of the error vector  $\epsilon = b - S \Delta p/p$  and of the vector  $\Delta p/p$ .

### 4.1 - Determination of the sensitivity matrix

Let us call the  $i^{th}$  construction parameter  $p_i$ . The eigensolutions  $\Lambda^{(e)}$ ;  $Y^{(e)}$  correspond to  $p_i$ . Let us call the first derivative of a  $V$  quantity  $V_{,i}$  in relation to the scalar  $p_i$ . The modification  $dp_i$  gives rise to new eigensolutions

$$\Lambda^{(e)} + \Lambda_{,i}^{(e)} dp_i + O(dp_i^2); Y^{(e)} + Y_{,i}^{(e)} dp_i + O(dp_i^2) \quad (17)$$

Introducing the basis change :

$Y_{,i}^{(e)} = Y^{(e)}_{,i} A$ , we obtain the following result after derivation of the orthonormality relations

(1) :

$$\begin{aligned} {}^T A_{,i} + {}^T A + {}^T Y_{,i}^{(e)} M_{,i}^{(e)} Y^{(e)} &= 0; \\ {}^T A \Lambda^{(e)} + \Lambda^{(e)}_{,i} A + {}^T Y_{,i}^{(e)} K_{,i}^{(e)} Y^{(e)} &= \Lambda_{,i}^{(e)} \end{aligned} \quad (18)$$



Knowing  $M_{i,i}^{(e)}$ ,  $K_{i,i}^{(e)}$ , and assuming that the eigensolutions of the initial model are also known, the matrices  $A_{i,i}$  and  $\Lambda_{i,i}$  would be easily calculable.

According to (17), the variations of the  $v^{\text{th}}$  eigenvalue  $\lambda_v^{(e)}$  and the  $v^{\text{th}}$  eigenvector  $y_v^{(e)}$  will be written as follows :

$$d\lambda_v = \lambda_{v,i}^{(e)} dp_i + O(dp_i)^2 \quad (19)$$

$$dy_v = i^a_v dp_i + O(dp_i)^2 \text{ where } i^a_v = i^a_{e_v} \text{ denotes the } v^{\text{th}} \text{ column of } i^a.$$

Comparing the latter relation to the difference vector  $\Delta y_v$  given by (3)

$$\Delta y_v = y_v^{(m)} - y_v^{(e)} = Y^{(e)} a_v, \text{ we deduce from it to the nearest second order terms :}$$

$$a_v = i^a_v dp_i, \quad (20)$$

$$\text{where we note : } a_v = T \{ T_{a_{11v}}; T_{a_{21v}} \}; \\ i^a_v = T \{ i^a_{11v}; i^a_{21v} \}.$$

Considering that the scalar  $d\lambda_v$  and the vector  $a_v$ ,  $v = 1, 2, \dots, n$ , characterize the differences of eigenvalues and eigenvectors between the initial and identified models, the hypothesis  $A_{21} = 0$  introduced in the first part leads us to consider only the following sub-vectors of dimension  $n$  :  $a_{11v} = A_{11} e_v$  and  $i^a_{11v}$  connected by the relation :

$$a_{11v} = i^a_{11v} \Delta p_i. \quad (21)$$

Considering in (19) and in (21) respectively the  $n$  scalar equations corresponding to the  $n$  identified eigenvectors, and writing them, i.e. (19) and (21) such that only dimensionless quantities appear, we obtain :

$$\frac{\Delta \lambda_v}{\lambda_v^{(e)}} = \frac{p_i}{\lambda_v^{(e)}} \lambda_{v,i}^{(e)} \frac{\Delta p_i}{p_i} \\ a_{11v} = p_i i^a_{11v} \frac{\Delta p_i}{p_i} \quad v = 1, 2, \dots, n.$$

These equations are grouped under the form :

$$\begin{bmatrix} \Delta \lambda_v \\ \lambda_v^{(e)} \\ \vdots \end{bmatrix} = p_i \begin{bmatrix} \lambda_{v,i}^{(e)} \\ \lambda_v^{(e)} \\ \vdots \end{bmatrix} \cdot \frac{\Delta p_i}{p_i} \quad \text{written :} \\ \begin{bmatrix} a_{111} \\ i^a_{111} \\ a_{112} \\ i^a_{112} \end{bmatrix} = b = s_i \frac{\Delta p_i}{p_i} \quad \text{where } b \text{ and } s_i \text{ are two vectors of dimension } n(n+1).$$

More generally, for  $q$  construction parameters, we make  $q$  modifications transforming the vector of the parameters  $p$ , of dimension  $q$  in  $p + dp$ . We can write to the nearest second order terms :

$$d\lambda_v^{(e)} = \sum_{i=1}^q \lambda_{v,i}^{(e)} dp_i, \\ dy_v^{(e)} = Y^{(e)} \sum_{i=1}^q i^a_v dp_i.$$

In similar manner as in the case of a single parameter by using the hypothesis  $A_{21} = 0$  and considering that the scalar  $\Delta \lambda_v^{(e)}$  and the vector  $a_{11v}$  mark the differences between the initial model and the identified model, we obtain :

$$\frac{\Delta \lambda_v}{\lambda_v^{(e)}} = \sum_{i=1}^q \frac{p_i}{\lambda_v^{(e)}} \lambda_{v,i}^{(e)} \frac{\Delta p_i}{p_i} \quad v = 1, 2, \dots, n \\ a_{11v} = \sum_{i=1}^q p_i i^a_{11v} \frac{\Delta p_i}{p_i},$$

relations being grouped under the matricial form:

$$b = S \frac{\Delta p}{p} \quad (22)$$

where  $b$  is a vector of dimension  $n \times (n+1)$   
 $S = [s_1; \dots; s_i; \dots; s_q]$  a rectangular matrix of order  $n \times (n+1) \cdot q$ ,  $\frac{\Delta p}{p}$  a vector of dimension  $q$ .

#### 4.2 - Determination of the solutions

The linear system (22) is assumed to be over-determined. In fact, the localization must

allow keeping only a limited number of D.O.F.'s, and the number  $q$  of physical parameters around these D.O.F.'s is assumed to be either inferior to  $n(n+1)$  or chosen so that it satisfies this condition.

In the strict sense, (22) admits no exact solution ; consequently we endeavour to reach an approximate solution that simultaneously minimizes :

- the square of the weighted error-vector norm :  $P\epsilon = P(b - S \frac{\Delta p}{p})$  where the matrix  $P$ , diagonal of order  $n \times (n+1)$ , definite positive, is arbitrarily chosen and plays the role of ponderation matrix fixing the relative importance accorded to each of the elements of the eigensolutions ;

- the square of the solution vector norm  $\frac{\Delta p}{p}$ .

We are therefore led to minimize real scalar function  $j$  :

$$j = T_{\epsilon} P^2 \epsilon + \alpha \frac{T_{\Delta p}}{p} \frac{\Delta p}{p}$$

where  $\alpha$  is a positive coefficient arbitrary chosen and specifying the compromise between the quality of adjustment and the importance of the modifications.

The solution of this minimum problem leads to the solution :

$$\left(\frac{\Delta p}{p}\right)_{\alpha} = \left[T_S P^2 S + \alpha E\right]^{-1} T_S P^2 b \quad (23)$$

#### 4.3 - Choice of a solution

The ponderation matrix  $P$  is determined in terms of the physical nature of the specific case dealt with, i.e. of the type of structure and of the application envisaged by means of the dynamical model.

The problem that remains to be solved is the determination of an acceptable value of the arbitrary coefficient  $\alpha$ . The examination of (23) shows the influence of this coefficient :

- for  $\alpha = 0$ , the square of the solution-vector norm is not minimized, and the calculation generally leads to physically unacceptable scalar values  $\Delta p_i/p_i$  ;

- for large values of  $\alpha$  (or more precisely  $\alpha \gg |^q \sqrt{\det(TSS)}|$ ), the square of the error-vector norm is no longer minimized and the solution vector no longer satisfies the constraint equations (22).

The propounded solution consists of calculating for a set of  $\alpha$  values the corresponding solution vectors. For every vector  $\left(\frac{\Delta p}{p}\right)_{\alpha}$ , we then calculate the vector  $\hat{b}_{\alpha} = S \left(\frac{\Delta p}{p}\right)_{\alpha}$ . This vector  $\hat{b}_{\alpha}$  represents the estimation of the quantities  $(\Delta \lambda_v / \lambda_v)$  and  $(a_{11v})$ , noted  $(\hat{\Delta \lambda}_v / \lambda_v)_{\alpha}$  and  $(\hat{a}_{11v})_{\alpha}$ , obtained by means of the sensitivity matrix  $S$ , when the parameter variation  $(\Delta p/p)_{\alpha}$  is made. The comparison of these estimated variations with those desired  $(\Delta \lambda_v / \lambda_v)$  and  $a_{11v}$  enables us to determine the influence of the coefficient  $\alpha$  on minimization.

In practice, the  $q$  number of parameters initially included in the calculation, is often physically superabundant. For instance a wrong modelization in a determined zone can be due to the erroneous estimation of a single parameter, whereas all the parameters of the zone are taken into account during the calculation.

The numerical simulation shows that when the value of  $\alpha$  varies the scalars  $(\Delta p_i/p_i)_{\alpha}$  corresponding to the superabundant parameters  $p_i$  tend to change signs more frequently than the others. The propounded method consists of eliminating the parameter (or parameters) showing the greatest number of sign changes and, by a new sweep in  $\alpha$  of recalculating the new scalar  $(\Delta p_i/p_i)_{\alpha}$  corresponding to the only remaining parameters. We then use, as sensitivity matrix, the matrix constructed by the columns of  $S$  corresponding to the remaining parameters.

The procedures is stopped when the sca-

lars  $(\Delta p_i/p_i)_{\alpha}$  do not show more than one sign change. Among the set of the solution vectors  $(\Delta p/p)_{\alpha}$  of order  $r < q$  obtained during the last sweep, we retain the solution  $(\Delta p/p)_{\alpha^*}$  considered as the optimum one in the compromise between adjustment quality and modification amplitude. This choice, left to the user's appreciation, consists of judging comparatively :

- if the values of  $\Delta p_i/p_i$  are acceptable,
- if the estimated variations  $(\Delta \hat{\lambda}_v/\lambda_v)_{\alpha^*}$  and  $(a_{||v})_{\alpha^*}$  are close to the desired variations.

#### 4.4 - Adjustment of the initial model

The value  $\alpha^*$  having been chosen, we carry out the modification  $(\Delta p/p)_{\alpha^*}$  on the initial model. This modification consists of adding, to the initial  $M^{(e)}$  and  $K^{(e)}$ , the adjustment matrices of inertia  $(\Delta M)_{\alpha^*}$  and of stiffness  $(\Delta K)_{\alpha^*}$  defined by :

$$(\Delta M)_{\alpha^*} = \sum_{i=1}^r p_i \frac{\partial M^{(e)}}{\partial p_i} \left( \frac{\Delta p_i}{p_i} \right)_{\alpha^*}$$

$$(\Delta K)_{\alpha^*} = \sum_{i=1}^r p_i \frac{\partial K^{(e)}}{\partial p_i} \left( \frac{\Delta p_i}{p_i} \right)_{\alpha^*}$$

#### 4.5 - Influence of the non-linearities

If the linear approximation introduced in the sensitivity method is acceptable, the estimated variations of the eigensolutions i.e., those specified by means of the sensitivity matrix :  $(\hat{b})_{\alpha^*} = S \left( \frac{\Delta p}{p} \right)_{\alpha^*}$ , must be close to the effective variations obtained through calculation of the exact solution of the new eigenvalue problem defined by the matrices :

$$M^{(e)} + (\Delta M)_{\alpha^*} ; K^{(e)} + (\Delta K)_{\alpha^*}$$

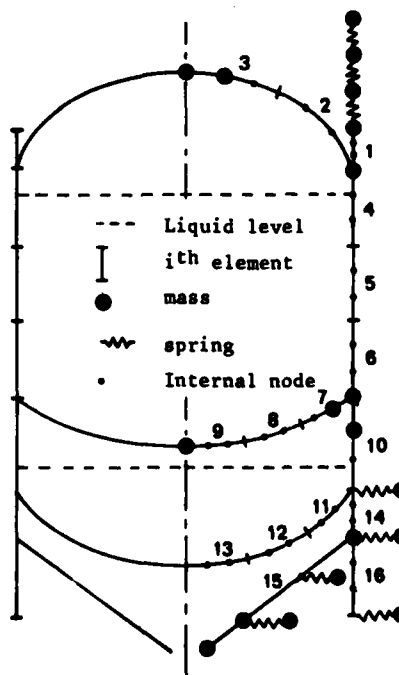
The observed differences arise essentially from the non linear terms that link the effective variations of the eigensolutions to the variations of the parameters. The introduction of the second order derivatives would notably limit these differences, but the resulting complexity

appears unacceptable to us, at least in the case of large systems. A more economical solution is obtained by arbitrarily reducing the norm of the modification vector  $\left( \frac{\Delta p}{p} \right)_{\alpha^*}$ , i.e. by replacing  $(\Delta p/p)_{\alpha^*}$  by  $\beta \left( \frac{\Delta p}{p} \right)_{\alpha^*}$  where  $\beta < 1$  - in practice  $\beta = 0.2$  to  $0.5$  -. The additional, corresponding matrices of inertia and stiffness are then calculated and the new eigenvalue problem is solved. These solutions serve as a starting point to a complete iteration of the localization and adjustment methods.

#### 5 - APPLICATIONS

The method was tested with numerical simulation, first, on simple elements, then, on industrial structures. We present 2 simulation examples illustrating its principle. We consider the axisymmetric vibrations of a tank composed of cylinders, ellipsoids and frustum of cones modelised in 16 distinct elements and 140 D.O.F's.

Its matrices of inertia  $M^{(e)}$  and stiffness  $K^{(e)}$  enable us to calculate the first seven eigenmodes of deformable body. We then dispose of an initial model  $M^{(e)} ; K^{(e)}$  whose partial



dynamic behavior is characterized by the diagonal spectral matrix  $\Lambda_1^{(e)}$  of order 7 and the rectangular modal matrix  $Y_1^{(e)}$  of order (140 x 7). The matrices  $Y_1^{(m)}$  (140 x 7) and  $\Lambda_1^{(m)}$  (7 x 7) simulating the measurement results are obtained by calculating the first 7 eigensolutions of the simulated identified model constructed by introducing a modification in the initial model. In this example, this modification consists of reducing by 20% Young's modulus of elements 11, 12 and 13.

In this case, the adjustment method must therefore enable us to solve the following problem. Knowing :

a) the first seven eigenvalues and eigenvectors (with 36 D.O.F. considered as unknown by eigenvector) of the simulated identified model,

b) the matrices of inertia and stiffness, and the first seven eigenvalues and eigenvectors of the initial model,

is it possible to determine :

a) the regions where the initial model differ from the simulated identified model,

b) the parametric modifications to be realized in the initial model in order to reduce simultaneously the differences between  $\Lambda_1^{(e)}$  and  $\Lambda_1^{(m)}$  on the one hand,  $Y_1^{(e)}$  and  $Y_1^{(m)}$  on the other hand.

The localization procedure underlines very clearly that the initial model and the simulated identified model differ in the regions of elements 11 and 12. The results obtained by applying the parametric modification method to these two elements are regrouped on the table below.

a) Adjustment of the eigenvalues. By

$$\frac{\Delta\lambda_v}{\lambda_v} = \frac{\lambda_v^{(m)} - \lambda_v^{(e)}}{\lambda_v^{(e)}} \quad v = 1, 2, \dots, 7$$

we show their relative variation.

$\left(\frac{\Delta\lambda_v}{\lambda_v}\right)_i$  represents the initial relative variation, i.e. the relative differences between the eigenvalues of the initial model and of the simulated identified model.

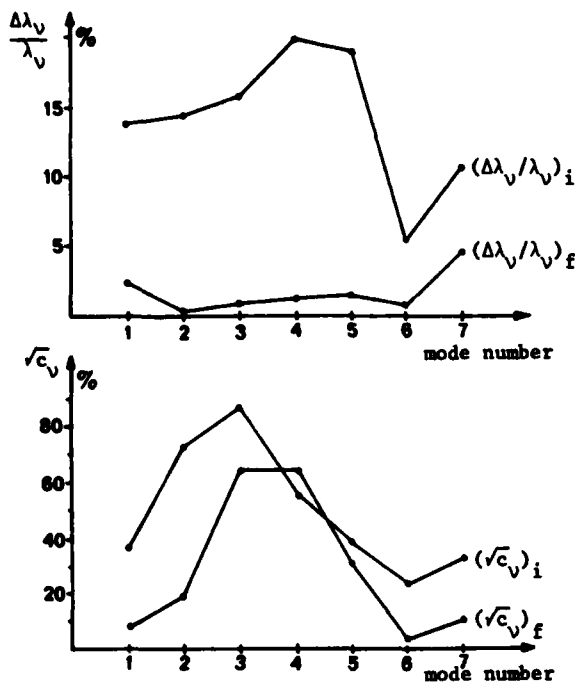
$\left(\frac{\Delta\lambda_v}{\lambda_v}\right)_f$  represents the final relative variation, i.e., the relative differences between the eigenvalues of the modified initial model  $(M^{(e)} + (\Delta M)_{\alpha\alpha}; K^{(e)} + (\Delta K)_{\alpha\alpha})$  and of the simulated identified model.

Eigenmode	$\sqrt{\lambda_v^{(e)}} \text{ (Hz)}$	$(\Delta\lambda_v/\lambda_v)_i$	$(\Delta\lambda_v/\lambda_v)_f$
1	33.15	$-13.6710^{-2}$	$-2.2310^{-2}$
2	37.09	$-14.3110^{-2}$	$-0.2510^{-2}$
3	39.05	$-15.7910^{-2}$	$-0.7810^{-2}$
4	40.15	$-19.8610^{-2}$	$-1.1810^{-2}$
5	41.11	$-18.9310^{-2}$	$-1.4810^{-2}$
6	43.90	$-5.0610^{-2}$	$-0.6710^{-2}$
7	60.72	$-10.5810^{-2}$	$-4.5710^{-2}$

b) Adjustment of the eigenvectors : their difference is characterized by the quadratic form  $c_v$  associated to the matrix  $M^{(e)}$  and formed by means of vectors  $\Delta y_v = y_v^{(m)} - y_v^{(e)}$

$$v = 1, 2, \dots, 7 : c_v = {}^T \Delta y_v M^{(e)} \Delta y_v = \|A_{11} e_v\|^2$$

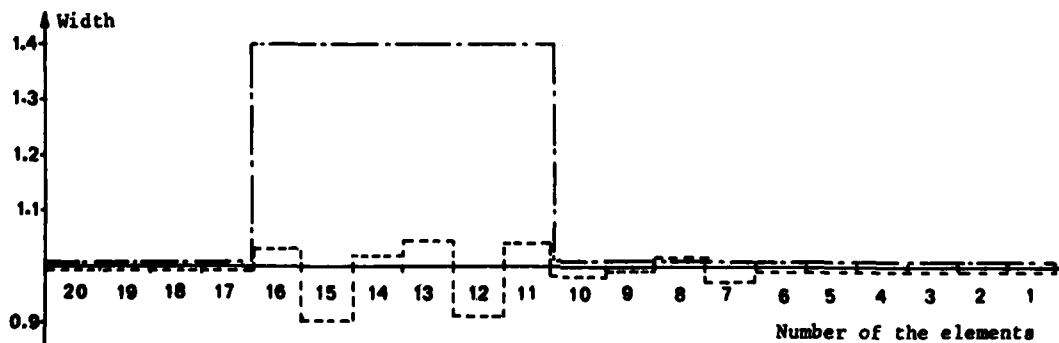
Eigenmode	$(\sqrt{c_v})_i$	$(\sqrt{c_v})_f$
1	$35.7910^{-2}$	$6.7110^{-2}$
2	$72.1910^{-2}$	$18.1210^{-2}$
3	$86.5910^{-2}$	$64.0310^{-2}$
4	$56.2310^{-2}$	$63.7910^{-2}$
5	$38.2710^{-2}$	$29.6110^{-2}$
6	$23.4910^{-2}$	$3.0110^{-2}$
7	$31.8210^{-2}$	$10.3510^{-2}$



These results are obtained without any iteration. The second example is a cantilever beam in transverse vibrations modeled in 20 elements with 2 D.O.F.'s per element. In this case :  $N = 40$  ;  $n = 5$ . We call the thickness and the width of the  $i^{\text{th}}$  element  $e_i$  and  $l_i$  respectively. The initial model is characterized by the following dimensions :

$$\begin{aligned} e_i &= e_0 & \text{for } i = 1, 2, \dots, 20 \\ l_i &= l_0 & \text{for } i = 1, 2, \dots, 10, 17, \dots, 20 \\ l_i &= 1.4 l_0 & \text{for } i = 11, 12, \dots, 16 . \end{aligned}$$

The repartition of the width and the thickness of the three models is described below :



The simulated identified model is characterized by the following dimensions :

$$e_i = e_0 ; l_i = l_0 ; \text{ for } i = 1, 2, \dots, 20 .$$

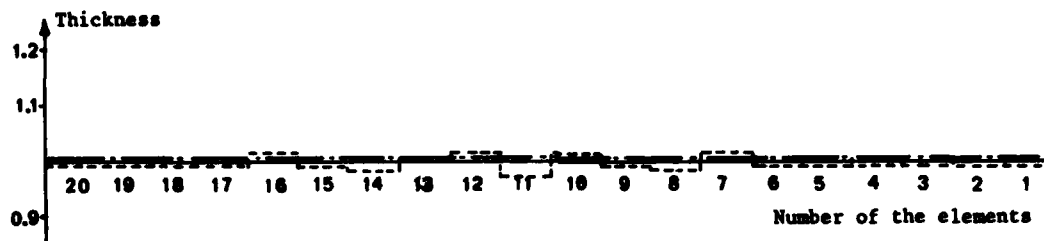
The following results are obtained with one iteration :

a) Adjustment of the eigenvalues :

Mode	$(\Delta\lambda_v/\lambda_v)_i$	$(\Delta\lambda_v/\lambda_v)_f$
1	$-7.71 \cdot 10^{-2}$	$0.69 \cdot 10^{-2}$
2	$6.01 \cdot 10^{-2}$	$0.09 \cdot 10^{-2}$
3	$3.52 \cdot 10^{-2}$	$-0.17 \cdot 10^{-2}$
4	$2.24 \cdot 10^{-2}$	$0.24 \cdot 10^{-2}$
5	$-0.03 \cdot 10^{-2}$	$-0.03 \cdot 10^{-2}$

b) Adjustment of the eigenvectors :

Mode	$(\sqrt{c_v})_i$	$(\sqrt{c_v})_f$
1	$2.80 \cdot 10^{-2}$	$0.79 \cdot 10^{-2}$
2	$11.54 \cdot 10^{-2}$	$0.63 \cdot 10^{-2}$
3	$14.82 \cdot 10^{-2}$	$0.69 \cdot 10^{-2}$
4	$8.24 \cdot 10^{-2}$	$0.43 \cdot 10^{-2}$
5	$10.37 \cdot 10^{-2}$	$0.49 \cdot 10^{-2}$



———: Initial model ( $M^{(e)}$  ;  $K^{(e)}$ )  
 - - - - : Simulated identified model ( $M^{(m)}$  ;  $K^{(m)}$ )  
 ..... : Initial model adjusted by the method ( $M^{(e)} + (\Delta M)_{\alpha}^*$  ;  $K^{(e)} + (\Delta K)_{\alpha}^*$ )

## 6 - CONCLUSIONS

The adjustment precision obtained from the set of test cases treated are very satisfactory. The method enables one to locate and correct the construction parameters initially modified for simulation. Random errors of  $\pm 2\%$  initially introduced on the identified eigensolution influence very slightly the localization process and the calculation of the modifications.

The extension of this method to the non conservative systems and to case of non symmetrical matrices makes up the continuation of this work and is the aim of present researches.

## BIBLIOGRAPHY

- [1] J.C.WHITE, B.D.MAYTUM : Eigensolution sensitivity to parametric model perturbation. Shock and Vibration, n°46 Part.5, pp.123-133
- [2] R.E.HULL, B.I.BEJMUH : Use of generalized mass contributions in correlation of test and analytical vibration modes. Shock and Vibration, Bulletin n°43, part.3, june 1973 p.79-86
- [3] DANEK O., Pouziti poruchovoho poctu v dynamickych ulohach, Strojnický Cassopis XXVI, 1975, c.5, pp.486-198
- [4] R.L.FOX, M.P.KAPOOR : Rates of change of eigenvalues and eigenvectors, AIAA Journal, vol.6, n°12, déc.1968, pp.2426-2429
- [5] LALLEMENT G., Modyfikacje własności dynamicznych układów lincowych, Dynamika maszyn, 1974, pp.49-133, Ossolineum, Warszawa, Polska.

(\*) This research was carried out under contract at the initiative of the CNES and in close collaboration with M. VEDRENNE.

(\*\*) Laboratoire de Mécanique Appliquée associé au C.N.R.S., Faculté des Sciences - 25030 BESANCON CEDEX.

FIRST-PASSAGE FAILURE PROBABILITY IN RANDOM VIBRATION  
OF STRUCTURES WITH RANDOM PROPERTIES

N. Nakagawa, R. Kawai  
Faculty of Engineering, Kobe University  
Kobe, Japan

and

K. Funahashi  
Kawasaki Heavy Industries, Ltd.  
Kobe, Japan

The first-passage failure problem is treated in random vibration of structures with damping, considered as a random variable. First, nonstationary responses are generally analyzed for random vibration of structures, which have random properties. Using the derivative method, statistical values of responses ( mean function and autocovariance function ) are obtained. Thereafter, the first-passage failure probability is considered. It is assumed that a structure with random properties is subjected to a weakly stationary random excitation. Applying the average technique, the Fokker-Plank and the Kolmogorov backward equations are derived. Then, the first-passage failure probability is obtained. From numerical examples, it is found that it is necessary to consider the influence of the structural random properties, since it increases the first-passage failure probability.

INTRODUCTION

In a structural response analysis, the ultimate purpose in using stochastic-process theory is to know the reliability of a structure which has been designed to withstand random excitations. In the stochastic treatments of structural responses, the first-passage failure probability that the absolute value of a random response will go beyond a safe domain for the first time, has been extensively under investigation because of its close relationship to the safe performance of systems.

Structures have random properties with respect to the cross-sectional area and mechanical properties etc. owing to errors in the manufacturing, heat-treatment, and measuring processes. In order to judge the reliability of structures more exactly, it is, therefore, necessary to treat the first-passage failure probability under consideration of random properties.

A excellent summary for the problem of a stationary narrow-band process with

a symmetric two-sided barrier has appeared in the papers by Yang and Shinozuka [1,2]. They have used the point-process approach. Gray [3] has investigated the moments of the distributive function of the first-passage time. Lennox [4] has obtained the distribution function of the nonstationary envelope first-passage time. The influence of the critical barrier's height on the value of  $P_f$  ( the probability of system failure ) was studied, in a nonstationary random vibration, by Roberts [5]. But, in these literatures, the random properties of structures are not considered. Authors [6-8] have investigated the longitudinal vibration and impact waves of an elastic bar, with random properties, and the impact waves in a viscoelastic bar, with stochastic properties.

This paper treats the first-passage failure probability in random vibration of structures, with random properties. First, nonstationary responses are generally analyzed for random vibration of structures, which have random properties. The stochastic differential equation of the system is described. Using the de-

relative method, the statistical values of responses ( mean function and autocovariance function ) are obtained. The damping coefficient is assumed as a structural random property. As an example, the responses of a single-degree-of-freedom system are calculated. This system consists of a mass connected to a Voigt model under a white noise excitation process. It is found that the standard deviations of responses increase with time and become constant after a long time. The contribution of the structural random property to the standard deviations of responses is ascertained.

Thereafter, the first-passage failure problem, which is the main theme in this paper, is treated. It is assumed that a structure with random properties is subjected to a weakly stationary random excitation. Then, the standard deviations of responses are derived. Introducing the change of variables of the amplitude and the phase, the elementary second-order equation is replaced by the two first-order equations. The analysis is an extension of Lennox's analysis. Applying the averaging technique, these equations are simplified and the Fokker-Planck equation is derived. Furthermore, the Kolmogorov backward equation is obtained. After the Kolmogorov backward equation is solved, under the given initial and boundary conditions, the transition probabilistic distributed function and the first-passage failure probability are obtained. Numerical examples are calculated and the first-passage failure probability and its density are obtained. Decreasing the barrier value, the first-passage failure probability becomes greater. It is found that it is necessary to consider the influence of the structural random properties, since it increases the first-passage failure probability.

#### NONSTATIONARY RESPONSES IN RANDOM VIBRATION OF STRUCTURES

##### General Analysis

Consider the nonstationary responses of structures, which have random properties, subjected to random excitations. The equation of motion to a single-degree-of-freedom system consisting of a mass connected to a Voigt model under random excitation  $F(t)$  is

$$\ddot{x}(t) + 2\zeta\omega_n\dot{x}(t) + \omega_n^2x(t) = \frac{1}{m}F(t) \quad (1)$$

where

$$\omega_n^2 = k/m, \quad \zeta = c/2m\omega_n$$

Letting  $x(0)=0$  as the initial condition without losing the generality, we obtain the solution of Eq.(1),

$$x(t) = \int_0^t F(\tau)h(t-\tau) d\tau \quad (2)$$

where

$$h(t) = \begin{cases} \frac{-j}{\sqrt{1-\zeta^2}\omega_n m} \exp(-\zeta+j\sqrt{1-\zeta^2}\omega_n t) & (t \geq 0) \\ 0 & (t \leq 0) \end{cases} \quad (3)$$

and

$$j = \sqrt{-1}$$

Considering the random properties of structures, the response is written as follows.

$$\left. \begin{aligned} x(t) &= E[x(t)] + \Delta x(t) \\ x(t) &\div \int \frac{\partial}{\partial p_1} x(t) \Delta p_1 \end{aligned} \right\} \quad (4)$$

where  $E[\cdot]$  is the mean function of  $[\cdot]$  and  $p_1$  is the statistical parameter. Considering Eq.(2), the impulse response function is rewritten as follows

$$\left. \begin{aligned} h(t) &= E[h(t)] + \Delta h(t) \\ \Delta h(t) &= \int \frac{\partial h(t)}{\partial p_1} \Delta p_1 \\ E[h(t)] &= h_0(t) \end{aligned} \right\} \quad (5)$$

Hence, the mean function and autocovariance function of  $x(t)$  are

$$E[x(t)] = \int_0^t E[F(\tau)]h_0(t-\tau) d\tau \quad (6)$$

$$\begin{aligned} K_x(t_1, t_2) &= \int_0^{t_1} \int_0^{t_2} K_F(\tau_1, \tau_2) \\ &\quad \times E[h(t_1-\tau_1)h(t_2-\tau_2)] d\tau_1 d\tau_2 \\ &= \int_0^{t_1} \int_0^{t_2} K_F h_0(t_1-\tau_1)h_0(t_2-\tau_2) d\tau_1 d\tau_2 \\ &\quad + \int_0^{t_1} \int_0^{t_2} K_F E[\Delta h(t_1-\tau_1)\Delta h(t_2-\tau_2)] d\tau_1 d\tau_2 \end{aligned} \quad (7)$$

If  $F(t)$  is a Gaussian random process,  $x(t)$  becomes a Gaussian random process, and then moment functions higher than the second order are equal to zero. The Gaussian random process is completely defined by Eqs.(6) and (7).

Letting the first term of Eq.(7) be  $K_{xF}$  and the second term be  $K_{xP}$ , we obtain



$$K_X(t_1, t_2) = K_{XF}(t_1, t_2) + K_{XP}(t_1, t_2) \quad (8)$$

#### Responses to Nonstationary Shot Noise Excitation

Although the nonstationary shot-noise process is simply mathematical idealization, justifications of such analysis to real problems have been found.

A nonstationary shot noise is given by

$$\left. \begin{aligned} F(t) &= \sum_{i=1}^N Y_i \delta(t - \tau_i) \\ E[F(t)] &= 0 \\ K_F(t_1, t_2) &= I(t_1) \delta(t_2 - t_1) \\ &= \lambda(t_1) E[Y^2] \delta(t_2 - t_1) \end{aligned} \right\} \quad (9)$$

where

- $N(t)$  : Poisson process with either stationary or nonstationary increments
- $Y_i$  : independent random variables with zero mean value
- $I(t)$  : intensity function of a shot noise
- $\lambda(t)$  : expected nonstationary arrival rate
- $\delta(t)$  : Dirac delta function.

Then, statistical value of responses are

$$E[x(t)] = 0 \quad (10)$$

$$\begin{aligned} K_{XF}(t_1, t_2) &= E[Y^2] \int_0^{t_1} \lambda(\tau_1) h_0(t_1 - \tau_1) \\ &\quad \times h_0(t_2 - \tau_1) d\tau_1 \\ &= \frac{E[Y^2]}{2m^2 \omega_d^2} e^{-\zeta \omega_0(t_1 + t_2)} \\ &\quad \times [\cos \omega_d(t_1 - t_2) \int_0^{t_1} \lambda(\tau_1) \\ &\quad \times e^{2\zeta \omega_0 \tau_1} d\tau_1 - \int_0^{t_1} \lambda(\tau_1) \\ &\quad \times e^{2\zeta \omega_0 \tau_1} \cos \omega_d(t_1 + t_2 - 2\tau_1) d\tau_1] \\ &\quad (t_2 \geq t_1) \quad (11) \end{aligned}$$

where

$$\omega_d = \sqrt{1 - \zeta^2} \omega_0$$

$$\begin{aligned} K_{X\zeta}(t_1, t_2) &= \frac{E[Y^2] \zeta \omega_0^3 \sigma_\zeta^2}{4m^2 \omega_d^2} \\ &\quad \times \int_{t_2 - t_1}^{t_2 + t_1} \lambda\left(\frac{t_1 + t_2 - \tau_1}{2}\right) e^{-\zeta \omega_0 \tau_1} \\ &\quad \times [(A_1 + A_2 \tau_1 + A_3 \tau_1^2) \cos \omega_d \tau_1 \\ &\quad + (A_4 + A_5 \tau_1 + A_6 \tau_1^2) \\ &\quad \times \sin \omega_d \tau_1 + A_7 \cos \omega_d(t_2 - t_1) \\ &\quad \times \tau_1^2 + (A_8 \cos \omega_d(t_2 - t_1) \\ &\quad + A_9 \sin \omega_d(t_2 - t_1) \\ &\quad \times \tau_1 + A_{10} \cos \omega_d(t_2 - t_1) \\ &\quad + A_{11} \sin \omega_d(t_2 - t_1)] d\tau_1 \\ &\quad (t_2 \geq t_1) \quad (12) \end{aligned}$$

(See Appendix I)

#### Responses to White Noise Excitation

A shot noise, which is weakly stationary random process, becomes a white noise because this random process has a constant spectral density. Examples of a weakly stationary random excitation are excitations of an automobile, travelling at a constant speed on a road having a weakly homogeneous random roughness and excitations which engines exert to the basis in steady motion.

A white noise is defined by the following properties.

$$\left. \begin{aligned} E[F(t)] &= 0 \\ K_F(t_1, t_2) &= 2\pi K \delta(t_1, t_2) \end{aligned} \right\} \quad (13)$$

The autocovariance function of responses are

$$\begin{aligned} K_{XF}(t_1, t_2) &= \frac{\pi K}{2m^2 \omega_0 \omega_d \zeta} [\cos \omega_d(t_1 - t_2) \\ &\quad \times e^{-\zeta \omega_0(t_1 + t_2)} (e^{2\zeta \omega_0 t_1 - 1}) - \frac{\zeta}{\omega_0} \\ &\quad \times [e^{-\zeta \omega_0(t_1 + t_2)} \{-\zeta \omega_0 \cos \omega_d(t_1 + t_2) \end{aligned}$$

$$\begin{aligned} & \pm \omega_d \sin \omega_d(t_1+t_2) \} - e^{-\zeta\omega_0(t_2-t_1)} \\ & \times \{ -\zeta\omega_0 \cos \omega_d(t_2-t_1) \\ & + \omega_d \sin \omega_d(t_2-t_1) \} \} \quad (14-a) \end{aligned}$$

$$\begin{aligned} K_{XP}(t_1, t_2) = \frac{\pi K \omega_0^2 \zeta \sigma_c^2}{2m^2 \omega_d^3} [ & \{ A_{10} \cos \omega_d \\ & \times (t_2-t_1) + A_{11} \sin \omega_d(t_2-t_1) \} Z_1 \\ & + \{ A_6 \cos \omega_d(t_2-t_1) + A_9 \sin \omega_d \\ & \times (t_2-t_1) \} Z_2 + A_7 \cos \omega_d(t_2-t_1) Z_3 \\ & + A_4 Z_4 + A_5 Z_5 + A_8 Z_6 + A_{12} Z_6 + \\ & + A_2 Z_7 + A_3 Z_8 ] \quad (14-b) \end{aligned}$$

( See Appendix II )

Setting  $t_1 = t_2$  in Eq.(14), we obtain the variance of responses,

$$\begin{aligned} \sigma_{XP}^2 = \frac{\pi K}{2m^2 \omega_d^3} [ & (1 - e^{-2\zeta\omega_0 t}) - \frac{\zeta}{\omega_0} \{ \zeta\omega_0 \\ & + e^{-2\zeta\omega_0 t} ( -\zeta\omega_0 \cos 2\omega_d t \\ & + \omega_d \sin 2\omega_d t ) \} ] \quad (15-a) \end{aligned}$$

$$\begin{aligned} \sigma_{XP}^2 = \frac{\pi K \omega_0^2 \zeta \sigma_c^2}{2m^2 \omega_d^3} ( & \hat{A}_{10} \hat{Z}_1 + \hat{A}_6 \hat{Z}_2 + \hat{A}_7 \hat{Z}_3 \\ & + \hat{A}_4 \hat{Z}_4 + \hat{A}_5 \hat{Z}_5 + \hat{A}_8 \hat{Z}_6 + \hat{A}_{12} \hat{Z}_6 \\ & + \hat{A}_2 \hat{Z}_7 + \hat{A}_3 \hat{Z}_8 ) \quad (15-b) \end{aligned}$$

where

$$\begin{aligned} \hat{A}_1 &= -\frac{\zeta\omega_0}{\omega_d^3}, \quad \hat{A}_2 = \frac{1}{\omega_d}, \quad \hat{A}_3 = \frac{1}{4}(\frac{\zeta\omega_0}{\omega_d} - \frac{\omega_d}{\zeta\omega_0}) \\ \hat{A}_4 &= 0, \quad \hat{A}_5 = -\frac{\zeta\omega_0}{\omega_d^2}, \quad \hat{A}_6 = \frac{1}{2}, \quad \hat{A}_{10} = -\hat{A}_1, \\ \hat{A}_7 &= \frac{1}{4} \frac{\omega_0}{\zeta\omega_d}, \quad \hat{A}_8 = -\frac{1}{\omega_d}, \quad \hat{A}_9 = 0 = \hat{A}_{11}, \end{aligned}$$

It is found that the variances are independent on  $t$  as  $t$  approaches  $+\infty$  in Eq. (14).

#### NUMERICAL EXAMPLES

Random responses of the next example were calculated. In a white noise excita-

tion process,

$$\text{spectral density } \Phi_P(\omega) = K \text{ (a constant)} \quad (16)$$

Values of statistical parameter and undamped natural frequency of the linear system are

$$E[\zeta] = 0, \quad \sigma_\zeta = 0.01 \text{ and } \omega_0 = 1 \text{ rad/s}$$

The standard deviation and the autocovariance of responses to the white noise excitation are illustrated in Fig.

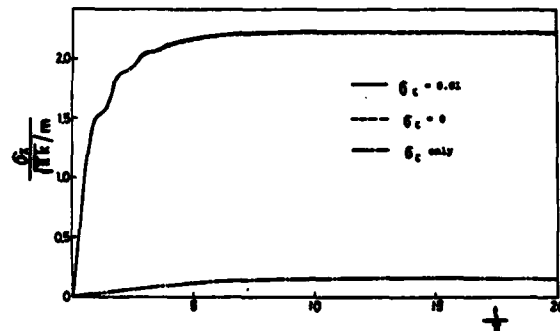


Fig.1-The standard deviation of responses to a white noise excitation.

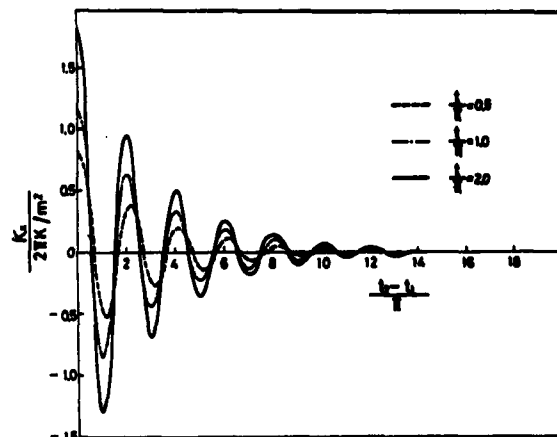


Fig.2 - The autocovariance of responses to a white noise excitation

1 and 2. In the case of the white noise excitation which is the weakly stationary excitation, the standard deviation of the response maintains constant, after a definite time. In fig. 1 the broken line denotes the standard deviation of the re-

sponse, when the influence of random property of the structure is neglected. The standard deviation of responses owing to  $\sigma_z$  only is also shown in Fig. 1.

The autocovariances have the frequency nearly equal to the undamped natural frequency of the system and it is, therefore, supposed that the spectral density of the autocovariance becomes greater when  $\omega$  tends to  $\omega_0$ ; indicating this the property of the white noise model.

#### FIRST-PASSAGE FAILURE

The important problem in using stochastic-process theory in a structural-response analysis is the first-passage failure problem. This problem treats the failure created when the dynamic response at a critical point in a structure, reaches for the first time, either an upper bound level or a lower bound level. In this section the first-passage failure of the structure, subjected to a weakly stationary random excitation, with random property will be considered.

#### Fundamental Equation

The equation of motion of the system is

$$\ddot{x}(t) + 2\zeta\omega_0\dot{x}(t) + \omega_0^2x(t) = \frac{F(t)}{m} \quad (17)$$

When  $F(t)$  is a wide-band excitation, the mean function and the autocorrelation function are

$$E[F(t)] = 0 \quad (18)$$

$$E[F(t_1)F(t_2)] = K_F(t_1 - t_2) \quad (19)$$

Further, the spectral density function is

$$\phi_F(\omega) = \frac{1}{2\pi} \int_{-\infty}^{\infty} K_F(t_2 - t_1) e^{-j\omega(t_2 - t_1)} \times d(t_2 - t_1) \quad (20)$$

When a lightly damped single-degree-of-freedom system is subjected to a wide-band stationary excitation, the stationary response is a narrow-band stationary process. The response has, therefore, zero mean function and the following variance.

$$\sigma_x^2 = \frac{\pi\phi_F(\omega_0)}{2\zeta\omega_0^3m^2} + \frac{\pi\sigma_z^2\phi_F(\omega_0)}{\zeta^2\omega_0^3m^2} \{ \zeta^4\omega_0^2\tilde{A}_1 + \zeta^2(2\zeta^2-1)\omega_0\tilde{A}_2 + \zeta^2\omega_0\omega_0\tilde{A}_0 \}$$

$$+ 2\zeta^4\omega_0\tilde{A}_3 + 2\zeta^2(4\zeta^2-1)\sqrt{1-\zeta^2}\tilde{A}_0 + 2\tilde{A}_7 + \zeta\omega_0\tilde{A}_8 + \zeta^2\omega_0^2\tilde{A}_{10} \}$$

$$= (V_F + V_z) \pi\phi_F(\omega_0) \quad (21)$$

(See Appendix III)

Let the envelope process of the response be  $a(t)$  and the phase angle be  $\psi(t)$ . When  $\zeta$  is small, it can be considered that the response is given as follows,

$$x(t) = a(t) \cos(\omega_0 t + \psi(t)) \quad (22)$$

$$\dot{x}(t) = -a(t) \omega_0 \sin(\omega_0 t + \psi(t)) \quad (23)$$

Substitution of the following statistical values of  $\zeta$ :

$$\left. \begin{aligned} \zeta &= (1+\epsilon) E[\zeta] \\ E[\zeta] &= 0 \\ \sigma_\zeta^2 &= E[(\zeta - E[\zeta])^2] \end{aligned} \right\} \quad (24)$$

into Eq.(17) yields

$$\ddot{x}(t) + 2E[\zeta]\omega_0(1+\epsilon)\dot{x}(t) + \omega_0^2x(t) = \frac{F(t)}{m} \quad (25)$$

Using Eqs.(22) and (23) we obtain

$$\dot{a} = \frac{1}{\omega_0 m} [ -\zeta\omega_0^2 m a (1+\epsilon) \{ 1 - \cos 2(\omega_0 t + \psi) \} - F(t) \sin(\omega_0 t + \psi) ] \quad (26)$$

$$a\dot{\psi} = \frac{1}{\omega_0 m} [ -\zeta\omega_0^2 m a (1+\epsilon) \sin 2(\omega_0 t + \psi) - F(t) \cos(\omega_0 t + \psi) ] \quad (27)$$

(See Appendix IV)

#### Fokker-Planck Equation

If the absolute value of the excitation  $F(t)$  is not so large, the envelope process of response changes very slowly and it is considered that both  $a(t)$  and  $\psi(t)$  change little during the first period  $0 \leq t \leq 2\pi/\omega_0$ . Then, by using the averaging technique into Eq.(26) and (27), we obtain

$$\dot{a}(t) = -\zeta\omega_0 a(1+\epsilon) - (F(t)/\omega_0 m)$$

$$x \sin (\omega_0 t + \psi) \quad (28)$$

and

$$\dot{\psi}(t) = -\frac{1}{\omega_0 m a} F(t) \cos (\omega_0 t + \psi) \quad (29)$$

By using the ensemble average and the fluctuating components, the terms containing the excitation process are re-written as follows,

$$(F(t)/\omega_0 m) \sin (\omega_0 t + \psi) = m_1(t) + v_1(t) \quad (30)$$

and

$$(F(t)/\omega_0 m a) \cos (\omega_0 t + \psi) = m_2(t) + v_2(t) \quad (31)$$

where

$$m_1(t) = -\frac{\pi \Phi(\omega_0)}{2a\omega_0^2 m^2} + \text{stationary term},$$

$$m_2(t) = 0 + \text{stationary term}$$

Omitting the stationary term in Eqs.(30) and (31) gives

$$\dot{a}(t) = -\zeta \omega_0^2 a(1+\epsilon) + \frac{\pi \Phi(\omega_0)}{2a\omega_0^2 m^2} - v_1(t) \quad (32)$$

and

$$\dot{\psi}(t) = -v_2(t) \quad (33)$$

The response process to the wide-band noise excitation becomes the narrow-band, if the correlation time of the excitation process is smaller than  $1/\zeta \omega_0(1+\epsilon)$ , since the relaxation time of the envelope process, in Eq.(32), is of order  $1/\zeta \omega_0(1+\epsilon)$ . Hence, the fluctuating component  $v(t)$  can be regarded as the delta correlation process and we obtain

$$\dot{a} = -\zeta \omega_0 a(1+\epsilon) + \frac{\pi \Phi_F(\omega_0)}{2a\omega_0^2 m^2} - \frac{\sqrt{\pi \Phi_F(\omega_0)}}{\omega_0 m} \times D(t) \quad (34)$$

and

$$\dot{\psi} = \frac{\sqrt{\pi \Phi_F(\omega_0)}}{\omega_0 m a} D(t) \quad (35)$$

where  $D(t)$  is the delta correlation process, i.e.,

$$E[D(t)D(t+\tau)] = \delta(\tau) \quad (36)$$

Introducing the nondimensional quantity  $r = a/\sigma_x$ , Eq.(34) becomes

$$\dot{r} = -\zeta \omega_0(1+\epsilon)r + \frac{1}{2r\omega_0^2 m^2(V_F+V_\zeta)} - \frac{1}{\omega_0 m \sqrt{V_F+V_\zeta}} D(t) \quad (37)$$

Using Eq.(37), the Fokker-Planck equation can be given as follows,

$$\frac{\partial}{\partial t} p_{\{r\}} = \frac{\partial}{\partial r} \left[ \zeta \omega_0(1+\epsilon) \left\{ r - \frac{1}{2\zeta \omega_0^2 m^2(V_F+V_\zeta)r} \right\} p_{\{r\}} \right] + \frac{1}{2\omega_0^2 m^2(V_F+V_\zeta)} \frac{\partial^2}{\partial r^2} p_{\{r\}} \quad (38)$$

where  $p_{\{r\}}(r, r_0; t, t_0)$  is the transition probability density of  $r(t)$ .

#### First-Passage Failure Probability

From Eq.(38), the Kolmogorov backward equation is

$$\frac{\partial p}{\partial t} = -\zeta \omega_0(1+\epsilon) \left\{ r_0 - \frac{1}{2\zeta \omega_0^2 m^2(V_F+V_\zeta)r_0} \right\} \times \frac{\partial p}{\partial r_0} + \frac{1}{2\omega_0^2 m^2(V_F+V_\zeta)} \frac{\partial^2 p}{\partial r_0^2} \quad (39)$$

In order to simplify the analysis, the following change of variables is made,

$$S_0 = \frac{r_0}{\alpha}, \quad r_0 = \frac{a(\tau_0)}{\sigma_x}, \quad \tau = \zeta \omega_0 t, \quad b = \alpha \sigma_x \text{ and } V = 2\zeta \omega_0^2 m^2(V_F+V_\zeta) \quad (40)$$

where  $b$  is the threshold level. Equation (39) now becomes

$$\frac{\partial p}{\partial \tau} = - (1+\epsilon) \left\{ S_0 - \frac{1}{\alpha^2(1+\epsilon)VS_0} \right\} \frac{\partial p}{\partial S_0} + \frac{1}{\alpha^2 V} \frac{\partial^2 p}{\partial S_0^2} \quad (41)$$

When  $P(S_0, \tau)$  is the transition probabilistic distributive function given by the transition probability density  $p(S, S_0; \tau, \tau_0)$ ,

we obtain

$$P(S_0, \tau) = \int_0^1 p(S, S_0; \tau, \tau_0) dS$$

and

$$\tau_0 = 0 \quad (42)$$

The initial and boundary conditions are set as following,

$$\left. \begin{aligned} P(S_0, 0) &= 1 \\ P(S_0, \infty) &= 0 \\ P(1, \tau) &= 0 \\ P(0, \tau) &< \infty \end{aligned} \right\} \quad (43)$$

Integrating Eq.(41) with respect to  $S$  gives

$$\frac{\partial P}{\partial \tau} = -(1+\epsilon) \left\{ S_0 - \frac{1}{\alpha^2(1+\epsilon)VS_0} \right\} \frac{\partial P}{\partial S_0} + \frac{1}{\alpha^2 V} \frac{\partial^2 P}{\partial S_0^2} \quad (44)$$

Thereafter, consider the statistical parameter  $\epsilon$ . Approximating

$$|\epsilon| \leq \sigma_\zeta / \zeta \quad (45)$$

we obtain

$$\frac{\partial P}{\partial \tau} = -(1 \pm \frac{\sigma_\zeta}{\zeta}) \left\{ S_0 - \frac{1}{\alpha^2(1 \pm \sigma_\zeta / \zeta)VS_0} \right\} \frac{\partial P}{\partial S_0} + \frac{1}{\alpha^2 V} \frac{\partial^2 P}{\partial S_0^2} \quad (46)$$

It is considered that the probabilistic distribution  $P$  exists in the region bounded by the two solutions of Eq.(46). Since Eq.(46) indicates two equations, each one, with different coefficients, the first equation will be treated.

The introduction of the following new parameters,

$$\left. \begin{aligned} y &= \frac{(1+\sigma_\zeta/\zeta)\alpha^2 V}{2} S_0^2 \\ t_1 &= 2(1+\sigma_\zeta/\zeta)\tau \end{aligned} \right\} \quad (47)$$

leads to the next equation,

$$\frac{\partial P}{\partial t_1} = (1-y) \frac{\partial P}{\partial y} + y \frac{\partial^2 P}{\partial y^2} \quad (48)$$

Initial and boundary conditions are

$$\left. \begin{aligned} P(y, 0) &= 1, \\ P\left(\frac{(1+\sigma_\zeta/\zeta)\alpha^2 V}{2}, t_1\right) &= 0 \\ P(0, t_1) &< \infty \end{aligned} \right\} \quad (49)$$

and

Using the technique of separation of variables,

$$P(y, t_1) = Y(y) \cdot T(t_1) \quad (50)$$

we obtain

$$\frac{\dot{T}}{T} = (1-y) \frac{Y'}{Y} + y \frac{Y''}{Y} = -\lambda \quad (51)$$

where the dot denotes the differentiation with respect to the time  $t_1$ , and the prime denotes the differentiation with respect to  $y$ .

From Eq.(51) we obtain

$$T = T_0 e^{-\lambda t_1} \quad (52)$$

$$yY'' + (1-y)Y' + \lambda Y = 0 \quad (53)$$

The series solution of Eq.(53) is the confluent hypergeometric function given as follows:

$$\begin{aligned} Y &= {}_1F_1(\lambda, 1, y) \\ &= 1 + \sum_{n=1}^{\infty} \frac{(-\lambda)(1-\lambda) \cdots (n-1-\lambda)}{(n!)^2} y^n \end{aligned} \quad (54)$$

Using Eq.(49-2), the eigenvalue  $\lambda$  is obtained from the next equation,

$${}_1F_1(-\lambda_n, 1, \frac{(1+\sigma_\zeta/\zeta)\alpha^2 V}{2}) = 0 \quad (55)$$

Hence, the general solution is

$$\begin{aligned} P(y, t_1) &= \sum_{n=1}^{\infty} \beta_n {}_1F_1(-\lambda_n, 1, y) e^{-\lambda_n t_1} \\ &\quad \left( 0 < y < \frac{(1+\sigma_\zeta/\zeta)\alpha^2 V}{2} \right) \end{aligned} \quad (56)$$

Coefficients  $\beta_n$  in Eq.(56) are given by Eq.(49-1). Thus, the required distribution function of the first-passage failure probability is obtained by the next equation,

$$F(y, t_1) = 1 - P(y, t_1) \quad (57)$$

and the first-passage probabilistic density function is

$$f(y, t_1) = \sum_{n=1}^{\infty} \beta_n \lambda_{n1} F_1(-\lambda, 1, y) e^{-\lambda_n t_1} \quad (58)$$

$$\left( 0 < y < \frac{1 + \sigma_{\zeta} / \zeta \alpha^2 V}{2} \right)$$

The moments are

$$m_k = \int_0^{\infty} t_1^k f(y, t_1) dt_1 \quad (59)$$

#### NUMERICAL EXAMPLE AND DISCUSSIONS

The following values were used in order to calculate the distribution functions and the density functions of the first-passage failure,

$$E[\zeta] = 0.02, \sigma_{\zeta} = 0.1 E[\zeta].$$

$$\omega_0 = 2 \text{ rad/s},$$

$$\text{initial conditions: } t=0, x(0)=0,$$

and

$$\text{threshold value: } b = \sigma_x, 2\sigma_x \text{ and } 3\sigma_x.$$

The first-passage failure distributive functions are illustrated in Fig.3 for the threshold values,  $b = \sigma_x$ ,  $2\sigma_x$  and  $3\sigma_x$ .

When the threshold value is taken to be small, the first-passage failure distributive function increases rapidly to 1. The results which neglect the influence of the structural random property are indicated by the broken lines for three values, respectively. These lines exist between the solid lines obtained for  $\sigma_{\zeta} = 0.1 E[\zeta]$ . Yang and Shinozuka [1,2]

have investigated the first-passage failure problem by using the point process which was assumed by the Poisson, Pseudo-Gaussian, and Markov types etc. They have concluded that the Markov process which was used in this paper, is the best approximation. For a greater threshold value, the area of oblique line becomes wide. This indicates that the influence of the structural random property is im-

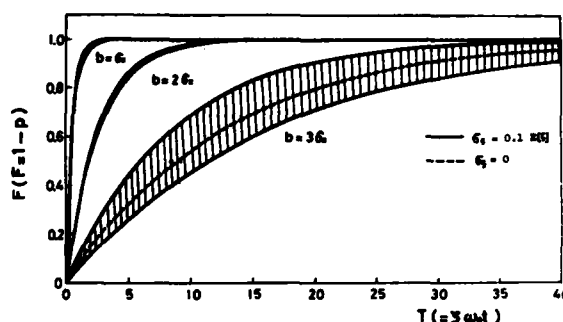


Fig.3 - The first-passage failure probability distributive function

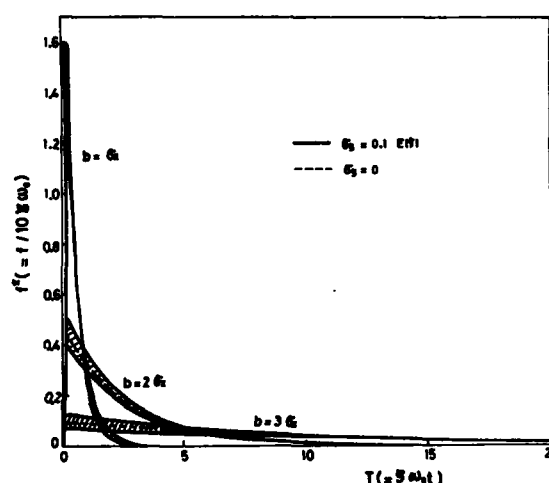


Fig.4 - The first-passage failure probability density

portant for this value.

The first-passage failure probability functions are shown in Fig.4 for three threshold values,  $b = \sigma_x$ ,  $2\sigma_x$  and  $3\sigma_x$ . The density function has the remarkable extreme value for  $b = \sigma_x$ .

#### REFERENCES

- 1 J.N. Yang and M. Shinozuka, "On the First-Excursion Probability in Stationary Narrow-Band Vibration I" J. Appl. Mech., Vol.38, Trans. ASME, Vol.93, Series E, pp. 1017-1022, 1971.
- 2 J.N. Yang and M. Shinozuka, "On the First-Excursion Probability in Stationary

AD-A148 084

THE SHOCK AND VIBRATION BULLETIN PART 3 STRUCTURAL  
ANALYSIS FATIGUE(U) NAVAL RESEARCH LAB WASHINGTON DC  
SHOCK AND VIBRATION INFORMATION CENTER SEP 78

2/2

UNCLASSIFIED

BULL-48-PT-3

F/G 20/11

NL

END

RECEIVED

DATE





Narrow-Band Vibration II; J. Appl. Mech., Vol. 39, Trans. ASME, Vol. 94, Series E, pp. 733-738, 1972.

3 A.H. Gray Jr., "First-Passage Time in a Random Vibration System; J. Appl. Mech., Vol. 33, Trans. ASME, Vol. 88, Series E, pp. 187-191, 1966.

4 W.C. Lennox and D.A. Fraser, "On the First-Passage Distribution for the Envelope of a Nonstationary Narrow-Band Stochastic Process; J. Appl. Mech., Vol. 41, Trans. ASME, Vol. 96, Series E, pp. 793-799, 1974.

5 J.B. Roberts, "Probability of First-Passage Failure for Nonstationary Random Vibration; J. Appl. Mech., Vol. 42, Trans. ASME, Vol. 97, Series E, pp. 716-720, 1975.

6 N. Nakagawa, T. Inagaki, T. Iwatsubo and R. Kawai, "The Longitudinal Vibration of a Bar with Random Properties; Memoirs of the Faculty of Engineering, Kobe Univ., No. 19, pp. 105-120, 1973.

7 N. Nakagawa, T. Iwatsubo and R. Kawai, "Longitudinal Impact Waves of an Elastic Bar with Random Properties; Trans. Japan Soc. Mech. Engrs. (in Japanese), Vol. 40, No. 338, pp. 2776-2783, 1974.

8 N. Nakagawa, I. Kawahara, T. Iwatsubo and R. Kawai, "Statistic Analysis of Impact Waves in Random Viscoelastic Rods; Theoretical and Appl. Mech., Vol. 25, pp. 187-197, 1977, Proceedings of the 25th Japan National Congress for Applied Mechanics, 1975.

#### Appendix I

$$A_1 = B_{11} - \frac{C_{11}}{2}(t_1+t_2) + \frac{D_{11}}{4}(t_1+t_2)^2$$

$$A_2 = \frac{C_{11}}{2} - \frac{D_{11}}{2}(t_1+t_2)$$

$$A_3 = \frac{D_{11}}{4}$$

$$A_4 = E_{12} - \frac{F_{12}}{2}(t_1+t_2) + \frac{(t_1+t_2)^2}{2}$$

$$A_5 = \frac{F_{12}}{2} - (t_1+t_2)$$

$$A_6 = \frac{1}{2}$$

$$A_7 = \frac{D_{12}}{4}$$

$$A_8 = \frac{C_{12}}{2} - \frac{D_{12}}{2}(t_1+t_2)$$

$$A_9 = -\frac{F_{12}}{2}$$

$$A_{10} = B_{12} - \frac{C_{12}}{2}(t_1+t_2) + \frac{D_{12}}{4}(t_1+t_2)^2$$

$$A_{11} = -E_{11} + \frac{F_{11}}{2}(t_1+t_2)$$

$$B_{11} = \frac{\zeta\omega_0}{\omega_d} t_1 t_2 \pm \frac{\omega_d}{\zeta\omega_0} T_1 T_2$$

$$C_{11} = \frac{\zeta\omega_0}{\omega_d} (t_1+t_2) \pm \frac{\omega_d}{\zeta\omega_0} (T_1+T_2)$$

$$D_{11} = \frac{\zeta\omega_0}{\omega_d} \pm \frac{\omega_d}{\zeta\omega_0}$$

$$E_{11} = T_1 t_2 \pm T_2 t_1$$

$$F_{11} = (T_1+t_2) \pm (T_2+t_1)$$

$$T_1 = t_1 - \frac{\zeta\omega_0}{\omega_d^2}$$

$$T_2 = t_2 - \frac{\zeta\omega_0}{\omega_d^2}$$

#### Appendix II

$$Z_1(t_1, t_2) = \frac{-1}{\zeta\omega_0} \{ e^{-\zeta\omega_0(t_1+t_2)} - e^{-\zeta\omega_0(t_2-t_1)} \}$$

$$Z_2(t_1, t_2) = \frac{-1}{\zeta^2\omega_0^2} [ \{ 1 + \zeta\omega_0(t_1+t_2) \} \times e^{-\zeta\omega_0(t_1+t_2)} - \{ 1 + \zeta\omega_0(t_2-t_1) \} \times e^{-\zeta\omega_0(t_2-t_1)} ]$$

$$Z_3(t_1, t_2) = \frac{-1}{\zeta^3\omega_0^3} [ \{ 1 + \{ 1 + \zeta\omega_0(t_1+t_2) \}^2 \} \times e^{-\zeta\omega_0(t_1+t_2)} - \{ 1 + \{ 1 + \zeta\omega_0(t_2-t_1) \}^2 \} \times e^{-\zeta\omega_0(t_2-t_1)} ]$$

$$Z_4(t_1, t_2) = \frac{1}{\omega_0^3} e^{-\zeta\omega_0(t_2-t_1)} \{ \zeta\omega_0 \times \sin \omega_d(t_2-t_1) + \omega_d \cos \omega_d(t_2-t_1) \} - \frac{1}{\omega_0^3} e^{-\zeta\omega_0(t_1+t_2)} \{ \zeta\omega_0 \sin \omega_d(t_1+t_2) + \omega_d \cos \omega_d(t_1+t_2) \}$$

$$Z_5(t_1, t_2) = \frac{1}{\omega_0^4} (t_2-t_1) e^{-\zeta\omega_0(t_2-t_1)} \times \{ \zeta\omega_0 \sin \omega_d(t_2-t_1) + \omega_d \cos \omega_d(t_2-t_1) \} + \frac{1}{\omega_0^4} e^{-\zeta\omega_0(t_2-t_1)} \times \cos \omega_d(t_2-t_1) + \frac{1}{\omega_0^4} e^{-\zeta\omega_0(t_1+t_2)} \times \{ (\zeta^2\omega_0^2 - \omega_d^2) \sin \omega_d(t_2-t_1) + 2\zeta\omega_0\omega_d \cos \omega_d(t_2-t_1) \} - \frac{1}{\omega_0^4} (t_1+t_2)$$

$$\begin{aligned}
& x e^{-\zeta\omega_0(t_1+t_2)} \{ \zeta\omega_0 \sin \omega_d(t_1+t_2) \\
& + \omega_d \cos \omega_d(t_1+t_2) \} - \frac{1}{\omega_0^2} e^{-\zeta\omega_0(t_1+t_2)} \\
& x \{ (\zeta^2\omega_0^2 - \omega_d^2) \sin \omega_d(t_1+t_2) \\
& + 2\zeta\omega_0\omega_d \cos \omega_d(t_1+t_2) \} \\
Z_6(t_1, t_2) &= \frac{1}{\omega_0^2} e^{-\zeta\omega_0(t_2-t_1)} \{ \zeta\omega_0 \\
& x \cos \omega_d(t_2-t_1) - \omega_d \sin \omega_d(t_2-t_1) \} \\
& - \frac{1}{\omega_0^2} e^{-\zeta\omega_0(t_1+t_2)} \{ \zeta\omega_0 \cos \omega_d(t_1+t_2) \\
& - \omega_d \sin \omega_d(t_1+t_2) \} \\
Z_7(t_1, t_2) &= \frac{1}{\omega_0^2} (t_2-t_1) e^{-\zeta\omega_0(t_2-t_1)} \\
& x \{ \zeta\omega_0 \cos \omega_d(t_2-t_1) - \sin \omega_d(t_2-t_1) \\
& x \omega_d \} + \frac{1}{\omega_0^2} e^{-\zeta\omega_0(t_2-t_1)} \{ (\zeta^2\omega_0^2 - \omega_d^2) \\
& x \cos \omega_d(t_2-t_1) - 2 \sin \omega_d(t_2-t_1) \\
& x \zeta\omega_0\omega_d \} - \frac{1}{\omega_0^2} (t_1+t_2) e^{-\zeta\omega_0(t_1+t_2)} \\
& x \{ \zeta\omega_0 \cos \omega_d(t_1+t_2) - \sin \omega_d(t_1+t_2) \\
& x \omega_d \} - \frac{1}{\omega_0^2} e^{-\zeta\omega_0(t_1+t_2)} \{ (\zeta^2\omega_0^2 - \omega_d^2) \\
& x \cos \omega_d(t_1+t_2) - 2\zeta\omega_0\omega_d \\
& x \sin \omega_d(t_1+t_2) \}
\end{aligned}$$

$$\begin{aligned}
Z_8(t_1, t_2) &= (t_1+t_2) G_1(t_1+t_2) \\
& - (t_2-t_1) G_1(t_2-t_1) + \frac{1}{\omega_0^2} \{ \zeta\omega_0 \\
& x Z_5(t_1, t_2) + \omega_d Z_7(t_1, t_2) \} + \frac{1}{\omega_0^2} \\
& x \{ (\zeta^2\omega_0^2 - \omega_d^2) Z_4(t_1, t_2) + 2\zeta\omega_0\omega_d \\
& x Z_6(t_1, t_2) \}
\end{aligned}$$

$$\begin{aligned}
Z_9(t_1, t_2) &= (t_1+t_2) G_2(t_1+t_2) \\
& - (t_2-t_1) G_2(t_2-t_1) + \frac{1}{\omega_0^2} \{ \zeta\omega_0 \\
& x Z_7(t_1, t_2) - \omega_d Z_5(t_1, t_2) \} + \frac{1}{\omega_0^2} \\
& x \{ -(\zeta^2\omega_0^2 - \omega_d^2) Z_6(t_1, t_2) \\
& + 2\zeta\omega_0\omega_d Z_4(t_1, t_2) \} \\
G_1(t) &= \frac{-1}{\omega_0^2} t e^{-\zeta\omega_0 t} (\zeta\omega_0 \sin \omega_d t \\
& + \omega_d \cos \omega_d t) - \frac{1}{\omega_0^2} e^{-\zeta\omega_0 t} \{ (\zeta^2\omega_0^2 - \omega_d^2)
\end{aligned}$$

$$\begin{aligned}
& x \sin \omega_d t + 2\zeta\omega_0\omega_d \cos \omega_d t \} \\
G_2(t) &= \frac{1}{\omega_0^2} t e^{-\zeta\omega_0 t} (-\zeta\omega_0 \cos \omega_d t \\
& + \omega_d \sin \omega_d t) - \frac{1}{\omega_0^2} e^{-\zeta\omega_0 t} \{ (\zeta^2\omega_0^2 - \omega_d^2) \\
& x \cos \omega_d t - 2\zeta\omega_0\omega_d \sin \omega_d t \}
\end{aligned}$$

### Appendix III

Let  $R_x(t_2-t_1)$  be the auto correlation function. When  $t \rightarrow \infty$ , we obtain

$$\begin{aligned}
\sigma_x^2 &= E[x^2(t)] = R_x(0) \\
&= \int_{-\infty}^{\infty} |H(\omega)|^2 \Phi_F(\omega) d\omega \quad (60)
\end{aligned}$$

where  $H(\omega)$  is the transfer function. In the case of a wide-band noise where the spectral density function changes slowly near at  $\omega = \pm\omega_0$  (undamped natural frequency), the value of the spectral density function can be neglected in the region far from  $\omega = \pm\omega_0$ . For  $\zeta \ll 1$ , we can rewrite Eq.(60) into

$$\sigma_x^2 \approx \Phi_F(\omega_0) \int_{-\infty}^{\infty} |H(\omega)|^2 d\omega \quad (61)$$

Using Eqs.(61) and (15), we obtain Eq.(21).

### Appendix IV

Differentiating Eq.(22) with respect to  $t$  gives

$$\begin{aligned}
\dot{x}(t) &= \dot{a} \cos(\omega_0 t + \psi) - a\omega_0 \sin(\omega_0 t + \psi) \\
& - \dot{\psi} a \sin(\omega_0 t + \psi) \quad (62)
\end{aligned}$$

Letting Eq.(62) be equal to Eq.(23), we obtain

$$\begin{aligned}
\dot{a} \cos(\omega_0 t + \psi) - \dot{\psi} a \sin(\omega_0 t + \psi) &= 0 \\
(63)
\end{aligned}$$

Further, differentiating Eq.(23) with respect to  $t$ , we obtain

$$\begin{aligned}
\ddot{x}(t) &= -\dot{a}\omega_0 \sin(\omega_0 t + \psi) - a\omega_0(\omega_0 + \dot{\psi}) \\
& x \cos(\omega_0 t + \psi) \quad (64)
\end{aligned}$$

Substituting Eq.(64) into Eq.(25) and using Eq.(63), Eq.(27) is obtained.

# FATIGUE

## FRACTURE MECHANICS APPLIED TO STEP-STRESS FATIGUE UNDER SINE/RANDOM VIBRATION

Ronald G. Lambert  
General Electric Company  
Aircraft Equipment Division  
Utica, New York 13503

A proposed cumulative fatigue damage law is derived which uses fracture mechanics theory as its basis in order to predict the fatigue life of structures subjected to several levels of sequentially applied stress. The proposed law applies to all initial crack (i.e., flaw) sizes in the structure. The proper boundary condition to be imposed at the interface of the two stress regions is analyzed.

### INTRODUCTION

This paper deals primarily with predicting fatigue life and/or probability of failure of structures with either known or undetected initial cracks (flaws) that are subjected to step-stress sinusoidal or random vibration. An example is an electronic assembly (e.g., an avionics computer) that is first subjected to a laboratory random vibration acceptance test and subsequently subjected to the in-flight random vibration of a high performance jet aircraft.

Initial cracks (flaws) either exist in the structural material as dislocations or metallurgical inclusions or are introduced during manufacturing fabrication or assembly operations. Initial crack sizes can range from microscopic to macroscopic. Such initial cracks reduce fatigue life. The larger the crack size, the shorter the fatigue life.

In some cases relatively large initial cracks go undetected for a variety of reasons. In other cases it is impractical to repair the crack or replace the part even if the crack is detected. These situations occur frequently enough to be of practical importance. Fracture Mechanics is the study of a material's ability to withstand such initial cracks and not fail catastrophically. Existing cumulative fatigue damage laws (e.g., Miner's linear cycle ratio law) do not attempt

to include the effects of initial cracks in the material being stressed.

### FRACTURE MECHANICS

Linear Elastic Fracture Mechanics theory will be used for this analysis to relate applied stress, crack geometries, material properties, and crack growth. Fig. 1 shows a particular loading and crack configuration. The specimen width is  $2b$ . In this article, the crack half-length,  $a$ , will be referred to as the crack length to simplify the wording. The actual crack length is,  $2a$ . The stress away from the vicinity of the crack is  $S$ .  $\Delta S$  is the stress range; that is, it is the double amplitude of the sinusoidal stress variation with time. Static stresses are not included.  $Y$  is a dimensionless geometrical parameter that depends on the dimensions of this particular configuration.

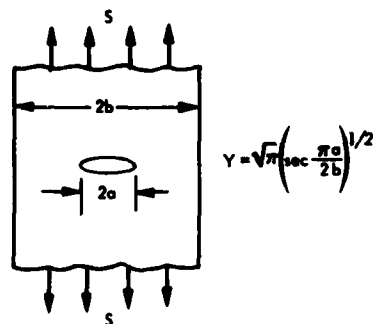


Fig. 1. Center Cracked Strip Loaded in Tension

$$Y = \sqrt{\pi} \left( \sec \frac{\pi a}{2b} \right)^{1/2} \quad (1)$$

The stress intensity range  $\Delta K$  is a function of  $Y$ ,  $\Delta S$ , and the crack size.

$$\Delta K = Y \Delta S \sqrt{a} \quad (2)$$

MPa  $\sqrt{\text{metre}}$  (ksi  $\sqrt{\text{in.}}$ )

Fig. 2 shows a typical cyclic fatigue crack growth rate curve as a function of stress intensity range.  $N$  is the number of applied stress cycles. There is a threshold value  $\Delta K_{th}$  below which cracks will not propagate. Eq. (2) indicates that  $\Delta K_i$  (the product of  $Y$ ,  $\Delta S$ , and the square root of the initial crack size) must be less than  $\Delta K_{th}$  for the crack to be in the nonpropagating region. For larger values of  $\Delta K$ , the curve becomes a straight line on the log-log plot. This is the stable crack growth region. The governing equation is that of Paris 1, 2:

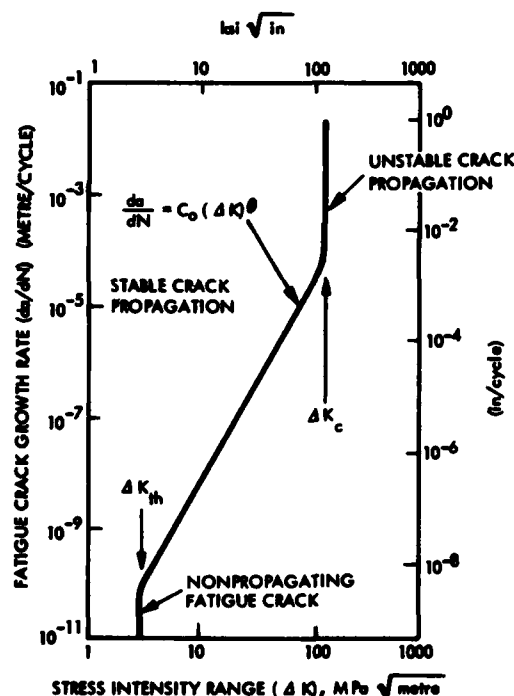


Fig. 2. Typical Fatigue Crack Growth Rate as a Function of Stress Intensity Range

$$\frac{da}{dN} = C_0 (\Delta K)^\theta \quad \text{metre/cycle} \quad (3)$$

(in./cycle)

where  $\theta$  and  $C_0$  are equation constants.

The crack will grow in a stable fashion until  $\Delta K$  reaches the material's critical value  $\Delta K_c$  (fracture toughness) at which time the crack growth becomes unstable and the part fails catastrophically. Table 1 shows several typical material parameters.

Eq. (3) can be integrated by substituting Eq. (2) for  $\Delta K$ , by separating variables, and letting  $\theta$  and  $Y$  be constants. The case of interest for this paper is for  $\theta > 2$ . The result is

$$N = \frac{2}{C_0 \Delta S^\theta Y^\theta (\theta - 2)} \quad (4)$$

$$\left[ \left( \frac{1}{a_i} \right)^{\frac{\theta-2}{2}} - \left( \frac{1}{a} \right)^{\frac{\theta-2}{2}} \right] \text{ cycles}$$

or

$$a = \left[ \left( \frac{1}{a_i} \right)^{\frac{\theta-2}{2}} - \frac{(\theta-2) C_0 \Delta S^\theta Y^\theta N}{2} \right]^{-\frac{2}{\theta-2}} \quad (5)$$

$$\text{metre (inches)}$$

where  $a_i$  = initial crack size (length)

$a$  = crack size at  $N$  cycles

It should be noted that these equations apply in the stable crack growth region (i.e.,  $\Delta K_{th} < \Delta K < \Delta K_c$ )

The critical crack size  $a_c$  where unstable crack growth occurs can be calculated using Eq. (5) by letting  $N = N_f$ , where  $N_f$  is the cycles at failure (i.e., infinite crack growth rate).

$a_c$  can also be calculated using Eq. (2):

$$a_c = \left[ \frac{\Delta K_c}{Y \Delta S} \right]^2 \quad (6)$$

#### EXAMPLE 1

For the configuration shown in Fig. 1, calculate the critical crack length and cycles to failure for the stress ranges of 69 MPa (10 ksi), 138 MPa (20 ksi), and 207 MPa (30 ksi). Also calculate the crack size versus cycles for  $\Delta S = 138$  MPa (20 ksi). Calculate  $a/a_c$  versus  $N/N_f$  for the above three values of stress range.

TABLE 1. Material Parameters

Material	$\theta$	$C_0$		$\Delta K_C$	
		(m/cycle)	(in./cycle)	MPa $\sqrt{m}$	(ksi $\sqrt{in.}$ )
A-286	3.24	$2.8 \times 10^{-11}$	$1.1 \times 10^{-9}$	132	120
A 471 CL 4	1.4	$7.4 \times 10^{-14}$	$2.9 \times 10^{-12}$	220	200
Cr-Mo-V	4.09	$9.2 \times 10^{-14}$	$3.6 \times 10^{-12}$	33	30
4340	4.65	$5.0 \times 10^{-14}$	$2.0 \times 10^{-12}$	55	50
7075-T6	4.00	$1.5 \times 10^{-10}$	$6.0 \times 10^{-9}$	22	20

Given:

Material 7075-T6 Aluminum Alloy

$$2a_i = 5.08 \text{ mm (0.2 inch);}$$

$$2b = 127 \text{ mm (5 inches)}$$

Refer to Fig. 1 and Table 1

$$\Delta K_C = 22 \text{ MPa } \sqrt{m} \text{ (20 ksi } \sqrt{in.});$$

$$\Delta K_{th} = 2.2 \text{ MPa } \sqrt{m} \text{ (2 ksi } \sqrt{in.})$$

$$C_0 = 1.5 \times 10^{-10} \text{ m/cycle}$$

$$(6.0 \times 10^{-9} \text{ in./cycle}); \quad \theta = 4$$

$$Y = 1.77 \text{ from Eq. (1)}$$

$$\Delta K_i = 6.2 \text{ MPa } \sqrt{m} \text{ (5.6 ksi } \sqrt{in.})$$

$$\text{for } \Delta S = 69 \text{ MPa (10 ksi)}$$

$$\Delta K_{th} < \Delta K < \Delta K_C$$

Therefore the crack is in the stable propagation region.

$\Delta S$ (MPa)	$\Delta S$ (ksi)	$a_c$ (mm)	$a_c$ (inches)	$N_f$ (cycles)
69	10	32.5	1.28	$1.57 \times 10^4$
138	20	8.10	0.319	729
207	30	3.61	0.142	62

It can be seen that  $a_c$  is inversely related to  $\Delta S$ . The crack size versus cycles for  $\Delta S = 138 \text{ MPa (20 ksi)}$  is shown in Fig. 3. Fig. 4 shows the relative crack size versus cycle ratio for three values of  $\Delta S$  and an initial crack size  $a_i$  of 2.54 mm (0.1 in.). It can be seen that  $a/a_c$  is dependent upon  $\Delta S$ . Examination of Eqs. (4) and (5) shows that both  $a/a_c$  and  $N/N_f$  are dependent upon  $\Delta S$ . Therefore, cumulative damage laws such as  $\sum(a/a_c) = 1$  and  $\sum(N/N_f) = 1$  do not accurately apply for step-stress situations.

#### STEP STRESS

The growth of a crack under sinusoidal stressing will be analyzed from its initial size  $a_i$  through two

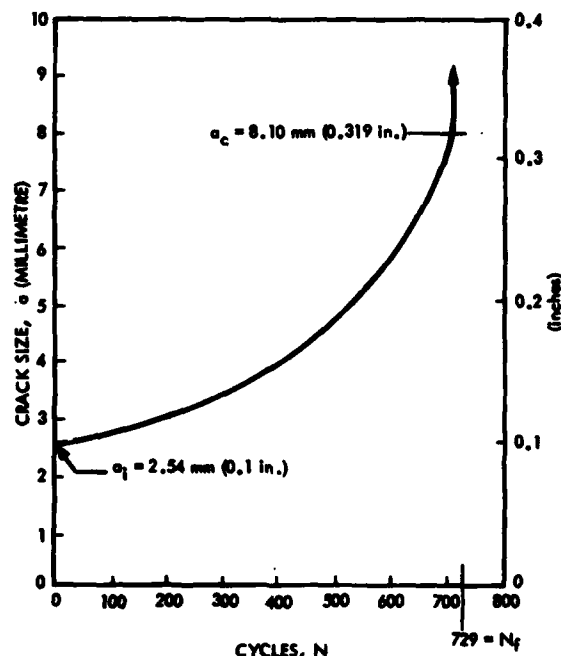


Fig. 3. Crack Size versus Cycles for  $\Delta S = 138 \text{ MPa (20 ksi)}$

levels of step-stress until the critical value is reached and the part fails. The previously described fracture mechanics equations will be used. Fig. 5 shows crack growth to failure for both levels of step-stress  $\Delta S_1$  and  $\Delta S_2$  applied independently. Fig. 6 shows the crack growing from an initial value  $a_{i1}$  to  $a_1$  after  $N_1$  cycles at  $\Delta S_1$ .

The stress level is then changed to  $\Delta S_2$ . The initial crack size  $a_{i2}$  at stress  $\Delta S_2$  is the same as the final crack size  $a_1$  after  $N_1$  cycles at  $\Delta S_1$ . Thus, the crack size remained the same at the interface of the two stress regions. This is the only boundary condition imposed and is the key element of the entire analysis.

The crack continues to grow at stress level  $\Delta S_2$  for  $N_2$  cycles until

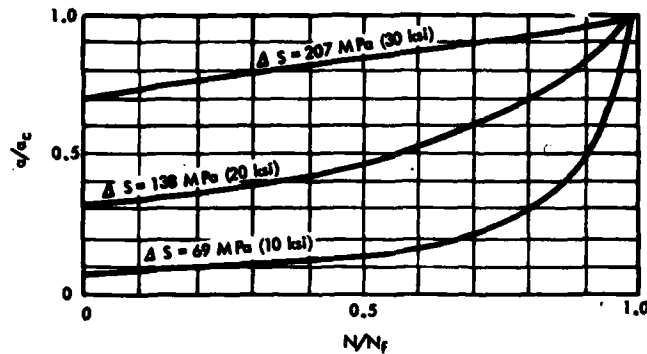


Fig. 4. Relative Crack Size versus Cycle Ratio for  $a_i = 2.54 \text{ mm (0.1 in.)}$

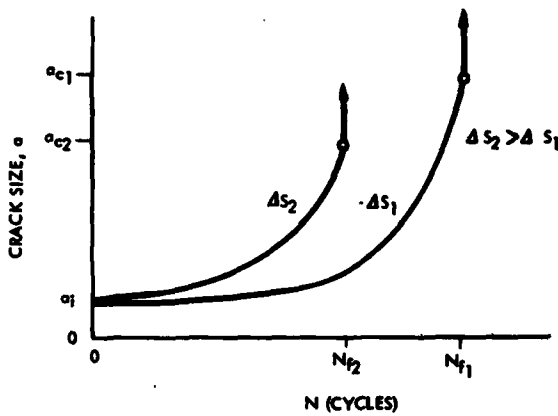


Fig. 5. Crack Growth versus Cycles;  $\Delta S_1$  and  $\Delta S_2$  Applied Independently

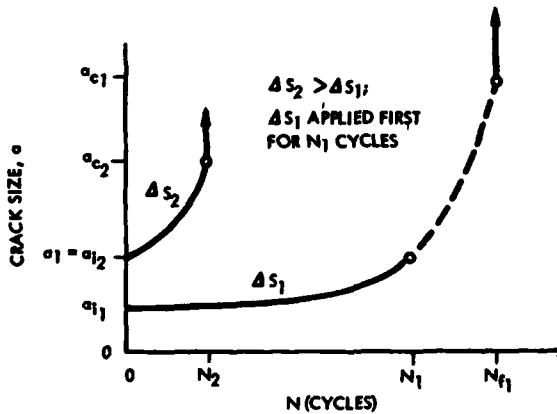


Fig. 6. Crack Growth versus Cycles;  $\Delta S_1$  and  $\Delta S_2$  Applied Sequentially

the critical size  $a_{c2}$  is reached; at which point failure occurs.  $N_2$  is the fatigue life that is desired to be calculated.

Define:

$$D_1 = \frac{N_1}{N_{f1}} = \quad (7)$$

cycle ratio partial damage at  $\Delta S_1$

$$D_2 = \frac{N_2}{N_{f2}} = \quad (8)$$

cycle ratio partial damage at  $\Delta S_2$

$$\text{Therefore, } N_2 = D_2 N_{f2} \quad (9)$$

Using Eqs. (4) through (8) and algebraic manipulations,  $D_2$  can be calculated. The result is

$$D_2 = 1 - D_1 \quad (10)$$

where

$$X = \frac{\left[ 1 - \left( \frac{a_i}{a_{c1}} \right)^{\frac{\theta-2}{2}} \right]}{\left[ 1 - \left( \frac{a_i}{a_{c2}} \right)^{\frac{\theta-2}{2}} \right]} \quad (11)$$

$$= \frac{\left[ 1 - \left( \frac{a_i Y^2 \Delta S_1^2}{\Delta K_c^2} \right)^{\frac{\theta-2}{2}} \right]}{\left[ 1 - \left( \frac{a_i Y^2 \Delta S_2^2}{\Delta K_c^2} \right)^{\frac{\theta-2}{2}} \right]}$$

The fatigue life  $N_2$  can then be calculated using Eq. (9).

Eq. (10) may be rearranged in a form that represents the proposed damage law. Failure occurs for two sequentially applied stresses with

cycle ratio damage expressions  $D_1$  and  $D_2$  when

$$D_1 X + D_2 = 1 \quad (12)$$

$X$  is an algebraic function of the initial crack size, the applied stresses, a geometrical parameter, and the material's fracture toughness value.

The proposed law is a simple expression similar to Miner's law and reduces to Miner's law for  $X = 1$ .  $X$  may be thought of as a correction factor to account for the crack propagation and failure dependency upon the values of  $\Delta S$ ,  $a_i$ ,  $Y$  or  $\Delta K_c$ . Given that  $a_i$ ,  $Y$  and  $\Delta K_c$  are constants for a particular configuration, the following can be noted:

$$X > 1 \text{ for } \Delta S_2 > \Delta S_1; D_1 + D_2 < 1$$

$$X < 1 \text{ for } \Delta S_2 < \Delta S_1; D_1 + D_2 > 1$$

$$X = 1 \text{ if } a_i \ll a_{c1} \text{ and } a_i \ll a_{c2}$$

For  $a_i = a_{c2}$  the part will fail as soon as  $\Delta S_2$  is applied.  $D_2 = 0$  for  $a_i = a_{c2}$ . By setting  $D_2 = 0$  in Eq. (12), the proposed damage law applies for

$$D_1 \leq \frac{1}{X}$$

#### EXAMPLE 2

Same configuration and dimensions as for Example 1.

$$a_i = 2.54 \text{ mm (0.1 inch)}$$

$$\Delta S_1 = 138 \text{ MPa (20 ksi);}$$

$$\Delta S_2 = 207 \text{ MPa (30 ksi)}$$

$$X = 2.327; \frac{1}{X} = 0.43$$

$$N_{f1} = 729 \text{ cycles; } N_{f2} = 62 \text{ cycles}$$

$$\text{Let } N_1 = 219 \text{ cycles}$$

Therefore  $D_1 = 0.3$  which is less than 0.43

$$D_2 = 1 - D_1 X = 0.302$$

$$N_2 = D_2 N_{f2} = 19 \text{ cycles}$$

Thus, the fatigue life at  $\Delta S_2$  is 19 cycles.

$$D_1 + D_2 = 0.602 \neq 1$$

Thus, Miner's law would not have accurately predicted the fatigue life  $N_2$  after the exposure to  $N_1$  cycles at stress level  $\Delta S_1$ . In this case  $X = 2.327 \neq 1$ .

#### EQUIVALENT DAMAGE

The term  $D_1 X$  in Eq. (12) may be thought of as the equivalent damage at  $\Delta S_2$  that is done by  $N_1$  actual cycles at  $\Delta S_1$ . There corresponds an equivalent number of stress cycles at  $\Delta S_2$  to produce the same damage as  $N_1$  cycles at  $\Delta S_1$ . Define the equivalent damage and cycles as  $D_{1e}$  and  $N_{1e}$  respectively. Figs. 7 and 8 show damage cumulation for the step-stress cases of  $\Delta S_2 > \Delta S_1$  and  $\Delta S_2 < \Delta S_1$ .  $D_1$ ,  $D_2$ ,  $D_{1e}$ , and  $N_{1e}$  are shown.  $N$  is the cycles at  $\Delta S_2$ . Failure occurs for  $N = N_2 = \text{fatigue life at } \Delta S_2$ .

$$D_{1e} = D_1 X \quad (14)$$

$$N_{1e} = N_{f2} D_{1e} \quad (15)$$

#### ELASTIC-PLASTIC LIMITATIONS

Gowda and Topper [3] have shown experimentally that for mild steel plates subjected to cyclic inelastic strains the crack growth rate can be expressed as

$$\frac{da}{dN} = c_1 (\Delta K)^3 + c_2 (\Delta K')^6 \quad (16)$$

The first term predominates in the elastic region. The second term predominates in the plastic region. Both terms are of the same form as the Paris crack growth rate expression in Eq. (3). Thus, it can be deduced that the proposed damage law (Eq. 12) accurately applies for cases where  $\Delta S_1$  and  $\Delta S_2$  are in either the elastic or plastic region exclusively but not for cases where they are in different regions.

Eq. (16) further suggests that a different damage law might apply for the case where  $\Delta S_1$  and  $\Delta S_2$  are in different elastic/plastic regions.

#### EXPERIMENTAL VERIFICATION

A literature search yielded no experimental results to verify or refute the proposed damage law for the case where the initial crack size is large compared to the critical crack sizes at  $\Delta S_1$  and  $\Delta S_2$ . However, Dowling [4] reports on laboratory step-stress experimental results where the specimens presumably have very small initial crack sizes. An appraisal of the accuracy of Miner's law in this case would also be an appraisal of the proposed damage law.

Dowling defines crack initiation as a tensile mode crack across several

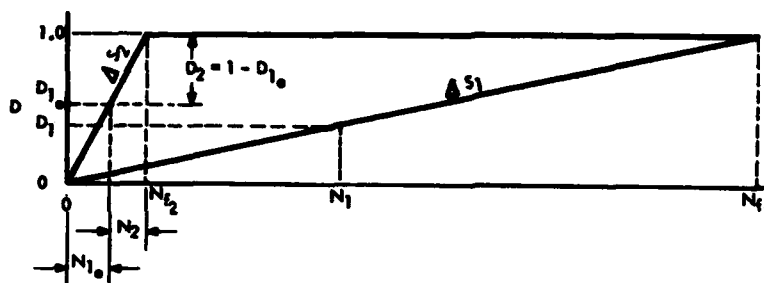


Fig. 7. Damage Cummulation for  $\Delta S_2 > \Delta S_1$

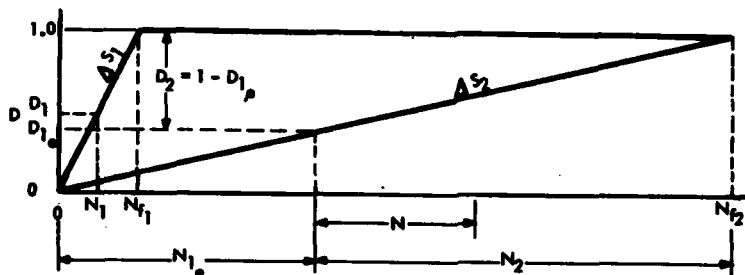


Fig. 8. Damage Cummulation for  $\Delta S_2 < \Delta S_1$

grains. The following results are reported:

Several cycles of plastic straining are required to initiate a crack.

Linear summation of cycle ratios (Miner's rule) is close to unity if (1) the specimen is subjected to several cycles of plastic prestraining to initiate a crack for the case of sinusoidal step-stress testing, or (2) if the specimen is subjected to random stressing where crack initiation normally occurs early in the life of the specimen.

Linear summations of cycle ratio damages deviate from unity for most when the difference between the applied stress levels  $\Delta S_1$  and  $\Delta S_2$  is greatest.

These test results are consistent with the analytical derivations in this paper; namely, the derived equations apply in the stable crack growth region ( $\Delta K_{th} < \Delta K < \Delta K_C$ ) and  $\Delta S_1$  and  $\Delta S_2$  must be in the same elastic or plastic stress region.

#### RANDOM STRESS CRACK GROWTH

For either single or two-degree-of-freedom systems, a calculable relationship [5] [6] exists between a material's sinusoidal "S-N" and random "σ-N"

fatigue curves. Thus, there exists a random root-mean-square (rms) stress  $\sigma$  that will propagate a crack in a given average number of cycles of the same size as that of a calculable corresponding sinusoidal stress  $\Delta S$ .

Fig. 9 shows both the sinusoidal and random fatigue curves for the 7075-T6 aluminum alloy. S is the sinusoidal stress amplitude which is equal to half the stress range  $\Delta S$ .  $\sigma$  is the random rms stress. For the random fatigue curve, N represents the average cycles to failure.

The general expressions for these fatigue curves are

$$S = \frac{\Delta S}{2} = A N^{-1/\beta} \quad (17)$$

$$\sigma = C N^{-1/\beta} \quad (18)$$

where A and C are material constants and  $\beta$  is a slope parameter [5].

At a given number of cycles,

$$\frac{\Delta S}{\sigma} = \frac{2A}{C} \quad (19)$$

For 7075-T6, A = 1240 MPa (180 ksi); C = 552 MPa (80 ksi)

$$\Delta S = 4.5\sigma$$



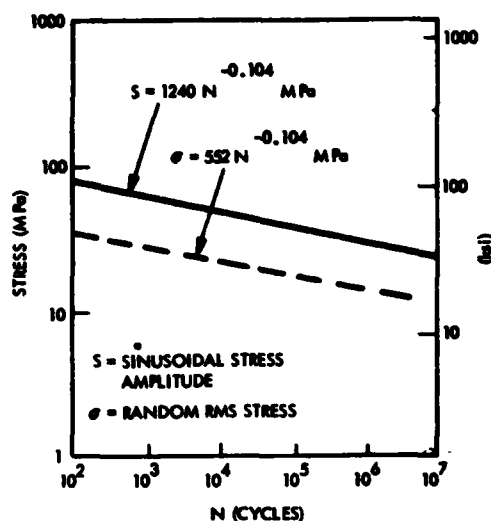


Fig. 9. Sinusoidal and Random Fatigue Curves for 7075-T6 Aluminum Alloy

In this case, a sinusoidal stress range that is equal in magnitude to  $4.5\sigma$  will propagate a crack the same size as a random stress of rms value  $\sigma$  for the same number of cycles.

#### RANDOM STEP-STRESS

For the case of two random rms step-stress levels  $\sigma_1$  and  $\sigma_2$ , the equivalent sinusoidal stress ranges can be determined using Eq. (19). For 7075-T6,  $\Delta S_1 = 4.5 \sigma_1$ ;  $\Delta S_2 = 4.5 \sigma_2$ . The fatigue life  $N_2$  is then calculated by using Eqs. (7) through (12) as in Example 2 with the above values of  $\Delta S_1$  and  $\Delta S_2$  appropriately substituted.

#### SCATTERBAND FATIGUE CURVE

A material's S-N fatigue curve is typically not a single line as shown in Fig. 9 but a wider scatterband of failure points. This scatterband can be represented by letting the constant A in Eq. (17) and Fig. 9 become a random variable. Let A be Gaussianly distributed with average value  $\bar{A}$  and standard deviation  $\Delta$ .

Define:

Region I:  $\Delta S = \Delta S_1$ ;  $0 \leq N_1 \leq N_{f1}$

Region II:  $\Delta S = \Delta S_2$ ;  $0 \leq N \leq$

$0 \leq N_2 \leq N_{f2}$

(See Fig. 7)

$F(N_1)$  = probability of failure at  $N_1$  cycles

$F(N_{1e})$  = probability of failure at  $N_{1e}$  cycles

$F(N)_{II} = F(N_{1e}, N)$  = probability of not failing in region I and failing in region II

The following can be shown [5]:

$$F(N_1) = \text{erfp} \left[ \frac{\bar{A}}{\Delta} \left\{ \left( \frac{N_1}{N_{f1}} \right)^{1/B} - 1 \right\} \right] + 0.5 \quad (20)$$

$$F(N_{1e}) = \text{erfp} \left[ \frac{\bar{A}}{\Delta} \left\{ \left( \frac{N_1 X}{N_{f1}} \right)^{1/B} - 1 \right\} \right] + 0.5 \quad (21)$$

$F(N)_{II} =$

$$\text{erfp} \left[ \frac{\bar{A}}{\Delta} \left\{ \left( \frac{N_1 X}{N_{f1}} + \frac{N}{N_{f2}} \right)^{1/B} - 1 \right\} \right] + 0.5 \quad (22)$$

where  $\text{erfp}(\alpha)$  = Papoulis' [7] Error Function

$$\text{erfp}(\alpha) = \frac{1}{\sqrt{2\pi}} \int_0^\alpha e^{-y^2/2} dy$$

$$\text{erfp}(0) = 0; \text{erfp}(\infty) = 0.5$$

$$\text{erfp}(-\alpha) = -\text{erfp}(\alpha)$$

It should be noted that  $F(N_1) \neq F(N_{1e})$  unless  $X = 1$  and that  $F(N_{1e}) = F(N)_{II}$  for  $N = 0$ . The reason is that  $N_{1e}$  is associated with region II where  $a_{c2} \neq a_{c1}$ . The probability of failure can be thought of as the probability of the crack size  $a$  exceeding the critical size  $a_c$ . If  $a_{c2} < a_{c1}$  (i.e.,  $X > 1$ ),  $F(N_{1e}) > F(N_1)$ . If  $a_{c2} > a_{c1}$  (i.e.,  $X < 1$ ),  $F(N_{1e}) < F(N_1)$ .

Regions I and II can be very disjoint in time. Many calendar days can exist between laboratory acceptance test vibration and in-flight vibration as an example. Each of the stress cycles  $N_1$  and  $N$  may be considered to be discrete, not continuous. A part may survive  $N_1$  cycles at  $\Delta S_1$  only to fail

during a portion of the first cycle at  $\Delta S_2$  if  $a_1 = a_{c2}$  or if  $\Delta S_2$  is large (e.g., = the ultimate stress). Thus,  $F(N_1) = F(N_{1e})$  is not a general condition to be imposed at the boundary of regions I and II.

### EXAMPLE 3

For the material, configuration, and dimensions of Example 1, calculate the fatigue life  $N_2$  for the step-stress random vibration stress case where  $\sigma_1 = 30.6$  MPa rms (4.44 ksi rms) and  $\sigma_2 = 46$  MPa rms (6.67 ksi rms).

Given:

$$N_1 = 146 \text{ cycles}; a_1 = 2.5 \text{ mm} \text{ (0.1 in.)}$$

$$\bar{A} = 1240 \text{ MPa (180 ksi)}; \Delta = 124 \text{ MPa (18 ksi)}; \bar{A}/\Delta = 10$$

$$\beta = 9.65$$

$$\sigma_1 = 30.6 \text{ MPa rms (4.44 ksi rms)}$$

$$\sigma_2 = 46 \text{ MPa rms (6.67 ksi rms)}$$

Equivalently

$$\Delta S_1 = 4.5 \sigma_1 = 138 \text{ MPa (20 ksi)}$$

$$\Delta S_2 = 4.5 \sigma_2 = 207 \text{ MPa (30 ksi)}$$

$$N_{f1} = 729 \text{ cycles}; N_{f2} = 62 \text{ cycles}$$

$$a_{c1} = 8.10 \text{ mm (0.319 in.)}$$

$$a_{c2} = 3.61 \text{ mm (0.142 in.)}$$

$$D_1 = N_1/N_{f1} = 0.2$$

$$a_1 = 2.95 \text{ mm} = a_{2i} \text{ (0.116 in.)}$$

$$\frac{a_1}{a_{c1}} = 0.363; \frac{a_{2i}}{a_{c2}} = 0.817$$

$$X = 2.327; D_{1e} = D_1 X = 0.465$$

$$D_2 = 1 - D_{1e} = 0.535$$

In crossing the boundary from region I to region II,  $a/a_c$  went from 0.363 to 0.817 and the damage went from  $D_1 = 0.2$  to  $D_{1e} = 0.465$ . The crack size  $a_1 = a_{2i} = 2.95$  mm (0.116 in.) remained the same at the boundary.  $a_c$  changed from 8.10 mm (0.319 in.) to 3.61 mm (0.142 in.).

$$N_2 = D_2 N_{f1} = 33 \text{ cycles to failure}$$

$$F(N_1) = 0.0618$$

$$F(N_{1e}) = 0.222$$

$$F(N=N_2=33) = 0.5$$

It can be seen that the probability of failing at  $N = N_2$  is 0.5, not unity. This is because the scatterband representation of the fatigue curve places failure both before and after the value of  $N_2$  as shown in Fig. 7.

The fatigue life is  $N_2 = 33$  cycles.

### CONCLUDING REMARKS

1. The proposed damage law for either sinusoidal or random step-stress fatigue is similar to Miner's linear cycle ratio law but contains a correction term which accounts for the dependency upon the values of stress range, initial crack (flaw) size, the geometrical parameter, and the material's fracture toughness.
2. The proposed damage law reduces to Miner's law when the correction factor has a value of unity.
3. The proposed damage law is limited in application to those cases where the crack growth is in the stable crack propagation region and where both stress levels are in the elastic or plastic stress regions. These are not considered to be very severe limitations on applicability.
4. Reported step-stress test results tend to confirm the proposed damage law. Further verification for large initial crack sizes is required.
5. The proper boundary condition to be imposed at the interface of the two stress regions is that the crack size not change. The values of cycle ratio damage and probability of failure will change at the interface in general.

### SYMBOLS

$a$  crack half-size (i.e., half length)

$a_c$  } critical values of crack half-size  
 $a_{c1}$  }  
 $a_{c2}$  }

$a_i$  } initial crack half-size  
 $a_{i1}$  }  
 $a_{i2}$  }

A material constant; true ultimate stress

$\bar{A}$  average value of A

b specimen half-width

C constant of random fatigue curve

$\left. \begin{matrix} C_0 \\ C_1 \\ C_2 \end{matrix} \right\}$  constants of crack growth rate curves

$\left. \begin{matrix} D_1 \\ D_{1e} \\ D_2 \end{matrix} \right\}$  cycle ratio damage functions

$\frac{da}{dN}$  crack growth rate

erfp error function defined by Papoulis [7]

F(N) probability of failure in N cycles

in. inches

$\left. \begin{matrix} K \\ K' \\ K_i \end{matrix} \right\}$  stress intensity factor

$\Delta K_c$  fracture toughness

$\Delta K_{th}$  threshold stress intensity factor

ksi thousands of pounds per square inch

$\left. \begin{matrix} N \\ N_1 \\ N_{1e} \end{matrix} \right\}$  number of stress cycles

$\left. \begin{matrix} N_f \\ N_2 \end{matrix} \right\}$  number of stress cycles to failure

S sinusoidal stress amplitude

$\Delta S$  sinusoidal stress range

sec trigonometric secant

rms root-mean-square

X damage law correction factor

y dummy variable

Y geometrical parameter

$\alpha$  dummy variable

B fatigue curve slope parameter

$\Delta$  standard deviation of A

$\sigma$  random rms stress value

$\left. \begin{matrix} \theta \\ \theta_1 \\ \theta_2 \end{matrix} \right\}$  constants of crack growth rate curves

m metre

mm millimetre

MPa megapascals

#### REFERENCES

1. P.C. Paris, "The Fracture Mechanics Approach to Fatigue," Proc. 10th Sagamore Army Mater. Res. Conf., p. 107, Syracuse University Press, Syracuse, N.Y. 1964
2. P.C. Paris and H.H. Johnson, "Sub-Critical Flaw Growth," Eng. Fracture Mechanics, Vol. 1, p. 3, 1968
3. C.V.B. Gowda and T.H. Topper, "Crack Propagation in Notched Mild Steel Plates Subjected to Cyclic Inelastic Strains," American Society for Testing and Materials, STP 519, Cyclic Stress-Strain Behavior-Analysis, Experimentation and Failure Prediction
4. N.E. Dowling, Fatigue Failure Predictions for Complicated Stress-Strain Histories, Journal of Materials, Vol. 7, No. 1, American Society for Testing and Materials, Philadelphia, Pa., March 1972
5. R.G. Lambert, "Analysis of Fatigue under Random Vibration," The Shock and Vibration Bulletin, Naval Research Laboratory, Washington, D.C., August 1976
6. R.G. Lambert, "Fatigue Analysis of Multi-Degree-of-Freedom Systems under Random Vibration," Presented at 47th Shock and Vibration Symposium, Albuquerque, New Mexico, October 1976
7. A. Papoulis, Probability, Random Variables, and Stochastic Processes, McGraw-Hill Book Co., New York, 1965

## RANDOM FATIGUE DAMAGE APPROACH TO MACHINERY MAINTENANCE

T. S. Sankar, G. D. Xistris  
Concordia University  
Montreal, Quebec, Canada

and

G. L. Ostiguy  
Ecole Polytechnique  
Montreal, Quebec, Canada

Machinery vibrations are employed to obtain an estimate of the stresses in critical mechanical elements under operating conditions. The amount of fatigue damage incurred as a result of these stresses is computed using a linear damage accumulation law and expressions are developed for the expected value of the damage sustained over a specific time period. The behavior of these statistical parameters with operating time and with various system fatigue properties is discussed. The calculated damage provides a reliable indication of the remaining trouble-free life and can be employed in the maintenance field to monitor the performance of industrial machinery.

### INTRODUCTION

A significant part of the operating cost of industrial processes is due to machinery down-time and periodic maintenance. These expenditures are the direct result of defects either inherent in individual elements, or introduced during the assembly of components. The severity of these defects is progressively enhanced during normal operation of machinery resulting in certain deterioration of overall unit performance and this is commonly known as "wear". When equipment performance falls below design specifications, the unit is deemed to have failed. Such failures may be catastrophic, if arising from rapid degradation of defective parts, or gradual, if caused by normal wear and tear.

Catastrophic failures are associated with the presence of a single dominant defect such as a badly damaged antifriction bearing, severe misalignment of rotors or gross imbalance of rotating elements. Dominant defects produce high stress values in the affected components and failure occurs after a small number of operational cycles. The resulting stress histories

are then narrow band, high amplitude processes and hence, the nature and source of the defect can be easily identified through a frequency analysis. On the other hand, normal wear failures which are associated with wide band, low amplitude stress histories, cannot be assessed by any of the currently available machinery monitoring techniques.

This paper proposes a machinery health monitoring procedure based on the estimates of the accumulation of gradual fatigue damage in specific machine elements. The characteristics of the incremental damage functions incurred by the critical components of a machine during its life span, are inferred from the vibration histories, that form generally a random process, obtained at appropriate locations of the machine system. The damage increments are subsequently employed to calculate the amount of fatigue life expended in a given time interval, thus providing an estimate of the remaining expected maintenance-free life of the equipment.

### MACHINERY RESPONSE AS A CONDITION MONITOR

Machinery breakdowns occur due to

the gradual accumulation of fatigue damage incurred by the machine elements which are subjected to fluctuating stresses. These stresses are caused by a resultant excitation representing the complex combined effect of imbalance in the rotating elements, misalignment between segments of rotors installed with multiple rigid supports, bearing friction and the presence of bearing defects, the meshing of gear trains, differences in thermal expansion characteristics of parts in the same sub-assembly and other internal, as well as, external load variations imposed by the operating environment.

Individual direct measurement of each of these disruptive forces is not practical. Neither is it possible, to obtain their combined effect through the actual stress histories under different operating conditions. However, measurements of the vibratory response history are feasible and in most cases available. Under the assumption that machinery elements are elastic and isotropic, a simple relationship between the response measured at an exterior point and the stress at a corresponding element within the machine, may be developed. For the purpose of defining a machinery maintenance program, in general it may be sufficient, as well as practical, to assume a linear relationship between stress and response in the form

$$s(t) = \alpha x(t) \quad (1)$$

where,  $s(t)$  is the stress history of one or more machine elements which is reflected by a response history  $x(t)$  at a judiciously selected measurement location. The constant of proportionality  $\alpha$ , takes into account all the combined effects of material and system properties such as damping, stiffness and configuration relative to the particular monitoring location. In complicated machines where several monitoring stations may be used,  $\alpha$  will assume different values reflecting the internal structure and properties at each particular location.

The use of equipment response  $x(t)$  as a condition monitoring parameter appears to be a widely accepted practice in the machinery maintenance field. The current literature, contains several successful applications of this technique [1,2,3]\*.

\*[ ] designates references listed at the end.

## CHARACTERIZATION OF THE STRESS-RESPONSE HISTORY

In view of the assumed linearity between stress and response functions,  $s(t)$  can be characterized indirectly by assigning to it all the observed attributes of  $x(t)$ .

The first of such attributes is that the stress history  $s(t)$ , constitutes a sample function of an ergodic Gaussian, stochastic ensemble. The large number of factors which contribute to the presence of  $s(t)$ , together with the surface texture characteristics of the interacting mechanical components, dictate that the stress process in machines must be stochastic with possibly a Gaussian distribution [4]. The ergodicity assumption implies that the stress process may be represented by a single sample function. Although no analytical or experimental proof of ergodicity exists, the observed good correlation between vibration and defects for similar pieces of equipment [2], would appear to justify such a treatment.

The second constraint on  $s(t)$  is that it must be considered piecewise stationary. Experimental evidence [1,2] shows that the inevitable deterioration of dimensional clearances coupled with the progressive worsening of latent mechanical and material defects are associated with an increase in vibration levels. Thus, over the complete life span of a machine, the observed response and hence  $s(t)$  must be nonstationary. This phenomenon will be quite dominant in the later stages of operation when the rate of deterioration is generally accelerated. However, if the total operating period is subdivided into  $\Delta T_1$  intervals, it is always possible to consider the process as stationary within each segment  $\Delta T_1$  [3].

The third constraint deals with the spectral characteristics of  $s(t)$ . Because of the many contributing factors and their related harmonics,  $s(t)$  is expected to be wide band. This assertion is substantiated in part by the evidence that modern equipment operating under normal conditions, exhibit a relatively flat velocity spectrum up to about 1.5 kHz [2]. Narrow band stress histories are associated with equipment where a single defect, such as a strong first order imbalance, is predominant. Defects of this type lead to very rapid catastrophic breakdowns as opposed to failures resulting from the gradual accumulation of damage. Since predominant defects can be easily identified and, as a rule, have to be rectified immediately, purely narrow

band stress histories are not considered in this investigation as a contributing factor for gradual deterioration of equipment.

Machinery vibration histories that are piecewise stationary exhibit zero mean over a limited number of cycles. Since machine systems are rigidly attached, it follows that even though instantaneous values of  $x(t)$ ,  $\dot{x}(t)$  and  $\ddot{x}(t)$  may not necessarily be zero, the mean values of the vibratory response process and the corresponding rate parameters, over an appropriately chosen period of time, must tend to zero.

The final constraint on  $s(t)$  is invoked in order to assure that the primary mode of machinery breakdown is accumulated damage under random fatigue. This is accomplished by assuming that  $s(t)$  is bounded so that  $s_{max}$  does not exceed the component ultimate or yield strength. The effect of placing an upper limit on  $x(t)$  and thereby on  $s(t)$ , is to eliminate failures caused by the sudden application of overloads which are outside the domain of normal operating conditions. Such overloads may arise from the presence of distinct machinery defects or external impact type loads which if not rectified immediately, will lead to premature failure. It should be pointed out, that predominant defects and extraneous impacts are practically always associated with narrow band spectra. Also in order to facilitate the analysis, it has been assumed that  $s(t)$  is continuous and differentiable at least twice.

#### FATIGUE DAMAGE FOR MACHINERY COMPONENTS

Because of the experimental scatter in the reported material fatigue properties, it is customary to treat fatigue life as a random variable having a particular mean value and probability distribution at failure. It is reasonable therefore, to define the fatigue damage  $D(\Delta T)$ , incurred as a result of the ensemble of stress histories  $s(t)$  during the time interval  $\Delta T$ , as a random variable. In order to interpret the behavior of  $D(\Delta T)$ , it is desirable to establish its probability distribution. This would be possible if a large number of identical machines were subjected to the same operating and environmental conditions. Clearly, this is a formidable undertaking. However, for the purpose of developing a machinery health monitoring program based on accumulated damage estimates, it is sufficient to be able to calculate the mean value of the random variable  $D(\Delta T)$ .

The random variable  $D(\Delta T)$  repre-

sents the contributions of the individual fatigue damage increments  $\delta D$ , accrued as a result of each stress cycle occurring within the time interval  $\Delta T$ . Here, it can be assumed that the  $\delta D$ 's are directly proportional to the amplitude of the corresponding stress cycles. This is essentially known as the linear fatigue damage hypothesis [5,6] which states that the amount of damage incurred as a result of a single whole stress cycle of amplitude  $s$  is related to the total number of cycles  $N(s)$ , that the specimen can withstand at a constant stress amplitude  $s$ . The magnitude of the incremental damage functions  $\delta D$ , can be calculated from material fatigue data.

The most widely used method of presenting material fatigue properties is the  $s$ - $N$  curve where the stress amplitude is plotted against the number of cycles for different loading arrangements. However, when the stress history is a wide band stochastic process, the stress intensity cannot be adequately characterized by the amplitude parameter alone. In such cases, it has been suggested that a plot of  $\sigma_a$ - $N$  is a more meaningful method of defining fatigue properties [7]. Obviously, the calculation of  $\delta D$  and thereby  $D(\Delta T)$ , will depend on the method used to correlate the fatigue data appropriate to each case.

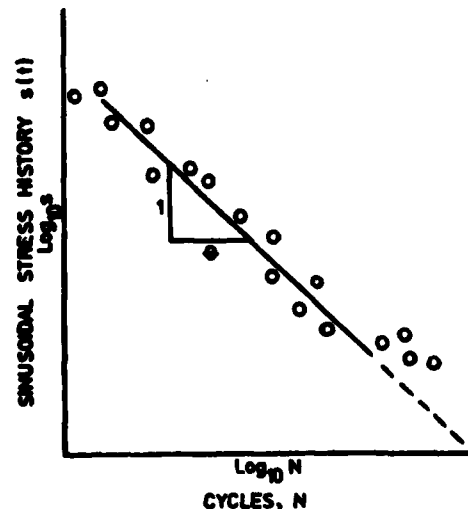


Fig. 1: Typical  $s$ - $N$  Representation of Fatigue Data for Constant Amplitude Stress Histories.

## DAMAGE ESTIMATES USING s-N CURVE

Figure 1 depicts a typical s-N curve for constant amplitude stress histories. An approximate correlation of the reported experimental results is given by

$$N(s) = \left[ \frac{C}{s} \right]^\theta \quad (2)$$

where C is a material constant and the exponent  $\theta$  is the negative reciprocal of the slope of the mean s-N curve. Since machinery stresses are expected to have a zero mean over a number of cycles, by approximating each cycle to a sinusoid, any stress peak amplitude can be found from the relation

$$s = \frac{|\ddot{s}|}{\omega^2} \quad (3)$$

where  $\omega$  is the circular frequency of the corresponding cycle. In several cycles of a wide band process, the average circular frequency can be represented by

$$\omega = 2\pi E[n] \quad (4)$$

where  $E[n]$  is the expected value of the frequency of the peaks for any stationary random process.

Combining Equations (2), (3) and (4) and taking into account the inverse relationship between  $\delta D$  and  $N(s)$ , it can be shown that

$$\delta D(|\ddot{s}|) = \left[ \frac{|\ddot{s}|}{C(2\pi E[n])^2} \right]^\theta \quad (5)$$

To obtain an expression for the expectation of the damage accumulated in time  $\Delta T$ , the interval  $\Delta T$  is subdivided into smaller segments. The condition for a stress peak to occur within any of the smaller time segments and thereby cause an increment of damage equal to  $\delta D(|\ddot{s}|)$  to be accrued, is given by the joint probability density function for all possible  $\ddot{s}(t)$  with  $s(t) = 0$ . Following a procedure analogous to [8], it can be shown that

$$E[D(\Delta T)] = \Delta T \int_{-\infty}^{\infty} \delta D(|\ddot{s}|) |\ddot{s}| p(0, \ddot{s}) d\ddot{s} \quad (6)$$

where the joint probability density function  $p(\ddot{s}=0; \ddot{s})$  has been written as  $p(0, \ddot{s})$ .

For a normal process with zero mean, the joint probability density function  $p(0, \ddot{s})$  is [9]

$$p(0, \ddot{s}) = \frac{1}{2\pi \sigma_{\ddot{s}}^2} e^{-\ddot{s}^2 / 2\sigma_{\ddot{s}}^2} \quad (7)$$

Also, Lin [10] has shown that

$$E[n] = \frac{\sigma_{\ddot{s}}}{2\pi \sigma_s} \quad (8)$$

Substitution of Equation (8) into Equation (5) and using the resulting expression for  $\delta D(|\ddot{s}|)$  together with Equation (7) into Equation (6), the mean accumulated damage can be obtained as

$$E[D(\Delta T)] = \frac{\Delta T}{\pi} \left( \frac{\sqrt{2}}{C} \sigma_{\ddot{s}} \right)^\theta \Gamma\left(\frac{\theta}{2} + 1\right) \left( \frac{\sigma_{\ddot{s}}}{\sigma_s} \right)^{\theta-1}$$

This, expressed in terms of the response process parameters for application to machinery health monitoring reduces to

$$E[D(\Delta T)] = \Delta T A(\theta) (Z\sigma_x)^\theta \left( \frac{\sigma_{\ddot{x}}}{\sigma_x} \right)^{\theta-1} \quad (9)$$

where  $A(\theta) = \frac{(\sqrt{2})^\theta}{\pi} \Gamma\left(\frac{\theta}{2} + 1\right) R^{\theta-1}$ ,

$$Z = \frac{\alpha}{C}$$

and  $R = \sigma_{\ddot{s}}^2 \sigma_x^2 / \sigma_s^2 \sigma_x^2$

In most cases where the processes are orderly, R is expected to be equal to unity. The material response parameter Z embodies the effects of damping, configuration and fatigue strength particular to each measurement source.

## DAMAGE ESTIMATES USING $\sigma_s$ -N CURVE

Figure 2 illustrates an alternate method of presenting fatigue test data. Such data are obtained by subjecting specimens of the same material and geometry to a continuous stationary random stress process  $\{s(t)\}$ , under identical environmental conditions. A sample function of  $\{s(t)\}$  is illustrated in Figure 3.

Wirsching and Haugen [7] have postulated that each tensile peak of  $\{s(t)\}$  causes a certain amount of damage. The total damage in time  $\Delta T$ , due to all peaks which lie in the interval  $[s_j, s_j + \Delta s]$  is given by

$$\delta D_j(\Delta T) = \begin{cases} \frac{n_j(\Delta T)}{\Delta} s_j^\phi & \text{for } s_j > 0 \\ 0 & \text{for } s_j \leq 0 \end{cases} \quad (10)$$

where  $n_j(\Delta T)$  is the expected total number of stress peaks with amplitude in the interval  $[s_j, s_j + \Delta s]$  in time  $\Delta T$ ,

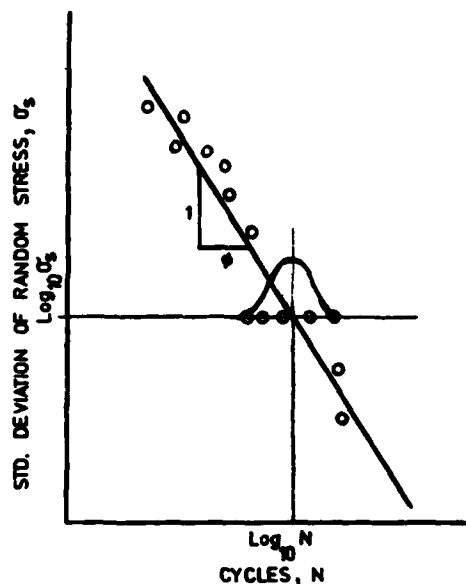


Fig. 2: Typical  $\sigma_s$ -N Representation of Fatigue Data for Random Stress Histories.

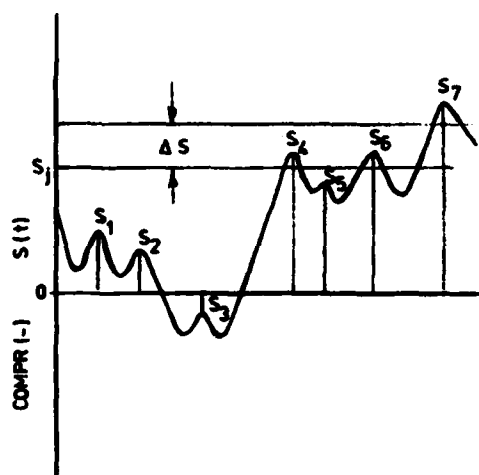


Fig. 3: Sample Function of a Wide Band Random Stress Ensemble

$\phi$  is the negative reciprocal of the slope of the random fatigue curve and  $\Lambda$  is a random variable which reflects the variability of strength properties of similar specimens of a given material.

Denoting the total expected number of peaks of  $\{s(t)\}$  in time  $\Delta T$  by  $n(\Delta T)$  then

$$n_j(\Delta T) = n(\Delta T) p(s_j) \Delta s \quad (11)$$

where  $p(s_j)$  is the probability density function of the peak heights of  $\{s(t)\}$  covering the interval  $[s_j, s_j + \Delta s]$ . Defining a non-dimensional random variable  $k = s/\sigma_s$  and integrating Equation (10) with (11) yields

$$D(\Delta T) = \frac{n(\Delta T)}{\Lambda} \sigma_s^\phi \beta \quad (12)$$

where  $\beta = \int_0^\infty k^\phi p(k) dk$ . The integral  $\beta$  which is a function of the spectral and mean value properties of the stress process has been computed in [7]. Values of  $\beta$  appropriate to machinery elements have been summarized in Table 1. From Equation (8)

$$n(\Delta T) = \frac{\Delta T}{2\pi} \frac{\sigma_s''}{\sigma_s'} \quad (13)$$

Substituting Equation (13) into Equation (12) and averaging both sides of the resulting expression yields in terms of the response process parameters

$$E[D(\Delta T)] = \Delta T (z_r \sigma_x)^\phi \left( \frac{\sigma_x''}{\sigma_x'} \right) F \quad (14)$$

where

$$z_r = \frac{\alpha}{C_r}$$

$$C_r = E[\Lambda]^{1/\phi}$$

and

$$F = \frac{R\beta}{2\pi}$$

$z_r$  is the material response parameter for random fatigue and the constant  $R$  has been defined in Equation (9).

#### DISCUSSION AND ANALYSIS OF RESULTS

Figure 4 shows the variation of  $E[D(\Delta T)]$  with operating time for different values of the exponent of the appropriate fatigue curve as predicted by Equations (9) and (14). It is apparent from the nature of these equations, that in both cases the expected value of the accumulated damage increases linearly with operating time. The upper limit for  $E[D(\Delta T)]$  is taken as unity in accordance with Miner's criterion.

Further, Figure 4 shows that  $E[D(\Delta T)]$  varies inversely with  $\phi$  and  $\theta$ . For example, after  $10^6$  seconds of operation, the mean accrued damage is



TABLE 1  
Values of the Function  $\beta$  for  $R = 1.0$  and Zero Mean Stress Calculated from [7].  
The Parameter  $\gamma$  is the Ratio of Expected Number of Zero Crossings from Below  
per Unit of Time to the Expected Number of Peaks per Unit of Time.

$\phi$	$\gamma = 1.0$	$\gamma = 0.9$	$\gamma = 0.8$	$\gamma = 0.7$	$\gamma = 0.6$	$\gamma = 0.5$
3	3.776	3.398	3.021	2.719	2.417	2.115
5	19.30	17.37	15.44	13.51	11.97	10.42
7	132.3	119.0	105.8	92.58	79.35	68.77
9	1215	1093	971.6	825.9	704.4	607.3

TABLE 2  
Material Fatigue Constants for Stress Values in psi

Material and Loading form	Constant Amplitude			Random		
	$\theta$	C	Ref.	$\phi$	$C_r$	Ref.
Mild Steel - Axial Su = 365 MPa (53 ksi)	11.5	$0.9 \times 10^5$	[12]	7.2	$1.5 \times 10^5$	[15]
Al 2024 - T3 Bending	8	$1.0 \times 10^5$	[13]	5.7	$2.7 \times 10^5$	[14]
Al 2024 - T3 Axial	6.7	$1.2 \times 10^5$	[14]	5.8	$2.1 \times 10^5$	[15]
Al 7075 - T6 Bending	6.7	$1.7 \times 10^5$	[14]	3.2	$7.8 \times 10^5$	[15]

$1.3 \times 10^{-5}$  and  $9.1 \times 10^{-3}$  for  $\phi = 7$  and  $\phi = 5$  respectively. Large values of  $\phi$  imply a relatively flat  $\sigma_s$ -N curve and therefore, for a given random stress environment, the mean number of cycles to failure will be high. Thus, for large  $\phi$ , each stress cycle is associated with a small damage increment resulting in the behavior illustrated in Figure 4. Similarly after  $10^6$  seconds of operation  $E[D(\Delta T)]$  attains values of  $3.0 \times 10^{-6}$  for  $\theta = 9$  and  $0.7$  for  $\theta = 5$ . This variation is consistent with the interpretation of the s-N curve. Since  $\phi$  and  $\theta$  are independent, direct comparison of  $E[D(\Delta T)]$  for identical values of the exponents is not meaningful. In general, values of  $\phi$  tend to be somewhat lower than  $\theta$  for the same material subjected to the same stress mode. This is evident in Table 2 where fatigue parameters for typical materials are summarized.

$E[D(\Delta T)]$  is also dependent on the material response parameter. Table 2 shows that  $Z_r$  is usually smaller than  $Z$

as can be inferred from the general trend of the constants C and  $C_r$ . Small values of C and  $C_r$  are characteristic of materials with low fatigue resilience and hence, a low number of cycles to failure. For a given  $\alpha$ , small C and  $C_r$  will result in large  $Z$  and  $Z_r$  yielding high damage accumulation rates. This is illustrated in Figures 5 and 6 where it is seen that  $E[D(\Delta T)]/\Delta T$  increases linearly with  $Z$  and  $Z_r$  respectively when plotted on log-log axes.

Figures 5 and 6 also delineate the inverse dependence of  $E[D(\Delta T)]/\Delta T$  on  $\phi$  and  $\theta$ . However, the influence of the fatigue exponents on  $E[D(\Delta T)]/\Delta T$  appears to diminish with increasing values of the material response parameter. This is manifested by the convergence of the plotted curves. It would appear that for the range of  $\theta$  and  $\phi$  values considered in the investigation and for high values of the corresponding material response parameter,  $E[D(\Delta T)]/\Delta T$  may be approximated as a function of  $Z$  or  $Z_r$  only.

It is evident from the above discussion that estimates of  $E[D(\Delta T)]$  will involve either form of the material response parameter as indicated above. When analyzing the performance of similar machines, it can be reasonably assumed that they possess the same structural characteristics (this implies that the constant  $\alpha$  is the same) and therefore, the rate of damage accumulation will depend only on the standard deviations of the response signals. A machine which exhibits a high value of  $E[D(\Delta T)]/\Delta T$  will reach its fatigue limit before a unit with a correspondingly lower damage accumulation rate. In all other applications, it becomes necessary to select a value of  $Z$  or  $Z_r$  appropriate to each location. Preliminary data developed in connection with this investigation have established that for most industrial machines  $0.1 < Z < 50$ . This result was obtained by extrapolating available vibration and performance records of torsional systems in the 1000 to 3000 HP range and electrically driven pump sets up to 100 HP. The wide range in the observed values of  $Z$  clearly indicate the need for further experimental work in this area.

#### CUMULATIVE DAMAGE AS A MONITORING TOOL

Since the primary cause of normal wear machinery breakdowns has been identified as some form of fatigue failure, the cumulative damage calculated from Equations (9) or (14) can be employed as a condition monitoring tool in an industrial equipment maintenance scheme. In such an application, the  $E[D(\Delta T)]$  can be interpreted as an indication of the average amount of trouble-free life expended over a given operating period. Alternately, it is an estimate of the probable remaining useful life of machine systems.

The maintenance programs proposed in this investigation require measurement of the vibratory response time history at selected points of the machine system. The actual number of signal monitoring stations will depend on the complexity of the machine structure. For most common equipment the number of measurement sources corresponds to the number of principal bearings in the system.

The standard deviations required in Equations (9) and (14) may be obtained for each signal using digital data analysis techniques. The relative fluctuations in these process rate parameters depend primarily on the length of the signal record chosen [11]. Ideally, the signal should be available in a continuous form. However, such a monitoring

procedure is uneconomical and impractical. An alternate approach is to approximate the ideal continuous record with periodic discrete measurements each lasting  $\Delta t$  seconds taken  $\Delta T$  intervals apart as illustrated in Figure 7. This method would be acceptable provided that the  $\Delta T$  intervals are chosen in the following manner: Select a signal recording length  $\Delta t$  which is adequate to represent the salient signal characteristics and it is compatible with the storage capability of the digital data processing devices used for computing the standard deviations. The choice of a particular  $\Delta t$  defines the limit of accuracy which is attainable in the determination of the process rate parameters. The interval  $\Delta T$  between successive records of  $\Delta t$  duration, should be such that the variation in the standard deviations calculated from these two signals does not exceed the confidence limits dictated by the choice of  $\Delta t$ . If the rate parameters obtained at  $\Delta t_i$  and  $\Delta t_{i+1}$  differ by more than what can be attributed to the influence of the recording length used, then over this  $\Delta T$ , the calculation of  $E[D(\Delta T)]$  should be made using mean values for the rate parameters obtained from  $\Delta t_i$  and  $\Delta t_{i+1}$ . Subsequent measurements should be made at smaller intervals, i.e.  $\Delta t_{i+1} = \Delta t_i/2$ . As long as the rate parameters remain relatively constant on the basis of the above described procedure, the process can be considered stationary and  $E[D(\Delta T)]$  calculated over the sum of all the intermediate  $\Delta T_i$ . For machinery approaching failure (i.e.,  $E[D(\Delta T_i)] < 0.7$ ), the deviation of the rate parameters can be expected to be significant and proper care must be exercised in the choice of  $\Delta t$ 's and  $\Delta T$ 's.

Initial experimental evidence indicates that this method of ascertaining machinery reliability is promising, particularly in cases where previous experience of equipment vibratory behavior is unavailable. The main advantage of this approach is that machinery condition assessment can be made in terms of component fatigue properties and the actual stress histories which arise under operating conditions.

#### ACKNOWLEDGMENT

This research was carried out under FCAC Grant 042-110 from the Government of Quebec.

# REFERENCES

1. Maten, S., "Vibration Velocity Measuring Program," ASME Paper No. 70-PEM-27, March, 1970.
2. Glew, C.A.W. and Watson, D.C., "Vibration Analysis as a Maintenance Tool in the Canadian Navy," Trans. of Inst. of Marine Engineers, Canadian Division, Suppl. No. 32, June, 1968.
3. Sankar, T.S. and Xistris, G.D., "Failure Prediction Through the Theory Stochastic Excursions of Extreme Vibration Amplitudes," J. Eng. Ind., Trans. ASME, Vol. 94, pp. 133-138, 1972.
4. Sankar, T.S. and Osman, M.O.M., "Profile Characterization of Manufactured Surfaces Using Random Function Excursion Technique," J. Eng. Ind., Trans. ASME, Vol. 97, pp. 190-202, 1975.
5. Miner, M.A., "Cumulative Damage in Fatigue," J. of Applied Mechanics, Trans. ASME, Vol. 12, pp. A159-A164, Sept. 1945.
6. Saunders, S.C. and Birnbaum, Z.W., "A Probabilistic Interpretation of Miner's Rule," Boeing Scientific Research Laboratories, Math. Note No. 505, April, 1967.
7. Wirsching, P.H. and Haugen, E.B., "A General Statistical Model for Random Fatigue," J. of Eng. Materials and Technology, Trans. ASME Vol. 96, pp. 34-40, 1974.
8. Mark, W.D., "The Inherent Variation in Fatigue Damage Resulting from Random Vibration," Ph.D. Thesis, Department of Mechanical Engineering, Massachusetts Institute of Technology, 1961.
9. Lin, Y.K., "Probabilistic Theory of Structural Dynamics," p. 72, McGraw-Hill, 1967.
10. Ibid.9, p. 302.
11. Morrow, C.T., "Averaging Time and Data Reduction Time for Random Vibration Spectra," J. Acoust., Soc. of Am., Vol. 30, pp. 456-461, 1958.
12. Faires, V.M., "Design of Machine Elements," MacMillan, 4th ed., 1965, pp. 580.
13. Osgood, C.C., "Fatigue Design," p. 429, Wiley & Sons, 1970.
14. Ibid.13, p. 428.
15. Swanson, S.R., "Random Load Fatigue Testing: State of the Art Survey," Materials Research and Standards, pp. 10-45, April, 1968.
16. Hillberry, B.M., "Fatigue of 2024-T3 Aluminum Alloy Due to Broad Band and Narrow Band Randoms Loading," Ph.D. Dissertation, Iowa State University, 1967.

Fig. 4: Mean Accumulated Damage as a Function of Operating Time  
 Computed for a Stress Process Characterized by  
 $\sigma_x = 0.225 \times 10^{-3} \text{ cm}$  ( $0.887 \times 10^{-3} \text{ in}$ ),  $\sigma_z = 3.383 \text{ cm/s}$   
 ( $1.332 \text{ in/s}$ ),  $\sigma_z^2/\sigma_x^2 = 1502 \text{ sec}^{-1}$  and for the Following  
 System Parameters  $\bar{z} = 10.0$ ,  $\bar{z}_r = 5.0$  and  $\gamma = 1.0$ .

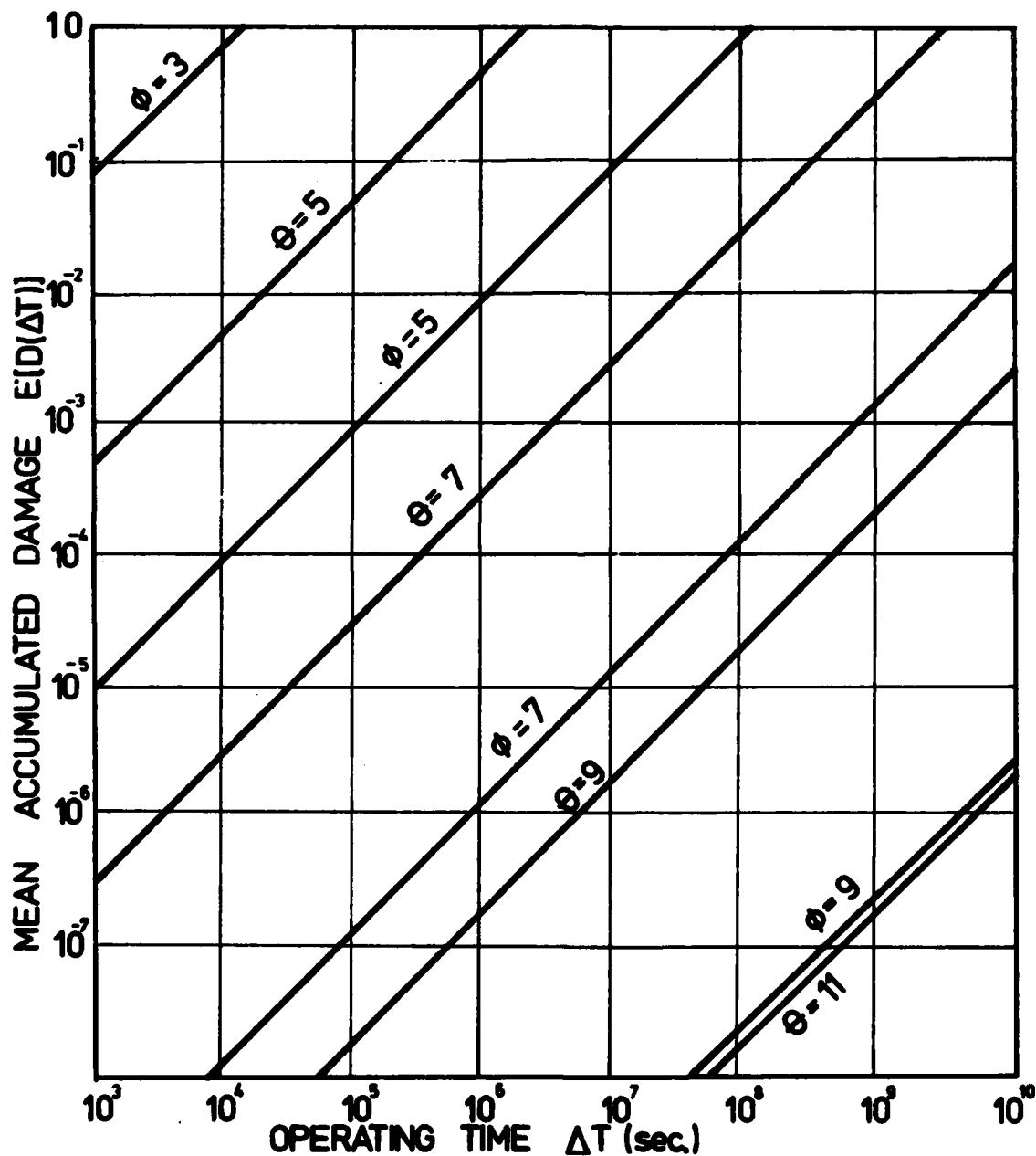


Fig. 5: Damage Accumulation Rate as a Function of the Random Fatigue Material Response Parameter for  $\gamma = 1.0$ ,  $\sigma_x = 0.225 \text{ cm}$  ( $0.887 \times 10^{-3} \text{ in}$ ) and  $\sigma_{\dot{x}}/\sigma_x = 1502 \text{ sec}^{-1}$ .

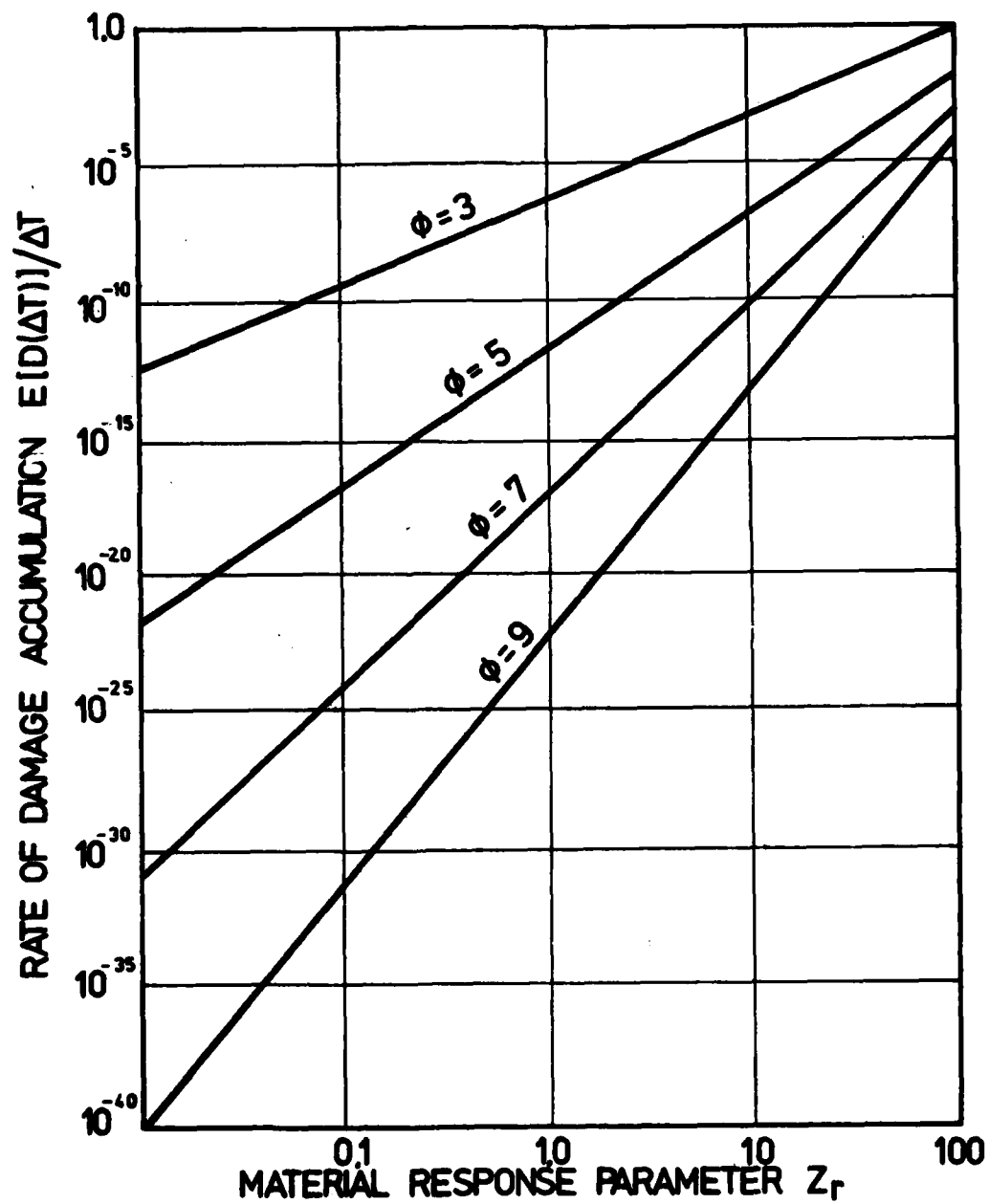
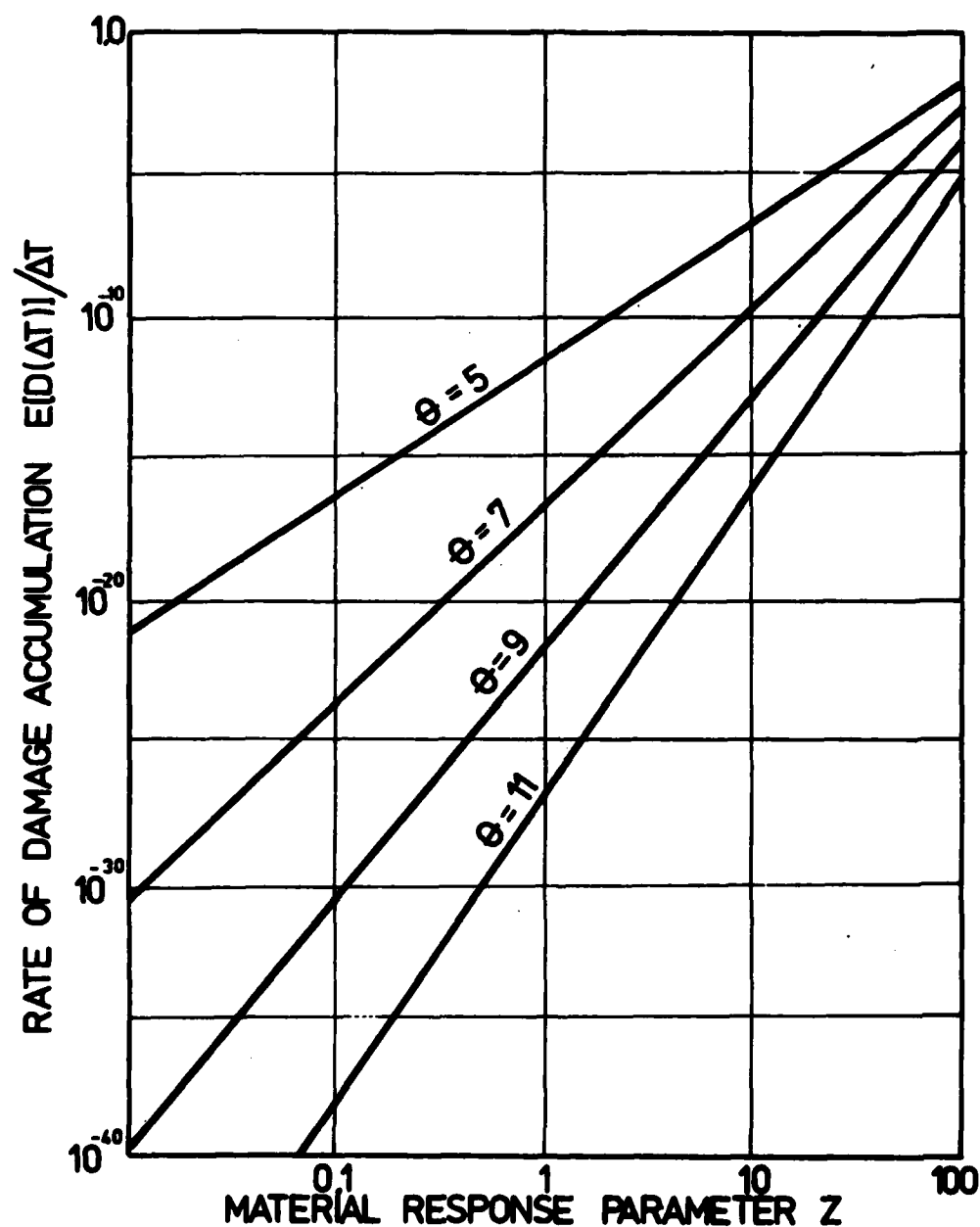


Fig. 6: Damage Accumulation Rate as a Function of the Constant Amplitude Fatigue Material Response Parameter for a Stress Process with  $\sigma_x = 3.383$  cm/s (1.332 in/s) and  $\sigma_x^2/\sigma_x^2 = 0.667 \times 10^{-3}$  sec.



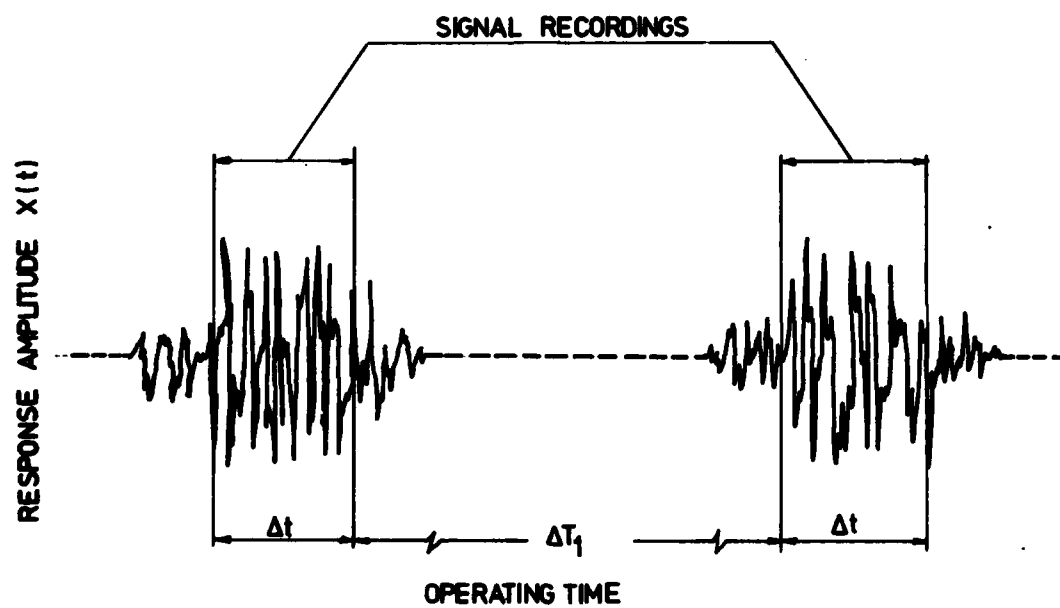


Fig. 7: Schematic Representation of the Signal Recording Durations and the Period of Stationarity Intervals.

THE SHOCK AND VIBRATION BULLETIN CLASSIFICATION CHANGE NOTICE (U)

(U) NOTICE #2 (July 1978)

1. Shock and Vibration Bulletin 35, Part 1 of March 1966.
  - a. Article Page 1 - "A Simulated 25-30 CPS Deck for Shock Testing", Culver J. Floyd, Raytheon Company - Declassified
  - b. Article Page 13 - "Blast Loading of Model Antenna Structures", R. Kirk Gregory, Southwest Research Institute - Declassified
  - c. Article Page 23 - "Background and Current Status of Underwater Explosion Shock Specifications and Testing", Gerald M. Mayer, Navy UWSL - Declassified
  - d. Article Page 29 - "Magnetic Tape Recording in a Severe Missile Environment-A Case History", J.P. White and J. Montsma, Bell Telephone Laboratories - Declassified
  - e. Article Page 101 - "Analysis of Response of Equipment on a Drop Test Shock Machine", R.L. Bort, DTMB - Classified  
CONFIDENTIAL by Authority of NAVSHIP INSTR 5510.67,  
Exempt from GDS of E.O. 11652, Exempt Category 3,  
Automatically declassified 31 December 1996.
2. All of the articles included in Shock and Vibration Bulletin 35, Part 1 of March 1966 have been reviewed for current classification, and only the article on page 101 remains classified (Confidential as indicated in paragraph 1. (e) above).
3. AUTHORITY - NRL ltr 1240-221:HWO:lm of 4 August 77 and NRL ltr 1240-5:HWO:sbn of 1 February 1978

NOTE: Authors and Contributors to previous Shock and Vibration Bulletins are requested to review their submissions and to inform the Shock and Vibration Information Center of any changes in classification and/or declassification.



**END**

**FILMED**

**12-84**

**DTIC**